A Thesis entitled

Ab initio Study of Solid Energetic Materials

Submitted to

University of Hyderabad

For the award of the degree of

Doctor of Philosophy

in

Physics

by

Prathap Kumar Jharapla (15ACPA11)

 $Under\ the\ Supervision\ of$

Dr. G. S. Vaitheeswaran





Advanced Centre for Research in High Energy Materials (ACRHEM) **School of Physics** University of Hyderabad Hyderabad-500046

(November, 2021)

Dedicated to

"To my grandparents" Jharapla Sajya Naik & Naji





Declaration

I, Prathap Kumar Jharapla hereby declare that, the work reported in this thesis entitled, "Ab initio Study of Solid Energetic Materials", is original and has been carried out by me under the supervision of Dr. G. S. Vaitheeswaran, ACRHEM, School of Physics, University of Hyderabad, Telangana, India, as per the Ph.D. ordinances of the University. I also declare that, this work is free from plagiarism and it has not been submitted for the award of a research degree at any other University. I hereby agree that my thesis can be deposited in Shodhganga or INFLIBNET.

A report on plagiarism statistics from the university librarian is enclosed.

(Jharapla Prathap Kumar)

Reg. No: 15ACPA11

(Dr. G. S. Vaitheeswaran)

G. Vaithesmoner

Thesis Supervisor,

ACRHEM, School of Physics,

University of Hyderabad.

Dr. G.S. Vaitheeswaran Associate Professor School of Physics University of Hyderabad Hyderabad-500 046. (TS) INDIA





Certificate

This is to certify that, the thesis entitled "Ab initio Study of Solid Energetic Materials", submitted to the University of Hyderabad by Mr. Prathap Kumar Jharapla bearing Reg. No. 15ACPA11 in partial fulfilment of the requirements for the award of Doctor of Philosophy in Physics, is a bonafide work carried out by him under my supervision and guidance, which is a plagiarism free thesis. The thesis has not been submitted previously in part or in full to this or any other University or Institution for the award of any degree or diploma.

> Dr. G.S. Vaitheeswaran Associate Professor School of Physics University of Hyderabad Hyderabad-500 046. (TS) INDIA

(Dr. G. S. Vaitheeswaran)

G. Vaithees war

Thesis Supervisor,

ACRHEM, School of Physics,

University of Hyderabad.

Director.

ACRHEM.

University of Hyderabad.

Director ACRHEM Dean,

School of physics,

University of Hyderabad.

School of Physics University of Hyderabad Hyderabad-500 046, INDIA



Certificate of Course Work

This is to certify that the thesis entitled "Ab initio Study of Solid Energetic Materials", submitted to the University of Hyderabad by Mr. Prathap Kumar Jharapla bearing Reg. No. 15ACPA11, in partial fulfilment of the requirements for the award of Doctor of Philosophy in Physics at ACRHEM, School of Physics, University of Hyderabad, is a bonafide work carried out by him under my supervision and guidance. This thesis is free from the plagiarism and has not been submitted previously in part or in full to this or any other University or Institution for the award of any degree or diploma.

Further, the student has the following publications before submission of the thesis for adjudication:

- Prathap Kumar Jharapla, E. Narsimha Rao, G. Vaitheeswaran, *Unusual optical isotropy in anisotropic alkali metal perchlorates MClO₄ (M=Li, Na, K, Rb, Cs)*, J. Phys. Condens. Matter, **2018**, 28, 30, 47,475402. (Chapter 3)
- Prathap Kumar Jharapla, Subrata Mondal, G. Vaitheeswaran, Comparative DFT study of vibrational, electronic and optical properties of energetic metal salts based on nitrogen rich 5-aminotetrazole, J. Comput. Chem., 2021, 42, 180-191. (Chapter 4)
- Prathap kumar Jharapla, G. Vaitheeswaran, M. K. Gupta, R. Mittal, Comparative study of electronic structure, optical properties, lattice dynamics and thermal expansion behavior of energetic ammonium and potassium dinitramide salts, Mater. Chem. Phys., 2021, 267, 124645. (Chapter 5)

Manuscripts under preparation/review:

• Prathap Kumar Jharapla, First principle study of potential replacement of lead azide and Ammonium dinitramide: DBX-1 and HNF, 2021 (Chapter 5 and 6)

Also, made presentations in the following conferences:

• B. Moses Abraham, **Prathap Kumar Jharapla** and G. Vaitheeswaran, *High pressure studies of hydrogen bonded energetic material 3,6-dihydrazino-s-tetrazine using*

DFT, International Conference on Electronics, Physics and Chemistry, Jyothi Nivas College, Bangalore, February, (2017-ORAL) .

- Subrata Mondal, **Prathap kumar Jharapla**, G. Vaitheeswaran, Structure-property correlations of bis(nitrofurazano) furazan (BNFF-1): A density functional theory study, DAE Solid State Physics Symposium, AIP Conf. Proc., (2018-POSTER).
- Prathap Kumar Jharapla, Subrata Mondal, G. Vaitheeswaran, Comparative DFT study of vibrational, electronic and optical properties of energetic metal salts based on nitrogen rich 5-aminotetrazole, International conference on condensed matter physics, Institute of Engineering and Management, Kolkata, collaboration with AIP, 14-16th November, (2019-ORAL)

The following courses have taken as part of the course work:

Course No.	Course offered at	Title of the Course	Credits	Pass/Fail
PY801	School of Physics	Advanced Quantum Mechanics	4	Pass
AC804	School of Physics	Advanced EM Theory	4	Pass
AC801	ACRHEM	Research Methodology	4	Pass
AC804	School of Physics	Advanced Mathematical Methods	4	Pass

Dr. G.S. Vaitheeswaran
Associate Professor
School of Physics
University of Hyderabad
Hyderabad-500 046 (TS) INDIA

(Dr. G. S. Vaitheeswaran)

Thesis Supervisor,

ACRHEM, School of Physics,

University of Hyderabad.

Director,

ACRHEM.

University of Hyderabad.

Director ACRHEM Dean,

School of physics,

University of Hyderabad.

DEAN

School of Physics
University of Hyderabad
Hyderabad-500 046, INDIA

Acknowledgments

हरे कृष्ण हरे कृष्ण कृष्ण कृष्ण हरे हरे हरे राम हरे राम राम राम हरे हरे

"...may the LORD KRISHNA bless us all..."

Pursuing a Ph.D. is a difficult and sometimes a lonely path. In pursuing this path, my immeasurable appreciation and deepest gratitude for the help and support are extended to the following persons who in one way or another have contributed to making this research possible.

First and foremost, I am entirely indebted to my supervisor *Dr. G. S. Vaitheeswaran* whose expertise, understanding, continuous support, professional guidance, and consistent encouragement throughout the research period made it possible for me to work on the topic of interest. His guidance has been instrumental in my development as a researcher, and his patience and highly coherent suggestions have allowed me to mature. He spent endless hours proofreading my research papers and giving me excellent suggestions which always resulted in improved versions of documents. His wisdom, encouragement, and willingness to assist at odd hours was a unique formula for the successful completion of this work, and I am sure these words are not sufficient to thank my supervisor.

I extend my sincere thanks to the director $Dr.\ V.\ Kameswara\ Rao$ and former director's of ACRHEM, Dean $Prof.\ Ashok\ Chatterjee$ and former deans of School of Physics for their unconditional academic support. My sincere and heartfelt gratitude and appreciation to the doctoral advisory committee $Prof.\ Ashok\ Chatterjee$ and $Dr.\ G.\ Manoj\ Kumar$ University of Hyderabad for their suggestions and their continuous support during my doctoral research work. I also like to thank $Prof.\ Subhash\ Chaturvedi,\ Prof.\ E.\ Harikumar,\ Prof.\ S.\ Venugopal\ Rao\ and\ Prof.\ A.\ K.\ Chaudhary\ for\ their\ suggestions and teachings in the course work. I greatly appreciate the support received through the collaborative work undertaken with the <math>Prof.\ Ranjan\ Mittal$, Homi Bhabha National Institute and $Dr.\ Mayank\ Gupta$, Solid State Physics Division, Bhabha Atomic Research Center. I would like to thank DRDO, Govt of India through ACRHEM for their financial support and office staff (ACRHEM and School of Physics) for their administrative support. I would like to thank the Centre for Modelling Simulation and Design CMSD, University of Hyderabad for providing the computational facilities.

I have to mention my best thanks to all my group members Dr. S. Appalakondaiah, Dr. N. Yedukondalu, Dr. E. Narsimha Rao, Dr. Nagaraju Guthikonda, Bushnagar Adivaiah, Subrata Mondal, Dr. B. Moses Abraham, T. Aiswaraya, Supratik Mukherjee. I also thank my flatmates and close friends Dr. Samuel Anurag, Raja Galla, Dr. Kesaban Sankar Roy Choudhury, Somnath Chatterjee for being a partner in Maggie, a partner in stupidity, a partner in late-night parties, and for having my back always. I also thank S. Leelashree, Dr. M. S. S. Bharathi Ramana, Phani Sree, Akash kumar Tarai, Dr. M. V. Jyothirmai, Janapati Yellaiah, for your wonderful patience, warm humor, extending their sympathetic attitude, timely motivation, unstinted support, and unfailing help during the entire study. I am lucky to have made such great friends. Further, I would like to express my sincere thanks to all ACRHEM and School of Physics friends for helping and supporting me unconditionally on this long and sometimes difficult journey.

Especially, I convey my heartfelt thanks and love to my wife *Shirisha*, for her understanding of research life and continued encouragement/support for fulfilling my dream. I would like to give my lovely heartfelt wishes and blessings to my sweet younger brother *J. Sagar* and my sister in law *J. Aparna*, for taking care of responsibilities at home in my absence. I am grateful to my best buddies *N. B. Tomthin, Akash Nag, Shivaraj, Asith, Ajay, Vikas Adithya, Dr. T. Vamshi Krishna, Deepika Lahari, Ujwala Kiranmai, Manoj Kumar, Lidhyal Leena, P. Indu, Y. Joythi, Masath for being with me whenever I needed. I will never forget the teachers (from school to college days) who inspired and encouraged me throughout my career for laying the necessary foundations to achieve my big dream.*

I use this opportunity to especially thank my parents, J. Balram Naik and J. Balamani and my aunt M. Shyamala for their unconditional love support, (infinitely; the word is not enough), for their continuous blessings from my childhood, for giving me full freedom and having faith in me to achieve my dreams. A special thanks to my Maternal grandpa T. Phool Singh and grandma T. Bhanki bai. A big THANK YOU to my parents, my family, and friends for their unconditional love and support!!!.

JAI HIND!!!

-Jharapla Prathap Kumar

Table of Contents

				Page
Li	st of	Figure	es	xvii
Li	st of	Tables	${f s}$	xxi
1	Intr	roducti	ion	1
	1.1	Energe	etic Materials	. 1
		1.1.1	Propellant	. 2
		1.1.2	Green Propellant	. 2
		1.1.3	Pyrotechnic	. 3
		1.1.4	High performance explosive	. 4
	1.2	Densit	ty functional theory	. 4
	1.3	Outlin	ne of thesis	. 6
2	The	oretice	$al\ background$	13
	2.1	The M	Many body problem	. 14
		2.1.1	Hohenberg and Kohn theorem	. 16
		2.1.2	Kohn-Sham Equation	. 17
	2.2	Excha	inge-correlation functionals	. 18
		2.2.1	Local density approximation	. 18
		2.2.2	Generalized gradient approximation	. 19
		2.2.3	Dispersion correction methods	. 20
	2.3	The B	Born-Oppenheimer approximation	. 21
	2.4	Densit	ty functional theory	. 22
	2.5	Metho	$\operatorname{odology}$. 23
		2.5.1	Density functional perturbation theory	. 23
		2.5.2	Full-potential linearized augmented plane wave (FP-LAPW) $$. 25
	2.6	Pseud	opotentials	. 26

		2.6.1	Norm-Conserving (NC)	. 28
		2.6.2	Ultrasoft	. 28
		2.6.3	Projector augmented wave(PAW) method	. 28
		2.6.4	Tran-blaha modified Beck-johnson potential (TB-mBJ)	. 29
3	Alk	ali Me	$etal\ Perchlorates\ MClO_4\ (M=Li,\ Na,\ K,\ Rb,\ Cs)$	35
	3.1	Introd	luction	. 36
	3.2	Comp	utational details	. 37
	3.3	Result	ts and discussion	. 38
		3.3.1	Crystal structure and the equation of state	. 38
		3.3.2	Vibrational properties	. 43
		3.3.3	Born effective charges (BEC's)	. 47
		3.3.4	Electronic band structure and density of states	. 47
		3.3.5	Optical properties	. 52
	3.4	Concl	usions	. 57
4	Ali	kali m	$etal \ 5 ext{-}Aminotetrazole \ M5 ext{-}At \ (M=Li,\ Na,\ K,\ Rb,\ Cs)$	63
	4.1	Introd	luction	. 64
	4.2	Comp	outational details	. 65
	4.3	Result	ts and discussion	. 66
		4.3.1	Structural properties of Alkali metal 5-Aminotetrazole	. 66
		4.3.2	Vibrational properties	. 70
		4.3.3	Born effective charges (BEC's)	. 74
		4.3.4	Electronic structure and density of states	. 74
		4.3.5	Optical properties	. 81
	4.4	Concl	usions	. 86
5	En	ergetic	c Eco-friendly Oxidizers HNF, ADN, and KDN	91
	5.1	Introd	luction	. 92
	5.2	Comp	outational details	. 93
	5.3	Result	ts and discussion	. 95
		5.3.1	Structural properties of HNF, ADN, KDN	. 95
		5.3.2	Vibrational properties	. 97
		5.3.3	Phonon dispersion of ADN and KDN	
		5.3.4	Born effective charges (BEC's)	
		5.3.5	Elastic constants	
		5.3.6	Electronic structure and chemical bonding	
		5.3.7	Optical properties	
	5.4	Concl		. 118

6	Po	tentia	$oldsymbol{l}$ Replacement of Lead Azide: $oldsymbol{DBX-1}$ ($C_2Cu_2N_{10}O_4$)	125
	6.1	Introd	luction	. 126
	6.2	Comp	utational details	. 127
	6.3	Result	ts and discussion	. 128
		6.3.1	Crystal structure	. 128
		6.3.2	Vibrational properties	. 128
		6.3.3	Born effective charges (BEC's)	. 135
		6.3.4	Elastic properties	. 135
		6.3.5	Electronic band structure and density of states	. 137
		6.3.6	Optical properties	. 138
	6.4	Concl	usions	. 142
7	Sun	nmary	& Future scope	147
	7.1	Summ	nary	. 147
	7.2	Future	e scope	. 151
Li	st of	Public	cations	153

List of Figures

2.1	Self-consistent algorithm for solving Kohn-Sham	19
2.2	Sketch of pseudopotential	27
3.1	Crystal structure of $LiClO_4$, $NaClO_4$, $KClO_4$, $RbClO_4$, $CsClO_4$	40
3.2	Vibrational animations at various frequencies for alkali metal perchlorates	
	$LiClO_4$, $NaClO_4$, $KClO_4$, $RbClO_4$, $CsClO_4$	45
3.3	Calculated IR spectra of alkali metal perchlorates (M= Li, Na, K, Rb, Cs)	
	$MClO_4$	46
3.4	Calculated electronic band structure of $LiClO_4$, $NaClO_4$, $KClO_4$, $RbClO_4$,	
	$CsClO_4$ using TB-mBJ functional at experimental crystal structures	50
3.5	Calculated Total and partial density of states of $LiClO_4$, $NaClO_4$, $KClO_4$,	
	$RbClO_4$, $CsClO_4$ using TB-mBJ potential at experimental crystal structures.	51
3.6	The figure represnts Dielectric constant, Dielectric loss, Absorption, Re-	
	fraction, Eloss function, Reflectivity of LiClO ₄ , NaClO ₄ , using TB-mBJ	
	functional at experimental crystal structures	54
3.7	The figure represents Dielectric constant, Dielectric loss, Absorption, Re-	
	fraction, Eloss function, Reflectivity of $KClO_4$, $RbClO_4$ using TB-mBJ	
	functional at experimental crystal structures	55
3.8	The figure represents Dielectric constant, Dielectric loss, Absorption, Re-	
	fraction, Eloss function, Reflectivity of CsClO ₄ using TB-mBJ functional	- a
	at experimental crystal structures	56
4.1	Crystal structure of Alkali metal 5-Aminotetrazole (a) Li 5-At, (b) Na 5-At,	
	(c) K 5-At, (d) Rb 5-At, (e) Cs 5-At	68
4.2	Pressure variation of IR spectra of 5-At based alkali metal salts (Li 5-At, K	
	5-At, Rb 5-At, Cs 5-At) in the (a) Low frequency range (b) Mid frequency	
	range (c) High frequency range	72

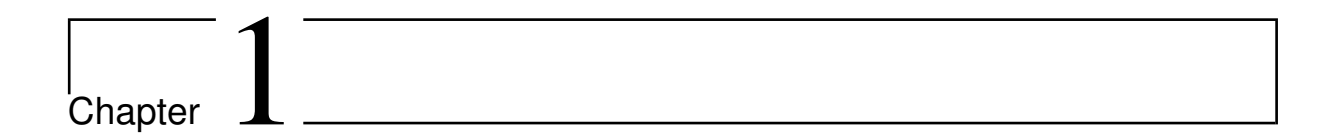
4.3	Pressure variation of IR spectra of Na 5-At (a) Low frequency range (b)	
	Mid frequency range (c) High frequency range	73
4.4	Calculated electronic band structure of Li 5-At, Na 5-At, K 5-At, Rb 5-At,	
	Cs 5-At using TB-mBJ functional at experimental crystal structures. $\ . \ .$	77
4.5	Calculated total and partial density of states of Li 5-At and K 5-At using	
	TB-mBJ functional at experimental crystal structures	79
4.6	Calculated total and partial density of states of Na 5-At using TB-mBJ	
	using TB-mBJ functional at experimental crystal structures	80
4.7	Calculated total and partial density of Rb 5 At and Cs 5-At using TB-mBJ	
	functional at experimental crystal structures	81
4.8	The figure represents Dielectric constant $\varepsilon_1(\omega)$, Dielectric loss $\varepsilon_2(\omega)$, Ab-	
	sorption ($\alpha(\omega) \times 10^4 \text{ cm}^{-1}$), Refraction n(ω), Reflectivity R(ω), Eloss func-	
	tion $L(\omega)$ of Li 5-At and Na 5-At using TB-mBJ functional at experimental	
	crystal structure.	83
4.9	The figure represents Dielectric constant $\varepsilon_1(\omega)$, Dielectric loss $\varepsilon_2(\omega)$, Ab-	
	sorption $(\alpha(\omega) \times 10^4 \text{ cm}^{-1})$, Refraction $n(\omega)$, Reflectivity $R(\omega)$, Eloss func-	
	tion $L(\omega)$ of K 5-At and Rb 5-At using TB-mBJ functional at experimental	
	crystal structure.	84
4.10		
	sorption $(\alpha(\omega) \times 10^4 \text{ cm}^{-1})$, Refraction $n(\omega)$, Reflectivity $R(\omega)$, Eloss func-	
	tion $L(\omega)$ of Cs 5-At using TB-mBJ functional at experimental crystal	
	structure	85
5.1	Unit cell for (Left top) Hydrazinium nitroformate (HNF), (Right top) Am-	
	monium dinitramide (ADN), (Bottom) Potassium dinitramide (KDN)	96
5.2	Theoretical IR spectrum of Hydrazinium nitroformate: 0-3500(cm ⁻¹), Am-	
	monium dinitramide: $0-3500(\text{cm}^{-1})$, Potassium dinitramide: $0-1530(\text{cm}^{-1})$.	99
5.3	Calculated phonon dispersion of ADN and KDN	105
5.4	Calculated phonon density of states for ADN and KDN crystal structures.	106
5.5	Calculated band gap of (a) Hydrazinium nitroformate (b) Ammonium	
	dinitramide (c) Potassium dinitramide	111
5.6	Total and Partial DOS of Hydrazinium nitroformate (HNF)	112
5.7	Total and Partial DOS of Ammonium dinitramide (ADN) and Potassium	
	dinitramide (KDN)	113
5.8	The figure represents Dielectric constant $\epsilon_1(\omega)$, Dielectric loss $\epsilon_2(\omega)$, Ab-	
	sorption $\alpha(\omega)$, Reflectivity $R(\omega)$, Refraction $n(\omega)$, Eloss function $L(\omega)$ of	
	HNF using TB-mBJ functional at experimental crystal structures	116

5.9	The figure represents Dielectric constant $\epsilon_1(\omega)$, Dielectric loss $\epsilon_2(\omega)$, Ab-
	sorption $\alpha(\omega)$, Reflectivity $R(\omega)$, Refraction $n(\omega)$, Eloss function $L(\omega)$ of
	ADN and KDN using TB-mBJ functional at experimental crystal structures.117
6.1	Crystal structure of DBX-1 (Copper(I) 5-nitrotetrazolate) 129
6.2	Calculated IR spectra of DBX-1
6.3	Electronic band structure of DBX-1 along the high symmetry directions in
	the Brillouin zone
6.4	Calculated partial and total density of states of DBX-1
6.5	The figure represents Dielectric constant, Dielectric loss, Absorption, Re-
	fraction, Reflectivity, Eloss function of DBX-1 using TB-mBJ functional at
	the experimental crystal structure

List of Tables

3.1	Calculated lattice parameters (a, b, c in Å) and Volume (V in Å ³) of of $MClO_4$ (M = Li, Na, K, Rb, Cs) using standard LDA (CA-PZ),GGA	
	(PBE) and semiempirical schemes LDA+OBS, PBE+G06, PW91+OBS with the expirement data.	41
3.2	Calculated Theoretical (T) and Experimental(E) inter-atomic distances (in	41
0.2	Å) of $MClO_4$ (M = Li, Na, K, Rb, Cs)	42
3.3	Calculated phonon frequencies (in cm ⁻¹) along with corresponding assign-	
	ment	44
3.4	Calculated BEC's and percentage of deviation of the Li, Na, K, Rb, Cs,	
	Cl, O1, O2, O3 atoms at the theoretical equilibrium volumes	48
3.5	Calculated band gap of $MClO_4$ M =(Li, Na, K, Rb, Cs) along high sym-	
	metry directions using PBE-GGA, EV-GGA, TB-mBJ potential	49
3.6	Calculated optical transitions corresponding to the peaks below 15 eV. $$	53
3.7	Linear optical properties such as real part of dielectric function $\varepsilon_1(\omega)$ and	
	absorption coeffcient $(\alpha(\omega) \times 10^4, \text{ cm}^{-1})$ of MClO ₄ (M = Li, Na, K, Rb, Cs).	54
4.1	Calculated structural lattice parameters (a, b, c in Å) and Volume (V	
	in \mathring{A}^3) of Li 5-At, Na 5-At, K 5-At, Rb 5-At, Cs 5-At using LDA (CA-	
	PZ) and GGA (PBE) functionals as well as with van der Waals corrected	
	LDA+OBS, PBE+G06, PW91+OBS schemes along with experimental re-	
	sults	69
4.2	Born effective charges of Li 5-At, K 5-At, Rb 5-At and Cs 5-At	75
4.3	Born effective charges of Na 5-At	76
4.4	Computed band gap (in eV) of Li 5-At, Na 5-At, K 5-At, Rb 5-At, Cs 5-At	
	with different schemes such as PBE-GGA and TB-mBJ potential	78
4.5	Optical transitions corresponding below 10 eV	85
4.6	Values of dielectric real part $\varepsilon_1(0)$ and refractive index $n(0)$ as a function of energy (eV) (M = Li, Na, K, Rb, Cs) 5-Aminotetrazole	85

5.1	The relaxed lattice parameters ($a, b, c \text{ in } \text{Å}$) and Volume (V in Å^3), of KDN
	and HNF using standard LDA (CA-PZ),GGA (PBE) and semiempirical
	schemes LDA+OBS, PBE+G06, PW91+OBS with deviation percentage
	and experimental data
5.2	The Calculated vibrational modes from 41 cm ⁻¹ to 184 cm ⁻¹ representing
	Translation:Trans, Rotation:Rotat., for KDN
5.3	The Calculated vibrational modes 188 cm ⁻¹ to 1451 cm ⁻¹ representing
	Bending:bend., Scissoring:Sciss.,Rocking:Rock, Wagging:Wagg. streatch-
	ing: Stre., symmetric:symm.stre., asymmetric:asymm.stre., for KDN 101
5.4	The Calculated vibrational modes from 42 cm ⁻¹ to 719 cm ⁻¹ representing
	Translation:Trans, Rotation:Rotat., for HNF
5.5	The Calculated frequencies in(cm ⁻¹ of HNF 720 cm ⁻¹ to 3378 cm ⁻¹ , rep-
	resenting Bending:bend., Wagging:Wagg., Rocking:Rock, Scissoring:Sciss.,
	streatching: Stre., symmetric:symm.stre., asymmetric:asymm.stre., for HNF.103
5.6	Theoretical Born effective charge tensors and percentage deviation from
	nominal charge of ADN, KDN and HNF)(H=+1,N=-3,O=-2,C=+4, K=+1)
	at the theoretical equilibrium volumes
5.7	Comparison of elastic constants of Ammonium dinitramide (ADN), Potas-
	sium dinitramide (KDN) and Hydrazinium nitroformate(HNF) 109
5.8	Real part of dielectric function $\varepsilon_1(\omega)$ and refractive index $n(\omega)$ of HNF,
	ADN and KDN
C 1	C_{1} , C_{2} , C_{3} , C_{4} , C
6.1	Calculated lattice parameters (a, b, c in Å) and Volume (V in ų) of DBX-
	1 using standard LDA (CA-PZ), GGA (PBE) and semiempirical schemes
6.2	LDA+OBS, PBE+G06, PW91+OBS with the experiment data 129 Colculated vibrational fraguencies (in em ⁻¹) for DPV 1 (24 cm ⁻¹ to 221
0.2	Calculated vibrational frequencies (in cm^{-1}) for DBX-1 (24 cm^{-1} to 231 cm^{-1})
6.3	Calculated vibrational frequencies (in cm ⁻¹) for DBX-1 (233 cm ⁻¹ to 1253
0.5	cm ⁻¹)
6.4	Calculated vibrational frequencies (in cm ⁻¹) for DBX-1 (628 cm ⁻¹ to 1457
0.4	cm ⁻¹)
6.5	Calculated BEC's of DBX-1 (C, N, O, Cu) at the theoretical equilibrium
0.0	volumes
6.6	Calculated elastic constants of DBX-1 compared with previously reported
0.0	lead azide



Introduction

1.1 Energetic Materials

Energetic Materials (EMs) are used in both civilian and military applications. The term energetic materials are principally used for any material that can drive itself to a highly energetic state through a chemical reaction [1]. High energy materials are divided into three classes, i.e., explosives, propellants, and pyrotechnics. Primarily, an explosive is a substance that, after being initiated by forces such as heat, shock, or pressure, goes through an immense exothermic reaction resulting in either detonation or deflagration, ultimately creating a redox reaction. This results in a large volume of hot gases and sounds before expanding to create a blast wave. Explosives are known to be discovered by the Chinese in the first millennium AD; probable reference of gunpowder emerged in 142 AD. It is one of the great four inventions of the Chinese; gunpowder is often referred to as black powder in recent times. Gunpowder has been used for non-military objectives such as fireworks for amusement or explosives for mining and tunneling. However, explosives pursue to play a devastating role in the progress and prosperity of humankind, right from the time of the discovery of gunpowder several centuries ago. It also helps build the nation's infrastructure in terrains and inaccessible areas during road construction, quarrying, and mining. So, according to usage and application in various sectors, explosives are labeled as low and high. Low explosives are further categorized as propellants and pyrotechnics. The reaction velocity for these low explosives is considered to be from 600 to 900 m/sec. These mixtures are volatile substances when ignited, go through swift combustion. Whereas high explosives are categorized into primary and secondary explosives. The chemical mixture of high explosives detonates at a reaction velocity of about 1600 m/sec, generating a shock wave. Researchers have shown considerable interest in exploring pyrotechnic materials with low smoke and propellants with superior efficiency and enhanced insensitivity nature to thermal and shocks. Altogether, investigation towards eco-friendly, energetic explosives that do not contain any metal products and toxic ingredients while combustion is of interest.

1.1.1 Propellant

A propellant is an explosive material consisting of a fuel and an oxidizer, which undergoes a carefully controlled and rapid combustion without detonation, producing sustained pressure over a long period engendering in a giant volume of hot gas. This gas can be used to propel a projectile or can be used as a gas generator. Fuel is a substance that inflames when incorporated with oxygen-producing gas for propulsion. At the same time, an oxidizer releases oxygen for combustion with the fuel. To produce gas instantly, a propellant must fetch its oxygen together with an appropriate quantity of fuel elements like carbon, hydrogen, etc. Propellants are categorized into three sections according to their state that is solid, liquid, and hybrid. To begin with, solid propellants (SP) produce high-temperature gaseous products on combustion and are used in gun and rocket propulsion systems. Solid propellants consist of chemical ingredients such as fuel, curing agent, oxidizer, stabilizer, cross-linking agent, and binder. However, solid propellants blaze constantly, restricting their utilization in numerous applications. Rockets employed with SP consist of the initial (boost) phase of military missiles, commercial missiles, and the beginning stage boosters connected to either side of the liquid-fuel tank on the space shuttle. Whereas in liquid propellants (LP), oxidizer and fuel are deposited in independent tanks and are fueled by means of pipes, pumps, and valves to a combustion compartment where they merge and generate a thrust. LP offers various advantages and is more complex than solid propellants (SP). When compared with LP, SP is easy to store, handle and transport with simple engines designs. Whereas the liquid propellants have high specific impulse and manipulation of the fuel and calibration of the engine is easy, which is quite the opposite in the case of SP. Liquid propellants used in rocketry can be sorted into three types: petroleum, cryogens, and hypergolic. Hybrid propellant (HP) engines serve as an intermediate group among solid and liquid propellants, wherein solid is one of the substances, usually the fuel, while the other is the oxidizer, which is liquid. Hybrid rockets avert several drawbacks of solid rockets, like the risk of propellant handling, and also evade some drawbacks of liquid rockets such as mechanical intricacy. Due to the difficulty in mixing fuel and oxidizer intimately, hybrid propellants tend to fail.

1.1.2 Green Propellant

The current research on green propellants was intensified due to the high usage of hydrazine which is of concern. Mono propellant hydrazine propulsion systems are cuttingedge for numerous applications ranging from launchers to large-scale and small satellites. It has severe drawbacks of being highly toxic, carcinogenic and consequently requires extensive safety procedures. To find environment-friendly ("green") and non-toxic propellants, intense research was initiated in the field of new green propellant utilization.

"Green propellant" represents the one that has the potential to be non-toxic, reduced adverse impact to the environment, storable and safe, while still having the performance to meet mission requirements. In the open literature, ADN (Ammonium Dinitramide), HAN (Hydroxylammonium Nitrate), and HNF (Hydrazinium Nitroformate) are oxidizers of new aqueous ionic mono propellants considered to be green propellants. The main advantage of these new formulations is the lower melting point, high density, high volumetric impulse, and accessibility on a semi-industrial scale. ADN and HNF are available in solid form but whereas HAN is available only in aqueous solutions. The oxygen balance of HAN is around 33% which is higher than ADN (26%) and HNF (13%). The only disadvantage of these compounds is the hygroscopic nature which they possess. While HAN has the highest volumetric thrust than ADN and HNF. Among the three compounds, HAN was considered to have the feasibility to synthesis at laboratory scale, comfortable in storage and handling properties, and also safety properties. We investigate ADN, KDN (KDN is an intermediate compound in the course of ADN synthesis), and HNF, a potential alternative for ADN.

1.1.3 Pyrotechnic

Pyrotechnic from the Greek word 'pyros' means fire and 'technic' means art [2], this art produces optical and acoustical effects. Pyrotechnics falls under the category of low explosives, usually consisting of metal powder and an inorganic oxidizer. These materials are quite slow-burning, non-explosive powders such as metals, alloys, and hydrocarbon mixtures. These low explosives contain a combination of substances intend to produce heat, smoke, sound, gas, and light with self-sustained exothermic chemical reactions. The exothermic reactions used in pyrotechnics are build on easy redox reactions. By variation in the composition of reducing agents and oxidizers, the redox reaction can be influenced to achieve well-defined effects. These effects include reaction rate, the heat of reaction, reaction temperature, gas production, glowing particles, and colored light. The application of these effects can be noticed in products such as airbags, cable cutters, igniters, thermites, even in fire extinguishers and they are also widely used in the military as flares, colored and white smoke generators, tracers, incendiary delays, signals, relays, photo-flash compounds, and fuses [3, 4]. To enhance the performance of pyrotechnics, fuel and oxidizer must be premixed with double-base pyrotechnics or single-base pyrotechnics with minimum positive oxygen balance. They should be extremely exothermic in condensed form. This combination helps to produce much gas. Whereas in double-base pyrotechnics, the oxidizing agents may be nitrates, chlorates, peroxides, oxides, chromates, and perchlorates [5] for providing oxygen, while reducing agents may be carbon, sulfur, and metal powders. In this process, an oxidizing material provides oxygen support to the combustion of other materials. In this thesis, we tried to shed light on alkali metal perchlorates, mainly used in rocket fuel, fireworks. In addition to these, perchlorates being toxic to the environment and humans, the coloring of pyrotechnics is considered a tough topic as the absence of any metal ions. Hence, green energetic alkali metal 5-aminotetrazole materials were chosen as the next study. While, flame tests show that high nitrogen content is a reason for alkali metal 5-aminotetrazole materials can be used as coloring agents in recent pyrotechnics. All compounds show the cation specific flame colors i.e $LiCN_5H_2(Red)$, $NaCN_5H_2(orange)$, $KCN_5H_2(purple)$, $RbCN_5H_2(lavender)$, $CsCN_5H_2(pink)$.

1.1.4 High performance explosive

Primary explosive materials are used to detonate the whole explosive device which is typically connected to some other external device known as a fuse, which starts the detonation. The face of contemporary primary explosives can be described by lead styphnate (LS), lead azide (LA), where LA is the main filling for detonators and LS is used for primers. Despite its outstanding initiating and filling properties, it undergoes indubitable flaw like the tendency to go through hydrolysis in the presence of moisture, inconsistent with copper, component of the detonator fuze casing, quick deterioration into carbon dioxide, and high friction sensitivity. Primary explosives differ considerably in their sensitivity to heat and undergo a rapid deflagration to the detonation transition process. Due to the high degree of sensitivity to initiation through of fire, spark [6], impact [7] and friction [8] primary explosives generate a large amount of heat, gas, shock wave [9]. The most regularly employed primary explosive are lead azide (LA) [10], lead styphnate (LS) [11], barium styphnate, lead mononitroresorcinate (LMNR), potassium dinitrobenzofurozan (KDNBF), mercury azide and mercury fulminate [12], silver azide, tetracene [13], Diazodinitrophenol (DDNP) [14]. The energy discharged from the detonation of the primary material is used to set off the booster which in sequence sets off the main charge which is made up of secondary (insensitive) material. Secondary explosives are those that do not readily detonate, don't trigger electrostatically with ease, and depend upon larger shocks to detonate. They are used in explosive charges as well as in the propellant formulation. Some of the well-known explosives are nitrocellulose, Pentaerythritol tetranitrate (PETN), and desensitized nitroglycerine (NG), RDX [15] and Trinitrotoluene (TNT) [16]. Furthermore, the tertiary explosives are known as blasting agents which consists of ammonium nitrate (AN:NH₄NO₃), ammonium perchlorate (AP:NH₄ClO₄) [17, 18], ammonium dinitramide $(ADN:NH_4N(NO_2)_2)$ [19], aminonitrotoluene(MNT) and many more. These materials are very insensitive materials that need an intermediate explosive booster to detonate them. Even though they have superior detonation velocities and pressure than NG explosives, they are much safer to be produced in enormous quantities. In this thesis, we address the ground state properties of primary explosive DBX-1, a possible replacement of lead azide.

1.2 Density functional theory

Density-functional theory (DFT) is an outstanding theory implemented in many fields of the physical, chemical, and material sciences. From condensed matter physics, it has broadened into mineralogy, material science and high-pressure physics and efforts have

been made to extend it to obtain excited state properties. This success of DFT in the last few decades is demonstrated by overwhelming research articles published. The elemental postulate of DFT is that the total energy of the system is a distinctive function of the electron density, hence computing the full many-body wave function of the system can be avoided. Modern ab-initio simulations become a widespread method for obtaining the ground-state properties of interacting many-electron systems (atoms, molecules, and solids). Given an experimental structure, it is straightforward to observe and compute vast observable quantities such as structural information, bond angles and bond length, electronic band gaps in solids, optical and electron-energy loss spectra (EELS), elastic, born effective charges (BEC's), nuclear magnetic resonance (NMR), infrared (IR) and Raman spectra, and thermodynamic properties. The potential of the high energetic materials to liberate a large amount of energy should be controlled by minimizing the sensitivity, essentially for military purposes. HEM's having a complex crystal structure and high sensitivity to small external stimuli is a challenging problem to conduct experiments. So to have a quantitative understanding of the physical and chemical properties we have conducted simulations using DFT to understand the ground state and high-pressure properties of high energetic materials. From fundamental laws of quantum mechanics, it has been easy for the development of accurate density functionals. The general extensions for exchange and correlation terms are LDA (local density approximation) and GGA (generalized-gradient approximations). The obtained crystal structure parameters and bond lengths from geometry optimization with uncorrected DFT show an undesirably large error when compared with experimental data. The poor dispersion of interactions by exchange-correlation functionals commonly used in DFT calculations is a well-known problem. This is due to standard electron-electron interaction treated using in LDA [20, 21] and GGA [22] which fail to address weak intermolecular interaction. To correct the standard functionals, a dispersion correction method has been included to check the non-local weak van der Waals forces. After the inclusion of the dispersion corrected method, significant improvements in equilibrium unit cell volume for molecular crystals are observed. The dispersion corrected Grimme (G06) [23], Tkatchenko-Scheffler(TS) [24], and Ortmann, Bechstedtand Schmidt(OBS) [25] are used. It has long been acknowledged that various materials properties are understood by their electronic structure, recently it has become possible to compute this behavior with better precision. Calculating the electronic bandgap with the Kohn-Sham potential significantly underestimates the fundamental gap for a maximum number of semiconductors, insulators, and strongly correlated systems. Also, widely known for predicting a metallic ground state for numerous transition-metal oxides [26]. The fundamental problem from functionals LDA and GGA is the self-interaction error and derivative discontinuity which is quite important to compare the obtained Kohn-Sham bandgap. Recently Becke and Johnson designed to reproduce the exact exchange potential in atoms, known as TB-mBJ potential. All the electronic structure and optical properties calculations in this thesis are done using TB-mBJ potential with the FP-LAPW method.

1.3 Outline of thesis

The Chapter is a introductory about the High energetic materials and Chapter gives a brief introduction of the approaches and theories used in this work. These two chapters familiarize the reader with the objectives of the work. Chapter provides a detailed investigation on structural, vibrational, born effective charge (BEC's), electronic and optical properties of $MClO_4(M=Li, Na, K, Rb, Cs)$. Despite the anisotropic structure, these materials tend to show optical isotropic nature. While perchlorate is dangerous for the environment and humans, Chapter4 addresses various properties of nitrogen-rich alkali metal 5-aminotetrazole materials. The use of energetic nitrogen-rich materials towards the substitution of perchlorate in pyrotechnics is a topic of interest. Nitrogen-rich molecules are one approach in developing environmentally sustainable green energetic products since the earth's atmosphere occupies 78% composition of molecular nitrogen. This can be an alternate route to improve the performance and sensitivity to impact, friction, and shock. Heterocyclic nitrogen-rich molecules like Imidazoles, Triazoles, Tetrazoles, Triazines, Tetrazines [27] are extensively used as the effective precursors for the preparation of HEDM's (High energy density materials), owing to great density when compared to its carbon analogs. These compounds carry a considerable percentage of nitrogen atoms with a high heat of formation, $+237.2 \text{ kJ-mol}^{-1}$ [28]. In particular, tetrazoles has excellent property of amalgamating high positive heat of formation as well as large nitrogen content with good thermal stability owing to their aromatic ring system [29, 30]. Tetrazoles group are known for explosive or combustive properties, besides this group even shows a wide range of important applications in pharmaceutical and agricultural sector. Moreover, due to the environment-friendly nature, non-poisonous, inexpensive, easy to prepare, and nitrogen gas remaining the significant end product during combustion, tetrazole is of high concern. 5-Aminotetrazole (5-At) is a tetrazole-based material, while tetrazole is a five-membered heterocyclic ring structure, which possesses aromatic reactivity, non-toxic reaction products at high temperature, high burn rate, and relative stability. Hence, we have addressed structural, vibrational, BEC's, electronic and optical constants of alkali metal 5-Aminotetrazole. The reported literature reveals that these materials show quite interesting properties such as coloring agents in pyrotechnics and acting as gas generators. Alkali metal 5-aminotetrazole are found to be good absorbents in the ultraviolet region with anisotropic nature in Li 5-At, K 5-At, Rb 5-At, Cs 5-At, and isotropic nature in [100] and [010] direction in Na 5-At. Furthermore, In Chapter 5, we present a comparative study of structural, electronic, optical, elastic properties, vibrational, and BEC's of HNF, ADN, and KDN. Previously reported results by Yedukondal et al. are used to address structural, high pressure vibrational, and elastic properties of ADN [31]. In continuation

to this work, we have investigated electronic and optical properties and full phonon dispersion of ADN and KDN. A comparative study with all the above mention properties has been conducted. To have more understanding about ADN and KDN compounds, we have included another eco-friendly oxidizer, Hydrazinium nitroformate (HNF), which is also a possible alternative to ammonium dinitramide. ADN and KDN are dinitramide anion-based compounds, whereas HNF is acquired from hydrazine and nitroform. In the purview of nitrogen oxide chemistry, oxy acid nitrogen is of interest. These salts consist of a new oxyanion of nitrogen called the dinitramide anion. The dinitramide anion depends on the extension of nitramide and gas-phase structure, which has C2 symmetry. Dinitramide-related compounds can replace many energetic materials in different applications such as primary and secondary explosives, insensitive ammunition, lead-free detonators, pyrotechnics as well as oxidizers. As mentioned about the toxic and harmful nature of perchlorates used in propellant and pyrotechnics, the dinitramide-based salts can be a potential replacement for these compounds. ADN is known as a replacement for ammonium perchlorate (AP), which is because ADN is a chlorine-free compound. But due to the several drawbacks of ammonium perchlorate: ADN and HNF have been considered as a possible replacement or an alternative material; at the same time, KDN is also studied since it has an intermediate compound during ADN synthesis. Chapter6 presents a unique primary explosive material with transition metal copper in the composition and a possible replacement of lead azide. Due to the environmental toxicity of lead, a green primary explosive is sought. New materials such as sliver azide, diazodinitrophenol (DDNP), calcium nutrition-tetrazole, and calcium chlorotetrazolate, all have limitations avoiding their use. While copper(1) 5-nitrotetrazolate (DBX-1) is known to be the best replacement of lead azide to date. Although, the sensitivity of DBX-1 has put a limitation on the applications of this material. This work provides a basic understanding of the structure, sensitivity, and optical nature by calculating the structural, vibrational, elastic, electronic, and optical properties of DBX-1. In the last Chapter7, the entire thesis work is summarized, and future work has been proposed. A brief abstract of the chapters is mentioned below:

Chapter3:This chapter reports a detailed study on structural, vibrational, born effective charge (BEC), electronic and optical properties of the alkali metal perchlorates, $MClO_4(M = Li, Na, K, Rb, Cs)$ based on Density functional theory. The ground-state calculations are done using the plane-wave pseudopotential method by including the dispersion corrected method for a more accurate prediction of structural and vibrational frequencies. The calculated lattice parameters and bond lengths are consistent with the experimental values. Further, detailed interpretation of the zone-centered vibrational modes yields good concurrence between the experimental and calculated values. There is a decrease in wavelength with an increase in frequency (blueshift) from $Li \rightarrow Na \rightarrow K \rightarrow Rb \rightarrow Cs$.

The obtained BEC shows the mixed covalent-ionic character of the compounds. The electronic and optical properties are calculated using the full potential linearized augmented plane wave method by TB-mBJ potential. The TB-mBJ band structure shows an indirect bandgap with O-2p states dominating in the valence band. Despite the anisotropic structure, alkali metal perchlorates are found to possess optical isotropy. These results are published in "Journal of Physics: Condensed Matter, Volume 30, November 2018, pages 475402".

Chapter4: This chapter presents a thorough density functional theory-based comparative study on nitrogen-rich 5-aminotetrazole alkali metal salts M 5-At (M=Li, Na, K, Rb, Cs). The calculated structural parameters using the plane-wave pseudopotential method are consistent with the experimental results. The computed vibrational frequencies at ambient pressure show that vibrational modes in high energy regions are due to the N-H bond of NH₂ group and NO₂ in Na 5-At. Pressure variation IR spectra of these materials clearly show frequency shifts, where Li 5-At shows an overall redshift below 900 cm⁻¹ contrary to the blue shift seen in other materials. The born effective charge values reveal the presence of strong covalency between N, H, and C atoms whereas an increased ionic nature is seen as the atomic number of metal atoms increases. Furthermore, we used the full potential linear augmented plane wave (FP-LAPW) method for calculating electronic structure and optical properties with TB-mBJ potential which provides an enhanced band gap for all materials compared to standard GGA functional. Electronic structure calculation reveals that all the compounds are indirect bandgap insulators except for Li 5-At. The computed partial density of states shows mixed ionic-covalent nature in metal-N/C bonds and covalent nature in N-C bonds. In addition, we are also presenting the optical properties such as real and imaginary dielectric constant, absorption, refraction, reflection, loss spectrum as functions of photon energy. From the optical properties, we can conclude that all the studied compounds are optically anisotropic and are good absorbers in the ultraviolet (UV) region. These results are published in "Journal of Computational Chemistry, Volume 42, 2021, 180-191".

Chapter 5:In this chapter, we present a detailed first-principles study addressing the electronic band structure, optical, vibrational, born effective charge, elastic properties of energetic salts potassium dinitramide (KDN), and Hydrazinium nitroformate (HNF). As KDN is the intermediate compound during ADN synthesis, so to have a better picture, structural, elastic, vibrational properties of ammonium dinitramide results previously reported by Yedukondalu et.al are compared with KDN and HNF. From the electronic structure, it is vivid that both the compounds are wide-bandgap insulators with an indirect bandgap of the value of 3.01 eV for HNF, 4.1 eV for ADN, and 4.37 eV for KDN. Optical constants reveal that HNF, ADN, and KDN possess considerable optical anisotropy. Analysis of the vibrational modes reveals that the N(NO₂) group contributions are considerably large

in the high-frequency region in KDN. In addition, born effective charges show a strong covalent bond between NO_2 group in ADN and KDN while N-C bond in HNF. Phonon dispersion relations computed within the harmonic approximation unambiguously show that both the compounds are dynamically stable in the reported monoclinic structure. In addition, the optical and acoustical modes are highly interactive as evident from the dispersion spectra, which might lead to low thermal conductivity, quite desirable for an energetic material. These results are published in "Materials Chemistry and Physics, Volume 267, 2021, 124645".

Chapter6: In the present chapter plane-wave, pseudopotential method (PW/PP) is used to calculate structural, vibrational, elastic, Born effective charges, and full-potential linearized augmented plane-wave (FP-LAPW) method for calculating electronic structure and optical properties of DBX-1. The optimized structural parameters, volume, are in good agreement with experimental data. The characteristic behavior of vibrational modes are assigned and the high-frequency optic modes are due to symmetric and asymmetric stretching of NO₂ group. The calculated elastic properties show that DBX-1 is mechanically stable at ambient conditions. Furthermore, Born effective charge tensors show strong covalent interaction between the N-C bond and dielectric constant exhibit ionic contribution. Electronic band structure and various optical constants are computed using TB-mBJ potential. The fundamental energy bandgap appears to be an indirect bandgap around 1.08 eV. To illustrate the participation of anion and cation states in the electronic band structure, the partial and total density of states for these compounds have been analyzed. The valence band and conduction band is dominated by Cu-p/d states, O-2p and N-p state. Using electronic structure results, we discuss directional independent optical properties, and the results reveal that DBX-1 is optically anisotropic. These results will be communicated for formal publication in an international journal.

Chapter7: The conclusion obtained from the present thesis work is presented in this chapter along with some future directions.

References

- [1] Weingart, G.W., Pyrotechnics, Chemical Publishing Company, Inc., 1947, New York, USA.
- [2] (a) Dhar, D. N. Chem. Rev. 1967, 67, 611; (b) Fatiadi, A. J. Synthesis, 1986, 249; c) Roland,
 J. R., McKusick, B. C. J. Am. Chem. Soc. 1961, 83, 1652.
- [3] Dennis. A. Teefy, Remediation Technologies Screening Matrix and Reference Guide: Version III, 8, 1, 1997, 115-121.
- [4] (a) Miura. T., Masaki, Y. Tetrahedron, 1995, 51, 10477; (b) Masaki. Y., Miura, T. Ochiai, M. Bull., Chem. Soc. Jpn. 1996, 69, 195.
- [5] Richard, P. Pohanish, Sittig's Handbook of Pesticides and Agricultural Chemicals (Second Edition), 2015, 839-842.
- [6] Fedoroff. B. T., Sheffield O. E., Encyclopedia of Explosives and Related Items (Picatinny Arsenal, Dover, NJ), 1966, 5, p E38-E55.
- [7] Fedoroff. B. T., Sheffield O. E. Encyclopedia of Explosives and Related Items (Picatinny Arsenal, Dover, NJ), 1966,7, p I35-I55.
- [8] Fedoroff. B. T., Sheffield O. E. 1966 Encyclopedia of Explosives and Related Items (Picatinny Arsenal, Dover, NJ), 1966, 1, XIII.
- [9] Fedoroff. B. T., Sheffield O. E. 1966 Encyclopedia of Explosives and Related Items (Picatinny Arsenal, Dover, NJ), 1966, 1, XVII.
- [10] Curtius. T., Chem. Ber., 1891, 24, 3345-3346.
- [11] Herz. E. V., Beilstein, 1914, 6, 405, 830.
- [12] Fedoroff. B. T., Sheffield O. E., Encyclopedia of Explosives and Related Items (Picatinny Arsenal, Dover, NJ), 1966, F217-F223.
- [13] Matyas. R., Pachman, J., Primary Explosives; Springer: Heidelberg, Germany, 2013.
- [14] Davis. T. L., The Chemistry of Powder and Explosives; GSG and Associates: San Pedro, CA, USA, 1943.

- [15] Bachmann. W. E., Sheehan, J. C., A new method of preparing the high explosive RDX, J. Am. Chem. Soc., 1949, 71, 1842-1845.
- [16] Thompson. M., The 50 best inventions of 2010: Less dangerous explosives. Time Magazine, 11 November 2011. (accessed on 29 December 2015).
- [17] Serullas. G. S., Ann. Chim. Phys., 1831, 2, 46.
- [18] Serullas. G. S., Ann. Chim. Phys., 1831, 2, 304.
- [19] Shmitt. R.J., Bottaro. J. C., Penwell. P. E. et al., Process for Forming Ammonium Dinitramide Salt by Reaction Between Ammonia and a Nitronium Containing Compound, US Patent 5316749, SRI International, USA, 1993.
- [20] Ceperley. D., Alder. B. J., Ground-State of the Electron-Gas by A Stochastic Method. Phys. Rev. Lett., 1980., 45, 566-569.
- [21] Perdew. J., Zunger. A., Self-Interaction Correction to Density-Functional Approximations for Many-Body Systems. Phys. Rev. B., 1981, 23, 5048-5079.
- [22] Perdew. J., Burke. K., Ernzerhof. M., Generalized Gradient Approximation Made Simple. Physical review letters., 1996, 77, 3865-3868.
- [23] Grimme. S., Semiempirical GGA-Type Density Functional Constructed with a Long-Range Dispersion Correction. Journal of computational chemistry., 2006, 27, 1787-1799.
- [24] Tkatchenko. A., Scheffler. M., Phys. Rev. Lett., 2009, 102, 073005.
- [25] Ortmann, F., Bechstedt. F., Schmidt. W., Semiempirical van der Waals correction to the density functional description of solids and molecular structures. Phys. Rev. B., 2006, 73.
- [26] Hasnip. P. J., Refson. K., Probert. M. I. J., Yates. J. R., Clark. S. J., Pickard. C. J., Density functional theory in the solid state. Phil. Trans. R. Soc. A, 2014, 372, 20130270.
- [27] Irannejad. H., Nitrogen Rich Heterocycles as a Privileged Fragment in Lead Discovery., Med. Analy. Chem. Int. J, 2018, 2, 3, 000125.
- [28] Li. N., Chai. C.P., Gan. Z. Y., Luo. Y. J., Review on Molecular Design and performance of Energetic ionic compounds, Chin J. Energ. Mater, 2010, 18, 467-475.
- [29] Chen. H., Zhang, Tong. L., Zhang, Jian. G., Crystal Structure and Thermal Decomposition Mechanism of a 5-aminotetrazole copper(II) complex. Struct. Chem., 2012, 23, 153-159.
- [30] Stierstorfer. J., Tarantik. K., Klapötke. T., New Energetic Materials: Functionalized 1 Ethyl 5 aminotetrazoles and 1 Ethyl 5 nitriminotetrazoles. Chemistry (Weinheim an der Bergstrasse, Germany), 2009, 15, 5775-92.
- [31] Yedukondalu. N. Ghule V., Vaitheeswaran. G., High pressure structural, elastic and vibrational properties of green energetic oxidizer ammonium dinitramide. J. Chem. Phys., 2016, 145. 064706.



Theoretical background

In this thesis, the ground state and high-pressure studies of high-energy materials are reported through density functional theory calculations. This chapter provides an overview of the theoretical background and the approximations used in this study. A wide range of information about the physical, chemical, and bulk properties of any periodic solid rely on the derivative of the total energy with reference to perturbations such as strain, electric field, atomic displacement. So, to understand several material characteristics, an accurate determination of the molecule's electronic structure is an important factor as it controls the properties of the whole system. In the last few decades, experimentalists and theoreticians have been studying these properties for various scientific and technological applications. However, due to the complexity of the condensed matter systems, experimentally studying these properties under intense conditions such as pressure and temperature remains tedious and difficult work. A computational study is a well-established field that provides an insight into the physics and chemistry of the systems subjected to study. It is usually possible to interpolate or extrapolate various models to anticipate the performance of systems that are not examined experimentally. Moreover, developments in computational simulations have made it possible to study properties of materials from the first principle calculation with good accuracy. Thus it enables the explanations and prediction of the properties of the material, which are difficult to study experimentally. Numerous approaches have been determined to calculate electronic structure in the past, and modern physics has always faced a challenge to develop theoretical approaches which accurately treat the interactions between the many electrons and nuclei.

This chapter deals with the detailed methodology implemented to study the structural optimization, vibrational, elastic, born effective charges, electronic and optical properties of proposed materials. The solution of the Schrödinger equation for many-particle systems is done by approximation methods. It is well known that a system includes many electrons

and many nuclei to describe this system, we need a many-body wave function (Ψ) , which can take account of the state of each atom and ions.

2.1 The Many body problem

This chapter tries to address and introduce the theoretical methods and some quantum mechanics used to understand the ground state properties of various materials. The abinitio techniques used in material science to obtain electronic structure calculations work explicitly with correlated multi-electron wavefunction but can be applied to relatively small systems, whereas the semi-empirical schemes allow one to simulate systems with thousands of atoms. Clearly, it shows that the ab-initio approach has a big advantage in giving very detailed knowledge of the physical quantities understudy and being predictive with respect to the experiments. Electrons and nuclei are the determining factors to understand the physical and chemical properties of condensed matter and molecules. In the late seventeenth century, after discovering Newton's laws for classical mechanics, physicists found that these laws do not correctly describe the motion of the particles on the microscopic scale, such as the electrons and nuclei in atoms and molecules. So, solving the many-body Schrodinger equation is the starting point for investigating the properties of a material where the nature of interacting electrons in a solid is very difficult to understand and can not be addressed properly. This is due to the very well-known interactingelectron problem, which has been known for 80 years. To solve this, approximations are made, which allow numerical methods to be applied to find approximate solutions. These approximate solutions for the electronic wave functions are obtained by solving equations derived from quantum mechanics. We begin with the primary postulate of quantum mechanics, the so-called wave function, Ψ , exists for any (chemical) system, and relevant operators which act upon Ψ return the observable properties of the system. The most important foundation of theoretical chemistry is the Schrödinger equation [1], in which an operator acts upon Ψ to return the system energy, E. This can be written as:

$$H\Psi(r_1, r_2, \dots, r_N, R_1, R_2, \dots, R_M) = E\Psi(r_1, r_2, \dots, r_N, R_1, R_2, \dots, R_M)$$
(2.1)

H is the Hamiltonian operator for the system. For a system consisting of N electrons and M nuclei, the properties of this system can be determined by solving the Schrödinger equation with the Hamiltonian of the system of nuclei and electrons can be written as

$$H = -\frac{\hbar^2}{2} \sum_{k=1}^{M} \frac{\nabla_k^2}{M_k} - \frac{\hbar^2}{2} \sum_{i=1}^{N} \frac{\nabla_i^2}{m_e} + \frac{1}{2} \sum_{k \neq l}^{M} \frac{Z_k Z_l e^2}{|R_k - R_l|} + \frac{1}{2} \sum_{i \neq j}^{N} \frac{e^2}{|r_i - r_j|} + \sum_{i,k}^{M,N} \frac{Z_k e^2}{|r_i - R_k|}$$
(2.2)

$$H = T^{N} + T^{e} + V^{NN} + V^{ee} + V^{Ne}$$
(2.3)

Where \hbar is Plank constant, R_k is the coordinate for the k^{th} the nucleus, r_i the coordinate for the ith electron, M_k and m_e are the corresponding masses, and Z is the nuclear charge. The classic form of the Hamiltonian operator considers five contributions to the total energy of a system: the first two terms in Eq.(2.2) correspond to the kinetic energy operators of the electrons and nuclei, the third, fourth, and fifth terms are the potential operators describing the interactions between nucleus-nucleus, electron-electron, and nucleus-electron, respectively. However, the solution to Eq.(2.1) is only possible for the hydrogen atom, as it goes to higher-order consisting of two-electron systems helium atom it becomes difficult. In solids and molecules, we have a complicated many-body problem, and the accurate solution of this set of equations involving 3(N + M) spatial degrees of freedom is an extraordinarily complex task and not feasible for systems involving many particles. So having this in mind, we introduce various reasonable approximations to reduce the degrees of freedom and hence the computational effort. In the first step of simplification, the so-called Born-Oppenheimer approximation. This approximation treats the nuclei as frozen, with the electrons moving in instantaneous equilibrium with them. This implies that the nuclei clamped at certain positions in space create an external potential, V_{ext} , to the electron cloud. This approximation is reasonable because of the huge dissimilarity in the mass of electrons and nuclei, the latter being three orders of magnitude heavier. This allows the nuclei to be considered as static particles, and their kinetic energy can be neglected. Thus, the total wave function of the studied system can be separated into two components, the electronic part and the nuclear part. The electronic wave function can be obtained by working out the following Schrödinger equation.

$$H_e\Psi_e(r_1, r_2, \dots, r_N, R_1, R_2, \dots, R_M) = E_e\Psi_e(r_1, r_2, \dots, r_N, R_1, R_2, \dots, R_M)$$
(2.4)

with the electronic Hamiltonian given by

$$H = -\frac{\hbar^2}{2} \sum_{i=1}^{N} \frac{\nabla_i^2}{m_e} + \frac{1}{2} \sum_{i \neq j}^{N} \frac{e^2}{|r_i - r_j|} + \sum_{i,k}^{M,N} \frac{Z_k e^2}{|r_i - R_k|} = T + U + V_{ext}$$
 (2.5)

Based on this approximation, the complexity of solving the Schrödinger equation of solids and molecules can be significantly reduced. Nevertheless, it remains still difficult to answer the problem of an interacting many-body system due to electron-electron interaction (the second term of Eq.(2.5)). Different approximations are required to rewrite the Eq.(2.5)

in a simplified form, which can be solved explicitly. One way to solve the many-body Schrödinger equation is to expand the wavefunction in Slater determinants as it is done in Hartree-Fock methods [2],

$$\Phi = \frac{1}{\sqrt{N!}} \begin{vmatrix}
\phi_1(\overrightarrow{x}_1) & \phi_2(\overrightarrow{x}_1) & \dots & \phi_N(\overrightarrow{x}_1) \\
\phi_1(\overrightarrow{x}_2) & \phi_2(\overrightarrow{x}_2) & \dots & \phi_N(\overrightarrow{x}_2) \\
\vdots & \vdots & \ddots & \vdots \\
\vdots & \vdots & \ddots & \vdots \\
\phi_1(\overrightarrow{x}_N) & \phi_2(\overrightarrow{x}_N)) & \dots & \phi_N(\overrightarrow{x}_N)
\end{vmatrix}$$
(2.6)

However, the problem of this method is the neglect of electron correlations, which leads to large deviations from experiment results, mostly for solids. Hartree Fock gives a great starting position for several other methods to describe the system more accurately. Another method is the independent particle approximation which states that electrons are uncorrelated but obey the Pauli exclusion principle. DFT is introduced in the coming section, which provides a path to the many-body problem onto a single-body problem. In most parts of this thesis, DFT is used as the computational method. Therefore, a more detailed description of this method is presented in the following sections.

2.1.1 Hohenberg and Kohn theorem

Hohenberg and Kohn(H-K) are the central theorems of DFT [3]

Theorem 1: The ground state electron density of a system determines the external potential $V_{ext}(r)$ (within a trivial additive constant). In other words there is one to one correspondence between the ground state density, $\rho(r)$ and the external potential $V_{ext}(r)$.

$$\langle \Psi | A | \Psi \rangle = A[n_0(r)] \tag{2.7}$$

Theorem 2: The density that minimizes the variational energy is the true ground state density for the external potential, V_{ext} i.e. the total energy functional has a minimum equal to the ground state energy at the ground state density of the system.

$$E[n(r)] = F_{HK}[n(r)] + \int dr V_{ext}(r)n(r)$$
(2.8)

where $F_{HK}[n(r)]$ incorporate the kinetic energy and electron-electron interaction term of the interacting particle system. This leads to the global minimum of this functional,

which is the accurate ground-state total energy of the system, E_0 , and the particle density that minimizes this functional is the exact ground-state density $n_0(r)$. The first theorem signifies that the ground-state density can completely obtain all ground-state properties of a system. It highlights the significance of the ground-state density. The term $F_{HK}[n(r)]$ in the second theorem is a universal functional and is the same for any N-electron system. The external potential, $V_{ext}(r)$, is a non-universal functional depending on the system under study. $V_{ext}(r)$ is specified for a specific system. Whereas the second theorem describes that the ground-state density can be obtained by minimizing the energy functional, which can further be used to compute other ground-state observables.

2.1.2 Kohn-Sham Equation

Due to poorly known functionals, the robust Hohenberg-Kohn theorems were not adequate to find the exact solution [4]. While H-K theorems in 1964 reported that the many-body system is a functional of electron density. Using this concept, Kohn-Sham ansatz states that many-body interaction problems can be substituted by a corresponding one-particle non-interacting system. So the total energy functional can be mentioned as Kohn-Sham (KS) functional

$$E[n(r)] = T_0[n(r)] + \int V_{ext}n(r)dr + \frac{1}{2}\int \int \frac{n(r)n(r')}{|r - r'|}dr'dr + E_{xc}[n(r)] + E_{II}$$
 (2.9)

The first term describes the kinetic energy, the second term represents external potential specifying the interaction between valence electrons and the nuclei Eq.(2.9). While the third and fourth term describes the (Hartree term) Coulomb potential and includes all the many-body effects as a single term know as exchange-correlation functional. Although the fourth term cannot be calculated exactly and considered by different approximations. Finally, the end term represents the energy contribution given by the interaction of nuclei. Based on the second theorem, the variational principle is used to reduce the K-S functional with respect to the density n(r) which leads to the one-particle Kohn-Sham equations:

$$\left(\frac{-\hbar}{2m_e}\nabla^2 + V_{KS}\right)\varphi_i(r) = \varepsilon_i\varphi_i(r) \tag{2.10}$$

where ε_i are the eigenvalues, $\varphi_i(\mathbf{r})$ are the K-S orbitals and V_{KS} is the K-S potential,

$$V_{KS} = V_{ext} + \int \frac{n(r')}{|r - r'|} dr' + V_{xc}$$
 (2.11)

and the exchange-correlation potential is defined by

$$V_{xc} = \frac{\delta E_{xc} [n]}{\delta n(r)} \tag{2.12}$$

The K-S orbitals and the non-interacting electrons are described by the K-S equations, where $\varphi_i(\mathbf{r})$ has no physical significance. However, the density obtained from the interacting electrons and K-S equation should be the same. In order to obtain the exact ground state density and the energy by determining the single-particle K-S equations, the exchange-correlation potential should be defined. But the effective potential depends on the electron density, which relies upon the K-S orbitals, which in turn, depends on the effective potential. Therefore, one needs to work out the K-S equations in a self-consistent fashion.

2.2 Exchange-correlation functionals

The main task to implement the Kohn-Sham equation for practical use is to obtain an accurate approximation for the exchange-correlation functional. Although the K-S equation allows deriving the ground state of a many-body electron system, this happens only if the exchange and correlation between electrons are known. So, approximations are required to estimate the exchange-correlation term as it is not known. Generally, the exchange term describes the interactions which minimize the total energy by reducing their Coulombic repulsion through the segregation of electrons by the same spin. While the correlation effects result from the collective nature of electrons screening each other and decrease their overall Coulombic interaction. Besides, exchange interactions can be calculated accurately from independent-particle methods such as Hartree-Fock, but not generally for KS methods. Moreover, the correlation effects are more notable for electrons with opposite spins as they are more likely to take up nearby locations. The self consistence for solving Kohn-Sham in Figure-2.1

2.2.1 Local density approximation

The Local Density Approximation (LDA), also known as the local functional proposed by Kohn-Sham in 1965, is an important solution to the many body-based problem. According to this approximation, the electron density differs extremely slow in reference to space coordinates allowing a locally uniform electron density $\rho(\mathbf{r})$, leading to form exchange-correlation potential. This demonstrates, to some extent, its better performance in explaining structural and elastic properties of both bulk solids and surfaces.

$$E_{xc}^{LDA} = \int \rho(\vec{r}) \varepsilon_{xc} [\rho(\vec{r})] d\vec{r}$$
 (2.13)

where Eq.(2.13), E_{xc} is the exchange-correlation energy density of the uniform electron gas [5] of density. It remains accurate for a homogeneous electron gas, so it serves well

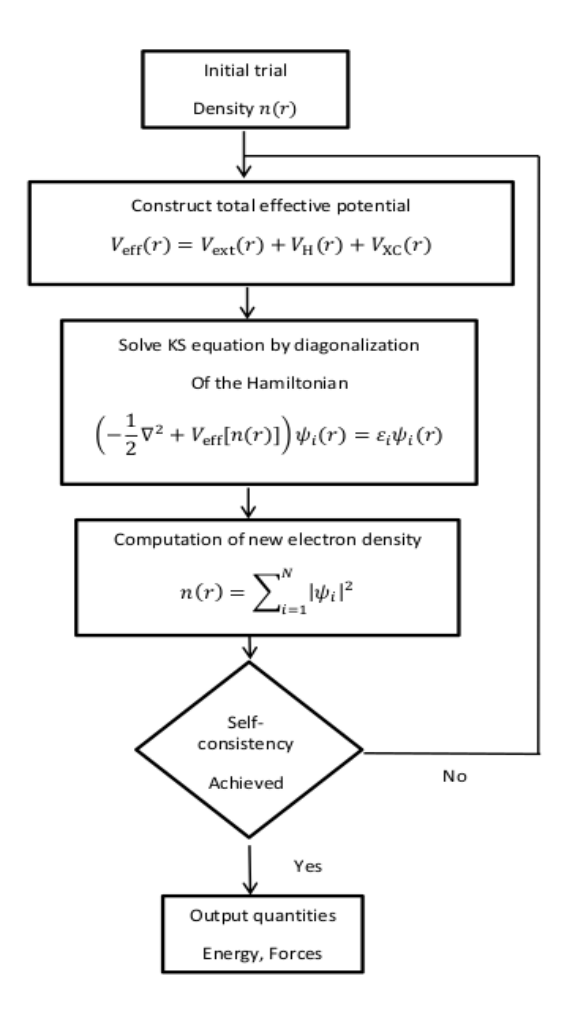


Figure. 2.1 Self-consistent algorithm for solving Kohn-Sham.

for systems where the electron density does not change immediately. The LDA functional reproduces the ground state properties of several systems very correctly. They are also known to predict the energy band gap of insulators, and semiconductor materials inaccurately [6,7]. However, the LDA functional often leads to significant errors for the bonding of both molecules and solids. This systematically leads to an overestimation of cohesive energy and molecular bond energies of solids. The drawbacks of LDA are that there is no dependence on the density gradient and that the correlation energy goes to infinity as the Wigner-Seitz radius approaches zero in the limit of large densities, whereas the exact correlation energy approaches a constant. Therefore an accurate description of material properties requires functionals that go beyond LDA.

2.2.2 Generalized gradient approximation

Besides the local density approximation (LDA), numerous non-local approximations have been proposed due to the large value of density gradient in some materials. Further, if the gradient is not small, LDA yields better outcomes. The approximation which accounts for spatial variation of density is normally termed as the generalized gradient approximation

(GGA) [8]. In GGA, the gradient of the charge density is incorporated in the exchange-correlation functional to account for the non-homogeneity of the true electron density, i.e., the exchange-correlation potential is a function of both the charge density at a given point and the first-order gradient of the charge density at the same point. Thus, the generalized gradient approximation (GGA) E_{xc} is given by Eq.(2.14):

$$E_{xc}^{GGA} = \int \rho(\vec{r}) \varepsilon_{xc} [\rho(\vec{r}), \vec{\nabla} \rho(\vec{r})] d\vec{r}$$
 (2.14)

The key idea behind this is to not only use the knowledge regarding the density $\rho(r)$ at a point r, but also to use the gradient of the charge density $\nabla \rho(r)$ to consider the non-homogeneity of the true electron density [9]. Typically, GGA functionals are more suitable and precise than LDA for molecular structures and hydrogen-based bonded systems. Nevertheless, GGA does not provide a tenacious development over LDA for solids. However, it is very tough to satisfy every constraint simultaneously. So, the functions are chosen according to the systems under chosen.

2.2.3 Dispersion correction methods

An accurate description of the non-covalent intermolecular interaction is very important to study solid energetic materials. Considering the complexity of energetic materials, standard electron exchange-correlation functionals are unsuccessful in accurately describing the weak intermolecular interactions. This can be clearly noticed in various energetic materials including CL-20, HMX ,FOX-7, TATB, RDX [10–15]. Also, these results exhibit that LDA and GGA underestimate or overestimate the structural volume nearly $\sim 30\%$ when compared with experimental data.

In standard DFT, several dispersion correction approaches have been developed to improve the description of dispersion interactions. These different approaches have been classified into three sections, (i) Pairwise additive dispersion-correction methods,(ii) Reparametrization for the existing functionals, and (iii) non-local correction methods. Pairwise additive corrections handle long-range interactions, including dispersion correction energy term to the internuclear energy term, strengthening the total energy obtained by the standard DFT calculation. Then a group of empirical corrections known as DFT-D and DFT+ E_{disp} models were introduced by Grimme and co-workers. Particularly, the Tkatchenko and Scheffler (DFT-TS) [16], and Grimme (DFT-D2) [17] improvements to PBE are the most successful methods. Whereas the second method mentions that the fitting data sets include noncovalent systems. While the hybrid meta-GGA functions are developed by Zhao and Truhlar [18], which account for the medium-range electron correlation. Finally, the third method uses the electronic charge density as data and includes the non-local correlation contribution to the semi-local exchange functionals [19–23]. Fur-

thermore, In 2004 Langreth, Lundqvist [24], and co-workers developed a nonlocal vdW density functional (vdW-DF) and (vdW-DF2) in 2010 [25]. Overall, in this thesis, pairwise additive corrections are used. Therefore, to treat VdW interactions accurately, we have adopted the vdW improvement to the exchange-correlation functional to standard density functional theory at a semi-empirical level. As stated in the semi-empirical dispersion correction method, the total energy of the system is defined as:

$$E_{total} = E_{DFT} + E_{Disp} (2.15)$$

with

$$E_{Disp} = s_i \sum_{i=1}^{N} \sum_{j>i}^{N} f(S_R R_{ij}^0, R_{ij}) C_6^{ij} R_{ij}^{-6}$$
(2.16)

Here C_6^{ij} is described as a dispersion coefficient linking any atom pair i and j, which completely relies upon the material, and R_{ij} is the distance between the atom i and j and 'f' is damping function, respectively. Various types of damping functions C_6^{ij} are proposed to capture the dispersion energy.

2.3 The Born-Oppenheimer approximation

The accurate answer of the specified SE will be difficult to obtain due to a large number of interacting particles in a system (around 10 ²³). Born-Oppenheimer proposed the first fundamental assumption in the many-body Hamiltonian, which states that the electronic part and the nuclear part in molecules can be decoupled. It points to a molecular wave function in words of electron positions and nuclear positions. The physical idea behind this approximation is that the mass of an electron is lightest than the nucleus; electrons react spontaneously to the displacements of nuclei, so the movement of nuclei on any timescale is relatively smaller than that of electrons. Therefore it is quite convenient to represent the electronic part by considering that the nuclei are stationary and solve the corresponding SE of a fixed molecular structure. The detailed derivation of the approximation and the implications applied can be found [26, 27]. Viewing this approximation, the nucleus-nucleus interaction and the kinetic energy in the Hamiltonian can be analyzed.

The electronic Hamiltonian is considered by ignoring the kinetic energy and the nucleusnucleus interaction term of the nucleus in the equation and can be expressed as:

$$T_H = T_e + V_{ee} + V_{Ne} (2.17)$$

All the significant terms needed for quantum mechanical properties of the system are captured by Born-Oppenheimer approximation. After which, the complexity of solving the SE of solids and molecules is significantly reduced, but it is still an extremely difficult task to solve a many-body system due to the behavior of electron-electron interactions. To overcome the problem, many approximate electronic structure methods have been proposed from the Hartree-Fock method to solve SE. As a result, DFT emerged as a popular simulation tool today in the field of material science. The approximation proves advantageous for numerous systems, but this method is complicated to address strongly correlated solids. So to get more incite DFT approach is explained in the next section.

2.4 Density functional theory

. For more than 30 years, density functional theory (DFT) has long been the backbone of the quantum mechanical simulation of periodic systems. In recent times, quantum chemists have also adopted the DFT methodology, which is now extensively used to compute the energy surfaces in molecules. Since the balance between accuracy and the computational cost was provided by approximate functionals. This allowed treating larger systems by standard ab initio methods, although retaining much of their accuracy. Back in time, everything started back then in the year 1927, a procedure to calculate the approximate wave function and energies for atoms and ions was introduced by Hartree, known as Hartree function. By considering Pauli principles Slater and Fock proposed a self-consistent function to overcome the antisymmetry of the electron system, and the multi-electron wave function is considered in the form of a determinant of particle orbitals. Due to the complexity of Hartree Fock, it was not popular till 1950's, knowing that the result obtained is a near approximation for the real result. Later in the same year, in 1927, Thomas and Fermi presented a statistical model to calculate the energy of atoms by approximating the distribution of the electrons in an atom. This resulted in the kinetic energy of the atom by the functional of electron density. In addition, two classic terms of electron-electron and nuclear-electron interaction can be represented as electron density to calculate the energy of an atom. Although, it did not contain the exchange energy functional, which was later proposed by Dirac in 1928 [28]. Moreover, the Thomas-Fermi model is the first step, but its inaccuracy is very much limited in its applicability. The origin of failure was due to the kinetic energy term represented just as an approximation, while the other error was due to the ignored electron correlation effect. Although, it is a predecessor of the DFT. The Foundation of the DFT was done in the year 1964 by Hohenberg, and Kohn [3]. Obtaining the proper interpretation of a many-body system by considering the wave function is extremely complex since the wave function depends on 3N variables, where N is the number of electrons. The first theorem of Hohenberg and Kohn pronounces that ground state energy exceptionally depends on the electron density, which indicates it is a function of electron density. While the following theorem reveals that ground state energy can be obtained by reducing the system's energy according to the electron density. It must be recognized that HK theorems exhibit one-to-one mapping relations among electron density and properties. So minimizing the system energy Kohn - Sham method was used, which was published one year later in 1965. The KS method states a many-body problem onto a single-body problem (a non-interacting system with the same total density). This also incorporates the external potential and the effects of the Coulomb interactions among the electrons. Based on the ideas of Thomas, Fermi, and many others, in 1964, including the formulation of Hohenberg and Kohn's fundamental theorems, DFT came into existence. The central theorem by H-K demonstrates that the ground-state electron density can specifically obtain all the system properties. This DFT methodology is applied to various areas to several problems, while ground-state electronic structure problems are the most common.

2.5 Methodology

2.5.1 Density functional perturbation theory

As of now, we know to compute ground state properties from ab initio. More sophisticated methods are used to calculate accurate vibrational energy. Here, (DFPT) density-functional perturbation theory comes into the picture. DFPT is based on perturbation theory to compute the response of electron density of the system to an external perturbation given. It uses perturbation theory to compute the electron density response of the system subject to an external perturbation [29]. In the case of phonon, this perturbation corresponds to the ionic displacements.

We use the Born-Oppenheimer approximation proposed in 1927, which allows us to decouple the motion of the atomic nuclei from the electrons. Adopting this approximation lattice-dynamical properties of a solid system can be achieved by working out the energy eigenvalues and eigenfunctions. The reduced Born-Oppenheimer many-body Hamiltonian equation is

$$\hat{H}_{BO}(R) = \hat{T}_e + \hat{V}_{ee} + \hat{V}_{en} + \hat{V}_{nn} \tag{2.18}$$

Right side terms in the above equation, the first term \hat{T}_e represents the kinetic energy operator of electrons followed by electron-election electrostatic interactions \hat{V}_{ee} , then \hat{V}_{en} is represented by electron-nuclei, then the last term \hat{V}_{nn} is nuclei-nuclei interactions. The equilibrium geometry of the solid can be reached by equating the interatomic forces (initial derivative of Born-Oppenheimer energy surface) to zero

$$F_I \equiv -\frac{\partial E(R)}{\partial R_I} = 0 \tag{2.19}$$

whereas ω is the vibrational frequencies determined by the eigenvalues of the Hessian of the Born-Oppenheimer energy, scaled by the nuclear masses:

$$det\left|\frac{1}{\sqrt{M_I M_J}} \frac{\partial^2 E(R)}{\partial R_I \partial R_J} - \omega^2\right| = 0$$
 (2.20)

Hellmann-Feynman (HF) theorem is the fundamental tool used to solve the first and second derivatives of BO. According to this, the first derivative of the eigenvalues of a Hamiltonian, that depends on a parameter λ is given by the expectation value of the derivative of the Hamiltonian:

$$\frac{\partial E_{\lambda}}{\lambda} = <\psi_{\lambda} | \frac{\partial H_{\lambda}}{\lambda} | \psi_{\lambda} > \tag{2.21}$$

Here E_{λ} represents eigenvalue and ψ_{λ} eigenfunction. Therefore the forces acting on the nucleus \mathbf{F}_{I} can be written as

$$F_{I} \equiv -\frac{\partial E(R)}{\partial R_{I}} = -\langle \psi(R)| \frac{\partial H_{B}O(R)}{\partial R_{I}} | \psi(R) \rangle$$
 (2.22)

$$F_{I} \equiv -\int n_{R}(r) \frac{\partial V_{R}(r)}{\partial R_{I}} - \frac{\partial E_{N}(R)}{\partial R_{I}}$$
(2.23)

Here the first term $(n_R(r))$ represent the electron charge density, then $(V_R(r))$ the second term is electron-nucleus interaction potential and the $(E_N(R))$ last term describes the electrostatic interaction among different nuclei. Ultimately, the Hessian of the BO energy surface is obtained by differentiating the HF forces with reference to nuclear coordinates:

$$\frac{\partial^2 E(R)}{\partial R_I \partial R_J} = \int \frac{\partial n_R(r)}{\partial R_J} \frac{\partial V_{en}(R)}{\partial R_I} dr + \int n_R(r) \frac{\partial^2 V_{en}(R)}{\partial R_I \partial R_J} dr + \frac{\partial^2 V_{nn}(R)}{\partial R_I \partial R_J}$$
(2.24)

The electron charge density $n_R(r)$ and the $\frac{\partial n_R(r)}{\partial R_I}$ linear response of electron density are the prerequisites to solve the inter-atomic force constants (IFC) matrix (Hessian matrix). The Fourier transform of IFC will give us the required dynamical matrix in the reciprocal space. Therefore the vibrational frequencies obtained with this DFPT method are an accurate and efficient tool to calculate the lattice dynamics. To analyze the polarization mechanism in the thesis, we have used the born effective charge method. By using Huang's Phenomena, the long-wavelength/low energy region, long-range Coulomb forces will give macroscopic electric fields for longitudinal optic phonon. The general expression of energy as a function of phonon optic coordinates and the field can be written as:

$$E(u, E) = \frac{1}{2}M\omega_0^2 u^2 - \frac{\Omega}{8\pi}\epsilon_\infty E^2 - eZ^* u.E$$
 (2.25)

 Ω is unit cell volume, ϵ_{∞} is the static dielectric constant with fixed nuclei(u=0) position, and M is the reduced mass. Z* is the Born effective charge of ions, where coupling between u and E. Therefore the macroscopic electric polarization can be written as

$$P = \frac{1}{\Omega} \sum_{s} eZ_s^* u_s + \frac{\epsilon_\infty - 1}{4\pi} E$$
 (2.26)

Hence the Z *Born effective charge tensor can be written as the S^{th} ion can be defined as a partial derivative of macroscopic polarization (P) with respect to periodic displacement of all ions at zero electric fields.

$$eZ_s^{*\alpha\beta} = \Omega \frac{\partial P_\alpha}{\partial u_s^\beta(q=0)}|_{E=0}$$
 (2.27)

The dielectric constant tensor can be written as derivative of P with respect to E and clamped nuclei

$$\epsilon_{\infty}^{\alpha\beta} = \delta_{\alpha\beta} + 4\pi \frac{\partial P_{\alpha}}{\partial E_{\beta}}|_{u_{s}(q=0)=0}$$
(2.28)

Therefore, within the harmonic limit, to calculate Born effective, phonon frequencies, and dielectric properties DFPT is a very well-known method.

2.5.2 Full-potential linearized augmented plane wave (FP-LAPW)

The full-potential linearized augmented plane wave (FP-LAPW) method is one of the most precise DFT methods, with reasonable computational efficiency, to simulate the electronic properties of materials. The FP-LAPW combines the choice of the LAPW basis set with the treatment of the full-potential and charge density without any shape approximations in the interstitial region and inside the muffin-tins. The FP-LAPW (+ local orbitals) method with various exchange and correlation schemes is embodied in the WIEN2k package. WIEN2k [30, 31] code facilitates the computation of structural, electronic, magnetic, and optical properties, etc., of materials in different forms like bulk, thin-film, nano. It is now well known that the LAPW method is used for solving the Kohn-Sham equations by avoiding an artificial core-valence separation of electrons described by

the Pseudopotential. In this method, all-electron basis sets are explicitly used in the computation.

In the FP-LAPW method, the crystal's unit cell is separated into two parts, the muffintin (MT) region, and the interstitial region. The MT (non-touching) atomic spheres are centered at the atomic sites. In a general form of the LAPW method, the crystal potential expands in the following form, the crystal potential is build-up by spherical harmonics within the MT spheres. The basis set is approximated by radial solutions of the one-particle Schrodinger equation. Outside the MT spheres (interstitial region), the expansion of crystal potential is in the form of plane waves. In such calculations, no shape approximation is made for charge density or potential, and the band calculations are expected to be reasonably accurate. To perform the calculations by the WIEN2k package, two components, namely initialization and SCF cycle, need utmost care. The initialization process generates a structure file for a defined space group and ensures the non-overlapping of MT spheres. After that, it accounts for symmetry operations, generates k (reciprocal vector) mesh in its Brillouin zone (BZ), and inputs the initial electron density. The SCF cycle of the code starts after the successful completion of initialization because the input (electron density) of SCF is the output of initialization. The SCF part calculates potential from input density and generates eigenvalues and eigenvectors. Using the latest eigenvalues computes the valence and core electron density. After that, it mixes all the input and output electron densities and generates a new electron density. This part also checks the self-consistency and the properties of the system, either they are converged or not. It stops after achieving the self-consistency or starts for a new cycle.

2.6 Pseudopotentials

The conceptual term pseudopotential dates back to 1935 by Hans Hellman, who developed an effective potential for valence electron scattering from metallic ion cores. These potentials ended up being too hard, and perturbation methods at the time did not allow for accurate calculations. Later Slater [32] in 1937 proposed that the crystal lattice can be divided into two main parts, where the first part is defined as atomic sphere centered muffin-tin (MT) region at each atom position, and the remaining part is termed an interstitial region. While in 1940, Herring proposed models using augmented plane-wave expansions with spherical solutions to the atomic problem (APW, augmented plane-wave method) and linear combinations of plane-wave and core wavefunctions for valence wavefunctions (OPW, orthogonalized plane-wave method). These advances led to more developments, and the origin of the modern pseudopotential method in the familiar paper from Philips and Kleinmann in 1959 [33].

The electronic states of an atom can be divided into core and semi-core states. While the core states tend to be highly localized and do not participate in chemical bonding,

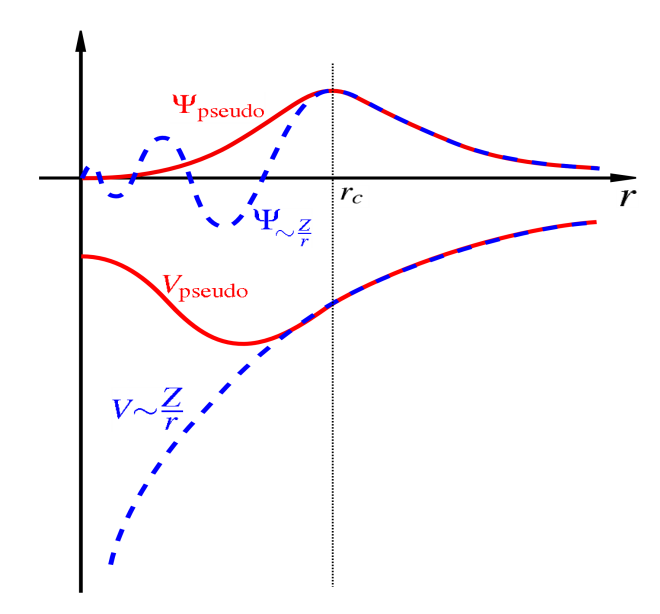


Figure. 2.2 Sketch of pseudopotential.

whereas the semi-core states are polarizable and localized but do not actively participate in chemical bonding between valence states. The problem of the core electron wavefunctions has already been alluded to in the description of plane-wave basis sets. To combat the use of larger and larger basis-sets, the strong Coulomb potential of the nucleus and the core electrons (those not participating in any relevant chemistry) is replaced by an effective ionic potential that acts on the valence electrons. Thus, the core states are effectively fixed in an atomic reference configuration (frozen core approximation), and the ground state pseudo-wavefunction identically mimics the all-electron wavefunction outside of the core cut-off radius. Fitting of the pseudopotentials is generally accomplished by comparison to all-electron wavefunctions, with the advantage of reducing the number of electrons, electronic states, and basis sets to be considered, and therefore the calculation expense.

The struggles of developing pseudopotential methods are based on the following objectives: (i) the plane waves considered to describe pseudo-eigenstates needs to be as tiny as possible (ii) the valence charge density should be formed through the pseudo-charge density as accurately as possible (iii) the ability toward a particular atomic configuration should ever address accurate results in several solids. In this thesis, we have used the pseudopotential method to optimize the experimental given structure and calculated various properties as mentioned in CASTEP. In addition, to address the strong bonding, electronic and optical properties, we used the FP-LAPW technique as executed in WIEN2k. This concept was extended and led to the development of pseudopotential methods such as 'norm-conserving pseudopotentials, ultra-soft pseudopotentials (US-PP), and the Projector Augmented Wave (PAW) method. The sketch of pseudopotential is shown in Figure-2.2

2.6.1 Norm-Conserving (NC)

To reproduce the valence charge density associated with chemical bonds is the main demand of Pseudopotential. Norm-conserving pseudopotentials were initially studied by Hamann, Schlüter, and Chiang [34] in 1979, and further guided to the next level by Kleinman and Bylander [35]. This approximation presents that the charge density of the all-electron core is formed within the cut-off radius which is comparatively short. Hence, kinetic energy tends to be high, so large plane waves are considered to describe the potential encountered by the valence electrons. The NC pseudopotentials depend on the following properties which produce wave function with accurate charge density. All-electron plus pseudo-valence eigenvalues allow for accepted atomic reference states and wavefunctions to agree beyond a determined core radius, Rc. While the pseudo wavefunction and all-electron wavefunction logarithmic derivatives agree at the point Rc. Finally, integrated charge for each wavefunction agrees inside Rc, and also the first energy derivative of the log derivatives of both wave functions agree at Rc.

2.6.2 Ultrasoft

The advancements in the NC pseudopotentials have paved the way to compute precise simulations in solid-state properties. However, the problems encountered with normconserving pseudopotentials are their hardness and high energy cut-off values causing a large number of plane waves, which often makes calculations prohibitively expensive and time-consuming. Larger cut-off energy is required for plane waves basis if the system has orbitals tightly bonded with a portion of their weight inside the core area. To allow these calculations to be performed, the only way is the reduced basis set is to breach the NC pseudopotential by excluding the charge related to these orbitals from the core region resulting in the lowest accurate cut-off energy for the plane-wave basis set. So, to alleviate the complication in NC, ultrasoft Pseudopotential was introduced by Vanderbilt (1990), allowing for softer potentials with a large reduction in the energy cut-off values [36] and considerably fewer plane-waves for calculations with the same accuracy. The softness of these potentials is linked to their use of fewer basis sets, re-expressing the difficulty in terms of a smooth function and an auxiliary function localized throughout the core to represent the swiftly changing region of the density, allowing for larger cut-off radii. The difference in the charge density as it is a function of the wave function is compensated by an additional term to produce accurate results from all-electron wavefunction.

2.6.3 Projector augmented wave(PAW) method

In this section, a brief outline is given about the projected augmented wave (PAW) method. The major problem with the PAW method happens due to fast oscillations of the wavefunction near the core area, this is because of the high kinetic energy of the electrons, and while at delocalized region they are smooth. To deal with this problem, Augmented wave and pseudopotential approaches have been extended by Andersen [37] and Hamann,

Schlüter, and Chiang. However, it was in 1994 that Blöchl [38] found the missing link between them and developed the method, which is called the PAW method. This describes the all-electron frozen core method, which combines both the concept of ultrasoft pseudopotentials and the augmented plane wave method. Usually, the PAW potentials remain more reliable than the above discussed ultra-soft potentials. This is due to the core radii which tends to be smaller than the radii used within ultrasoft PP, whereas the PAW potentials recreate the valence wave function in the core region which is exact. So the PAW method extends those methods and combines them into a unified electron structure method. In this section, one of the augmented wave functions known as PAW is going to be discussed here:

PAW method developed by Blöchl is based on a modification of the pseudo wave function to the all-electron wave function. The all-electron wavefunction Ψ is expressed by the three parts:

$$\Psi = \Psi + \sum_{i}^{N} c_i \phi_i - \sum_{i}^{N} c_i \phi_i$$
 (2.29)

Where ϕ_i are the pseudo partial waves, Ψ is the pseudo wave function, and ϕ_i are the all-electron partial waves. The tilde is used to differentiate between all-electron and pseudo quantities representing one part of the all-electron solution. The pseudo wavefunction represented by plane waves is a good elucidation of the wavefunction in regions apart from the nuclei but deviates notably from the all-electron wavefunction close by the nucleus. Hence the all-electron partial waves ϕ_i are introduced to correct this error. Moreover, all electron partial waves are computed once as solutions of the radial part of the Schrödinger for the isolated atoms. Inside the augmented core region, they deviate from the pseudo wavefunction outside this region they match. All electron partial waves ensure that the nodal structure of the wave function is physically correct near the nucleus. The contribution of the pseudo partial waves ϕ_i located near the atomic nuclei is subtracted from the pseudo wavefunction since this region is already included in all-electron partial waves. Similar to the all-electron partial waves, the ϕ_i are built as solutions of the radial Schrödinger equation for isolated atoms fitted to match the pseudo wavefunction.

2.6.4 Tran-blaha modified Beck-johnson potential (TB-mBJ)

Back in 2006, Becke and Johnson (BJ) modified exchange effective potential to calculate band gaps and tested on several solids which are challenging to describe theoretically. Even though BJ potential improves over LDA and PBE for the bandgap calculations, but still underestimated. Further improvement is done by Tran and Peter Blaha in 2009 has been achieved through simple modification to the BJ potential with a comparable accuracy of GW and hybrid functional. Since, then TB-mBJ [39,40] functional picked up

more interest as it is computationally less expensive. The modified exchange-correlation proposed BJ potential can be expressed as follows:

$$\nu_{x,\sigma}^{MBJ}(r) = c\nu_{x,\sigma}^{BR}(r) + (3c - 2)\frac{1}{\pi}\sqrt{\frac{5}{12}}\sqrt{\frac{[2t_{\sigma(r)}]}{\rho_{\sigma}(r)}}$$
(2.30)

where ρ_{σ} is the electron density t_{σ}

$$\rho_{\sigma} = \sum_{1,N} |\Psi_{i,\sigma}|^2 \quad t_{\sigma} = \frac{1}{2} \sum_{1,N_{\sigma}} \nabla \Psi_{i,\sigma}^* \cdot \nabla \Psi_{i,\sigma}$$
 (2.31)

$$\nu_{x,\sigma}^{BR}(r) = -\frac{1}{b_{\sigma}(r)} \left(1 - e^{-x_{\sigma}(r)} - \frac{1}{2}x_{\sigma}(r)e^{-x_{\sigma}(r)}\right)$$
(2.32)

is the $\nu_{x,\sigma}^{BR}(r)$ Becke-Roussel potential was proposed to model the Coulomb potential created by the exchange hole. x_{σ} is determined from an equation involving ρ_{σ} , $\nabla \rho_{\sigma}$, t_{σ} , $\nabla^2 \rho_{\sigma}$, and then b'_{σ} is calculated

$$b_{\sigma} = \left[x_{\sigma}^3 e^{-x_{\sigma}} / 8\pi \rho_{\sigma} \right]^{\frac{1}{3}} \tag{2.33}$$

'c' was chosen to depend linearly on the square root of the average of

$$|\nabla \rho|/\rho$$
 (2.34)

$$C = \alpha + \beta \left(\frac{1}{V_{cell}} \int_{cell} \frac{|\nabla \rho(r')|}{\rho(r')} d^3 r'\right)^{\frac{1}{2}}$$
 (2.35)

Here where ' α ' and ' β ' are two free parameters, V_{cell} is the unit cell volume. The calculated band gaps are known to increase linearly with an increase in the c-parameter. The bandgap calculated for solids with a lower bandgap can be calculated using TB-mBJ potential by varying c-parameter. Overall, in the present research, we have implemented TB-mBJ potential to compute electronic band structure and optical properties based on the FP-LAPW method.

References

- [1] Schödinger E., An Undulatory Theory of the Mechanics of Atoms and Molecules, Ann. Physic., 1926, 81, 109.
- [2] Szabo. A., Ostlund N. S., Modern Quantum Chemistry Introduction to Advanced Electronic Structure Theory (Dover Publicaltions, New York, 1996.
- [3] Hohenberg, P., Kohn, W., Inhomogeneous Electron Gas, Phys. Rev., 1964, 136, 864.
- [4] Kohn. W., Sham. L., Self-Consistent Equations Including Exchange and Correlation Effects, Phys. Rev., 1965, 140, A1133.
- [5] Slater. J., A Simplification of the Hartree Fock Method, Phys. Rev., 1951, 81, 385.
- [6] Csonka. G. I., Perdew. J. P., Ruzsinszky. A., Philipsen. P. H. T., Lebègue. S., Paier. J., Vydrov. O. A., Ángyán. J. G., Assessing the performance of recent density functionals for bulk solids, Phys. Rev. B., 2009, 79, 155107.
- [7] Staroverov. V. N., Scuseria. G. E., Tao. J., Perdew. J. P., Tests of a ladder of density functionals for bulk solids and surfaces, Phys. Rev. B., 2004, 69, 075102.
- [8] Perdew. J. P., Accurate Density Functional for the Energy Real Space Cutoff of the Gradient Expansion for the Exchange Hole, Phys. Rev. Lett., 1985, 55, 1665.
- [9] Perdew. J. P., Ernzerhof M., Burke K., Rationale for mixing exact exchange with density functional approximations, J. Chem. Phys., 1999, 105, 9982.
- [10] Byrd. E. F. C., Rice. B. M., Ab Initio Study of Compressed 1,3,5,7-Tetranitro-1,3,5,7-tetraazacyclooctane (HMX), Cyclotrimethylenetrinitramine (RDX), 2,4,6,8,10,12-Hexanitrohexaazaisowurzitane (CL-20), 2,4,6-Trinitro-1,3,5-benzenetriamine (TATB), and Pentaerythritol Tetranitrate (PETN), J. Phys. Chem. C, 2007, 111, 2787.
- [11] Byrd. E. F. C., Scuseria. G. E., Chabalowski C. F., An ab-initio study of solid nitromethane, HMX, RDX and CL-20 sucesses and failures of DFT, J. Phys. Chem. B, 2004, 108, 13100.
- [12] Zhao. J. J., Liu. H., Density functional study of 1,3,5-trinitro-1,3,5-triazine molecular crystal with van der Waals interactions, Comput. Mater. Sci., 2008, 42, 698.

- [13] Appalakondaiah. S., Vaitheeswaran. G., Lebegue S., Structural, vibrational, and quasiparticle band structure of 1,1-diamino-2,2-dinitroethelene from ab initio calculations, J. Chem. Phys., 2014, 140, 014105.
- [14] Liu. H., Zhao. J. J., Du. J. G., Gong. Z. Z., Ji G. F., Wei D. Q., High-pressure behavior of TATB crystal by density functional theory., Phys. Lett. A, 2007, 367, 383.
- [15] Miao. M. S., Dreger. Z. A., Winey. J. M., Gupta Y. M., Density functional theory calculations of pressure effects on the vibrational structure of alpha RDX, J. Phys. Chem. A., 2008, 112, 12228.
- [16] Tkatchenko. A., Scheffler. M., Accurate Molecular Van Der Waals Interactions from Ground-State Electron Density and Free-Atom Reference Data, Phy. Rev. Lett., 2009, 102, 073005.
- [17] Grimme. S., Semiempirical GGA-type density functional constructed with a long-range dispersion correction, J. Compu. Chem., 2006, 27, 1787.
- [18] Zhao. Y., Schultz. N. E., Truhlar. D. G., Design of Density Functionals by Combining the Method of Constraint Satisfaction with Parametrization for Thermochemistry, Thermochemical Kinetics, and Noncovalent Interactions, J. Chem. Theory Comput., 2006, 2, 364.
- [19] Hesselmann. A., Jansen. G., Schutz. M., Density-functional theory symmetry adapted intermolecular perturbation theory with density fitting A new efficient method to study intermolecular interaction energies, J. Chem. Phys., 2005, 122, 014103.
- [20] Lilienfeld. O. A., Tavernelli. I., Roethlisberger. U., Sebastiani. D., Optimization of Effective Atom Centered Potentials for London Dispersion Forces in Density Functional Theory, Phys. Rev. Lett., 2004, 93, 153004.
- [21] Dion. M., Rydberg. H., Schroder. E., Langreth. D. C., Lundqvist. v, Erratum Van der Waals Density Functional for General Geometries, Phys. Rev. Lett., 2004, 92, 246401.
- [22] Vydrov. O. A., Voorhis. T. V., Nonlocal van der Waals Density Functional Made Simple, Phys. Rev. Lett., 2009, 103, 063004.
- [23] Vydrov. O. A., Van. Voorhis T., Nonlocal van der Waals density functional The simpler the better, J. Chem. Phys., 2010, 133, 244103.
- [24] Dion. M., Rydberg. H., Schro der. E., Langreth. D. C., Lundqvist. B. I., Phys. Rev. Lett., 2005, 95, 109902.
- [25] Lee. K., Murray. E. D., Kong L., Lundqvist B. I., Langreth. D. C., Phys. Rev. B, Condens., Higher-accuracy van der Waals density functional, Matter Mater. Phys., 2010, 82, 081101.
- [26] Born. M., Oppenheimer. J. R., Quantum Theory of the Molecules, Am. J. Phys., 1927, 84, 451.
- [27] Born. M., R. Oppenheimer, Annalen der Physik, 1927, 20, 457.
- [28] Dirac. Paul. A. M., The quantum theory of the electron, Proc. R. Soc. Lond., 1928, 117, 610-624.
- [29] Baroni. S., Gironcoli. S. D., Corso. A. D., Giannozzi. P., Rev. Mod. Phys., 2001, 73, 515.

- [30] Blaha. P., Schwarz. K., Madsen. G. K. H., Kvasnicka. D., Luitz. J., WIEN2k, An augmented plane wave +local orbitals program for calculating crystal properties, 2001, Karlheinz Schwarz, Techn. Universitat Wien, Austria.
- [31] Blaha. P., Schwarz. K., Sorantin. P. I., Tricky S. B., Full-potential, linearized augmented plane wave programs for crystalline systems, Comput. Phys. Commun., 1990, 59, 399.
- [32] Slater J. C., Wave Functions in a Periodic Potential, Phys. Rev., 1937, 51, 846.
- [33] Leonard. K., James. C. Phillips, Crystal Potential and Energy Bands of Semiconductors. I. Self-Consistent Calculations for Diamond, Phys. Rev., 1959, 116, 880.
- [34] Hamann. D., Schluter M., Chiang C., Phys. Rev. Lett., 1979, 43, 1494.
- [35] Kleinman. L., Bylander D., "Efficacious form for model pseudopotentials", Phys. Rev.Lett., 1982, 48, 1425.
- [36] Vanderbilt, D. "Soft self-consistent pseudopotentials in a generalized eigenvalue formalism", Phys. Rev. B., 1990, 41, 7892-7895.
- [37] Andersen. O. K., Linear methods in band theory, Phys. Rev. B, 1975, 12, 3060.
- [38] Bloch. P.E., Projector augmented-wave method, Phys. Rev. B., 1994, 50, 17953.
- [39] Becke. A. D., Johnson E. R., A simple effective potential for exchange, J. Chem. Phys., 2006, 124, 221101.
- [40] Tran. F., Blaha P., Accurate Band Gaps of Semiconductors and Insulators with a Semilocal Exchange-Correlation Potential, Phys. Rev. Lett., 2009, 102, 226401.

Chapter 3

Alkali Metal Perchlorates $MClO_4$ (M = Li, Na, K, Rb, Cs)

Abstract

This chapter reports a detailed study on structural, vibrational, born effective charge (BEC), electronic and optical properties of the alkali metal perchlorates, $MClO_4$ (M=Li, Na, K, Rb, Cs) based on Density functional theory. The ground state calculations are done using plane wave pseudopotential method by including dispersion corrected method for more accurate prediction of structural and vibrational frequencies. The calculated lattice parameters and bond lengths are consistent with the experimental values. Further, detailed interpretation of the zone centered vibrational modes yields good concurrence between the experimental and calculated values. There is a decrease in wavelength with an increase in frequency (blueshift) from $Li \rightarrow Na \rightarrow K \rightarrow Rb \rightarrow Cs$. The obtained BEC shows the mixed covalent-ionic character of the compounds. The electronic and optical properties are calculated using the full potential linearized augmented plane wave method by TB-mBJ potential. The TB-mBJ band structure shows indirect band gap with O-2p states dominating in the valence band. In spite of anisotropic structure, alkali metal perchlorates are found to possess optical isotropy.

Prathap kumar Jharapla, E. Narsimha Rao and G. Vaitheeswaran, "Unusual optical isotropy in anisotropic alkali metal perchlorates $MClO_4$ (M = Li, Na, K, Rb, Cs), **J. Phys. Condens. Matter**, **30**, 475402, (2018).

3.1 Introduction

Our current interest is to study alkali metal perchlorates held together by relatively weak intermolecular forces belonging to the class of molecular crystals. The metal perchlorate salts lead to decomposition and find applications in propellants, exploiting properties as oxidation agents due to their high positive oxygen balance [1]. The recent discovery of perchlorates on Mars could be a potential energy source for bacteria but a chemical hazard for humans [2]. The traces of perchlorate's high oxidiation and oxychloride's low oxidation state impact the habitability of Mars. Perchlorates are both naturally occurring and man-made chemicals having wide applications in rocket fuel, missiles, fireworks, flares, bleaching, fertilizers, treatment of thyroid disorders, batteries, sensors [3,4]. These various applications have grabbed the attention of metal perchlorate salts during the last few decades. These materials are being applied to external stimuli leading to initiation and ignition due to their strong bond between them [5], [6]. Perchlorate salts are always of interest when subjected to metal atoms showing positive oxygen balance [1]. But due to its toxicity nature, it is harmful to human beings in many ways. The origin of the perchlorate anion is from various salts due to the contamination and inappropriate disposal in the environment. These salts react sluggishly, are highly soluble and chemically stable in water, and have a tendency to absorb minerals with high activation energy for the product formation [7]. A good oxidizer can be judged by its high melting point, stability, high density, low cost, less toxicity, positive oxygen balance, low heat formation with a high oxidation potential are highly expected [8]. The final product obtained by high-temperature decomposition between perchlorates and chlorates is free chlorine. This chlorine is used to combine with some compounds to produce some hues [5]. The chemical compound perchlorate ion consists of one chlorine at its highest oxidation state +7surrounded by four oxygen atoms in a tetrahedral geometry. The chlorine and oxygen charge vary with the constraint that the overall charge is -1 so that the perchlorate group is maintained [9].

The alkali metal perchlorates crystallizes in orthorhombic structure with space group (Pnma) in case of $MClO_4$ M=(Li, K, Rb, Cs) and $NaClO_4(Cmcm)$ with four formulae units. The thermal studies conclude that alkali metal perchlorates undergo transitions from ambient orthorhombic phase to cubic phase at T_c values of 310°, 300°, 278°,221°C due to the onset rotation of ClO_4 ions [10]. At higher temperatures, the decomposition rate of K, Rb, Cs is lower, and an increase in thermal reactivity of $NaClO_4$ has been reported [11]. The potassium perchlorate is being used as signal flares compositions, explosive simulators, and pyrotechnic applications when combined with various compositions like barium nitrate, strontium oxalate, sodium oxalate, copper carbonate, and poly(vinyl chloride) to obtain the characteristic green, red, yellow, and blue colors [2,4]. Several studies such as Raman spectra, transport properties, application of lithium in

energetic materials and prepolymers have been reported on $LiClO_4$ [12–14]. The following Dielectric and AC conductivity, DSC studies on the phase transition, thermal properties with various particle sizes, phase relation at high pressure, studies have been reported in the case of $KClO_4$. These studies conclude that potassium perchlorate show phase transition at T-301°C which is not associated with ferroelectric phase change and orthorhombic/cubic transitions rises from 256°C to 566°C at 11.3 Kbar [15–18]. Limited work has been reported on Structural, vibrational, optical, and electronic properties. Despite being reported in the works of literature there is no complete picture of the bonding, polarizability, and optical nature of these compounds. We present structural with vibrational properties and born effective charges using the Plane-wave pseudopotential method by including dispersive corrected DFT-D methods. Optical and electronic properties are reported using TB-mBJ potential of (Tran-Blaha modified Becke Johnson) with FP-LAPW method to understand the bonding and optical nature. The results have been summarized in the following manner: computational details, structural, vibrational, born-effective charges, band structure with the density of states, and optical constants for perchlorate anion with the varying metal atom. In the end, the findings of the study have been concluded.

3.2 Computational details

Ab-Initio calculations performed in this work are through two different approaches such as (PW-PP) Plane Wave Pseudopotential and (FP-LAPW) Full-Potential Linearized Augmented Planewave Method. The structural and vibrational properties calculation were carried out by Cambridge Series of the Total Energy Package (CASTEP) [19, 20] which is based on PW-PP method by treating electron-electron interactions through Norm conserving pseudopotentials [21]. By using the conjugate gradient technique, the total energy of the system is minimized with respect to the plane wave's coefficient, and the ground state is calculated. For the calculation of self-consistent field, electron wave function was determined using the density-mixing minimization method. To calculate various properties, experimental structure was directly taken with cut-off energy level 1000 eV for LiClO₄, NaClO₄, KClO₄ and 1300 eV for RbClO₄, CsClO₄ in the process of optimization. The k-points sampling for LiClO₄ $4\times5\times7$, and $5\times5\times5$ for NaClO₄, $4\times6\times5$ for KClO₄, $4\times6\times4$ for RbClO₄, $3\times6\times4$ for CsClO₄ according to the Monkhorst-Pack grid [22]. The maximum tolerances forces for energy, the maximum force between atoms, maximum displacement, and stress were set as $5.0 \times e^{-6}$ (eV per atom), 0.01 eV/A, $5.0 \times 10^{-4} \text{Å}$ and 0.02 GPa respectively. The electronic wave functions were relaxed using the BFGS algorithm [23] to find the lowest energy structure. Initially, local density approximation LDA [24,25] and generalized gradient approximation (GGA) of Perdew-Burke-Ernzerhof (PBE) [26], Perdew-Wang 91 (PW91) [27] are used to treat electron-electron interactions.

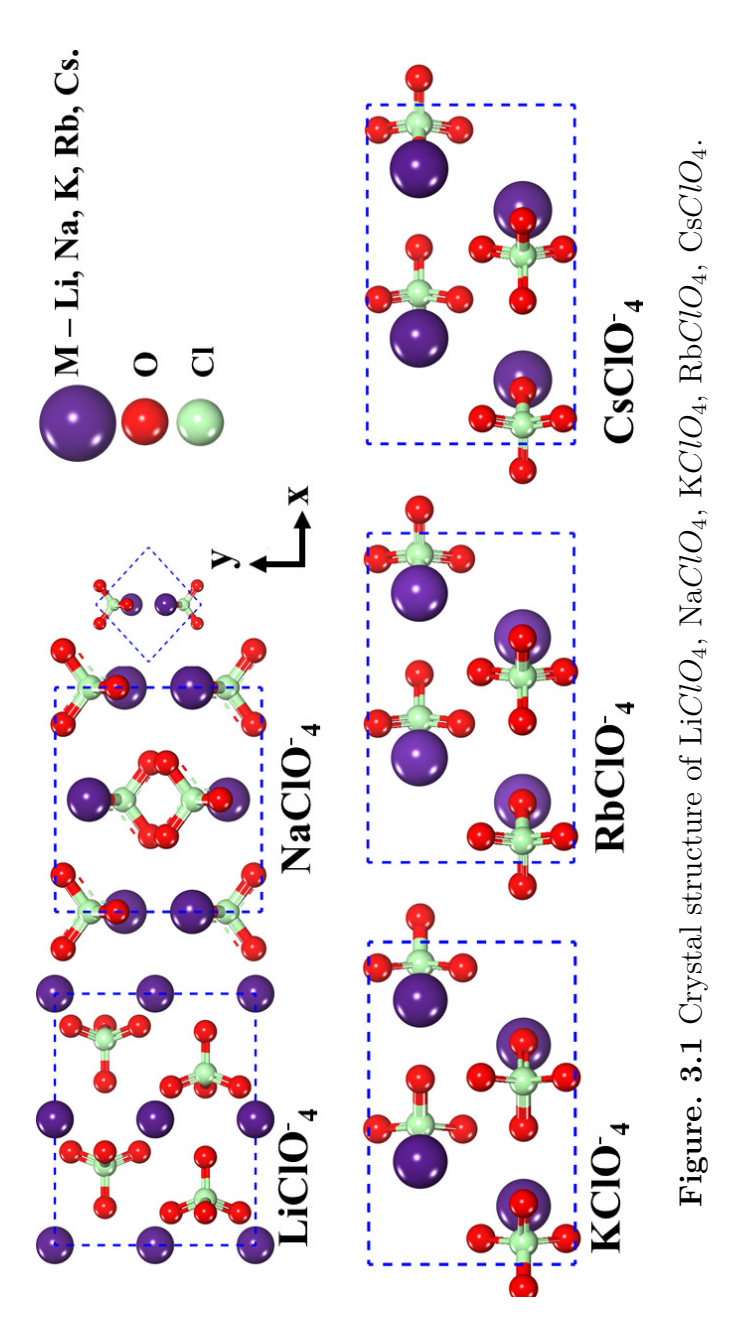
To correct the DFT missing dispersive interaction, semi-empirical dispersion correction methods are used i.e Grimme (G06) [28] to GGA, Ortmann-Bechstedt-Schmidt (OBS) [29] to Perdew-Wang 91 (PW91). The calculated zone center and BEC's are performed within density functional perturbation theory (DFPT) [30] which is a more efficient tool over finite displacement method to obtain frequencies with lower computation time [31]. The second part of the calculations includes electronic and optical properties which have been carried out by solving the Kohn-sham equation with a self-consistent scheme using an FP-LAPW method under the umbrella of density functional theory using the WIEN2K [32]. The exchange-correlation interaction is calculated using GGA [26], GGA-EV [33] and TBmBJ [34–37] approaches. The TB-mBJ potential has been employed to calculate the band structure, density of states, and optical constants of the metal-based alkali perchlorates. In these calculations, an energy threshold of -9 Ry is used for separating the core and valence electrons. The cut off for expanding the wave function in the intestinal region is restricted to $k_{max} = 7/R_{MT} (a.u)^{-1}$ where R_{MT} is the smallest atomic sphere radii of the muffin tin and the cut-off vector in the extension of charge density and potential is limited to G_{max} = 14 denote the magnitude of the largest K vector plane in the plane wave expansion. We have employed a set of 500 and 5000 kpoints to calculate band structure and optics in the irreducible Brillouin zone (IBZ).

3.3 Results and discussion

3.3.1 Crystal structure and the equation of state

The metal-based alkali perchlorates $MClO_4$ M=(Li, K, Rb, Cs) crystallize with space group (Pnma) and (Cmcm) for Na ClO_4 Figure-3.1. The unit cell of all compounds consists of four formula units (Z=4) with (24) an equal number of atoms. In LiClO₄ [38] structure Li is enclosed by oxygen atoms attached to ClO_4 ions. The Na ClO_4 [39] is slightly stretched along its two-fold axis which lies parallel to the crystallographic b-axis containing two different oxygen atoms (O1 and O2). In particular, KClO₄, RbClO₄, $CsClO_4$ [40,41] consists of four metal atoms and each metal ion is coordinated with eight O atoms that belong to ClO_4 and other six to different ClO_4 groups. The well-known ammonium perchlorate is proved to be closely isostructural with $RbClO_4$ [42]. To explore the structural stability with metal atom variation in perchlorate crystals, we took an interest to study the equation of state, BEC's tensor theory, and vibrational properties. We performed geometry optimization to obtain ground state structure by taking experimental data as input. The plane wave pseudopotential(PW/PP) approach with LDA/GGA functional has been done where LDA shows a large deviation compared with GGA from the experimental value. From Li \rightarrow Na \rightarrow K \rightarrow Rb \rightarrow Cs, the error percentage in the calculated volume increased with conventional LDA (from 7 to 10%), PBE & PW91 (from 6 to 12%) functional. As the standard functionals in DFT lack to obtain accurate groundstate structure, we have used dispersion correction methods to check non-local week vdW forces. Further, after the inclusion of different dispersion corrected methods the decrement in the error percentage of unit cell volume is observed LDA-OBS(around 13%), PBE-G06 (1%), PW91-OBS (from 2 to 5%). The calculated lattice constants and primitive cell volume is reported in Table-3.1 with an error percentage that is consistent with the experimental data reported. We used (PBE+G06) corrections for (Li/Na/K/Rb)ClO₄ and PW91+OBS for CsClO₄. The optimized cell volume shows slight increase (Li \rightarrow Na \rightarrow K \rightarrow Rb \rightarrow Cs) and lattice parameters a, b, c show the same order in all compounds as follows $a_{Cs} > a_{Rb} > a_{K} > a_{Li} > a_{Na}$ upon moving from lighter to heavier metal atom. Also, (Table-3.2) calculated inter-atomic distances match to experimentally reported data.

Further, we have calculated the equation of state (EOS) of these perchlorates which is a fundamental relationship between pressures-volume to describe the response of a solid under compression or expansion. By fitting pressure vs volume in third-order Birch - Murnaghan equation [43], we have calculated pressure derivative (B_0') and equilibrium bulk modulus B_0 of these five compounds which have been used widely for expressing the (PV)relationship. The obtained B_0 (B_0') value are for LiClO₄ 32.76 GPa (4.18), NaClO₄ 27.11 GPa (5.43), KClO₄ 23.87 GPa (5.52), RbClO₄ 23.01 GPa (4.24), CsClO₄ 13.7 GPa (5.93). The results indicate that these materials lose hardness as atomic number increases.



b. c in Å) and Volume (V in Å³) of of $MClO_4$ (M = Li, Na, K, Rb, Cs) using standard

 Table 3.1 Calculated lattice parameters (

Compound	Parameter	Experiment	LDA	LDA+OBS	$\overline{ m PBE}$	PBE+G06	PW91	PW91+OBS
$\mathrm{Li}ClO_4$	ದ	8.865	8.565	8.484	8.756	8.745	8.751	8.644
pnma, z=4	q	6.912	6.618	6.402	7.044	6.793	7.040	6.759
	C	4.832	4.737	4.629	4.962	4.820	4.958	4.839
	>	289.18	268.543(-7.1%)	251.485(-13.0%)	306.149(5.8%)	286.491(-0.9%)	305.506(5.6%)	282.80(-2.2%)
${ m Na}ClO_4$	ದ	4.816	4.628	4.556	4.902	4.763	4.909	4.0809
cmcm, z=4	q	4.816	4.628	4.556	4.902	4.763	4.909	4.080
	၁	7.048	6.891	6.798	7.225	7.213	7.239	7.123
	>	162.93	146.876(-9.8%)	140.443(-13.8%)	172.953(6.1%)	162.629(-0.2%)	173.787 (6.6%)	164.198(0.7%)
$\mathrm{K}ClO_4$	ಡ	8.866	8.394	8.323	9.039	8.905	9.012	8.829
pnma, z=4	q	5.666	5.439	5.323	5.878	5.580	5.8790	5.7249
	О	7.254	6.952	6.850	7.433	7.264	7.4623	7.2909
	>	364.40	317.445(-12.8%)	303.542(-16.7%)	394.98(8.3%)	360.99(-0.9%)	395.37(8.4%)	368.52(1.1%)
${\rm Rb}{ClO_4}$	ಡ	9.252	8.946	8.827	9.510	9.385	9.4999	9.323
pnma, z=4	q	5.789	5.548	5.471	6.025	5.732	6.035	5.903
	၁	7.211	7.211	7.114	7.731	7.498	7.7541	7.586
	>	400.19	357.982(-10.5%)	343.625(-14.1%)	443.069(10.7%)	403.461(0.8%)	444.587(11.0%)	416.600(4.1%)
$\mathrm{Cs}ClO_4$	ದ	9.823	209.6	9.579	10.100		10.120	9.922
pnma, $z=4$	q	600.9	5.740	5.578	6.267		6.2511	6.099
	О	7.764	7.576	7.472	8.118	1	8.1158	7.963
	11	86 927	41E 001/ 0 407)	700 907 /10 607 /	E19 001 (19 107)		(400 01)04 445(10)	100 000 (2 107)

Experiment 1 [38–41]

Table 3.2 Calculated Theoretical (T) and Experimental(E) inter-atomic distances (in Å) of $MClO_4$ (M = Li, Na, K, Rb, Cs).

$\mathrm{a})\mathrm{Li}ClO_4$	Theoretical	Experimental	Angle	Theoretical	Theoretical Experimental	Bond	Theoretical	Experimental
Li-O(1)	2.17	2.174	O(1)-Cl-O(2)	109.756	108.43	Cl-O(1)	1.448	1.449
-O(2)	1.989	1.989	O(2)-Cl-O(3)	109.481	109.50	-0(2)	1.436	1.430
-O(3)	2.412	2.412	O(2)-Cl- $O(2)$	111.200	111.2	-O(3)/(4)	1.4306	1.436
-O(4)	1.989	1.989	O(1)- Cl - $O(3)$	109.756	109			
$b)NaClO_4$								
Na-O(1)	2.644	2.644	O(1)- Cl - $O(1)$	106.9	107.0	CI-O(1)	1.432	1.432
-O(2)	-2.518	2.518	O(1)- Cl - $O(2)$	110.6	110.6	-0(2)	1.437	1.437
-0(3)	2.706	2.706	O(2)-Cl- $O(2)$	107.7	107.7			
-0(1)	2.385	2.385						
c) KClO ₄								
K-O(1)	2.87	2.85	O(1)-Cl-O(3)	110.611	110.62	Cl-O(1)	1.422	1.441
-0(2)	2.86	2.82	O(2)- Cl - $O(2)$	108.46	108.46	-0(2)	1.432	1.448
$-\mathrm{O}(2)$	2.88	2.84	O(1)- Cl - $O(2)$	109.22	109.17	-0(3)	1.441	1.431
-O(3)	2.87	2.83	O(2)-Cl-O(3)	109.70	109.69	-0(3)	1.441	1.440
$\mathrm{d})\mathrm{Rb}ClO_4$								
Rb-O(1)	3.03	3.03	O(1)- Cl - $O(2)$	111.206	111.1	Cl-O(1)	1.421	1.422
-O(2)	3.24	3.24	O(2)- Cl - $O(3)$	108.836	108.8	-0(2)	1.428	1.428
-O(3)	3.09	3.09	O(1)- Cl - $O(3)$	109.709	109.7	-0(3)	1.434	1.435
-O(3)	2.98	2.98	O(3)-CI-O(3)	108.575	108.6	-0(43)	1.434	1.435
-O(2)	3.24	2.99						
-0(1)	3.52	3.52						
-O(3)	2.99	2.99						
e) $CsClO_4$								
Cs-O(1)	3.043	3.043	O(1)-Cl- $O(2)$	112.206	112.2	CI-O(1)	1.426	1.427
-O(2)	3.137	3.137	O(2)-Cl-O(3)	108.675	108.7	-0(2)	1.422	1.422
-O(3)	3.152	3.152	O(1)- Cl - $O(3)$	109.291	109.3	-0(3)	1.441	1.422
-O(3)	3.179	3.180	O(3)-CI-O(3)	108.636	108.6	-0(3)	1.441	1.442
-0(3)	3.243	3.243						
-0(1)	3.591	3.592						
-0(2)	3.446	3.446						

xperiment 2 [38–4

3.3.2 Vibrational properties

The IR and Raman are hasty and versatile vibrational techniques consisting of two interactions, intermolecular and intramolecular. In which, intermolecular interactions are external (lattice) modes (liberation, translation, rotational) whereas intramolecular are internal modes (i.e bending and stretching). To visualize the collective vibrations from the cation and anion in the low-frequency region (i.e <100 cm⁻¹ to 1200 cm⁻¹), we used norm-conserving pseudopotential with van der Walls corrections to calculate vibrational frequencies. Here, we present the zone center vibrational frequencies using density functional perturbation theory. Metal perchlorates MClO₄ (M = Li, Na, K, Rb, Cs) show the same point group symmetry $D_{2h}(mmm)$ with an equal number of atoms in the primitive cell (24 atoms) and also there will be 72 vibrational modes. In all the crystal structures except in sodium perchlorate, the Cl atom is located at 4c Wyckoff cite and three inequivalent oxygen atoms O1/O2/O3 are located at 4c/4c/8d Wyckoff cites. Similarly, metal atoms Li/Na/K/Rb/Cs are located at 4b/4c/4c/4c. As NaClO₄ shows orthorhombic C-centred crystal structure having a primitive cell with 12 atoms, there will be a total of 36 modes out of which 33 are optical modes, and the O1, O2 atoms in $NaClO_4$ are located at 8f, 8g cites. The irreducible representation has been deduced from group theory with respect to the space group mentioned above:

```
\begin{split} &\Gamma_{acoustic} = B_{1u} \oplus B_{2u} \oplus B_{3u}; \\ &\Gamma_{optic} = Li: \ 9A_g \oplus 9A_u \oplus 6B_{1g} \oplus 11B_{1u} \oplus 9B_{2g} \oplus 8B_{2u} \oplus 6B_{3g} \oplus 11B_{3u}. \\ &\text{Na:} \ 6A_g \oplus 2A_u \oplus 5B_{1g} \oplus 4B_{1u} \oplus 2B_{2g} \oplus 5B_{2u} \oplus 5B_{3g} \oplus 4B_{3u} \\ &\text{K/Rb/Cs:} \ 11A_g \oplus 7A_u \oplus 7B_{1g} \oplus 10B_{1u} \oplus 11B_{2g} \oplus 6B_{2u} \oplus 7B_{3g} \oplus 10B_{3u} \end{split}
```

Among these various modes, B_{1u} , B_{2u} , B_{3u} are IR-active and A_g , B_{1g} , B_{2g} , B_{3g} are Raman active modes. Whereas A_u modes are silent or hyper Raman-active modes. Among the calculated 72 modes, 3 are acoustic and the remaining 69 are optical modes. We report an overall analysis of vibrational mode assignments in Table-3.3 and Figure-3.2 represents internal and external modes of five compounds at various frequencies. As we go down the periodic table from Li to Cs, the number of IR modes show decrement (Li-39, Na-15, K/Rb/Cs-23) whereas Raman modes increases (Li-30, Na-18, K/Rb/Cs-36) which clearly tells that polarizability/optical response is increased from Li \to Na \to K \to Rb \to Cs. The frequency modes (>900 cm⁻¹) arise because of the symmetric and asymmetric stretching vibration of ClO_4 . Whereas, mid frequencies (400 cm⁻¹ to 900 cm⁻¹) are due to scissoring, wagging, twisting type vibration of ClO_4 ion. The low frequencies (0 cm⁻¹ to 400 cm⁻¹) are because of translation and rotational modes of (Li/Na/K/Rb/Cs) metal atom and ClO_4 . It is also noticed that the internal modes vary with atomic size and are highly dominated by ClO_4 group. To analyze the intensity variations in the vibrational modes, we have plotted the IR-spectra reported in Figure-3.3. It is clear from the plot that there are three peaks except for sodium perchlorate which shows a redshift and these

Table 3.3 Calculated phonon frequencies (in cm⁻¹) along with corresponding assignment.

Mode number	$LiClO_4$	$NaClO_4$	$KClO_4$	$RbClO_4$	$CsClO_4$	Assignment
M6-M36	67 - 399	39 – 225	12 - 166	37 - 143	33 - 141	lattice modes
M37-M56	431 – 653	420 – 640	443 – 620	442 – 617	440 – 614	Scissioring of ClO_4
M57 - M60	928 – 934	925 – 928	909 – 911	907 – 911	904 – 905	Symm stretch ClO_4
M61-M69	1026 - 1177	1062 - 1132	1044-1165	1044 - 1157	1031-1147	Asymm stretch ClO_4

modes appear due to symmetric and asymmetric stretching of ClO_4 . Considering the mid-frequency region, there are three peaks mainly arising due to scissoring, twisting, rotation of ClO_4 and metal atom translations. It is observed that there are two peaks around 600 cm^{-1} in Li, Na, K, as atomic mass increases to Rb and Cs these peaks coincide with each other showing one mode. Another peak around 650 cm^{-1} decreases in intensity and considerably shows a redshift which is attributed to change in the metal atom and ClO_4 interaction. Also, it is noticed that peak around 652.8 cm^{-1} in $LiClO_4$ is found to be the silent mode (IR + Raman inactive) and as the metal atom increases from Li to Na, this mode shows Raman active nature whereas in K, Rb, Cs this mode becomes IR active. Overall, obtained vibrational frequencies and experimental investigation show a good agreement in the frequency range $935-940 \text{ cm}^{-1}$ [10].

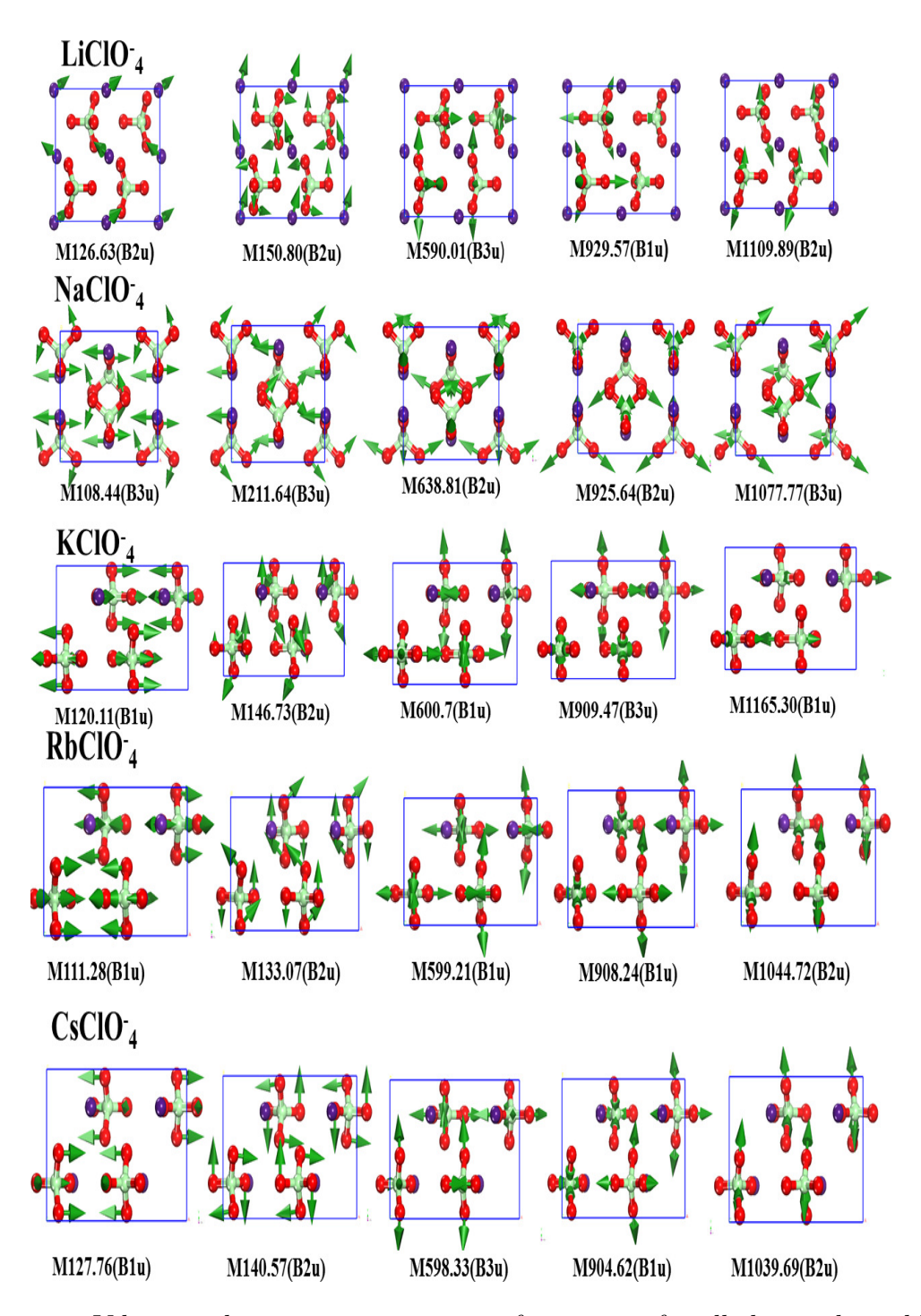


Figure. 3.2 Vibrational animations at various frequencies for alkali metal perchlorates $\text{Li}ClO_4$, $\text{Na}ClO_4$, $\text{K}ClO_4$, $\text{Rb}ClO_4$, $\text{Cs}ClO_4$.

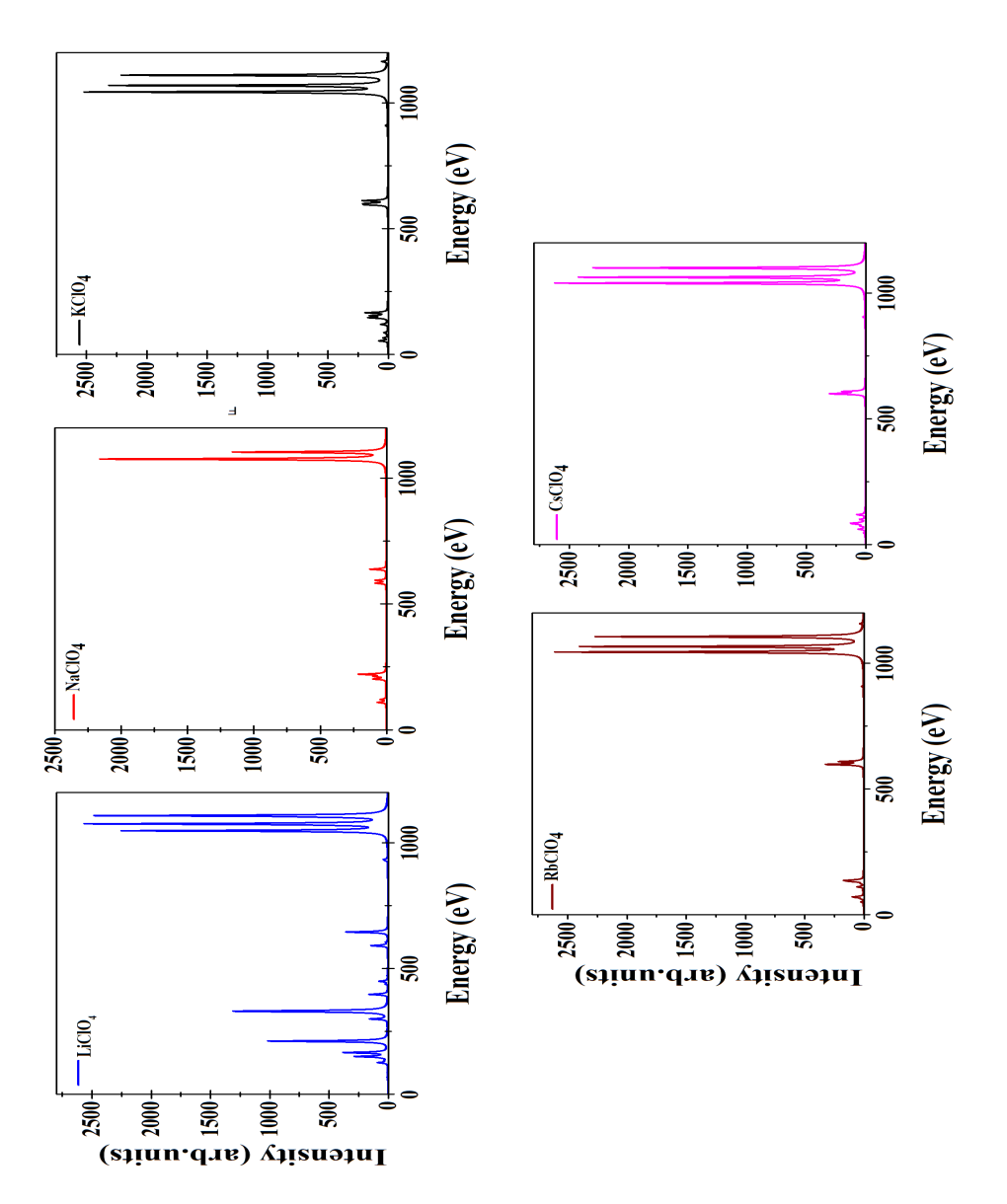


Figure. 3.3 Calculated IR spectra of alkali metal perchlorates (M= Li, Na, K, Rb, Cs) MClO₄.

3.3.3 Born effective charges (BEC's)

The spontaneous polarization $\triangle P$ is a fundamental bulk property of ferroelectric materials from which their dielectric permittivity, BEC's and piezoelectric tensor can be derived [44]. The born effective charge Z* (alias transverse charge or dynamic effective charge) was introduced by King-Smith and Vanderbilt in 1993 [45] where $\triangle P$ can be evaluated from the Bloch function describing the ground state by using Berry phase scheme [45,46]. $\triangle P$ is the difference in the dipole moment of the cell charge distribution between two different geometries and Z* is related to the change in the polarization (or dipole moment) for molecules created by sublattice displacements [46]. Recent advances in BCE's theory allow us to determine Z* using perturbation theory [47] or finite difference polarization [46]. In solid-state physics, the splitting of frequencies between LO-TO phonons is considered as a basic quantity which is due to long-range Coulomb interaction computed using first principles. It is known that the large BEC points towards the relative displacement of neighboring atoms against each other and can lead to large polarization. The later work suggested that fluorocarbonates [48] show a large Born effective charge value which explains strong covalent bonds between specific ions. Our results in Table-3.4 shows the diagonal BEC's and percentage deviation of M=(Li, Na, K, Rb, Cs), O and Cl atoms having three $(Z^*_{xx} \neq Z^*_{yy} \neq Z^*_{zz})$ independent components resulting from the orthorhombic structure. Here, the effective charge of the metal ion is close to its nominal ionic charge. So, it can be concluded that bonds between metal and oxygen ions are primarily ionic, the same as in density of states. Similarly, the effective charges of Cl and O deviate from their nominal ionic values indicating covalent bonding in all the compounds. The BEC value of Cl decrease in all axis as atomic size increase which results in a strong covalent bond and week ionic bond in $LiClO_4$ and shows strong ionic and week covalent nature as it goes to $CsClO_4$. The charge deviation of a metal atom, Cl, and O are non-identical along with three independent components which have been shown in Table-3.4.

3.3.4 Electronic band structure and density of states

In this section, we present the band structure and chemical bonding of alkali metal perchlorates. Extensive theoretical work has been carried out in the last few decades on alkali metal chlorates, perchlorates [49–52]. However, the reported results show characteristics of molecular crystals with complex chemical bonds. In this work, three different functionals are used PBE-GGA, EV-GGA, and TB-mBJ to study the bonding nature of these compounds. It is already established that functional LDA and GGA generally underestimate the energy band gaps about 50% as compared to experiments because it includes electron self-interactions and also lacks the derivative discontinuities of the exchange-correlation potential with respect to occupation number [53, 54]. So, more accurate hybrid methods such as GW approximations are needed to get reliable values for energy bandgap. These hybrid methods are computationally expensive whereas TB-mBJ

Table 3.4 Calculated BEC's and percentage of deviation of the Li, Na, K, Rb, Cs, Cl, O1, O2, O3 atoms at the theoretical equilibrium volumes.

Ion	Nominal ionic charge	Z_{11}	Z_{22}	Z_{33}	$Z_{11}\%$	$Z_{22}\%$	$Z_{33}\%$
Li	+1	1.37	1.19	1.31	37.17	19.45	31.22
Cl	-1	3.35	3.43	3.45	-235.22	-243.96	-245.78
O1	-2	-0.87	-1.45	-1.11	56.5	27.5	44.5
O2	-2	-2.12	-0.90	-0.70	6.0	55	65
O3	-2	-0.87	-0.83	-1.85	56.5	58.5	7.5
Na	+1	1.16	1.29	1.17	15.53	28.93	17
Cl	-1	3.12	3.25	3.26	-212.49	-225.98	-226.28
O1	-2	-0.68	-1.16	-1.54	66.0	42	23
O2	-2	-1.46	-1.11	-0.67	23	44.5	66.5
K	+1	1.26	1.23	1.24	26.34	23.945	24.06
Cl	-1	3.12	3.28	3.17	-212.283	-228.39	-217.28
O1	-2	-0.76	-1.53	-1.12	62	23.5	44
O2	-2	-1.28	-0.76	-1.24	14	62	38
O3	-2	-1.58	-0.70	-0.92	21	65	54
Rb	+1	1.34	1.29	1.29	34.46	29.39	28.9
Cl	-1	3.13	3.32	3.18	-212.57	-232.18	-218.38
O1	-2	-0.79	-1.56	-1.14	60.5	22	43
O2	-2	-1.60	-0.70	-0.90	-1.60	-0.70	-0.90
O3	-2	-1.29	-0.78	-1.28	-1.29	-0.78	-1.28
Cs	+1	1.38	1.33	1.33	38.12	33.51	33.44
Cl	-1	3.16	3.31	3.15	-212.588	-231.13	-214.76
O1	-2	-0.80	-1.57	-1.14	60	21.5	43
O2	-2	-1.65	-0.71	-0.85	20	65	55
O3	-2	-1.23	-0.77	-1.34	35.5	61	37.5

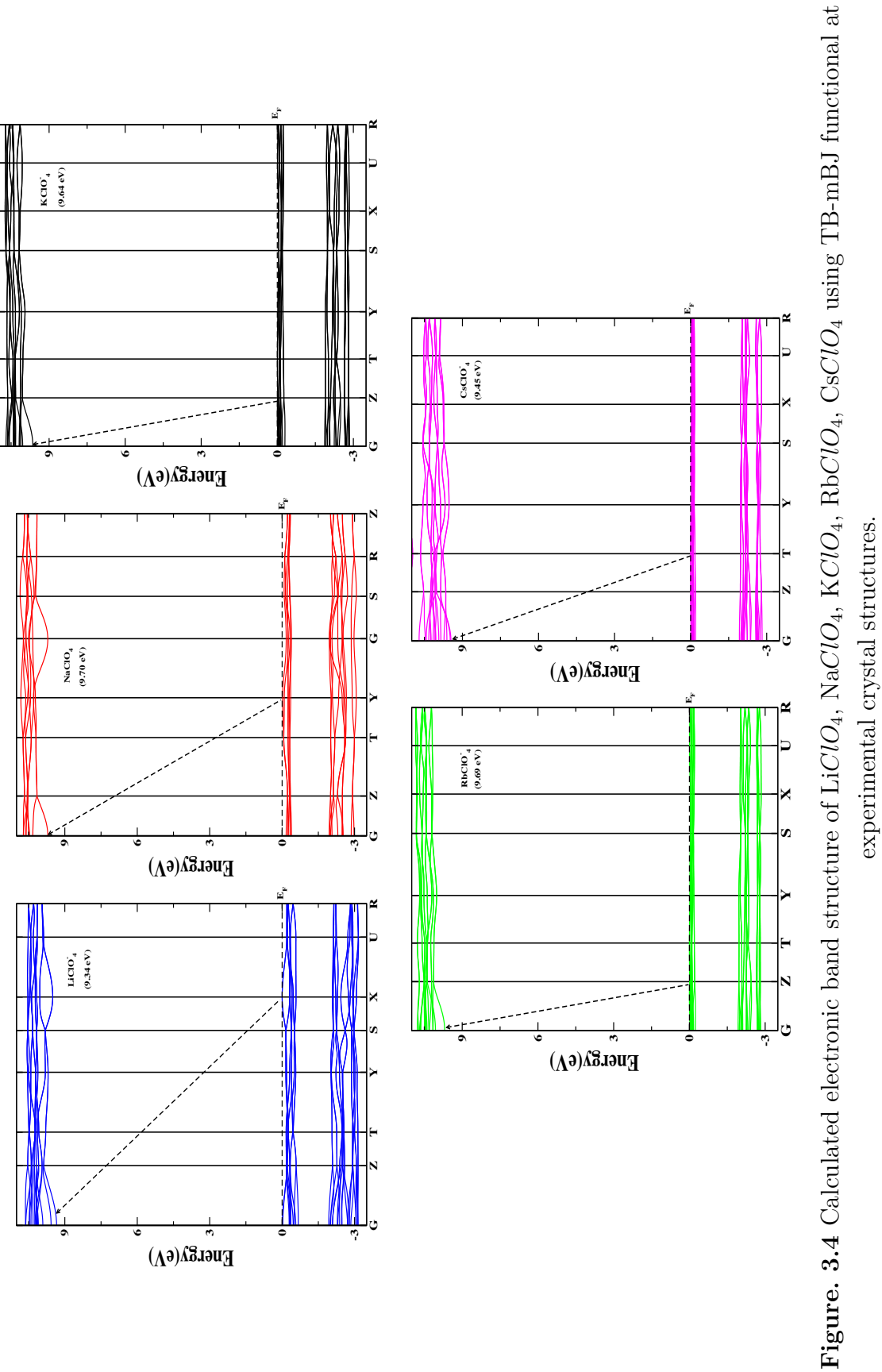
is not. So, we used recently developed TB-mBJ potential involving exchange energy which predicts accurate band gaps than any other semi-local functional for semiconductor and insulators [35, 55, 56]. By using this mBJ potential, the bandgap obtained for alkali metal nitrates, chlorates, orthovanadates, periodates, carbonate fluorides, fluorocarbonates are accurate when compared to experimental results [48, 57–62]. We could notice that TB-mBJ functional improves the energy bandgap when compared with PBE, EV-GGA functional, reflecting the same in the density of states.

Figure-3.4 and Table-3.5 indicate that bandgap (9 eV) with mBJ potential for all the compounds. The previously reported bandgap with oxygen edge experiment is very much similar to the result with LDA and GGA [49,51]. Therefore, we have done mBJ band

Table 3.5 Calculated band gap of $MClO_4$ M =(Li, Na, K, Rb, Cs) along high symmetry directions using PBE-GGA, EV-GGA, TB-mBJ potential.

Compound	GGA	EV	TB-mBJ	Experiment
$-$ Li ClO_4	6.413	6.854	9.337	-
$\mathrm{Na}ClO_4$	6.031	6.506	9.701	-
$KClO_4$	6.183	6.664	9.636	5.66*
$\mathrm{Rb}ClO_4$	6.154	6.636	9.690	
$\mathrm{Cs}ClO_4$	6.073	6.485	9.449	-
* Experiment 3 [49,50], [51] oxygen edge				

structure in the Brillouin zone which reveals that the studied compounds are having an indirect bandgap. From our analysis, in conduction band as atomic size increases, dispersive nature has been observed compared to valence band maximum. This observation shows holes are heavier than electrons in the conduction band. Consequently, electrons have higher mobility than holes. As a result, we can expect p' electrons to be tightly bound to their atom and make the valence band less mobile. The concentration of holes to the conductivity is expected to be smaller than that of conduction band electron. Valence bands of $MClO_4$ M=(Li,Na, K, Rb, Cs) are flat and narrow similar to periodates [58]. This implies a large effective mass for the holes in the first Brillouin zone. In other words, a less dispersive nature in the valence band reduces the mobility of charge carriers influencing less transport of carriers towards the emission center. The above discussion shows scintillation to occur in perchlorates similar to periodates [58]. In density of states Figure-3.5, the bands near the valence states are highly dominated with O-2p states and Cl-d states, and increasing s/p states in metal atoms have been observed as atomic mass increases. Around 3 eV, we observe there is overlap between O-2p and Cl-d states resulting in hybridization. The above observation shows ionic and covalent nature to be found in these compounds. This concludes that alkali metal perchlorates have a mixed nature of bonding and may find application as inorganic scintillators.



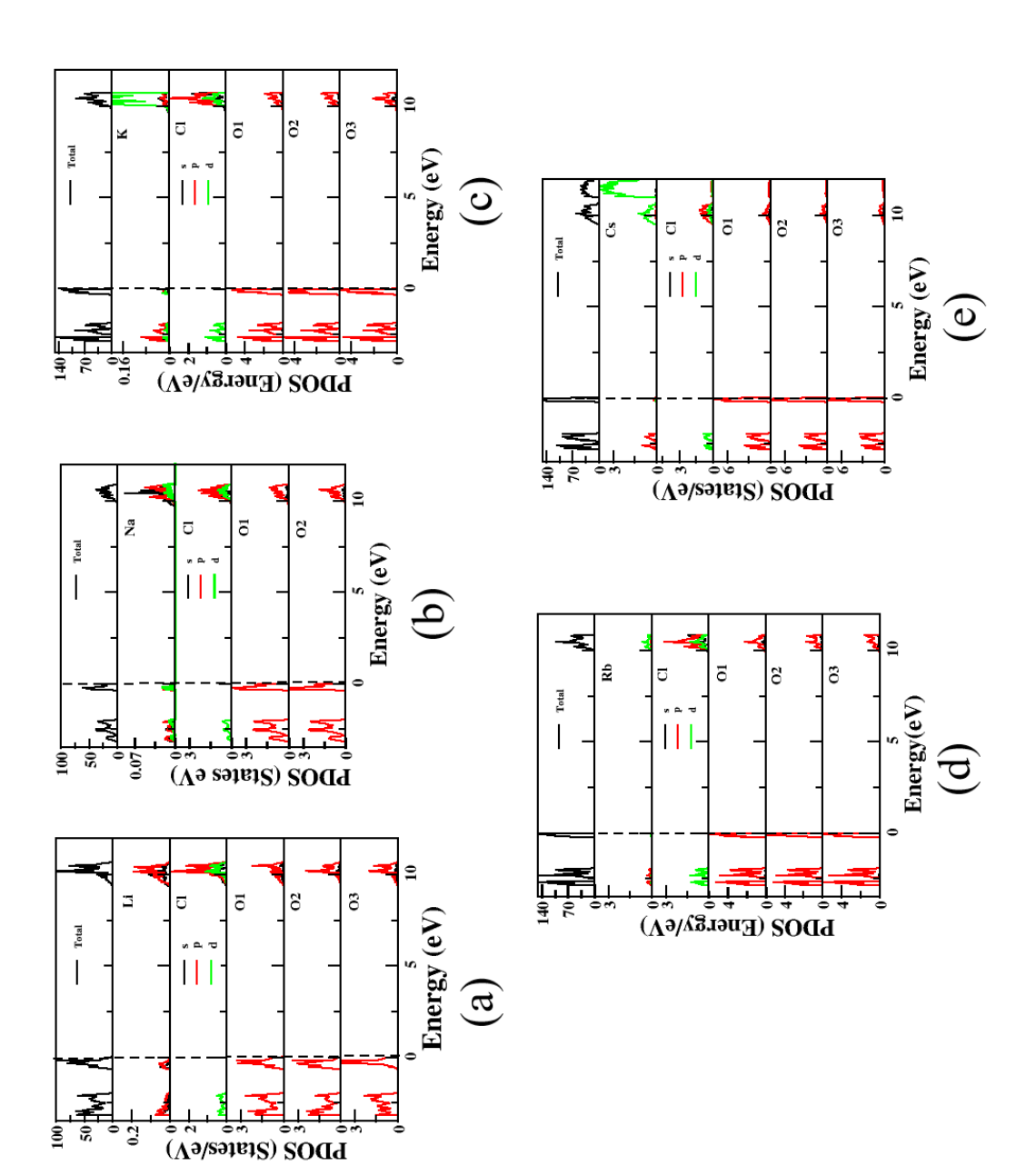


Figure. 3.5 Calculated Total and partial density of states of LiClO₄, NaClO₄, KClO₄, RbClO₄, CsClO₄ using TB-mBJ potential at experimental crystal structures.

3.3.5 Optical properties

In this subsection, we have investigated optical properties to improve applications of scintillators and photonic devices. The frequency-dependent dielectric function, absorption coefficient, reflectivity, and energy loss function are calculated for a better understanding of the electronic structure and optical properties of metal perchlorates (Figure-3.6 3.7,3.8). The optical response of a system to electromagnetic radiation is understood by dielectric function. The response of the interband transtions to the dielectric loss can be calculated by summing the occupied valence band to unoccupied conduction bands within selection rules. From the Kramers-Kronig relation, the dispersive part is deduced. And all other optical constants such as energy-loss function L(x), refractive index n(x), absorption coefficients are deduced from the real and imaginary part of dielectric constants. The optical spectra of metals (Li, Na, K) perchlorates, nitrates, chlorates and have been studied with DFT-LDA earlier [50]. Our main focus is on the imaginary part which illustrates optical transitions and refractive index as a function of energy (eV). Based on these results, we try to convey these materials may find application in scintillators.

Further, comparing the optical results with the electronic band structure is an easy way to understand the electronic transitions. The real and imaginary dielectric tensor of M=(Li, Na, K, Rb, Cs) versus energy (eV) along three crystallographic directions as per crystal lattice are shown in the Figure. The imaginary part has four prominent peaks at 10.5 eV, 13.2 eV, 17.29 eV, 19-24.5 eV due to interband transitions between the valance and conduction band along with three crystallographic directions. However, the imaginary part ϵ_2 of all the five compounds are forbidden in the range of 0-9 eV.

We noticed a small difference in the optical band gap which may originate due to the transition of an electron from the highest valence band to the lowest conduction band with respect to change in atomic mass. The electronic gap is usually larger than the optical gap and the difference is due to the Coulomb energy. The optical gap is a threshold for photons to be observed whereas the electronic gap is the threshold for creating electron-hole pairs bound together. These atomic transitions proceed rapidly if the coupling between the initial and final state is stronger. The optical transitions with the most probability corresponding to each peak are mentioned in Table-3.6. It is found that the optical transitions below 15eV are strong due to oxygen, chlorine and metal (Li, Na, K, Rb, Cs) atom and above 15eV the transitions are due to cation M=(Li, Na, K, Rb, Cs) p and s states. The dispersive part for all the compounds reported in Table-3.7; show very little variation in all three crystallographic directions. Absorption spectra($\alpha(\omega)$) illustrates without excitonic interaction from 10 eV to 25 eV. None of the structures show absorption peaks in low-energy regions implying that they are consistently transparent. It consists of small peaks (up to 15 eV) and two other peaks (16.5eV to 25.0eV). The absorption intensity of two peaks around 10-15 eV decrease as mass increases while the

Compound	Energy (eV)	Possible optical transitions
$\overline{\text{Li}ClO_4}$	A	O(p)- $Cl(d)$, $Cl(s)$, $Li(s)$, $Li(p)$ - $Cl(d)$
	В	O(p)- $Cl(d)$, $Cl(d)$ - $O(2p)$, $Li(p)$, $Li(s)$
$NaClO_4$	A	O(p)- $Cl(d)$, $Cl(s)$, $Na(s)$, $Na(p)$ - $Cl(d)$
	В	Cl(d)- $O(2p)$, $Cl(s)$, $Na(s)$, $Na(p)$, $Na(d)$ - $Cl(s)$, $O(p)$, $O(s)$
$\overline{KClO_4}$	A	O(p)-Cl(s), Cl(d), K(d)
	В	O(p)- $K(d)$, $Cl(s)$, $Cl(d)$, $K(s)$
$RbClO_4$	A	O(p)-Cl(s), Cl(d), Rb(d)
	В	O(p)- $Rb(d)$, $Rb(s)$, $Cl(d)$, $Cl(s)$
$CsClO_4$	A	O(p)-Cs(d), Cl(s), Cl(d
	В	O(p)- $Cs(d)$, $Cl(s)$, $Cl(d)$, $Cs(s)$

Table 3.6 Calculated optical transitions corresponding to the peaks below 15 eV.

rest of the peaks have shown an increase in intensity at different energies i.e $KClO_4$ at 23.5 eV, $RbClO_4$ at 21.04 eV and $CsClO_4$ 16.78. These absorption spectra show that more absorption after 15 eV in all the metal perchlorates which in turn indicates more absorption in the ultraviolet region.

The refractive index is very important to study photoelectronic devices. The calculated dielectric function and refractive indices of alkali metal perchlorates are almost equal in three crystallographic directions. The obtained refractive indices for metal M=(K, Rb, Cs) ClO_4 are consistent with experimental results reported to [42]. Here, the optical constants are almost isotropic, despite all the compounds having an orthorhombic crystal structure. In particular, peaks in $LiClO_4$ and $NaClO_4$ show slightly distorted peaks comparing with $KClO_4$, $RbClO_4$, $CsClO_4$. Similarly, $L(\omega)$ describes how fast the electron will lose its energy while traveling inside a material. The prominent peaks in $L(\omega)$ spectra indicate the characteristic associated with plasma peaks and the collective oscillations with corresponding frequencies are known as plasma frequencies. Materials with frequencies more than plasma frequencies behave like a dielectric $(\epsilon_1(\omega) > 0)$ and are lesser than that that acts as metal. The peak corresponding to 13eV reduces as atomic mass increases. These denote low plasma frequencies in $CsClO_4$. Unfortunately, since there are no experimental reports we could not compare the results obtained. The $R(\omega)$ reflectivity is shown (10 eV to 25 eV) in three crystallographic directions. The reflectivity of $LiClO_4$ and $NaClO_4$ indicate same and $KClO_4$ is similar to $RbClO_4$ and $CsClO_4$. All the compounds show different reflectivity range, as follows $LiClO_4$ and $NaClO_4$ at 13.45 eV (010) and 13.31 eV (100) direction, $KClO_4$ is 24.39 eV (010) and $RbClO_4$ at 21.51 eV (010) and finally $CsClO_4$ at 17.320 eV (010). The maximum reflection is M (ClO_4) where M = Li, K, Rb, Cs are in (010) direction and Na in (100) direction. Overall, the summation of the discussion shows alkali metal perchlorates may find their application in inorganic scintillators due to their isotropic nature.

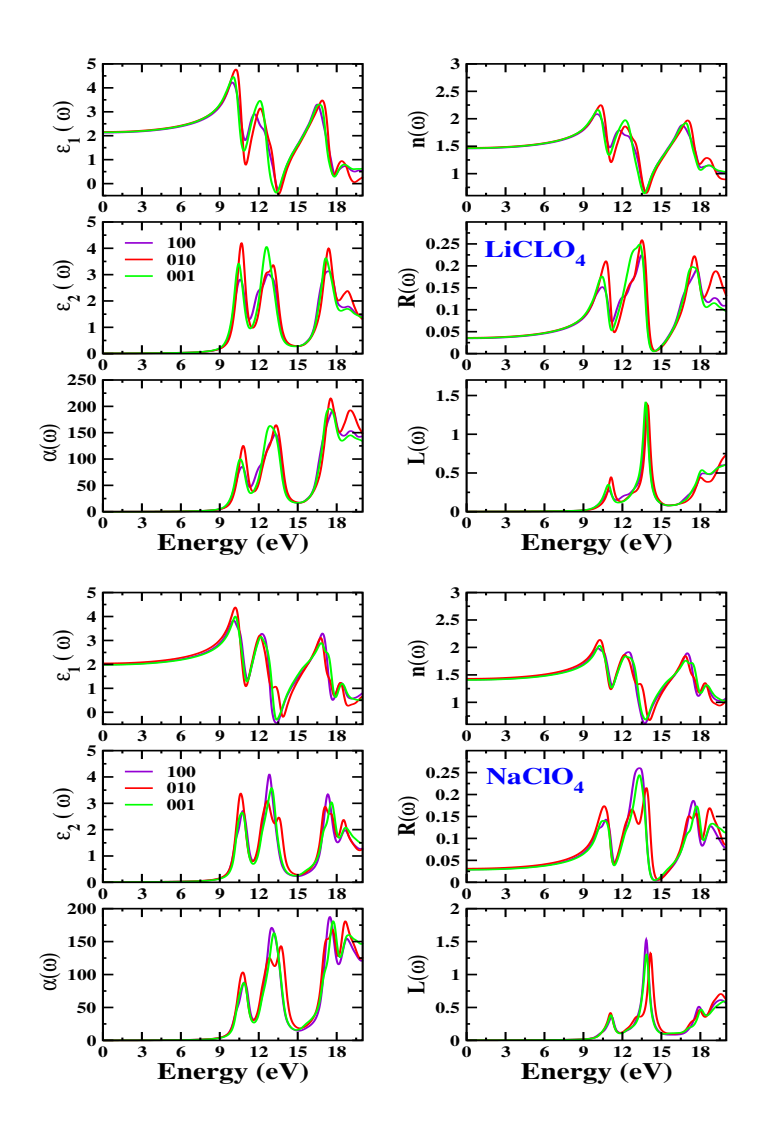


Figure. 3.6 The figure represents Dielectric constant, Dielectric loss, Absorption, Refraction, Eloss function, Reflectivity of $LiClO_4$, $NaClO_4$, using TB-mBJ functional at experimental crystal structures.

Table 3.7 Linear optical properties such as real part of dielectric function $\varepsilon_1(\omega)$ and absorption coeffcient $(\alpha(\omega) \times 10^4, \text{ cm}^{-1})$ of $MClO_4$ (M = Li, Na, K, Rb, Cs).

Compound	$\varepsilon_1^{[100]}(\omega)$	$\varepsilon_1^{[010]}(\omega)$	$\varepsilon_1^{[001]}(\omega)$	$\alpha^{[100]}(\omega)$	$\alpha^{[010]}(\omega)$	$\alpha^{[001]}(\omega)$
$LiClO_4$	1.45	1.46	1.46	192.21	215.03	195.34
$NaClO_4$	1.41	1.42	1.40	187.48	168.14	180.79
$KClO_4$	1.44	1.44	1.44	365.10	381.69	373
$\mathrm{Rb}ClO_4$	1.44	1.43	1.43	323	342.39	334.86
$CsClO_4$	1.46	1.45	1.45	272.47	280.41	264.50

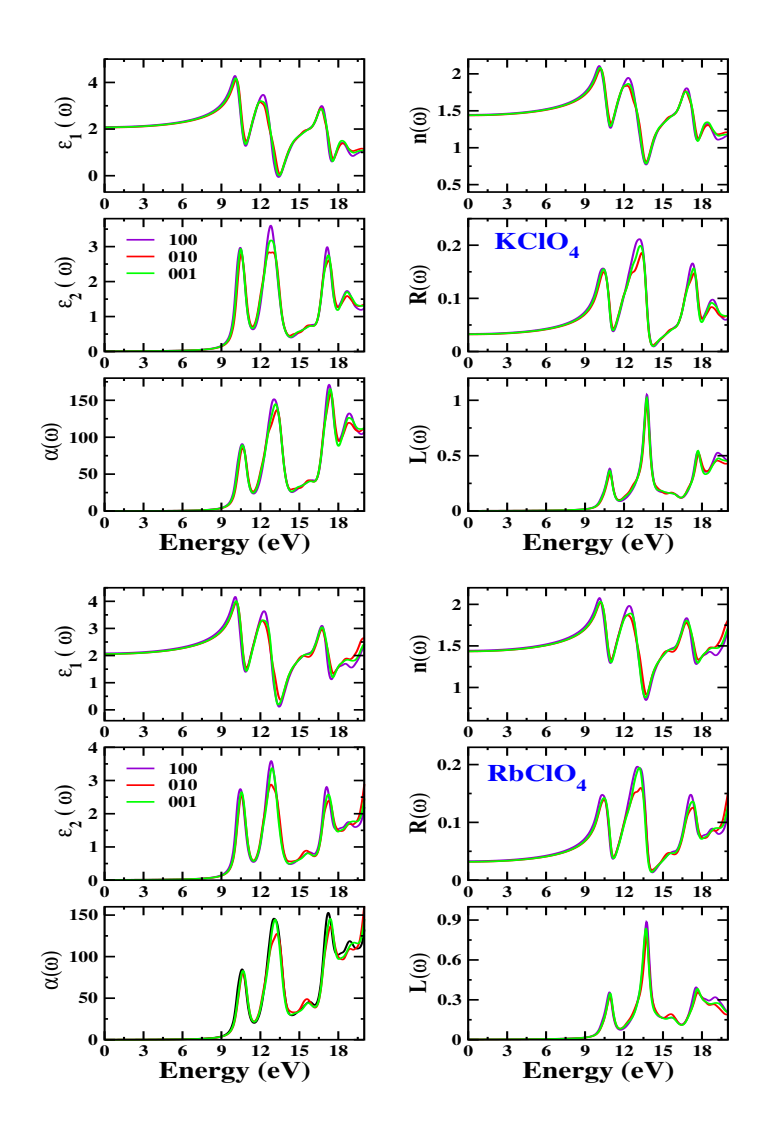


Figure. 3.7 The figure represents Dielectric constant, Dielectric loss, Absorption, Refraction, Eloss function, Reflectivity of $KClO_4$, $RbClO_4$ using TB-mBJ functional at experimental crystal structures.

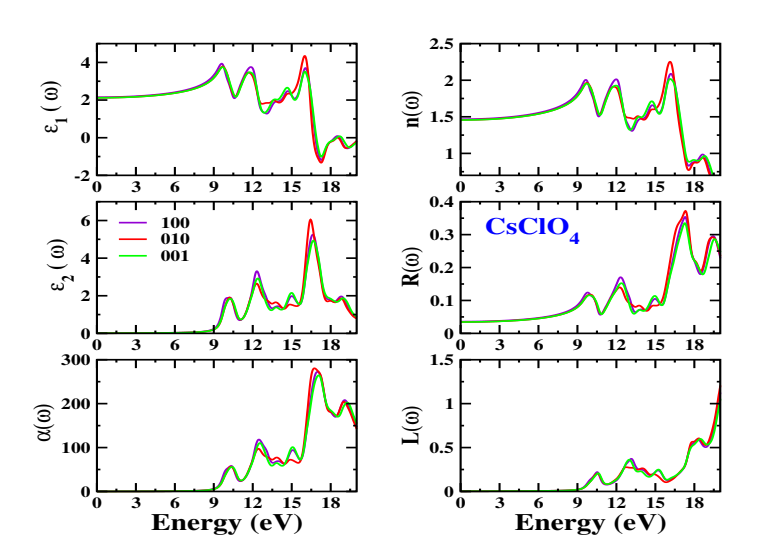


Figure. 3.8 The figure represents Dielectric constant, Dielectric loss, Absorption, Refraction, Eloss function, Reflectivity of $CsClO_4$ using TB-mBJ functional at experimental crystal structures.

3.4 Conclusions

To conclude, we carried out ab-initio calculations to study vibrational, Born-effective charges (BECs) tensors, band structure, the density of states, and optical properties of $MClO_4$ (M = Li, Na, K, Rb, Cs). The calculated lattice parameters and volume show good agreement with experimental results and the importance of Van der Waals forces. The present compounds lose hardness as atomic number increases. Further, the study of zone-center phonon frequencies and born effective charges within (DFPT) for all alkali metal perchlorates have been compared. The results show symmetric and asymmetric stretching modes are more pronounced in ClO_4 and the effective charge of Cl highly deviates from nominal charge indicating high polarization. The electronic and optical properties are summarized using FP-LAPW implemented in WIEN2k. From the Band structure analysis, TB-mBJ potential is found to improve over GGA and EV-GGA. Due to the increase in band dispersion and slope in the band structure, these compounds indicate weaker orbital interaction and slower carrier mobility. And in all the compounds O-2p states are highly dominating in valence state. The chemical bonding between the metal atom and perchlorate showed a mixed covalent and ionic nature. The study of optical constants shows that this material decomposes in the UV region and is found to be optically isotropic with an anisotropic structure, which may cause these materials to find application as inorganic scintillators. Our findings suggest further experimental investigations in this regard which could lead to applications of these materials in the field of Scintillators.

References

- Markowitz. M. M., Boryta. D. A., Harvey Stewart. Jr, Lithium Perchlorate Oxygen Candle, Pyrochemical Source of Pure Oxygen., Ind. Eng. Chem. Prod. Res. Dev., 1964, 321-330.
- [2] Davila. A., Willson. D., Coates. J. D. C., Mckay. P, Perchlorate on Mars a chemical hazard and a resource for humans, Int. J. Astrobiol., 2013, 321-325.
- [3] Kucharzyk. H. K., Soule. T., Paszczynski, Andrzej, Thomas. F. H, Perchlorate: Status and Overview of New Remedial Technologies, 2011.
- [4] Gilbert. M. B., Baohua. Gu, In:Gu B., Coates. J. D(eds) Perchlorates Springer, Boston, MA, The Chemistry of Perchlorate in the Environment, 2006.
- [5] Trumpolt. C. W., Crain. M., Cullison. G. D., Flanagan. S. J. P., Siegel. L., Lathrop. S., Perchlorate: Sources, uses, and Occurrences in the Environment, The Journal of environmental cleanup Costs technologies and techniques, 2005, 65-89.
- [6] Jotanovic. M., Andric. Z., Tadic. G., Vladan. M., A Further Study of Crystallization of Lithium Perchlorate from system, Appl. Technol. Innov., 2010, 15-22.
- [7] Gu. B., Coates J. D, 2006 Perchlorate Springer, Boston, MA.
- [8] Badgujar. D. M., Talawar, M. B., Zarko, V. E., New Directions in the area of Modern Energetic Polymers: An overview, Combust. Explos. Shock Waves, Combust. Explos. Shock Waves, 2017, 53-371.
- [9] Roberts. K. J., Telfer G. B., jackson. R. A., Wilde. P. J., Meenan. P., Determination of a Transferable Interatomic Potential for Alkali-metal Perchlorates and its Application to morphological Modelling, J. chem. soc faraday trans., 1995, 4133-4138.
- [10] Syal. S. K., Yoganarasimhan, S. R., Infrared and Permittivity Studies on Alkali Perchlorates, J. Solid State Chem., 1974, 332-340.
- [11] Verneker. V. R. P, Rajeshwar. K., Thermochim Acta, 1975, 293-304.
- [12] Klassen. B, Aroca. R, Nazri. G. A, Lithium Perchlorate Ab Initio Study of the Structural and Spectral changes associated with Ion pairing, J. Phys. chem., 1996, 100, 9334-9338.

- [13] Koch. E. C., special materials in pyrotechnics III application of Lithium and its Compounds in Energetic systems, 2004, Propellants Explos. Pyrotech.
- [14] Cheng. T. Z., Tuli. M., International Aero science, 2014, 3(1):1-5.
- [15] Abdelmoneim. H. M., Dielectric and AC Conductivity of Potassium Perchlorate, KCLO₄, Acta Phys. Pol., 2010, 117.
- [16] Carl. B.E.O., Shipley. H., The Decomposition of Potassium chlorate and its catalysis by potassium perchlorate, J. Am. Chem. Soc. 1924, 46, 2, 269-276.
- [17] Lee. J. S., Chung-King. H., Kuen-Shan., The Thermal Properties of KClO₄ with Different Particle Size, Thermochim Acta, 2001, 381-385.
- [18] Pistorius. C. W. F. T., J.Phys. Chem. Solids, 1970, 385-389.
- [19] Payne. M. C., Teter. M. P., Allan. D. C., Arias. T. A., Joannopoulos. J. D., Iterative Minimization Techniques for Ab Initio Total Energy Calculations: Molecular Dynamics and Conjugate Gradients, Rev. Mod. Phys., 1992, 64, 1045-1097.
- [20] Segall. M. D., Lindan.P. J. D., Probert. M. J., Pickard. C. J., Hasnip. P. J., Clark. S. J., Payne. M. C., First-principles Simulation: ideas, illustrations and the CASTEP code., J. Phys. Condens., 2002, 14, 2717-2743.
- [21] Troullier. N., Martins. J. L, Efficient Pseudopotentials for Plane-wave Calculations, Phys. Rev. B., 1991, 43, 1993-2006.
- [22] Monkhorst. H. J., Pack. J. D, Special Points for Brillouin-zone Integration, Phys. Rev. B., 1976, 13, 5188-5192.
- [23] Fischer. T. H, Almlof. J., General Methods for Geometry and Wave Function Optimization, J. Phys. Chem., 1992, 96, 9768-9774.
- [24] Ceperley. D. M, Alder. B. J., Ground State of the Electron Gas by a Stochastic Method, Phys. Rev. Lett., 1980, 45, 566-569.
- [25] Perdew. J. P., Zunger. A., Self-Interaction Correction to Density-Functional Approximations for Many-Electron Systems, Phys. Rev. B.,1981, 23, 5048-5079.
- [26] Perdew. J. P., Burke. S, Ernzerhof. M, Generalized Gradient Approximation Made Simple, Phys. Rev. Lett. 1996, 77, 3865-3868.
- [27] Perdew. J. P., Wang. Y, Accurate and Simple Analytic Representation of the Electron-Gas Correlation Energy, Phys. Rev. B., 1992, 45, 13244-13249
- [28] Grimme. S., Semiempirical GGA-Type Density Functional Constructed with a Long-Range Dispersion Correction. Journal of computational chemistry., 2006, 27, 1787-99.
- [29] Ortmann. F., Bechstedt. F., Schmidt. W, Semiempirical van der Waals correction to the Density Functional Description of Solids and Molecular Structures. Phys. Rev. B., 2006, 73.
- [30] Baroni. S., Gironcoli de. S., Dal Corso. A., Giannozzi. P., Phonons and Related Crystal Prop-

- erties from Density-Functional Perturbation Theory, Rev. Mod. Phys, 2001, 73, 515-562.
- [31] Milman. V., Refson. K., Clark. S. J, Pickard C. J., Yates. J. R., Gao. S.-p, Hasnip. P. J., Probert M. I. J., Perlov. A, Segall. M. D, Electron and Vibrational Spectroscopies using DFT, plane waves and pseudopotentials CASTEP implementation, J.Mol. Struct. Theochem., 2010.
- [32] Blaha.P., Schwarz. K, Madsen. G. K. H, Kvasnicka. D, Luitz. J, 2001, WIEN2K, an Augmented Plane Wave + Local Orbitals Program for Calculating Crystal Properties, Techn. Universitat: Wien, Austria.
- [33] Engel. E., Vosko. S. H., Accurate Optimized Potential Model solutions for Spherical Spin polarized atoms: Evidence for Limitations of the Exchange only Local Spin Density and Generalized Gradient Approximations, Phys. Rev. B, 1993, 47, 13164-13174.
- [34] Singh. D. J., Electronic structure Calculations with the Tran-Blaha Modified Becke-Johnson Density Functional, Phys. Rev. B., 2010, 82, 205102.
- [35] Koller. D., Tran. F, Blaha. P, Merits and Limits of the Modified Becke-Johnson Exchange Potential, Phys. Rev. B., 2011, 83, 195134.
- [36] Koller. D., Tran. F, Blaha. P, Improving the modified Becke-Johnson exchange potential, Phys. Rev. B., 2012, 85, 155109.
- [37] Tran. F., Blaha. P., Accurate and Gaps of Semiconductors and Insulators with a Semilocal Exchange-Correlation Potential, Phys. Rev. Lett., Proc. R. Soc. Lond, 2009, 102, 226401.
- [38] Wickleder. M. S., Crystal Structure of LiClO₄, Z. Anorg. Allg. Chem., 2003, 629, 1466-1468.
- [39] Wartchowand, V. R., Berthold, H. J., Kristallogr, Z., Cryst, Mater., 1978, 307-318.
- [40] Mani. N. V., Proc., The Crystal Structure of Potassium Perchlorate $KClO_4$, Indian Acad. Sci., 1957, 46, 2, 143-151.
- [41] Granzin. J., Zeitschrift für Kristallographie, 2010, 157-159.
- [42] Tutton. A. E. H., The Alkali Perchlorates and a New Principle Concerning the Measurements of Space-Lattice cells, Proc. R. Soc. Lond. Series A, Containing Papers of A Mathematical and Physical Character, 1926, 462-491.
- [43] Birch. F., Finite Strain Isotherm and Velocities for Single Crystal and Polycrystalline NaCl at High Pressures and 300K, J. Geophys. Res., 1978, 1257-1268.
- [44] Baranek. Ph., Dovesi. R, Ab Initio Approach to the Ferroelectric Properties of ABO₃ Perovskites, the Case of KNbO₃, Ferroelectrics, 2002, 268, 155-162.
- [45] King-Smith. R. D, Vanderbilt. D, Theory of Polarization of Crystalline solids, Phys. Rev. B., 1993, 47, 1651.
- [46] Resta. R, Macroscopic Electric Polarization as a Geometric Quantum Phase, Europhys. Lett, 1993, 22, 133
- [47] Gonze X., Allan. D. C, Teter. M. P, Dielectric tensor, Effective charges, and Phonons in α -quartz

- by Variational Density functional perturbation theory, Phys. Rev. Lett., 1992, 68, 3603.
- [48] Narsimha. Rao. E, Vaitheeswaran. G., Reshak. A. H, Auluck. S, RSC Adv., 2016, 6, 99885-99897.
- [49] Zhuravlev. Yu. N., Poplavnoi. A. S., J. Russ. Phys., 1996, 952-955.
- [50] Zhuravlev. Y. N., Korabelnikov. D. V., J. Russ. Phys., 2009, 52, 965.
- [51] Korabel'nikov. D. V., Zhuravlev .Y. N., Phys. Solid State., 2017, 254.
- [52] Zhuravlev Yu. N., Poplavnoi A. S., J. Russ. Phys., 2001, 44.
- [53] Perdew. J. P., Parr. R. G, Levy. M., Balduz J. L, Phys. Rev. Lett., 1982, 49, 1691-1694.
- [54] Sham. L. J, Schluter. M., Phys. Rev. Lett., 1983, 51, 1888-1891.
- [55] Martnez. J. A. C., Baquero. R., Phys. Rev. B., 2012, 86, 195106.
- [56] Jiang. H., J. Chem. Phys., 2013, 138, 134115.
- [57] Yedukondalu. N., Ramesh Babu. K., Bheemalingam. Ch., David Singh. J, Vaitheeswaran. G., Kanchana. V., Phys. Rev. B,2011 1098-0121.
- [58] Shwetha. G., Kanchana. V., Yedukondalu. N., Vaitheeswaran. G., Mater. Res. Express, 2012, 10591.
- [59] Shwetha. G., Kanchana. V., Phys. Rev. B, 2012, 86, 115209.
- [60] Shwetha. G., Kanchana. V., Vaitheeswaran. G., Mater. Chem. Phys., 2015, 376-386.
- [61] Yedukondalu. N., Vaitheeswaran. G., Mater. Chem. Phys., 2016, 181.
- [62] Narsimha Rao. E., Appalakondaiah. S., Yedukondalu. N., Vaitheeswaran. G., J. Solid State Chem., 2014, 212, 171-179

Chapter 4

Alkali metal 5-Aminotetrazole M5-At (M = Li, Na, K, Rb, Cs)

Abstract

As a continuation of the previous chapter, This article presents a thorough density functional theory-based comparative study on nitrogen-rich 5-aminotetrazole alkali metal salts M 5-At (M = Li,Na, K, Rb, Cs). The calculated structural parameters using the planewave pseudopotential method are consistent with the experimental results. The computed vibrational frequencies at ambient pressure show that vibrational modes in high energy regions are due to the N-H bond of NH₂ group. Pressure variation IR spectra of these materials show clear frequency shifts where Li 5-At shows an overall redshift below 900 cm⁻¹ contrary to the blue shift seen in other materials in this range. Furthermore, we used the full potential linear augmented plane wave (FP-LAPW) method for calculating electronic structure and optical properties with TB-mBJ potential which provides an enhanced band gap for all materials compared to standard GGA functional. Electronic structure calculation reveals that all the compounds are indirect bandgap insulators except for Li 5-At. In addition, we are also presenting the optical properties such as real and imaginary dielectric constant, absorption, refraction, reflection, loss spectrum as functions of photon energy.

Prathap kumar Jharapla, S. Mondal, G. Vaitheeswaran, "Comparative DFT study of Vibrational, Electronic and Optical properties of Energetic Alkali metal salts based on Nitrogen-rich 5-Aminotetrazole" **J. Comput. Chem.**, 42(3) **180-191**, (2021).

4.1 Introduction

The use of high nitrogen-based energetic materials towards the replacement of perchlorate in pyrotechnics is a subject of interest in recent times. Various derivatives of perchlorates are used for the last few decades due to their intrinsic stability, low cost, reactivity, hygroscopic nature, and large positive oxygen balance [1]. Perchlorate-based materials are now classified as environmentally dangerous and human health hazards [2]. These materials are believed to contaminate groundwater and interfere with the production and regulation of thyroid hormones, toxic and carcinogenic [3,4]. Research towards the replacement of rooted energetic materials (i.e KClO₄, NH₄ClO₄, Pb(N₃)₂) with increased performance and lower sensitivity to physical stimuli is hard to achieve. Over the last few decades, a rapid process in the development of environmentally compatible green energetic materials has been observed. Towards obtaining these goals, nitrogen-rich molecules are one approach in developing environmentally sustainable green energetic products since the earth's atmosphere occupies 78% composition of molecular nitrogen. This can be an alternate route to improve the performance and sensitivity to impact, friction, and shock. Heterocyclic nitrogen-rich molecules like Imidazoles, Triazoles, Tetrazoles, Triazines, Tetrazines [5] are extensively used as the effective precursors for the preparation of HEDM's (High energy density materials), owing to great density when compared to its carbon analogs. Materials with good density are always benefited with higher packing efficiency through strong intermolecular interaction. Various functional groups such as -NO₂, -NHNO₂, -N₃ are considered by researchers, however, the inclusion of too many energetic groups lead to instability of the materials. In particular, tetrazoles has excellent property of amalgamating high positive heat of formation as well as large nitrogen content with good thermal stability owing to their aromatic ring system [6,7]. Tetrazole is unsaturated organic five-membered heterocycles that contain one carbon and four nitrogen atoms. Tetrazoles are curious heterocyclic compounds and familiar for exhibiting both basic and acidic nature. As a result, these materials are known to exist as anionic, cationic, and neutral forms. These materials generally are extremely important due to their practical uses in military, civilian applications [8–10], medical [11] and primers in primer charges (the first component in an explosive train). Moreover, the derivatives of tetrazole are popularly used in organometallic chemistry as ligands [12]. In the pharma industry, tetrazole is used in a wide range of drugs that act as a powerful isoteric substituent for -CO₂H carboxylic group with the advantage of being metabolically more stable than the latter. In addition, it is even used as a corrosion inhibitor in copper polishing [13], and as an intermediate in synthesizing tetrazole-based compounds because of its ease of preparation and assorted reaction. From the environmental point of view, these materials are very much promising as they produce eco-friendly gaseous materials due to their diminishing carbon-containing products upon thermal decomposition [14–16]. The thermal decomposition of 5-At is of huge interest due to its tautomerism in the structure. Furthermore, it is of significant interest due to its combustion chemistry as a burn rate modifier and free suppressor [11]. Among different organic compounds, 5-At possess 82.3% of high nitrogen content, rich electron pairs, as well as exceptional donor group which has a lot of applications [5]. All these important properties made 5-At based materials possible candidates for different pharmaceutical, agricultural, industrial applications, gas generators, propellants, and high explosives [17–20]. Aminotetrazole based alkali metal salts show interesting features as coloring agents in present-day's pyrotechnics because of their large content of nitrogen. Alkali metal salts of 5-At coordinated with metal cations could construct high-density energetic compounds. Certain characteristics of these materials are color flames, easy to handle, insensitive from friction and impact point of view [21]. Herein, we present a comparative investigation of structural properties, vibrational properties with pressure dependence, Born effective charges (BEC's), electronic and optical properties of metal salts of tetrazole derivatives M5-At (M=Li, Na, K, Rb, Cs).

For presenting this work, we have first discussed the computational details associated with this study. Then the result and the discussion regarding this work were presented. The conclusion of the detailed investigation is summarized at the end.

4.2 Computational details

Calculations involved in this work were mainly carried out by implementing plane-wave pseudopotential (PW/PP) and full potential linear augmented plane-wave (FP-LAPW) methods. Structural properties which include ambient and pressure-dependent zonecentered vibrational properties and born effective charges (BEC's) were studied using the PW-PP method as implemented in the Cambridge series of the total energy package (CASTEP) [22–24]. We have considered exchange and correlation interaction between electrons through local density approximation (LDA) [25, 26] as well as generalized gradient approximation (GGA) [27]. For obtaining correct structural parameters at ambient conditions, various dispersion corrected schemes such as GGA+G06 [28] and PW91+OBS [29] have also been employed. Throughout the calculation, normconserving pseudopotential with an energy cutoff of 950 eV and spacing in kpoint sampling $\text{Li}(9\times4\times6)$, $\text{Na}(6\times5\times6)$, $\text{K}(6\times5\times6)$, $\text{Rb}(6\times7\times5)$, $\text{Cs}(5\times7\times5)$ are used. The total energy is minimized considering the plane wave coefficient to obtain the ground-state crystal structure. Further, the density mixing minimization technique has been considered to determine electronic wave functions. For making a stable configuration, all the structures were geometrically optimized using (Broyden Fletcher Goldfarb Shanno) BFGS [30] algorithm. As a first step, the experimental structure was considered as an input parameter and relaxed the ionic configurations, volume along with cell shape at ambient conditions. Convergence criteria chosen in this regard are as follows: maximum tolerances forces were set to $5.0 \times e^{-6}$ (eV per atom), the maximum force between atoms considered as 0.01 eV A^{-1} , maximum displacement and stress were set to 5.0×10^{-4} Å and 0.02 GPa, respectively. Electronic and optical properties are studied using the most accurate computational technique which is the FP-LAPW method implemented in WIEN2k [31]. For considering exchange-correlation potential, generalized gradient approximation (PBE-GGA) [27] has been used, which always underestimates the bandgap as Kohn Sham states do not take into account quasiparticle self-energy correctly. Thus to get better results we have used TB-mBJ [32] potential. The non-overlapping muffin-tin radii (Rmt) were determined to be Li-1.56, H-0.57, N-1.05, C-1.2 (a.u), Na-2.18, O-0.96, C-1.18, H-0.50 (a.u), K-2.1, H-0.53, N-1.0, C-1.19 (a.u), Rb-1.9, H-0.55, N-1.03, C-1.23 (a.u), Cs-2.4, H-0.57, N-1.07, C-1.18 (a.u). Plane-wave expansion in interstitial region was considered using energy cutoff value of $k_{max} = 5/R_{MT} (a.u)^{-1}$, whereas spherical harmonics were used in the non-overlapping muffin-tin spheres up to $l_{max} = 10$. The G_{max} expanded by Fourier expansion of potentials is held to be 20. The self-consistent convergence has been achieved using 500 kpoints in the irreducible Brillouin zone (IBZ) of the unit cell. The band structure was determined using 500 Kpoints (Li($11 \times 5 \times 8$), $(Na(12\times7\times5), K(9\times5\times9), Rb(8\times8\times6), Cs(7\times9\times6))$ and 5000 kpoints $(Li(25\times11\times17), Cs(7\times9\times6))$ $(Na(26\times15\times12), K(19\times12\times20), Rb(17\times19\times14), Cs(16\times19\times14))$ were used for the density of states and optical properties in the IBZ.

4.3 Results and discussion

4.3.1 Structural properties of Alkali metal 5-Aminotetrazole

We first present the structural details of studied materials in this section. Crystal structures of these compounds are shown in Figure-4.1 and preliminary knowledge from reported experimental results, clearly shows that Li and K 5-At crystallize in monoclinic structure with space group $P2_1/c$ whereas Rb and Cs 5-At crystallize in orthorhombic crystal structure with Pnma space group [21]. Additionally, Na 5-At crystalizes in centrosymmetric triclinic space group P1, which is quite different from other alkali metal 5-Aminotetrazoles. Crystal symmetry of Li 5-At reveals that atoms are seen to form distorted tetrahedrons with different types of inequivalent nitrogen atoms. The bond length of single-bonded nitrogen atoms and doubly bonded nitrogen atoms of tetrazole ring is reported to be 1.454 Å and 1.245 Å, respectively. Whereas shortest and longest distances between nitrogen atoms are found for N2, N3 (1.307 Å) and N1, N2 type of atoms (1.359 Å), respectively. In Na 5-At, bond angle and distance in the tetrazolate anion are minimal compared to lithium salt. The sodium atoms are coordinated octahedrally by one nitrogen atom and three different oxygen atoms, two of which are doubled by symmetry. The packing is affected by several strong hydrogen bonds. In the case of Potassium 5-At, different layers are connected via distorted trigonal coordination of K atoms that affect its packing. On the other hand, though the packing of the crystal is similar for Rb and Cs 5-At, cesium

5-At is found to be much denser than Rb 5-At. The main objective of this study is to investigate the bonding nature in 5-aminotetrazole with the change in the metal atom. To obtain a more in-depth understanding of hydrogen bonds, we have also studied the pressure dependence of these crystal structures to 3 GPa in a step of 1 GPa. Electronelectron interactions have been treated using different functionals which are based on local density approximation (LDA) and generalized gradient approximation (GGA) such as Perdew Burke Ernzerhof (PBE) and Perdew Wang 91 (PW91). Our calculated lattice constants with the LDA and GGA functional provide a large deviation from experimental results. To correct these structural properties found using standard functional and for obtaining proper structural parameters, the dispersion corrected method of Grimme (G06) and Ortmann Bechstedt Schmidt (OBS) have been considered along with GGA and PW91 functionals, respectively. We can see that obtained values with GGA+G06 and PW91+OBS are in agreement with experimental values. The reason behind choosing the PW91+OBS scheme for Cs is that the van der Waals parametrization for Cs is not available within GGA+G06 so we opted for the OBS scheme. Therefore GGA+G06 and PW91+OBS are considered for further calculations. The theoretical lattice parameters, volume, and error percentage are reported along with experimental lattice parameters in Table-4.1

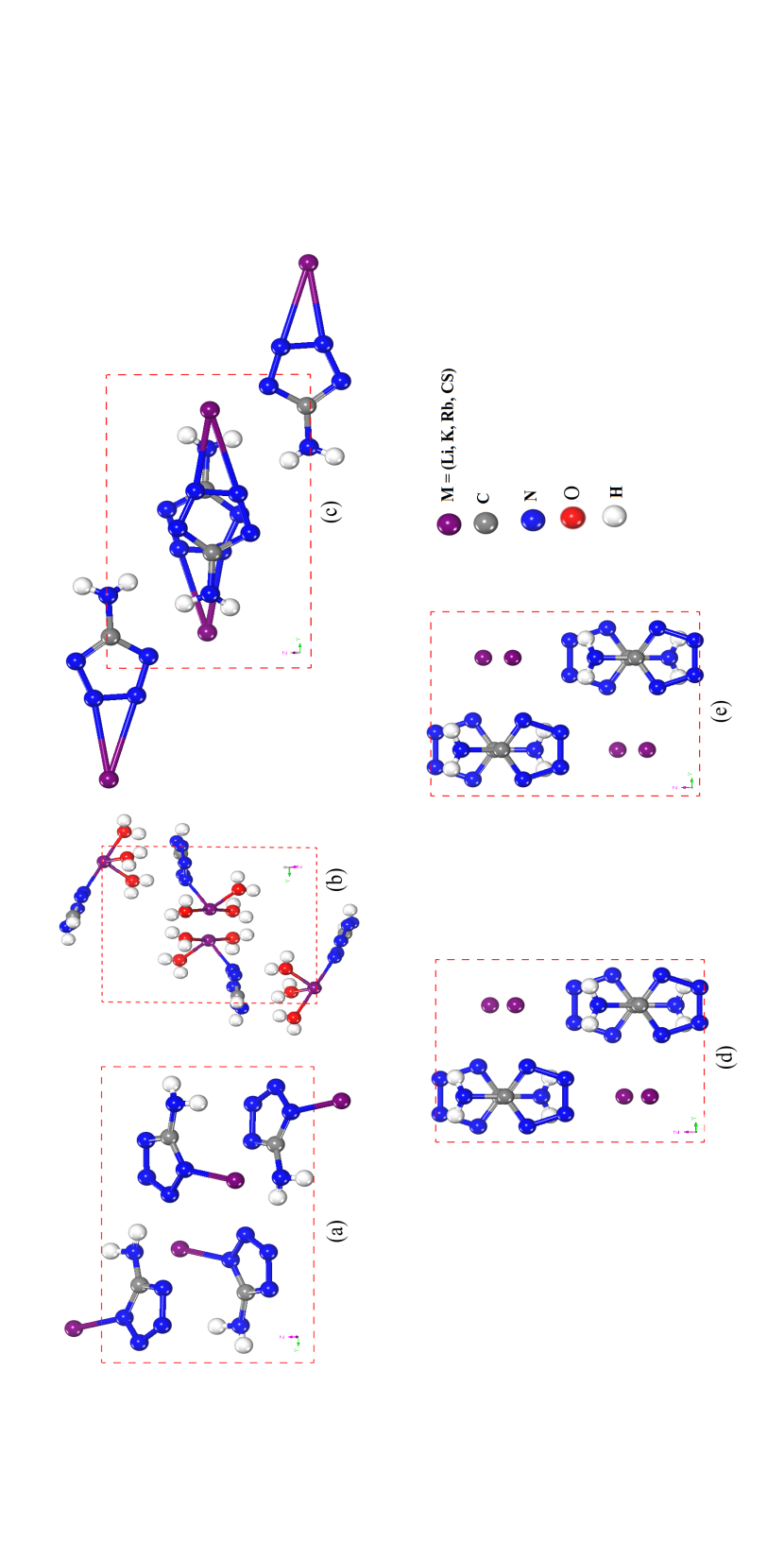


Figure. 4.1 Crystal structure of Alkali metal 5-Aminotetrazole (a) Li 5-At, (b) Na 5-At, (c) K 5-At, (d) Rb 5-At, (e) Cs 5-At.

Table 4.1 Calculated structural lattice parameters (a, b, c in Å) and Volume (V in ų) of Li 5-At, Na 5-At, R 5-At, Rb 5-At, Cs 5-At using LDA (CA-PZ) and GGA (PBE) functionals as well as with van der Waals corrected LDA+OBS, PBE+G06, $PW91+OBS\ schemes\ along\ with\ experimental\ results.$

Li 5-At a $P2_1/c$, z=4 b c c c β β Na 5-At a	4.79			LDE	1 11 1 000		1011	! ! ! ! ! ! ! ! !
		4.57	4.40	5.06	4.69	4.62	4.91	4.70
	10.6139	10.388	10.203	10.53	10.467	10.66	10.58	10.46
	7.0369	6.748	6.174	8.17	6.86	6.82	7.75	6.61
	103.26	102.128	97.64	107.67	101.47	100.71	107.65	101.29
	348.22	313.80(-9.88%)	275.27(-20.94%)	385.85(10.80%)	337.41(-3.10%)	330.644(-5.0%)	384.988(10.55%)	319.23(-8.32%)
	5.86	5.69	5.32	5.95	5.84	5.82	5.92	5.68
$P2_1/c, z=4$ b	10.02	9.49	8.98	10.10	9.84	9:90	10.07	9.36
0	12.17	11.75	11.47	12.78	12.07	12.04	12.84	11.94
Λ	92.889	610.03(11.46%)	526.66(23.53%)	739.26(7.37%)	669.88(-2.74%)	670.13(-2.70%)	736.26(6.89%)	615.01(10.70%)
K 5-At	6.8702	6.45	6.14	7.71	6.72	6.55	9.65	9.708
$P2_1/c, z=4$ b	9.851	9.64	9.47	9.98	98.6	9.644	8.25	7.406
0	6.872	6.53	6.41	6.94	6.87	6.497	8.67	8.966
β	115.61	114.38	113.03	119.20	115.32	113.49	132.30	134.42
Λ	417.29	370.60(11.18%)	343.3(-17.73%)	467.04(11.92%)	412.36(-1.18%)	376.637(9.74%)	511.11(22.48%)	460.44(10.34%)
Rb 5-At a	7.4221	7.098	6.659	8.33	7.30	7.087	8.277	7.349
Pnma, z=4 b	6.8053	6.514	6.519	6.48	6.715	6.456	6.470	9299
0	9.0133	8.98	8.831	9.73	60.6	9.266	9.726	9.180
Λ	455.26	416.42(-8.76%)	384.04(-15.77%)	525.995(15.53%)	445.80(-2.07%)	424.064(-6.85%)	523.472(14.43%)	452.36(0.642%)
Cs 5-At	8.0538	7.778	7.39	9.065		9.03	9.01	7.95
Pnma, z=4 b	6.9305	6.595	6.58	6.62		909.9	6.63	6.88
0	9.1021	8.985	8.76	69.6		9.77	69.6	9.16
Λ	508.05	460.994(-9.26%)	426.48(-16.05%)	583.129(14.77%)		583.957(14.94%)	579.83(14.12%)	508.37(0.06%)

4.3.2 Vibrational properties

In this section, we turn to investigate the vibrational frequencies for a proper understanding of the vibrational properties of an optimized crystal structure. In this regard, Density functional perturbation theory (DFPT) has proven to be very useful by giving them access to determine related data of any crystalline solid. To reach the accuracy in our calculated results, we have optimized these crystal structures using Norm-conserving pseudo-potential with van der Waals corrections. As GGA-G06 and PW91+OBS schemes were found to reproduce accurate structural parameters with respect to experimental values, we have used these schemes further to calculate the vibrational frequencies of these materials. As it has been mentioned in the previous section that Li 5-At and K 5-At crystallize in monoclinic structure and Rb, Cs 5-At crystallize in orthorhombic structure with four formulae units i.e. 36 atoms per unit cell a sum of 108 gamma centered phonon modes, addition to this Na 5-At consists of 72 atoms per unit cell a sum of 216 modes, gamma centered phonon modes for all the materials have been found. In particular, three acoustic modes and 3N-3 optical modes, so there are 105 optical modes and 3 acoustic modes. In detail, Li and K 5-At show a similar irreducible representation as:

 $\Gamma = \Gamma_{acoustic} (2B_u + A_u) + \Gamma_{IR} (26A_u + 25B_u) + \Gamma_{Raman} (27A_g + 27B_g), \text{ while Na 5-At}$ $\Gamma = \Gamma_{acoustic} (3A_u) = \Gamma_{IR} (105A_u) + \Gamma_{Raman} (108A_g), \text{ Rb and Cs based 5-At show different}$ irreducible representation which is $\Gamma = \Gamma_{acoustic} (B_{1u} + B_{2u} + B_{3u}) + \Gamma_{IR} (14B_{1u} + 11B_{2u} + 14B_{3u}) + \Gamma_{Raman} (15A_g + 12B_{1g} + 15B_{2g} + 12B_{3g}) + \Gamma_{silent} (12A_u).$

Phonon modes associated with molecular crystals are known to be classified as intra and intermolecular lattice vibrations. Among these modes, intermolecular lattice vibrations arise due to weak interactions present in the material and are characterized by low frequencies. Intramolecular vibrational modes are known to originate from the relatively strong interactions present within molecules. We can also subdivide these vibrational modes as Raman and IR active modes which are discussed in detail in the table and Figure-(4.2,4.3) represents the IR spectra of 5-aminotetrazole based alkali metal salts at 0 GPa and high pressure. Among these 105 optical modes, Li and K 5-At have 51 IR active (A_u, B_u) and 54 Raman active (A_q, B_q) modes, Na 5-At has 105 IR active (A_u) and 108 Raman active (A_g) modes. In the case of Rb and Cs 5-At, 39 IR active $(B1_u,$ B_{2u} , B_{3u}), 54 Raman active $(A_q, B_{1q}, B_{2q}, B_{3q})$ as well as 12 silent modes (A_u) have been found. We observe that there are no silent modes in the case of Li 5-At and K 5-At, whereas, in Rb and Cs 5-At, the number of silent modes increases along with a decrease in IR active modes. But interestingly the number of Raman active modes in all four crystals are the same. The appearance of silent modes can be justified with no change in dipole moment and polarizability associated with these modes. For the low-frequency region below 400 cm⁻¹, we observe the vibrations are mainly due to translation of metal atom (M = Li, Na, K, Rb, Cs) and Rotation of tetrazole (5-At). The mid-frequency range (400 cm⁻¹ to 1600 cm⁻¹) is due to rocking, wagging, bending, twisting and some mixed

vibrations i.e. mentioned in the table. Furthermore, in high-frequency limit symmetric and asymmetric stretching of N-H bond in NH₂ group are the vital reasons to have the prominent peaks in the IR spectra of Li, K, Rb, Cs 5-At whereas in Na 5-At case the prominent peaks are due to NO₂ and NH₂ group. Overall, Li 5-At, Na 5-At shows too many peaks in the lower frequency range concluding that these both compounds are IR active than other compounds. To understand further about these materials, vibrational analyses were also carried out under hydrostatic pressure till 3 GPa in steps of 1 GPa. The pressure variation of IR spectra for all the crystals shown in Figure-(4.2,4.3) depicts less significant changes observed in IR and Raman active modes with respect to pressure. Though a similar trend for Rb and Cs 5-At can be seen, peaks in Li 5-At have different trends than K 5-At even though both the materials crystallize in a similar crystal structure, while a different picture is noticed in Na 5-At.

A blue shift in wavenumber for all the materials can be seen except for Li 5-At in the low-frequency range. As pressure increases from 0 GPa to 3 GPa, the number of peaks near 500 cm⁻¹ increases in Li 5-At, Na 5-At whereas decreases in the case of K 5-At. In the mid-frequency range (shown in Figure-4.2), the IR peak of Li 5-At at 800 cm⁻¹ shows a redshift with increased intensity and a blue shift with decreased intensity at 1500 cm⁻¹. On the other hand, all the peaks show a blue shift with increased intensity for the rest of the materials. From Figure-4.3 mode analysis clearly shows that modes at 800 ${\rm cm^{-1}}$, 1100 ${\rm cm^{-1}}$ and at 1500 ${\rm cm^{-1}}$ are associated with the wagging of NH₂ group (NO₂ group in Na 5-At), stretching in the tetrazole ring and stretching of C-N bond along with scissoring of NH₂, NO₂ bonds, respectively. In the high-frequency region, two peaks in Li 5-At show a blue shift with an increased intensity which is different from the spectra of other materials. IR peaks of Cs 5-At due to symmetric and asymmetric stretching of N-H bonds in the NH₂ group show a redshift with increased intensity. A similar trend can also be observed in the case of Rb 5-At and K 5-At. Although vibrations in Na 5-At in the high-intensity region belong to NO₂, NH₂ group. Overall, from phonon frequencies, we can observe that Li 5-At shows a blue shift whereas Na 5-At, K 5-At, Rb 5-At, and Cs 5-At show a redshift, especially in the high-frequency range. In addition, increase in peak height and broadening of peaks as a function of pressure in the high-frequency region represent NH₂ interaction and hydrogen bond interaction in Li, K, Rb, Cs, and NH_2 , NO_2 in Na 5-At.

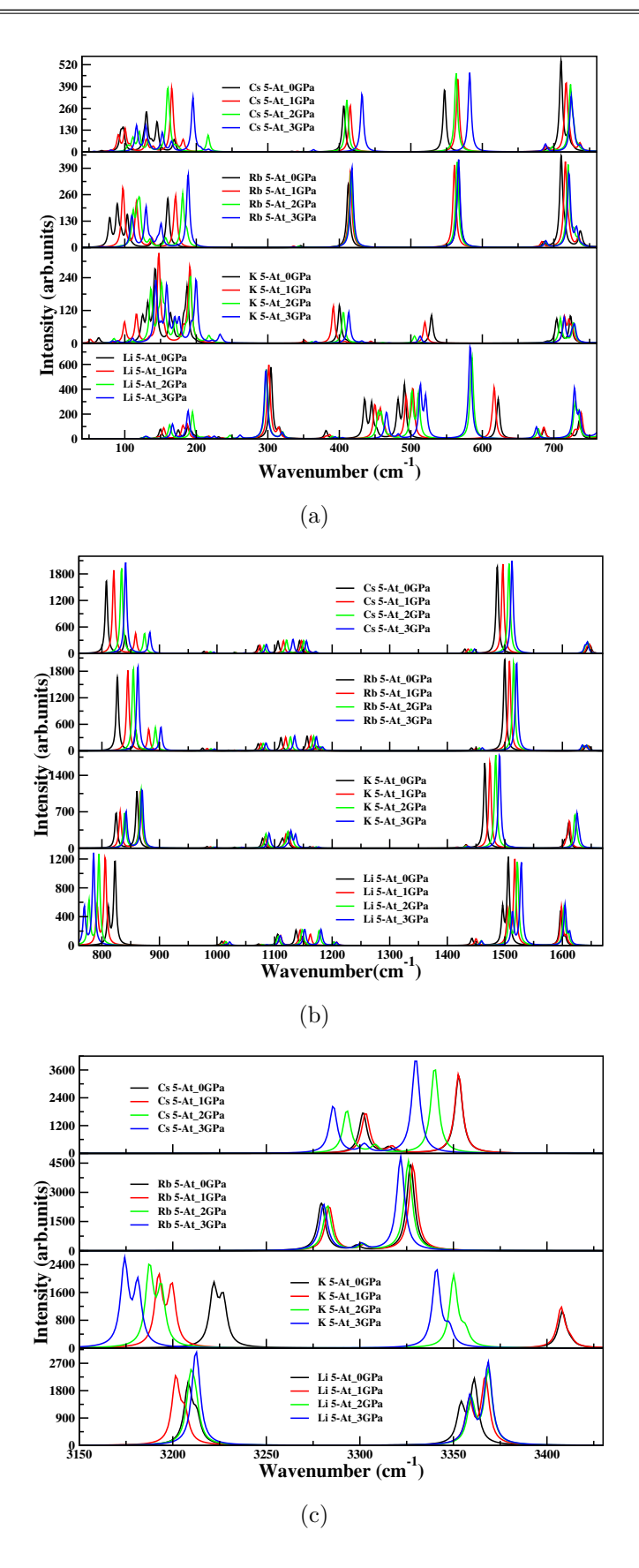


Figure. 4.2 Pressure variation of IR spectra of 5-At based alkali metal salts (Li 5-At, K 5-At, Rb 5-At, Cs 5-At) in the (a) Low frequency range (b) Mid frequency range (c) High frequency range.

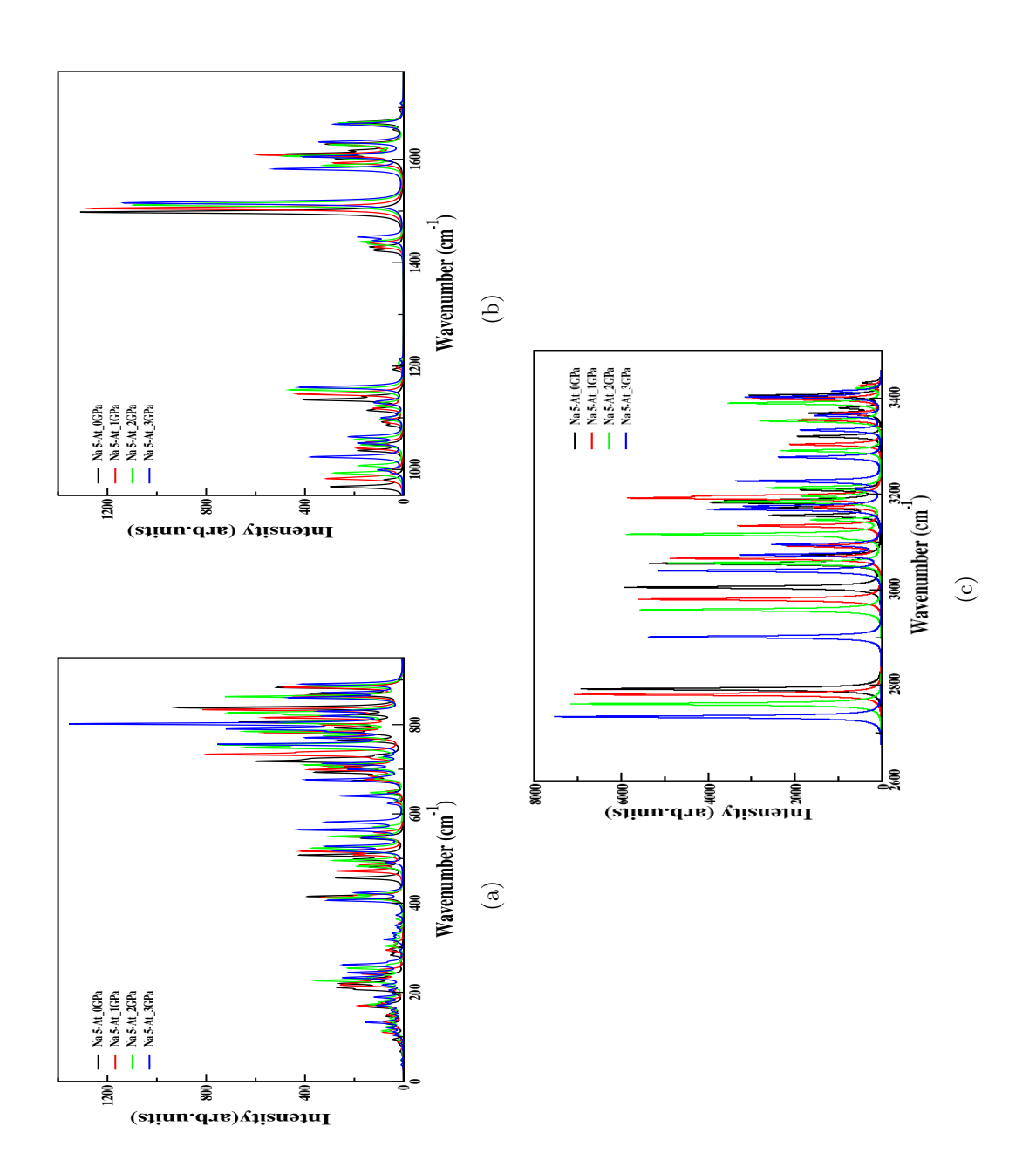


Figure. 4.3 Pressure variation of IR spectra of Na 5-At (a) Low frequency range (b) Mid frequency range (c) High frequency range.

4.3.3 Born effective charges (BEC's)

Born effective charges (BEC or Z*) are known as the fundamental quantity that describes the coupling between displacement in lattice and electrostatic fields used to calculate spontaneous polarization of the bulk, trilayer, bilayer, and strained systems. In recent times BEC's are obtained through ab-initio techniques using perturbation theory or finite difference in polarization. Table-(4.2,4.3) shows the amplitude of BEC's along principal axis for monoclinic(Li 5-At, K 5-At), triclinic (Na 5-At), and orthorhombic (Rb 5-At, Cs 5-At) crystals along with its percentage deviation from their nominal charges. It can be seen that the BEC's of all 9 inequivalent atoms in Li 5-At, K 5-At, 36 in Na 5-At, and 5 inequivalent atoms in Rb 5-At, Cs 5-At are different reflecting in their non-equivalence. The relation between the diagonal elements of Z* for four crystals shows $Z_{xx} \neq Z_{yy} \neq$ Z_{zz} . However, it is obvious from the results that the diagonal elements of BEC tensors of metal atoms are fairly close to their nominal ionic charge. Moreover, as atomic number increases, deviation of BEC from the nominal charge has slightly increased, from +14 \% for Li to a maximum of +37 % for Cs indicating an increase in ionic nature as we go down from Li to Cs. On the other hand, H atoms deviate significantly ranging from least -29 % to a maximum of -68% from its static charge. On the contrary, N and C atoms show anomalously large deviation in born effective charge ranging from -80 to -90\%, respectively. This indicates the reduction of nominal charges of H, N, and C atoms by sharing their electrons. In addition to the high electronegativity of N atoms, bonds associated with N and C atoms tend to be very strong. This could be also considered as strong hybridization, resulting in a strong covalent bond between these atoms. Furthermore, the effective charge of Cs 5-At is larger than that of Rb, K, Na, and Li. This is due to the higher atomic number of Cs. This indirectly increases the magnitude of Z* (N, C atoms) and atomic displacements of the partially covalent bonds between N and C atoms. Overall from the above discussion, large deviation in N and C atoms can be considered as the involvement of these atoms in covalent bonding whereas less deviation of metal atoms is associated with the ionic bonding.

4.3.4 Electronic structure and density of states

In general, the band structure of crystalline materials is known to provide a lot of information about chemical and physical properties. In this connection, using the experimental structure, the electronic band structure along with the total and partial density of states (PDOS) were computed using the FP-LAPW method for Li 5-At, K 5-At, Rb 5-At, and Cs 5-At. Initially, calculations were done with generalized gradient approximation (GGA), and later on, we have employed TB-mBJ potential to obtain more accurate results on the bandgap. To our knowledge, there are no reports on the bandgap of these materials in the literature. The bandgap values with GGA and TB-mBJ schemes are reported in Table-4.4. It is obvious that the bandgap values obtained from TB-mBJ potential increase

Table 4.2 Born effective charges of Li 5-At, K 5-At, Rb 5-At and Cs 5-At.

Compound	Nominal value	Z_{xx}	Z_{yy}	Z_{zz}	Z_{xx} %	Z_{yy} %	Z_{zz} %
Li	+1	1.164	1.142	0.990	16.4	14.2	-1
H	+1	0.311	0.706	0.315	-68.9	-29.4	-68.5
Н	+1	0.841	0.170	0.469	-15.9	-83	-53.1
N1	-3	0.180	-0.0623	-0.225	-106.	97.92	92.5
N2	-3	-1.125	1.406	-0.701	-62.5	-146.86	-76.63
N3	-3	-0.626	-0.148	0.328	-79.13	-95.06	-89.06
N4	-3	-0.846	-0.771	-0.454	-71.8	74.3	-84.86
N5	-3	-0.702	-0.934	-0.390	-76.6	-68.86	-87
$^{\mathrm{C}}$	+4	0.804	1.56	0.32	-79.9	-61	-92
K	+1	1.195	1.249	1.323	19.5	24.9	32.3
H	+1	0.513	0.451	0.408	-48.7	-54.9	-59.2
H	+1	0.359	0.317	0.357	-64.1	-68.3	-64.3
N1	-3	-0.489	-0.954	-0.627	-83.7	-68.2	-79.1
N2	-3	-0.518	-0.914	-0.591	-82.73	-69.53	-80.3
N3	-3	-0.247	-0.364	-0.233	-91.76	-87.86	-92.23
N4	-3	-0.419	-0.163	-0.334	-86.03	-94.56	-88.86
N5	-3	-0.672	-1.781	-0.563	-77.6	-40.63	-81.23
C	+4	0.278	2.160	0.259	-93.05	-46	-93.52
Rb	+1	1.242	1.378	1.333	24.2	37.8	33.3
H	+1	0.302	0.738	0.379	-69.8	-26.2	-62.1
N1	-3	-0.323	-0.340	-0.222	-89.23	-88.66	-92.6
N2	-3	-0.430	-0.851	-0.993	-85.66	-71.63	-66.9
$^{\mathrm{C}}$	+4	0.231	0.344	2.32	-94.22	-91.4	-42
Cs	+1	1.350	1.365	1.372	35	36.5	37.2
Н	+1	0.307	0.651	0.377	-69.3	-34.9	-62.3
N1	-3	-0.459	-0.834	-0.959	-84.7	-72.2	-68.03
N2	-3	-0.354	-0.338	-0.234	-88.2	-88.73	-92.2
C	+4	0.227	0.397	2.226	-94.32	-90.07	-44.35

considerably for all four compounds. This follows the normal trend of increasing bandgap with TB-mBJ potential for insulator which is reasonable and reliable [32]. Our calculations indicate that all five compounds are insulators, where Na 5-At(A-Z), K 5-At(A-Z), Rb 5-At(G-U), Cs 5-At(Z-G) show indirect bandgap and Li 5-At shows direct bandgap along B-B direction as shown in Figure-4.4. Band structure of Li 5-At, Na 5At, and K 5-At vary due to their different bonding properties and inclusion of d states in K atoms. In the case of Rb and Cs 5-At, band gaps are close to each other which could be due to the similar packing of both compounds. Moreover, a change in the dispersive nature of the valence and conduction band has been observed due to an increase in atomic size from Li 5-At to Cs 5-At. This implies that as atomic size increases, dispersion curves in both valence and conduction are smooth and flat, indicating an increase in ionic bonding of these structures.

 ${\bf Table~4.3~Born~effective~charges~of~Na~5-At}.$

Compound	Nominal value	Z_{xx}	Z_{yy}	\mathbf{Z}_{zz}	Z_{xx} %	Z_{yy} %	Z_{zz} %
Na	+1	1.08	1.22	1.13	8	22	13
Na	+1	1.07	1.17	1.12	7	17	12
O1	-2	-1.18	-1.22	-1.09	-41	-39	45.5
O2	-2	-1.08	-1.25	-1.05	-46	-37.5	-47.5
O3	-2	-1.18	-1.47	-0.68	-41	-26.5	-66
O4	-2	-1.19	-1.41	-0.95	-40.5	-29.5	-52.5
O_5	-2	-1.02	-1.18	-1.14	-49	-41	-43
O6	-2	-1.09	-1.06	-0.74	-45.5	-47	-63
C1	+4	1.36	1.13	0.40	-66	-71.75	-90
C2	+4	1.51	0.83	0.31	-62.2	-79.2	-92.5
N1	-3	-1.20	-0.90	-0.97	-60	-70	-67.6
N2	-3	-0.81	-1.00	-0.36	-73	-66.6	-88
N3	-3	-0.81	0.32	-0.29	-73	110.6	-90.3
N4	-3	-0.77	-0.94	-0.55	-74.3	-68.6	-81.6
N5	-3	-0.97	-0.77	-0.34	-67.6	-74.3	-88.6
N6	-3	-0.95	-0.81	-0.53	-68.3	-73	-82.3
N7	-3	0.30	-0.66	-0.28	-110	78	90.6
N8	-3	-1.70	-0.60	-0.88	43.3	-80	-70.6
N9	-3	-0.83	0.32	-0.37	-72.3	-110.6	-87.6
N10	-3	0.33	-0.67	-0.28	-111	77.6	-90.6
H1	+1	0.18	0.47	0.38	-82	-53	-62
H2	+1	0.18	0.32	0.38	-82	-68	-62
Н3	+1	0.59	1.22	0.30	-41	22	-70
H4	+1	0.87	0.93	0.25	-13	-7	-75
H5	+1	0.78	0.90	0.29	-22	-10	-71
H6	+1	0.36	0.33	0.88	-64	-67	-12
H7	+1	1.06	0.12	0.36	6	-88	-64
Н8	+1	0.70	1.30	0.24	-30	30	-76
H9	+1	0.31	0.44	0.83	-69	-56	-17
H10	+1	0.34	0.42	0.93	-66	-58	-7
H11	+1	0.72	0.61	0.30	-28	-39	-70
H12	+1	1.29	0.11	0.41	29	-89	-59
H13	+1	0.43	0.31	0.77	-57	-69	-23
H14	+1	0.77	0.73	0.34	-23	-27	-66
H15	+1	0.43	0.32	0.37	-57	-68	-63
H16	+1	0.32	0.33	0.43	-68	-67	-57

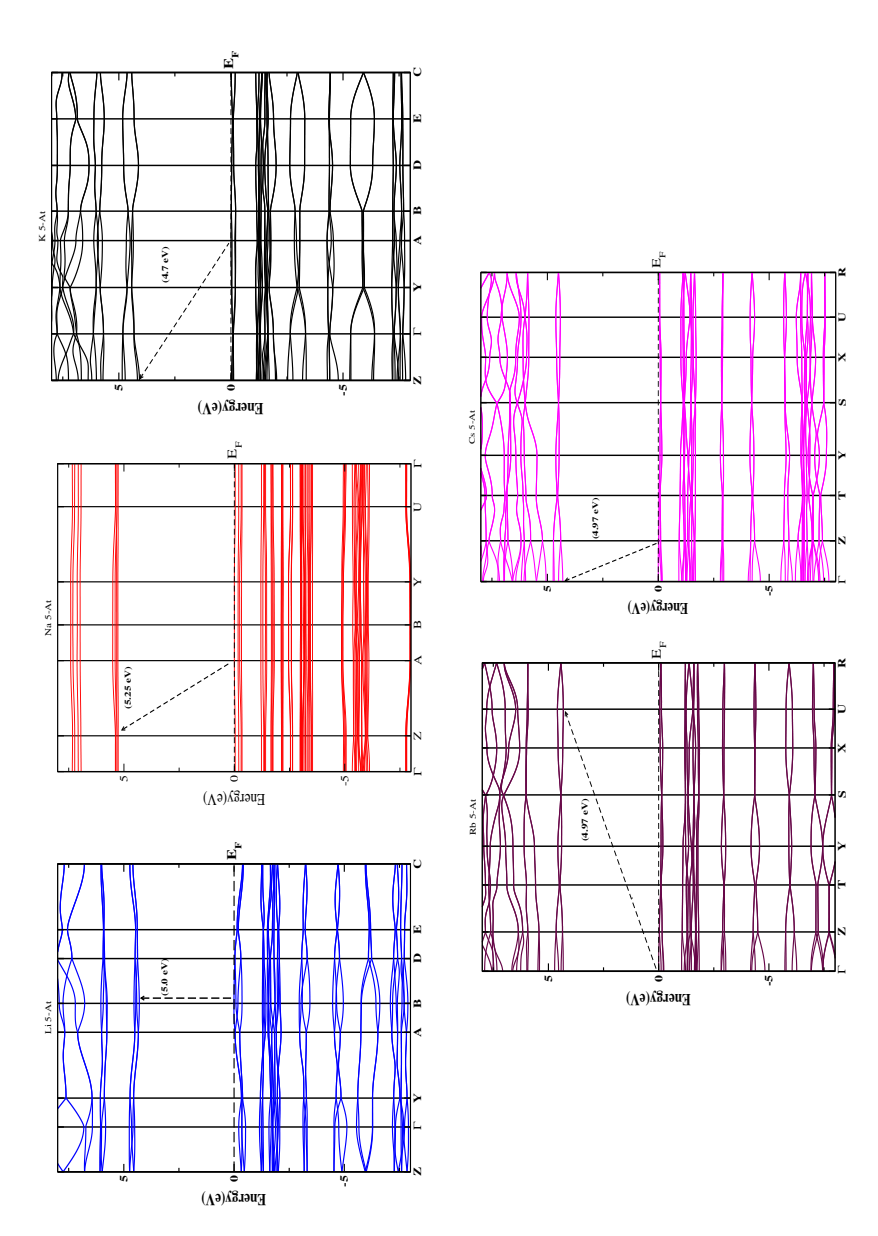


Figure. 4.4 Calculated electronic band structure of Li 5-At, Na 5-At, K 5-At, Rb 5-At, Cs 5-At using TB-mBJ functional at experimental crystal structures.

Table 4.4 Computed band gap (in eV) of Li 5-At, Na 5-At, K 5-At, Rb 5-At, Cs 5-At with different schemes such as PBE-GGA and TB-mBJ potential

Compound	GGA (eV)	TB-mBJ (eV)	Direct/Indirect
Li	4.30	5.0	В-В
Na	4.52	5.25	A-Z
K	4.07	4.7	A-Z
Rb	4.32	4.97	Γ-U
CS	4.30	4.97	$\operatorname{Z-}\Gamma$

Total as well as the partial density of states for monoclinic, triclinic and orthorhombic structures shown in Figure-(4.5,4.6,4.7) reveals that the ultraviolet response of alkali metal 5-aminotetrazole is mainly contributed by the transitions of N/C-p states in valence band (VB) to metal atom K, Rb, Cs-d states in conduction band (CB), in the same way in N-s states to Li/Na-p and Li/Na-s to N-p states. In all the compounds the topmost valence bands (-3.5 to 0 eV) are mostly due to nitrogen (N-s/p) and carbon (C-s/p)states. This gives rise to covalent bonding in between the N-C bond. Also, H-s states contributions are almost similar in all the compounds. Moreover, one can see that as atomic size increases (K \rightarrow Rb \rightarrow Cs), the contribution of p/d states increase gradually. This leads to hybridization between metal atoms d states and N/C -p states, concluding a mixed ionic-covalent nature. In the lowermost valence band around -7eV, the overlap of H- s and N5/N3-p states has been seen. The same has been noticed in Na 5-At. Furthermore, N5 atom in Li and K, N3 atom in Rb and Cs, and N5/N10 atoms in Na are bonded with C and H atoms, showing very less contribution of p states around -1.6 eV, when compared with other N atoms. Also, the contribution of N5 in Li, N5/N10 in Na, and N3 atom around 5eV in the conduction band are not observed. In all compounds, conduction band (near 5 eV) mainly originates from metal atoms p/d states and N1, N2, N3, N4-p states. Around 7.2 eV N/C-p states, metal atom's d-states contribution has been observed. Due to the different configurations of Na 5-At, the valence band occurs due to the strong hybridization between H-s and O-2p states. This shows that in Na 5-At, H-O and N-C bond play an important role, which is not observed in other Li, K, Rb, Cs 5-At compounds. From the above discussion, we conclude that an increase in atomic size changes the dispersive nature of alkali metal atoms series, the same was observed in our previous work based on alkali metal perchlorates [33]. Strong covalent nature between N and C (tetrazole ring) and ionic bonding between metal and surrounding N/C atoms has been observed.

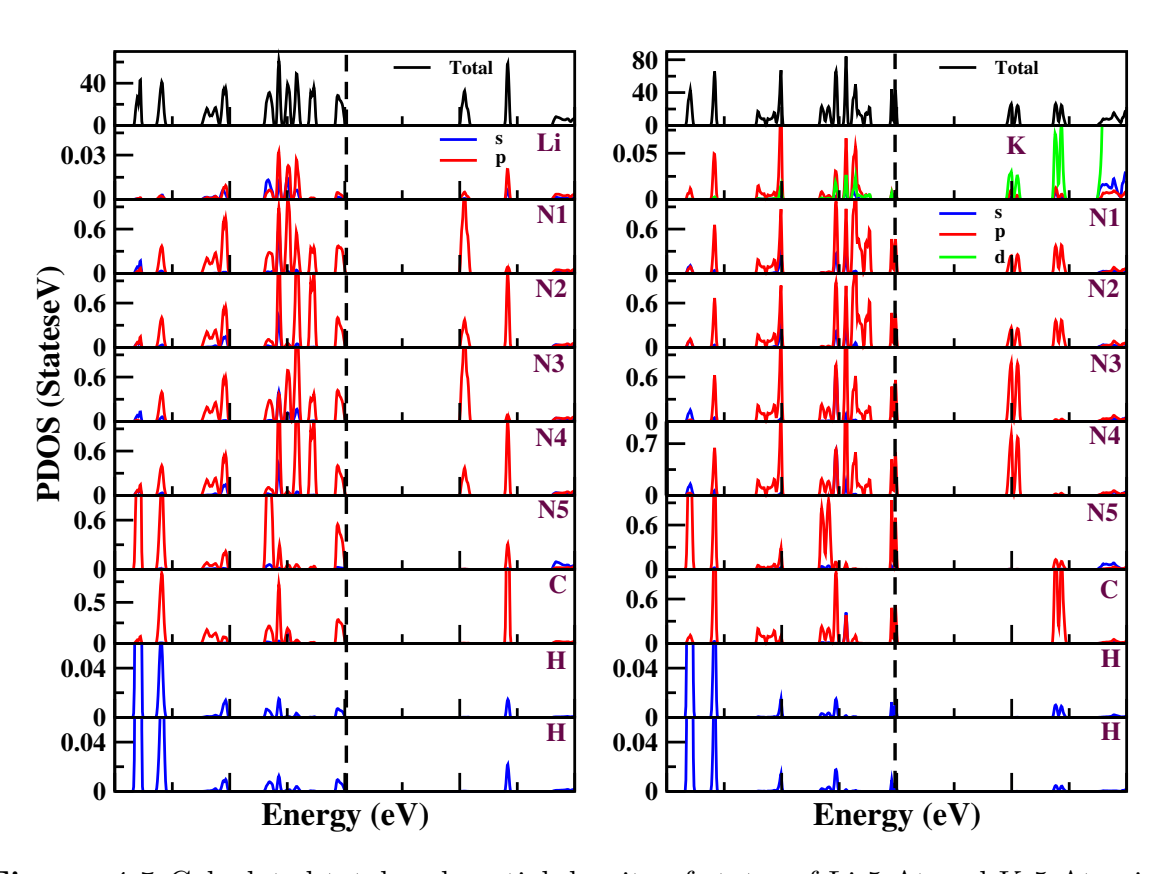


Figure. 4.5 Calculated total and partial density of states of Li 5-At and K 5-At using TB-mBJ functional at experimental crystal structures.

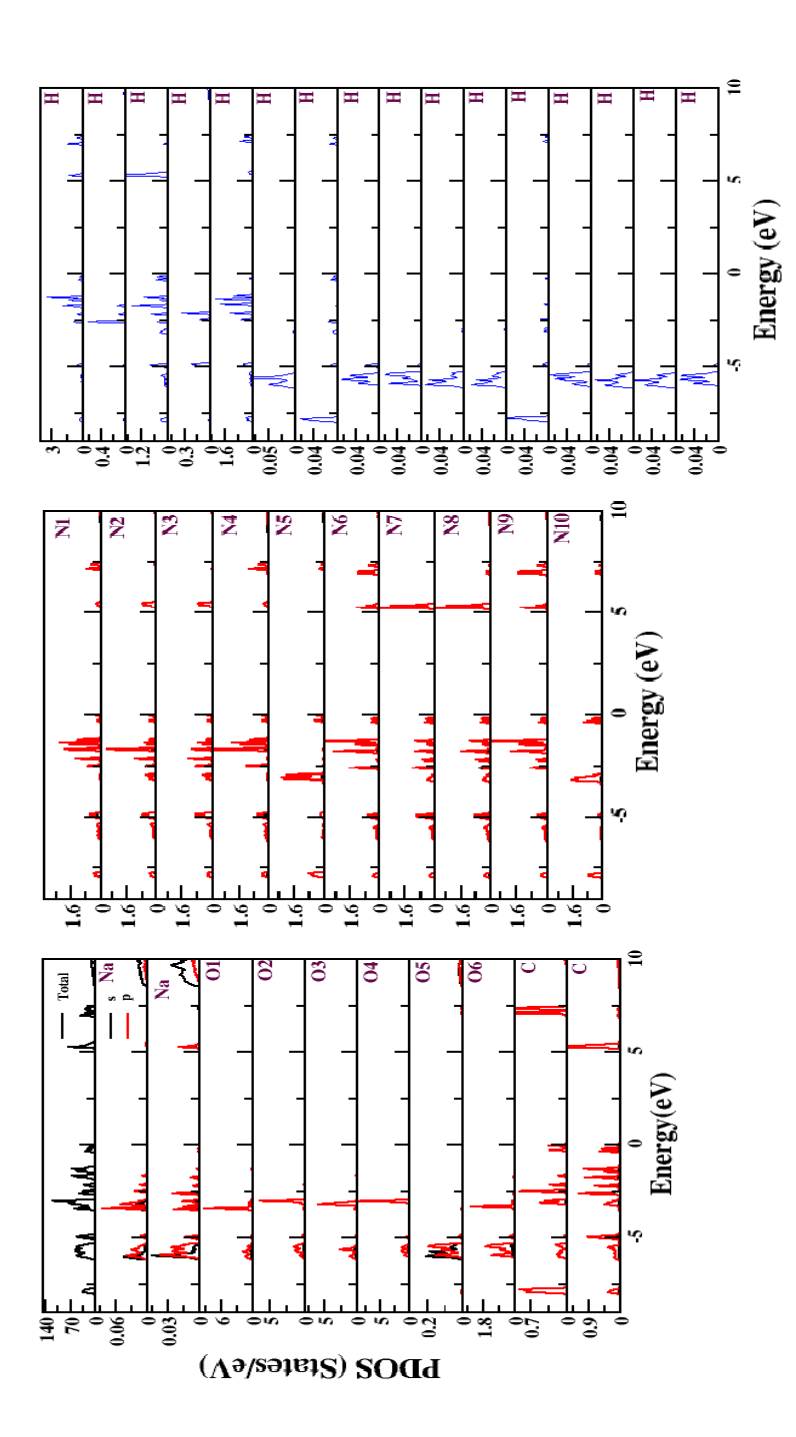


Figure. 4.6 Calculated total and partial density of states of Na 5-At using TB-mBJ using TB-mBJ functional at experimental crystal structures.

80

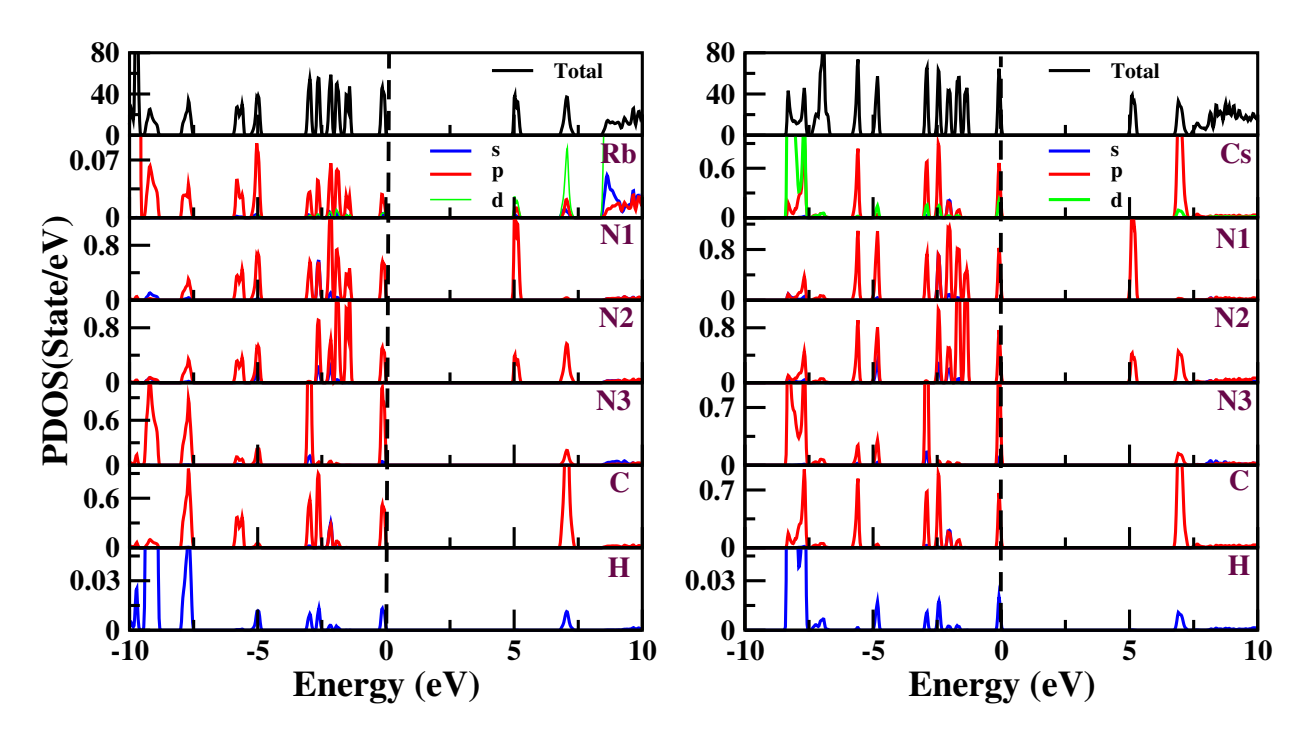


Figure. 4.7 Calculated total and partial density of Rb 5 At and Cs 5-At using TB-mBJ functional at experimental crystal structures.

4.3.5 Optical properties

In this subsection, we present the optical properties of alkali metal salts M 5-At (M = Li, Na, K, Rb, Cs) to get more insight into these materials. All the optical parameters such as the absorption coefficient, refractive index, reflection, and energy loss function were deduced from the imaginary and real part of the dielectric function Figure-(4.8,4.9,4.10). The imaginary part is calculated using the elements of the momentum matrix in between the wave functions of occupied and unoccupied states and selection rules. After that ε $_{1}(\omega)$ is derived from $\varepsilon_{2}(\omega)$ and with the help of Kramer-Kronig relation (KKR). From Figure, it can be seen that the optical constants of Li 5-At, Na 5-At, and K 5-At show quite different results, whereas Rb and Cs follow the same trend. The imaginary part of the complex dielectric constant from 0 to nearly 5 eV range for all compounds is characterized by high transparency, showing no absorption and a small reflectivity. However, the threshold of all the compounds is close to each other with a slight difference. The imaginary part exhibits three fundamental peaks in different directions. Which are A[100-5.42] eV], B [010-6.5 eV], C [010-7.36 eV] Li 5-At; A [010-6.57 eV], B [010-7.11 eV], C [010-8.55 eV] Na 5-At; A [001-5.62 eV], B [010-6.51 eV], C [010-6.11 eV] K 5-At; A [010-5.18 eV], B [001-6.46 eV], C [001-7.67 eV] Rb 5-At; A [010-7.46 eV], B [001-6.24 eV], C [001-7.03 eV Cs 5-At corresponding to optical transitions between VB and CB Table-4.5. At zero photon energy $\varepsilon_1(\omega)$ is denoted as $\varepsilon_1(0)$, static dielectric values for all the compounds are mentioned in Table-4.6. As photon energy increases, peaks in real dielectric part ε $_{1}(\omega)$ rises rapidly, reaching the maximum (Li (6.33 eV [010], Na (6.64 eV [010], K (6.41))

eV [010], Rb (6.35 eV [001], Cs (6.35 eV [001]). For all the compounds, in the energy range around 7 to 8.8 eV, the $\varepsilon_1(\omega)$ is smaller than zero which indicates that light cannot spread in this frequency range and incident photons are reflected in these regions. Moreover, as atomic size (Li \rightarrow K \rightarrow Rb \rightarrow Cs) increases $\varepsilon_1(0)$ static dielectric value decreases in [100] and [010] direction, whereas it increases in [001] direction. In the case of Na 5-At, [100] and [010] directions seem to overlap with each other and not many peaks can be observed in [001] directions. The absorption coefficient along three orientations $\alpha(\omega)$ gives the rate of attenuation of the intensity of light per unit of distance traveled in a medium. The absorption spectra $\alpha(\omega)$ exhibit different peaks with changes in frequency in three directions for all the compounds, this is due to the interband transitions between high symmetry points in the electronic spectrum. For all the compounds, as electron energy increases absorption coefficient increases (5 to 9 eV), this shows high absorption and gradually decreases to zero at 10 eV. In detail, Li, K show highest peaks in [010] directions around 7.36 eV, [010] direction at 8.61 eV in Na whereas Rb [010] at 8.36 eV, Cs [001] direction at 7.14 eV, which indicates good absorption coefficient in the ultraviolet region. The refractive index $n(\omega)(0)$ and real part $\varepsilon_1(0)$ of dielectric function are very similar and can be noticed in Table-4.5. This means the static dielectric constant corresponds to the static refraction index. Also, refraction index $n(\omega)(0)$ at 0 eV gradually rises as electron energy increases and for all the compounds Li, Na, K, Rb, Cs the values in each crystallographic direction indicate an optically anisotropic nature except in Na 5-At. In Na 5-At isotropic nature has been found in [100] and [010] direction. Starting from 0 eV, the reflection coefficient increases with an increase in photon energy which leads to three main peaks from 5 eV to 10 eV which eventually drops to zero near 10 eV. Li, Na, and K do not show a similar pattern but maximum reflection has been observed in [010] direction for three compounds around 6.7 eV to 8.5 eV, respectively. For Rb and Cs compounds, it has a nearly same trend in peaks, where maximum reflection can be observed around 7.5 for Rb and 7.3 eV in Cs in the same [001] direction. All four compounds show high reflectivity in the ultraviolet region. The loss function describes how fast an electron will lose its energy while traveling in a medium. Peaks near 8 - 9 eV in [001] and [010] directions show more energy loss for Li, for Na [100] and [010] direction at 8.8 eV and around 8.5 eV [010] direction in K, and in case of Rb and Cs, high energy loss has been observed in [001] direction around 8-9 eV. The above results concluded that alkali metal 5-aminotetrazole are good absorbers of UV light with anisotropic nature in Li, K, Rb, Cs in all three directions and Na show isotropic nature in [100] and [010] direction.

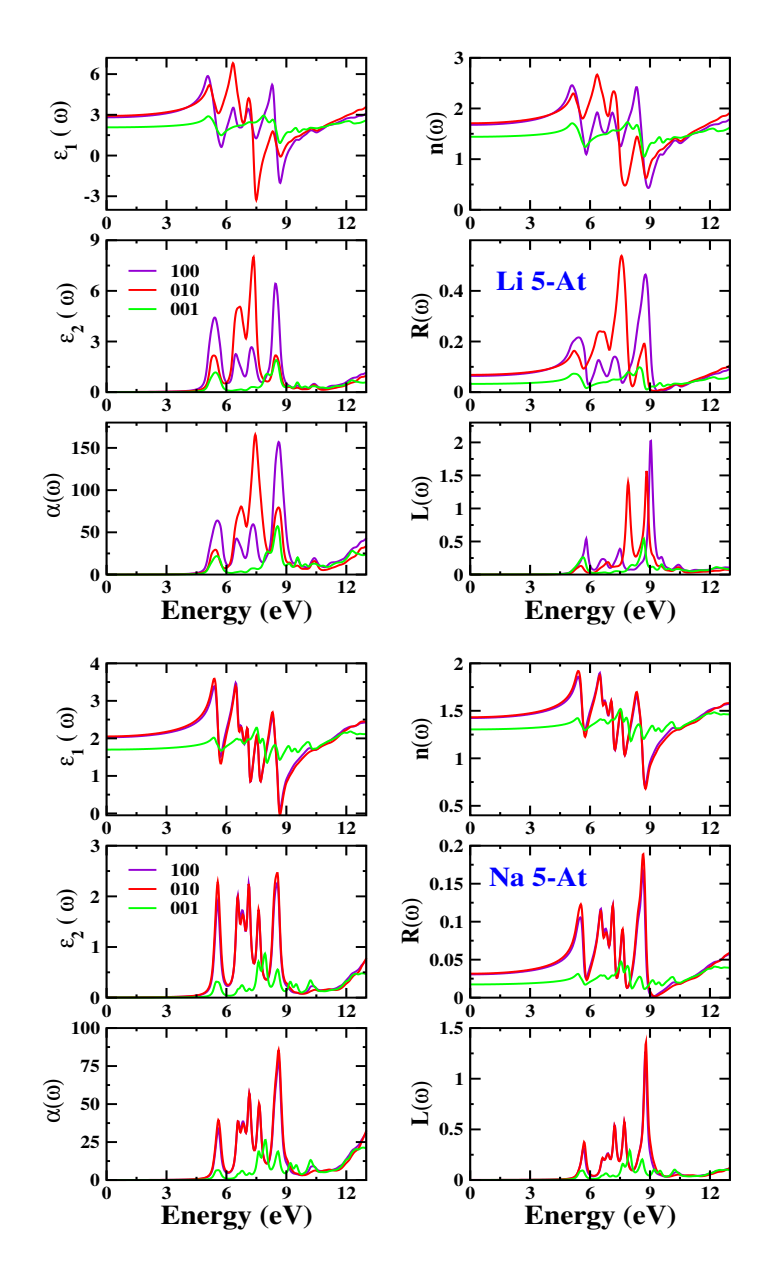


Figure. 4.8 The figure represents Dielectric constant $\varepsilon_1(\omega)$, Dielectric loss $\varepsilon_2(\omega)$, Absorption ($\alpha(\omega) \times 10^4 \text{ cm}^{-1}$), Refraction n(ω), Reflectivity R(ω), Eloss function L(ω) of Li 5-At and Na 5-At using TB-mBJ functional at experimental crystal structure.

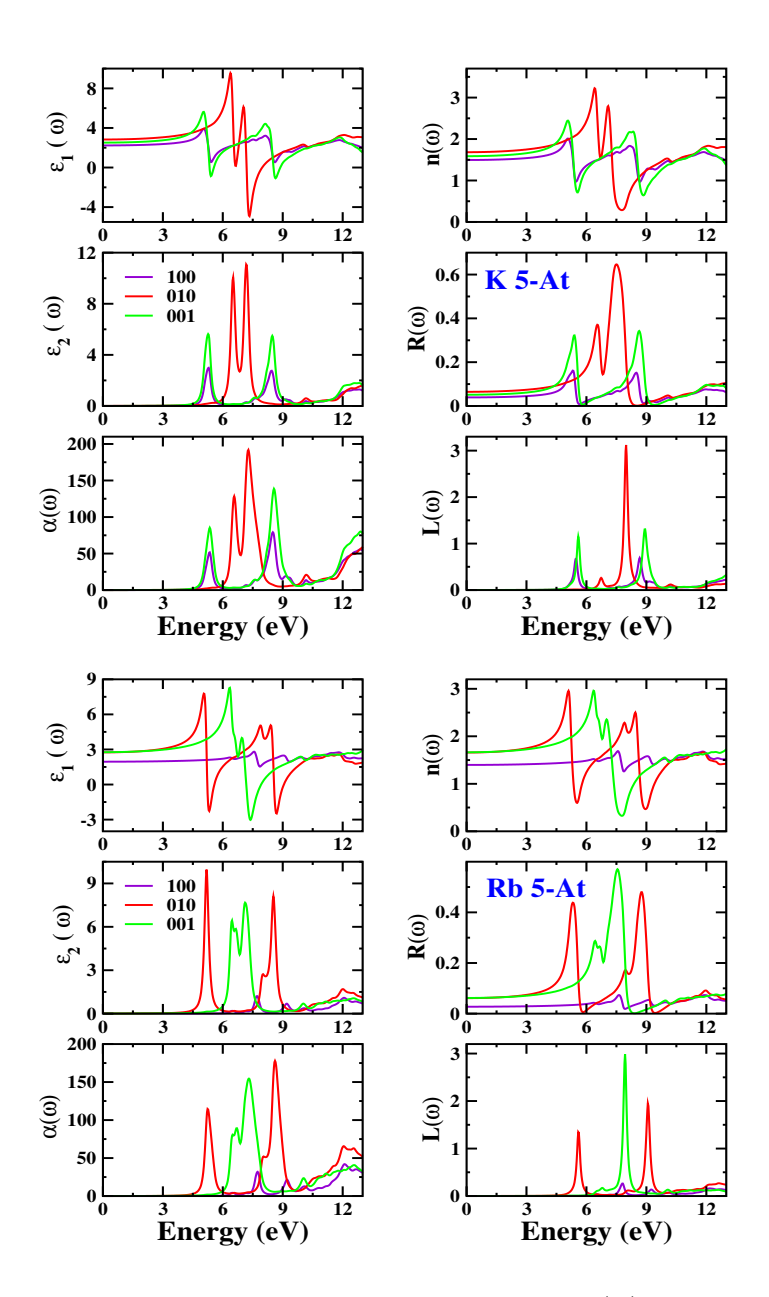


Figure. 4.9 The figure represents Dielectric constant $\varepsilon_1(\omega)$, Dielectric loss $\varepsilon_2(\omega)$, Absorption ($\alpha(\omega) \times 10^4 \text{ cm}^{-1}$), Refraction n(ω), Reflectivity R(ω), Eloss function L(ω) of K 5-At and Rb 5-At using TB-mBJ functional at experimental crystal structure.

Compound	Energy(eV)	Possible optical transitions
Li 5-At	A	N5(s)- $Li(p)$, $N(p)$, $H(s)$ - $N(p)$, $Li(p)$, $Li(s)$ - $N(p)$
	В	N(s) –Li(p), $N(p)$, $C(s)$ - $N(p)$, $H(s)$ – $N(p)$, Li(p), $C(p)$
	$^{\mathrm{C}}$	N(p) - Li(p), H(s)-N(p), Li(p)
Na 5-At	A	N(p)- K(d), C(p)-K(d), H(s)- N(p), K(p/d)
	В	$N(s)\text{-}\ K(p/d),\ C(p),\ N(p)\text{-}K(d),\ H(s)\text{-}\ K(p/d),\ N(p),\ C(p)$
	$^{\mathrm{C}}$	N(s/p) - K(p/d), H(s) - N(p), K(p/d)
K 5-At	A	N(p)- $K(d)$, $C(p)$ - $K(d)$, $H(s)$ - $N(p)$, $K(p/d)$
	В	N(s)- K(p/d), C(p), N(p)-K(d), H(s)- K(p/d), N(p), C(p)
	$^{\mathrm{C}}$	N(s/p) - K(p/d), H(s) - N(p), K(p/d)
Rb 5-At	A	N(p) -Rb(d), N3- Rb(p), H(s)- Rb(p/d), N(p)
	В	$N(s/p) - Rb(p/d), \ Rb(d) - N(p), \ C(p) - \ Rb(d), \ H(s) - \ Rb(p/d), N(p)$
	$^{\mathrm{C}}$	N(s/p)- $Rb(d)$, $C(p)$ - $Rb(p)$, $H(s)$ - $Rb(p/d)$, $N(p)$
Cs 5-At	A	N(p) - Cs(d), C(p)-Cs(d), H(s)-Cs(d), N(p)
	В	N(s/p) - Cs(p/d), Cs(d) - N(p), C(s/d) - Cs(p/d), H(s) - Cs(p/d), N(p)
	$^{\mathrm{C}}$	N(p) - Cs(d), $C(p)$ - $Cs(d)$, $H(s)$ - $Cs(p/d)$, $N(p)$

Table 4.5 Optical transitions corresponding below 10 eV.

Table 4.6 Values of dielectric real part $\varepsilon_1(0)$ and refractive index n(0) as a function of energy (eV) (M = Li, Na, K, Rb, Cs) 5-Aminotetrazole.

Compound	ε ₁ ^[100] (ω)	$\varepsilon_1^{[010]}(\omega)$	$\varepsilon_1^{[001]}(\omega)$	$n(\omega)^{[100]}$	$n(\omega)^{[010]}$	$n(\omega)^{[001]}$
Li 5-At	2.81	2.92	2.07	1.67	1.70	1.44
Na 5-At	2.09	2.05	1.7	1.42	1.43	1.30
K 5-At	2.23	2.83	2.51	1.49	1.68	1.58
Rb 5-At	1.95	2.75	2.76	1.39	1.65	1.66
Cs 5-At	2.07	2.77	2.78	1.43	1.66	1.66

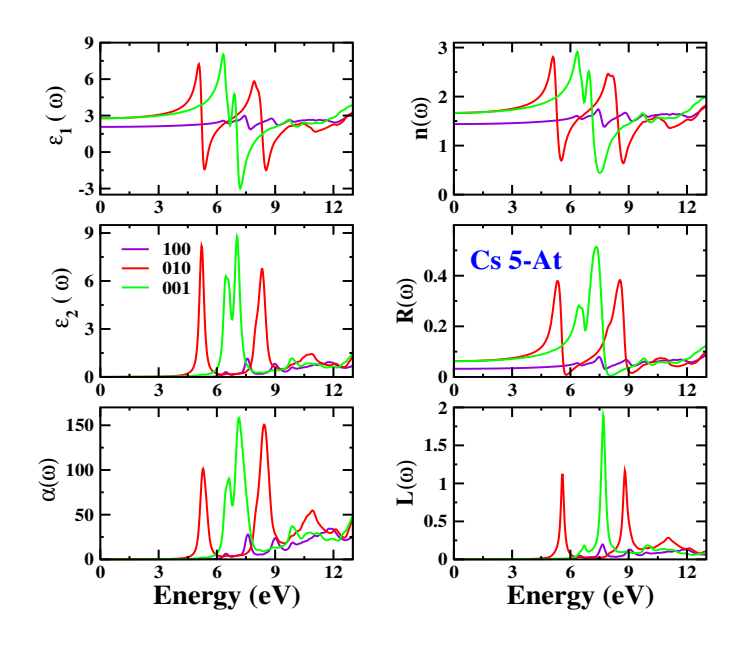


Figure. 4.10 The figure represents Dielectric constant $\varepsilon_1(\omega)$, Dielectric loss $\varepsilon_2(\omega)$, Absorption ($\alpha(\omega) \times 10^4 \text{ cm}^{-1}$), Refraction n(ω), Reflectivity R(ω), Eloss function L(ω) of Cs 5-At using TB-mBJ functional at experimental crystal structure.

4.4 Conclusions

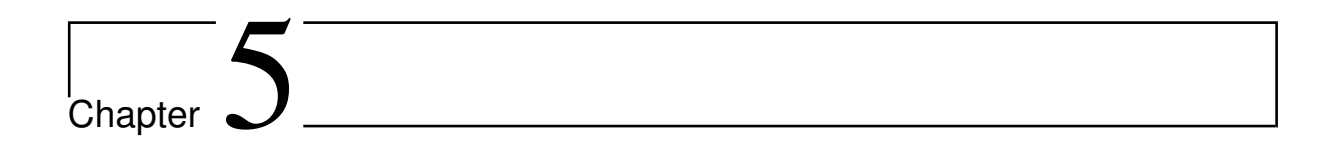
In summary, a comparative study of alkali metal salts of 5-aminotetrazoles has been performed using the ab-initio density functional theory. Complete assignment of the vibrational frequencies of M 5-At (M=Li, Na, K, Rb, Cs) in low, mid, and high-frequency ranges have been reported. In the high energy region, symmetric and asymmetric stretching are due to N-H bonds in NH₂ group for all the materials. Then, as pressure increases Li 5-At shows a blue shift in the high-frequency region where other materials K 5-At, Rb 5-At, Cs 5-At show redshift concluding weakening of hydrogen bond in Li 5-At. We find that the BEC's for metal atoms slightly increase (Li \rightarrow K \rightarrow Rb \rightarrow Cs) and large deviation between N and C leads to differences in the vibrational spectra and polar response. Calculated bandgap with TB-mBJ potential for all the compounds is found to be in between 4.5 to 5 eV range. Partial density of states depicts that as atomic size increases, the contribution of p/d states increases in K 5-At, Rb 5-At, Cs 5-At crystals. Also, the ionic nature between metal atoms is notably increased and a strong covalent nature due to hybridization between N and C atoms in tetrazole ring is observed. Optical constants show anisotropic nature in all directions. Though the variation in optical constants for Li and K 5-At can be seen Rb and Cs 5-At follow the same trend. Overall, these materials are found to be good absorbers in the ultraviolet range. The scope of this work also explores the different behavior of Li 5-At compared to other compounds in the context of hydrogen bonding.

References

- [1] Markowitz. M. M., Boryta D A, Harvey S Jr, Lithium Perchlorate Oxygen Candle. Pyrochemical Source of Pure Oxygen Ind. Eng. Chem. Prod. Res. Dev., 1964, 3, 321-30.
- [2] Davila. A., Willson D., Coates. J., Mckay. C., Perchlorate on Mars: A chemical Hazard and a Resource for humans. Int J Astrobiol., 2013, 12, 4, 321-325.
- [3] Jesse J. S., Jared D. M., High Nitrogen Based Pyrotechnics: Perchlorate Free Red and Green Light Illuminants Based on 5 Aminotetrazole, Chem. Eur. J., 2013, 19, 12839-12845.
- [4] Cheryl. H., Perchlorate in Drinking Water doesn't need US federal limits, EPA says, Chem. Eng. News, 2020, 98, 24.
- [5] Irannejad. H., Nitrogen Rich Heterocycles as a Privileged Fragment in Lead Discovery. Med. Analy. Chem. Int. J, 2018, 2(3): 000125.
- [6] Chen. H., Zhang, Tong. L., Zhang, Jian. G., Crystal Structure and Thermal Decomposition Mechanism of a 5-aminotetrazole copper(II) complex. Struct. Chem., 2012, 23, 153-159.
- [7] Stierstorfer. J., Tarantik. K., Klapötke. T. M., New Energetic Materials: Functionalized 1 Ethyl 5 aminotetrazoles and 1 Ethyl 5 nitriminotetrazoles. Chemistry (Weinheim an der Bergstrasse, Germany), 2009, 15, 5775-92.
- [8] Steinhauser. G., Klapötke. T. M., Green Pyrotechnics: A Chemists Challenge. Angewandte Chemie (International ed. in English), 2008, 47, 3330-47.
- [9] Ebespächer. M., Klapötke. T. M., Sabate, Carles, Nitrogen-Rich Alkali Metal 5,5'-hydrazinebistetrazolate salts: Environmentally Friendly Compounds in Pyrotechnic Mixtures. New J. Chem., 2009, 33, 517-527.
- [10] Williams. L., Quinn. M. J., Eck. W. S., Defense Technical Information Center (DTIC), 2009, 1-36.
- [11] Ostrovskii. V., Koldobskii. G., Katritzky. A. R., Ramsden. C. A., Scriven. E. F., Taylor. R. J., Comprehensive Heterocyclic Chemistry III, Elsevier, Oxford, 2008, 257.
- [12] Kiselev. V., Gritsan. N., Theoretical Study of the Nitroalkane Thermolysis. Computation of the

- Formation Enthalpy of the Nitroalkanes, Their Isomers and Radical Products., J. Phys. Chem. A, 2008, 112, 19, 4458-4464.
- [13] Jong. W. L., Min C. K., Jae. J. K., Erratum: Characterization of 5-Aminotetrazole as a Corrosion Inhibitor in Copper Chemical Mechanical Polishing J. Electrochem. Soc., 2006, 152, C827-C831, 2005.
- [14] Klapötke. T. M., Laub. H. A, Stierstorfer J, Synthesis and Characterization of a New Class of Energetic Compounds- Ammonium Nitriminotetrazolates. Propellants Explos. Pyrotech., 2008, 33, 421-430.
- [15] Kristian. W., Hurley. M., Irikura. K., Unimolecular Decomposition of 5-Aminotetrazole and its Tautomer 5-Iminotetrazole: New Insight from Isopotential Searching., J. Phys. Chem. A., 2009, 113, 2483-90.
- [16] Obata. S., Takeya. S., Fujihisa. H., Honda. K., Gotoh. Y., Phase Transition Analysis of 5-Aminotetrazole from Room Temperature to the Melting Point. J. Phys. Chem. B., 2010, 114, 12572-6.
- [17] Frija. L., Ismael. A., Cristiano. M., Chem Inform Abstract: Photochemical Transformations of Tetrazole Derivatives: Applications in Organic Synthesis. Molecules (Basel, Switzerland), 2010, 15, 3757-74.
- [18] Oga. S., Method for Producing Bitetrazole Amine Compound. Jpn. Kokai Tokkyo Koho, 2006, JP2006249061, A20060921.
- [19] Klapötke. T. M., Holl. G., Geith. J., Hammerl. A., Weigand. J. J., New Trends in Research of Energetic Materials, Proceedings of the Seminar, 2004, Pardubice, 7th, Czech Republic.
- [20] Stierstorfer T. M., Stierstorfer J., Phys. Chem. Chem. Phys. 2008, 10, 4340;(b)T M Klapötke, J Stierstorfer, Eur. J. Inorg. Chem. 2008, 26, 4055; (c)Stierstorfer T M, Stierstorfer J, Wallek A U, Chem. Mater., 2008, 20, 4519.
- [21] Ernst. V., Klapötke. T. M., Stierstorfer. J., Alkali Salts of 5 Aminotetrazole Structures and Properties. Zeitschrift für anorganische und allgemeine Chemie., 2007, 633, 879-887.
- [22] Payne. M. C., Teter. M. P., Allan. D. C., Arias. T. A., Joannopoulos. J. D., 1992, Iterative Minimization Techniques for Ab Initio Total Energy Calculations: Molecular Dynamics and Conjugate Gradients, Rev. Mod. Phys., 64, 1045-1097.
- [23] Segall. M. D., Lindan. P. J. D., Probert. M. J., Pickard. C. J., Hasnip P. J., Clark S. J., Payne M C, First-principles simulation: ideas, illustrations and the CASTEP code, J. Phys. Condens., 2002, 14, 2717-2743.
- [24] Milman. V., Refson. K., Clark. S. J., Pickard. C. J., Yates. J. R., Gao. S-P., Hasnip. P. J., Probert. M. I. J., Perlov. A., Segall. M. D., Electron and vibrational spectroscopies using DFT, plane waves and pseudopotentials: CASTEP implementation, J. Mol. Struct., 2010, 954, 1-3, 22-35.
- [25] Ceperley. D., Alder B. J., Ground-State of the Electron-Gas by A Stochastic Method. Phys. Rev. Lett., 1980., 45, 566.

- [26] Perdew. J., Zunger A., Self-Interaction Correction to Density-Functional Approximations for Many-Body Systems, Phys. Rev. B., 1981, 23, 5048-5079.
- [27] Perdew. J., Burke K., Ernzerhof M., Generalized Gradient Approximation Made Simple, Phys. Rev. Lett. 1996, 77, 3865-3868.
- [28] Grimme. S., Semiempirical GGA-Type Density Functional Constructed with a Long-Range Dispersion Correction, J. Comput. Chem., 2006, 27, 1787-99.
- [29] Ortmann. F., Bechstedt F., Schmidt W., Semiempirical van der Waals correction to the Density Functional Description of Solids and Molecular Structures, Phys. Rev. B., 2006., 73.
- [30] Fischer. T., Almlof J., General Methods for Geometry and Wave Function Optimization. 1992, J. Phys. Chem., 96.
- [31] Blaha. P., Schwarz. K., Madsen. G. K. H., Kvasnicka. D., and Luitz J., 2001, WIEN2K, an Augmented Plane Wave + Local Orbitals Program for Calculating Crystal Properties (Austria: Techn. Universitat).
- [32] Tran. F., Blaha, Accurate Band Gaps of Semiconductors and Insulators with a Semilocal Exchange-Correlation Potential, P, Phys. Rev. Lett., 2009, 102, 226401.
- [33] Jharapla. Prathap. K., Elaprolu. N., Vaitheeswaran. G., Unusual optical isotropy in anisotropic alkali metal perchlorates MClO₄ (M=Li, Na, K, Rb, Cs), J. Phys. Condens. Matter., 2018, 30, 475402.



Energetic Eco-friendly Oxidizers HNF, ADN, and KDN

Abstract

In this work, we present a detailed first-principles study addressing the structural, vibrational, born effective charge, elastic constants, electronic structure, and optical properties of energetic salts ammonium dinitramide $ADN(N_4H_4O_4)$ and potassium dinitramide $KDN(KN_3O_4)$. In order to have a comparative study, we have included another compound known as Hydrazinium nitroformate $HNF(CH_5N_5O_6)$, results discussed about HNF are yet to be published. Additionally, we have computed phonon dispersion for ADN and KDN. The structural details reveal that HNF, KDN crystallize in monoclinic space group $P2_1/n$ and ADN in different settings $P2_1/c$. Analysis of the vibrational modes reveals that the $N(NO_2)$, NH_2 group contributions are considerably large in the high-frequency region in KDN and HNF. In addition, the optical and acoustical modes are highly interactive as evident from the dispersion spectra, which might lead to low thermal conductivity, quite desirable for an energetic material. From the electronic structure, it is vivid that HNF and KDN are wide-bandgap insulators with an indirect bandgap of the value of 3.01 eV for HNF and 4.37 eV for KDN. Optical constants reveal that HNF, ADN and KDN possess considerable optical anisotropy.

Prathap kumar Jharapla,G. Vaitheeswaran, M. K. Gupta, R. Mittal "Comparative study of electronic structure, optical properties, lattice dynamics and thermal expansion behaviour of energetic ammonium and potassium dinitramide salts, **Mater. Chem. Phys.**, **267**, 124645, (2021).

5.1 Introduction

In recent years, space industries witnessed a tremendous increase in the frequency of rocket launches for space-related activities, and this grows concerns about the environment due to the various fuels used in rockets. Space ships can have a heavy carbon trace due to the burning of solid rocket fuels. To minimize the environmental pollution caused by solid rockets fuel, the development and replacement of existing fuel are of great curiosity in the research world. This draws attention towards new high-performance propellants and chlorine-free oxidizers that prevent the hydrochloric acid formation in the environment. The infamous ammonium perchlorate has long been utilized as an oxidizer rocket propellant because of its beneficial properties such as high thermal stability, good specific impulse, and low cost. However, perchlorate molecule in it causes an environmental problem such as ozone depletion in the stratosphere and acid rain. Researchers worldwide are working round the clock to replace AP due to its adverse effects on the environment and humans. In this continuous search, dynamic eco-friendly oxidizers ammonium dinitramide (ADN) and hydrazinium nitroformate (HNF) have joined the field of the superior propellant system a few decades ago as possible alternatives to AP because they are halogen-free propellant formulations. Unfortunately, both have several drawbacks, such as low thermal and chemical stability, extreme hygroscopicity, incompatibility, and industrially unviable synthetic routes, limiting their application in practical systems. Being peculiar representatives of this type of energetic materials, ammonium dinitramide (ADN) and hydrazinium nitroformate (HNF) is of particular interest from theoretical and practical standpoints ascertainment of their combustion mechanism.

Dinitramide is one of the strongest inorganic acids and a member of inorganic nitramine. The negative charge distributed evenly throughout the molecule is the main reason behind the stability of dinitramide, providing higher N-N bond order, which further strengthens N-NO₂ bonds [1]. It is of great interest due to its various properties, such as halogen-free, high performance, high oxygen density grouping, and eco-friendly energetic nature [2]. In addition, it forms oxygen-rich material with various combinations of cations with high density and energy. The high density of 2.0 g.cm^{-3} and high heat of formations result from N-N, N-O and N-C bonds obtained from organic molecules based on hydrogen (H), nitrogen (N), carbon (C), oxygen (O) [3]. Over past decades various salts of dinitramides apart from ammonium dinitramide (ADN) have been synthesized ranging from alkali metal to transition metals [4–7]. In addition to that, pyridinium dinitramide [8] and melaminium dinitramide [9] were also reported to exist experimentally. These energetic compounds have numerous applications based on different combinations of anion and cation. Out of various dinitramide-based compounds, α -ADN [10] is well known for extensive hydrogen bonding while the cation-anion interactions are electrostatic in alkali metal salts such as

lithium, potassium, and cesium dinitramide. HNF crystalizes quite straightforward from hydrazine N_2H_4 and nitroform $CH(NO_2)_3$, nitroform holds a unique position in nitro compounds. Oxidizing nitro group forms gaseous nitrogen upon decomposition. It has gained attention due to its superior combustion and explosive properties.

In this context, we tried to shed light on understanding and comparing the chemical and physical properties of KDN (intermediate compound during the synthesis of ADN) ADN and HNF, where these three crystallize in monoclinic structure. Several works are carried out for ADN, KDN and HNF in recent years [11–23] and few are discussed here pertaining to this work. These materials gained much attraction due to their high energetic characteristics, chlorine-free nature, and act as good oxidizing agents. ADN and HNF have several advantages over long preferred ammonium perchlorate (AP) and ammonium nitrate (AN) [24,25]. In detail, ADN possesses the best characteristics such as high specific impulse, positive oxygen balance, low molecular weight combustion products and high heat of formation [26]. Also, some disadvantages such as being highly hygroscopic, possessing needle-shaped crystalline structure do exist [1,27]. KDN acquires a special interest as it contains oxyanion of nitrogen. KDN possesses density (2.2 g.cm⁻³) [28] more than ADN $(1.831 \text{ g.cm}^{-3})$, HNF (1.87 g.cm^{-3}) , AP (1.95 g.cm^{-3}) , AN (1.73 g.cm^{-3}) [29] and is also classified as oxidizer due to its excess oxygen content. ADN decomposes into N₂O, NO₂, NH₄, HNO₃, N₂, NO, HONO, H₂O and NH₃ [30] and KDN decomposes primarily into KNO_3 , N_2O and NO_2 [31, 32]. Therefore, ADN is characterized as explosive, being less thermally stable, photosensitive, marginally shock sensitive. The oxygen balance of ADN tends to be around +51.6% higher than KDN +44.1% [33] and HNF +13%. In this study, we have performed a comparative ab initio study on structural, electronic, optical, vibrational properties, Born effective charger, elastic constants of ADN, KDN, and HNF.

5.2 Computational details

In the present work, a series of computational tools were employed to understand the various properties of HNF, ADN, and KDN. Plane-wave pseudo-potential method (PW/PP) implemented in CASTEP [34] is used to calculate vibrational properties, elastic constants, and Born effective charges. In these calculations, norm-conserving pseudopotential [35] is used to treat electron-electron interaction. Plane-wave cutoff energy of 950 eV was applied in the whole calculation process. A Monkhorst-pack grid [36] of $(3\times3\times4)$ HNF, $(4\times3\times4)$ KDN has been used to evaluate all the integrals in reciprocal space. The criteria that total energy change is smaller than 5.0×10^{-6} eV/atom, maximum force over each atom is below 0.01 eV/Å, pressure smaller than 0.02 GPa, maximum allowed atomic positions displacements are not exceeding 5.0×10^{-4} Åare used. The Broyden-Fletcher-Goldfarb-Shanon (BFGS) [37] minimizer scheme is used to relax electron wave functions. The accurate description of weak intermolecular interactions can be treated with exchange-correlation energy within the local density approximations (LDA) [38,39], generalized gra-

dient approximation-Perdew Burke Ernzerhof [40](GGA-PBE), PW91 [41] scheme, taking experimental structures as input. The inadequacies in predicting the intermolecular interactions affect the proper representation of crystal geometry and lead to fluctuations in the acquired properties, including density, cohesive energy, elastic moduli, and bandgap. Within the DFT+D framework, the total energy, including vdW revision, is provided by:

$$E_{DFT+D} = E_{DFT} + E_{disp}$$

 E_{DFT} is the standard self-consistent Kohn-Sham energy, and E_{disp} is the empirical dispersion revision represented as:

$$E_{disp} = -s_6 \sum_{i < j} \frac{C_{ij}}{R_{ij}^6} f_{damp}(R_{ij}),$$

Where R_{ij} and C_{ij} denotes the interatomic distance and dispersion coefficient for the pair of ith and jth atoms, respectively. S_6 is a global scaling factor that only depends on the density functional used. In order to avoid divergence for small R_{ij} , the damping function $f_{damp} = \frac{1}{1+e^{-d(R_{ij}/R_0-1)}}$ is introduced. In order to check the van der Waals interaction, semi-empirical dispersion corrections methods were included i.e LDA+OBS, GGA+TS [42], GGA+G06 [43], PW91+OBS [44]. The elastic properties were calculated using the stress-strain method, vibrational, and BEC's were determined within density functional perturbation theory (DFPT) [45] which is a more efficient tool over finite displacement method to obtain frequencies with lower computation time.

The electronic bandgap and optical properties calculations were carried out using the WIEN2k package [46] using the full potential-linear augmented plane wave method (FP-LAPW) method. In the muffin-tin approximation, the crystal is separated into the region, non-overlapping muffin-tin (MT) spheres centered at the atomic site, and the interstitial region. The conventional cell is categorized into two regions i.e., interstitial and overlapping muffin-tin sphere centered at atomic sites. Inside muffin-tin, spheres segregate into core (have spherical symmetry) and valence subsets. The exchange-correlation effects are treated within generalized gradient approximation GGA [40]. Additionally, Tran-Blaha modified Becke-Johnson potential is used for better accuracy to obtain band gap [47]. The maximum quantum number 'lmax' for atomic wave functions is expanded to L=10. To separate core states from valence states, the cut-off energy is considered to be -6 Ryd. In the interstitial region, cut-off energy for plane wave expansion of wave functions was $k_{max} = 5/R_{MT} (a.u)^{-1}$ for HNF, $K_{max} = 6/R_{MT} (a.u)^{-1}$ for ADN and $K_{max} = 7/R_{MT}$ $(a.u)^{-1}$ for KDN, respectively. RMT is the radius of muffin-tin radius, and the extension of charge density and potential is limited to $G_{max}=20$ in HNF, ADN and Gmax $= 14 \text{ (a.u)}^{-1}$ in KDN, which denote the largest k vector plane wave expansion. The self-consistency calculations are considered to be converged when the total energy of the system is stable within 10^{-5} Ryd. The RMT radius used in the calculations for HNF are H-0.56 a.u, N-1.04 a.u, O-1.18 a.u; ADN are H=0.54 a.u, N=1.01 a.u, O=1.18 a.u and for KDN K=2.0 a.u, N=1.12 a.u, O=1.18 a.u atoms. We used Monkhorst-Pack grid [36] in Brillouin zone sampling with 500 kpoints for electronic band structure and 5000 k points for the density of states and optical properties. HNF (hydrazinium nitroformate) and ADN (ammonium dinitramide) are seen as possible replacements for the common oxidizer ammonium perchlorate (AP) in composite rocket propellants. HNF, ADN, and KDN have the relatively great advantage to be chlorine-free. In the present chapter, we attempted to understand the crystal structural, vibrational properties, Born effective charge (BEC), elastic constants, electronic properties, optical properties. Matching these properties, we can quantitatively examine their variation in stability and sensitivity. The last set of calculations for thermal expansion and full phonon dispersion studies were done within the density functional theory using van der Waals corrections built in Vienna ab initio Simulation Package (VASP) [48–50]. The calculations are performed using the DFT-D2 method of Grimme [43]. The PW/PP with plane wave cut-off of 500 eV and integration over the Brillouin zone was sampled on the grid of kpoints by the Monkhorstpack grid [36] method for two compounds. The convergence of total energy less than 0.1 meV is found to be sufficient from the above parameters. The Hellman-Feynman forces are calculated using the finite displacement method using the supercell. The convergence criteria for the total energy and ionic force is set to 10^{-8} eV atom $^{-1}$ and 10^{-5} eV Å $^{-1}$. The full phonon dispersion, the density of states were extracted from subsequent calculations using the PHONON software [51]. The phonon calculations were performed using the crystal acoustic sum rule.

5.3 Results and discussion

5.3.1 Structural properties of HNF, ADN, KDN

ADN crystallize in monoclinic space group $P2_1/c$ and HNF, KDN in different setting $P2_1/n$ with four formula units per unit cell with 44, 68 and 32 atoms, respectively [52] Figure-5.1. Structural details of ADN were reported in our previous work by Yedukondalu et al. [24] and others [52]. To summarize about ADN, the structure was optimized using the DFT-D2 method, where the volume differs by +0.001%. The strong hydrogen bond in ADN is because of one nitrogen atom surrounded by four hydrogen atoms and oxygen atoms surrounding dinitramide ions. The crystal structure of HNF has two independent nitroformate anions with dihedral angles for the nitro groups. Then the two hydrazinium cations are different are staggered and eclipsed symmetry of the hydrogen atoms. The N-N bonds distance is about 1.446 (Å). The hydrogen bonds are linked by a three-dimensional network in ADN and a staggered arrangement in HNF, whereas KDN is an intermediate compound obtained during ADN synthesis on a large scale based on sulfamic acid derivatives [53]. The coordination number of potassium ions is nine with eight oxygen atoms, one nitrogen atom, and bond distance ranging from 2.81(Å) to 3.06(Å).

The ground state of the crystal is achieved by doing geometry optimization with respect to the unit cell parameters (lattice constants, bond length, volume). We have used different approaches to optimize the crystal structure where HNF: LDA(-7.42%), GGA-PBE(27%), PW91(27%); KDN (LDA (-11.9%), (GGA-PBE (10.68%), PW91 (10.72%) results underestimated the original volume, while the HNF: LDA + OBS(-13.65%), GGA + TS(7.3%), GGA + G06(2.55%), PW91 + OBS(2.87%); KDN: LDA+OBS (-16.0%), GGA+TS (-6.48%), GGA+G06 (0.168%), PW91+OBS (3.58%) scheme overestimate. The calculated lattice parameters are presented with the semi-empirical correction to show the effect of van der Waals interaction. It can be observed that the calculated GGA+G06 values show a good agreement with experimental data, concluding the presence of van der Waals interaction in HNF and KDN, similar to ADN. Therefore, GGA+G06 results are considered for further calculations. The calculated structural parameters with error percentage are summarized in Table-5.1 with experimental data.

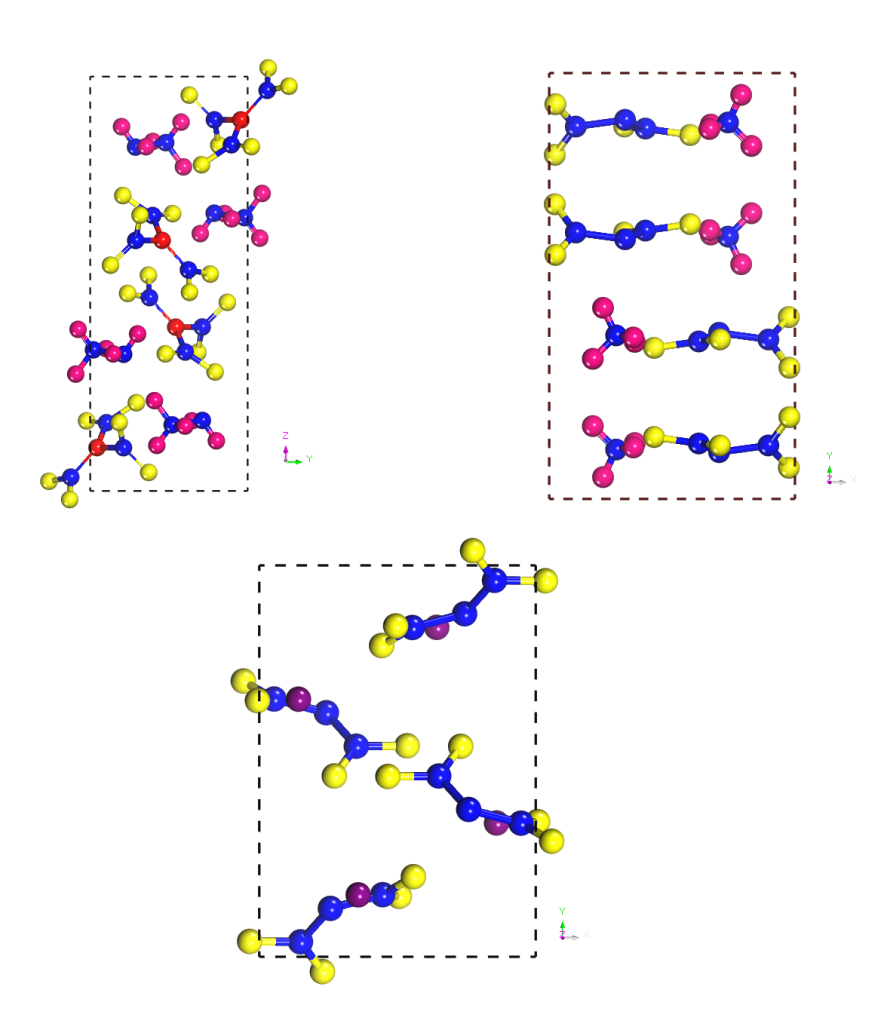


Figure. 5.1 Unit cell for (Left top) Hydrazinium nitroformate (HNF), (Right top) Ammonium dinitramide (ADN), (Bottom) Potassium dinitramide (KDN).

Table 5.1 The relaxed lattice parameters (a, b, c in Å) and Volume (V in Å³), of KDN and HNF using standard LDA (CA-PZ),GGA (PBE) and semiempirical schemes LDA+OBS, PBE+G06, PW91+OBS with deviation percentage and experimental data.

Funtionals	a (Å)	b (Å)	c (Å)	$V (Å^3)$
KDN				
LDA	6.45	8.68	6.95	385.65(-11.9%)
LDA+OBS	6.37	8.49	6.85	367.59(-16.0%)
GGA	6.70	9.833	7.39	484.74(10.68%)
GGA+G06	6.70	9.107	7.23	438.68(0.168%)
GGA+TS	6.64	8.83	7.08	409.53(-6.48%)
PW91	6.67	9.84	7.42	484.91(10.72%)
PW91+OBS	6.66	9.43	7.26	453.63(3.58%)
Experiment a	6.61	9.28	7.91	437.93
HNF				
LDA	7.95	5.19	14.18	580.84(-7.42%)
LDA+OBS	7.73	5.12	13.84	542.36(-13.65%)
GGA	9.53	5.70	14.94	802.21(27%)
GGA+G06	8.22	5.38	14.64	643.57(2.55%)
GGA+TS	8.43	5.36	14.96	673.74(7.3%)
PW91	9.53	5.7	14.94	801.86(27%)
PW91+OBS	8.30	5.31	14.70	646.100(2.87%)
Experiment b	8.04	5.44	14.50	627.4

^aRef. [52]

5.3.2 Vibrational properties

In this section, we turn to investigate the vibrational frequencies for HNF, KDN crystal within the framework of DFPT [45]. In our previous work, Yedukondalu et al. [24] reported that the strong hydrogen bonding present in ADN is mainly responsible for hygroscopic nature. Moreover, weakening and strengthening of hydrogen bond lead to blue and redshift in pressure-dependent IR spectrum expecting structural phase transition around 5-6 GPa. Additionally, Weihua Zhu et al. [54] reported a detailed analysis of ADN vibrational frequencies from 41.3 cm⁻¹ to 3187 cm⁻¹. Bending of N(NO₂) has been observed in the mid-frequency region and symmetric and asymmetric stretching from 1045 to 3187 cm⁻¹. In this work, we tried to compute IR spectra of HNF, KDN crystal at ambient conditions and compare the same with ADN.

The unit cell of HNF and KDN crystalize in same space group $P2_1/n$ with four formulae units where HNF has 204 phonons modes obtained from 68 atoms and KDN results in 32 atoms, yields a sum of total 96 modes, where 3 are acoustic in both crystals and remaining 201 and 93 are optical modes, respectively. The irreducible representation for HNF is $\Gamma_{acoustic} = A_u \oplus 2B_u$, $\Gamma_{optic} = 51A_g \oplus 50A_u \oplus 51B_g \oplus 49B_u$, which contain Raman modes $(51A_q \oplus 51B_q)$ active modes and IR active modes $(50A_u \oplus 49B_u)$ and for KDN Γ $acoustic = A_u \oplus 2B_u$ and $\Gamma_{optic} = 24A_g \oplus 23A_u \oplus 24B_g \oplus 22B_u$, which contain Raman $\operatorname{modes}(24A_q \oplus 24B_q)$ active modes and IR active modes $(23A_u \oplus 22B_u)$. The experimental IR spectra of $NH_4N(NO_2)$, $KN(NO_2)$, $CsN(NO_2)$ were recorded using FTIR spectrometer, no data for HNF has been reported. The calculated vibrational frequencies for ADN and KDN follow the same trend reported which matches with experimental paper [55,56]. The IR spectra and detailed classification of modes according to frequency are mentioned in Figure-5.2, Table-(5.2,5.3,5.4,5.5). We report the vibrational frequencies of HNF ranging from $(42.27 \text{ cm}^{-1} \text{ to } 3400 \text{ cm}^{-1})$. Primarily, 20 peaks in the low frequency $(<600^{-1})$ region corresponds to the translation and rotation in NO₂ group in nitroform and NH₂, NH₃ in hydrazine. The mid-frequency region consists of 24 peaks; these peaks are mainly due to rocking, wagging, scissoring, bending, twisting, and some mixed vibrations including stretching in N-H, C-N, N-O. The high-frequency region has seven peaks; these intense IR peaks are mainly due to the symmetric and asymmetric stretching of the NH₂ group. Furthermore, vibrational frequencies in KDN range from 30 cm⁻¹ to 1500 cm⁻¹, where $30-300 \text{ cm}^{-1}$ consist of seven peaks, representing a translation of K atoms and $N(NO_2)_2$ anion and rotational modes of NO_2 and N_2O . The mid frequencies (400-800 cm⁻¹) show mainly four main peaks, due to dinitramide bending, i.e. (Scissoring, twisting, wagging) of NO₂, which matches with experimental data. In the high-frequency region (900-1500 cm⁻¹), from 1108-1284 cm⁻¹, vibrations are due to N-N-N stretching and NO₂ symmetric stretching and 1365-1451 cm⁻¹ are due to asymmetric stretching of NO₂ group. Here we have observed 45 infra-red active modes, 48 Raman active modes with no silent modes. In HNF our analysis shows that the vibration in the mid-frequency region occurs due to NO_2 , N_2H_5 , and mixed vibrations caused by N and C related bonds. Also, due to the lower atomic mass of the H atom, vibrations in the high-frequency region are only due to the N-H bond in NH₂ group while in KDN mid and high frequencies are mainly due to vibrations caused by NO_2 group in dinitramide.

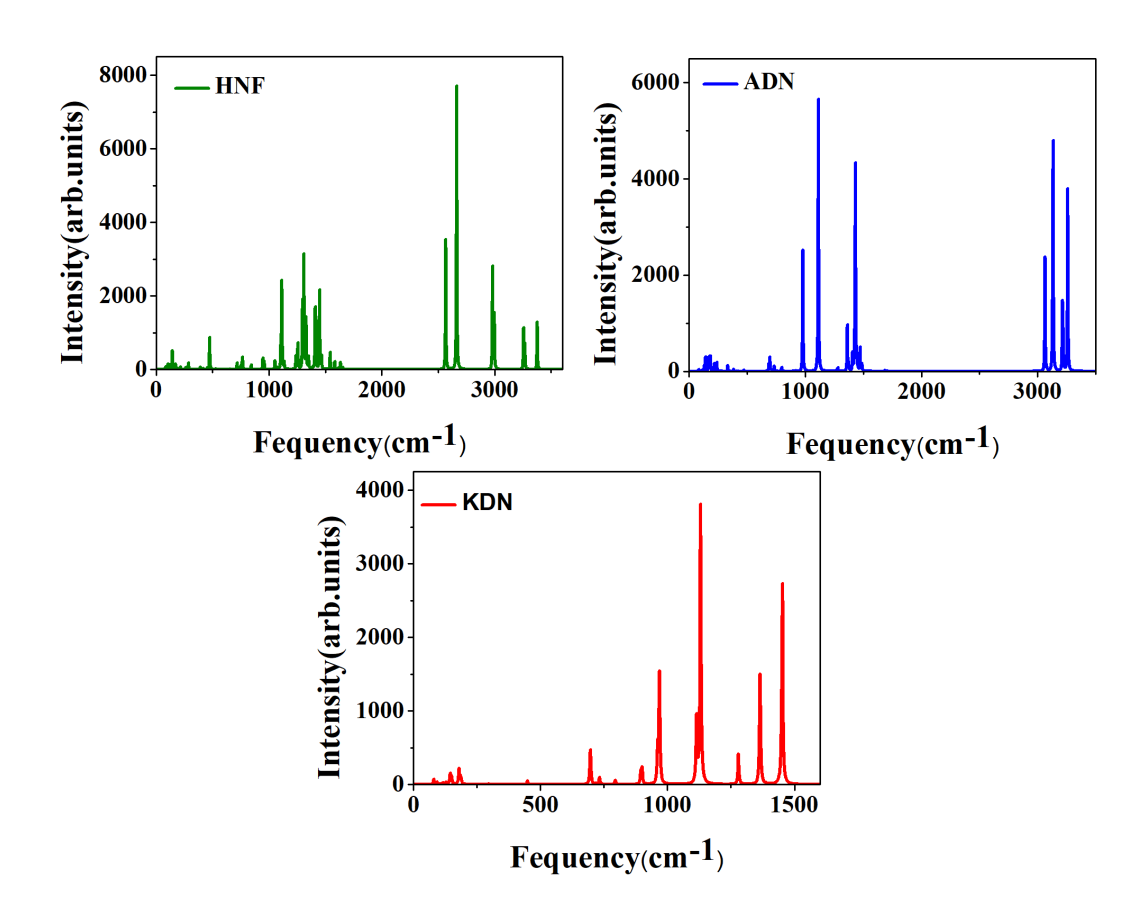


Figure. 5.2 Theoretical IR spectrum of Hydrazinium nitroformate: 0-3500(cm⁻¹), Ammonium dinitramide: 0-3500(cm⁻¹), Potassium dinitramide: 0-1530(cm⁻¹).

 ${\bf Table~5.2~The~Calculated~vibrational~modes~from~41~cm^{-1}~to~184~cm^{-1}~representing} \\ {\bf Translation:Trans,~Rotation:Rotat.,~for~KDN.}$

Mode	Assignment of modes	Mode	Assignment of modes
41.68 I	K and $N(NO_2)_2$ Trans.	121.08	NO ₂ Rotat.
51.88 l	κ and $N(NO_2)_2$ Trans.	124.91	K Trans.
58.87 l	κ and $N(NO_2)_2$ Trans.	127.11	K Trans., $N(NO_2)_2$ Rotat.
59.81 l	κ and $N(NO_2)_2$ Trans.	128.07	NO_2 Rotat.
74.48	$N(NO_2)_2$ Trans.	131.61	$N(NO_2)$ 2 Rotat.
78.22 l	κ and $N(NO_2)_2$ Rotat.	136.66	K Trans., NO_2 Rotat.
80.05	k and NO_2 Rotat.	137.33	K Trans., NO_2 Rotat.
85.41	k and NO_2 Rotat.	138.49	N-O Trans.
86.78 l	x and $N(NO_2)_2$ Trans.	144.51	K Trans., $N(NO_2)_2$ Rotat.
88.46	NO_2 Trans.	147.03	NO_2 Rotat.
92.58	NO_2 Trans.	148.55	K Trans., NO_2 Rotat.
95.28	NO_2 Trans.	149.42	K Trans., $N(NO_2)_2$ Rotat.
95.44	K Trans., NO ₂ Rotat.	154.52	K Trans., N_2O Trans.
99.92	N-O Trans.	157.75	K Trans., N_2O Trans.
103.27	K- Trans., N-O trans.	169.32	K Trans., N-N Trans.
107.74	K- Trans., N-O trans.	171.28	N_2O_2 Trans., NO_2 Rotat.
108.64	K Trans., NO ₂ Rotat.	175.01	N_2O Rotat.
111.34	K Trans., NO ₂ Trans.	179.08	K Trans., N_2O_2 Trans
113.51 K	Trans., $N(NO_2)_2$ Rotat.	182.78	K Trans., N_2O Trans
116.98	NO_2 Rotat.	184.49	N_2O Rotat.

^aRef. [55]

Table 5.3 The Calculated vibrational modes 188 cm⁻¹ to 1451 cm⁻¹ representing Bending:bend., Scissoring:Sciss.,Rocking:Rock, Wagging:Wagg. streatching: Stre., symmetric:symm.stre., asymmetric:asymm.stre., for KDN.

Mode	Assignment of modes	Mode	Assignment of modes
188.04	N ₂ O Rotat.	795.68	NO_2 sciss., N-N-N bend
293.17	NO_2 Rotat.	796.48	NO_2 sciss., N-N-N bend.
294.17	NO_2 Rotat.	895.22	N-N stre.
294.50	NO_2 Rotat.	898.38	N-N stre.
294.68	NO_2 Rotat.	900.15	N-N-N stre.
445.27	NO_2 Rotat.	901.86	N-N-N stre.
447.85	NO_2 Rotat.	956.57	N-N-N Asymm.stre.
447.93	NO_2 Rotat.	961.94	N-N-N Asymm.stre.
448.50	NO_2 Rotat.	968.58	N-N-N Asymm.stre.
464.78	NO_2 wagg.	971.22	N-N-N Asymm.stre.
464.85	NO_2 wagg.	1108.76	NO_2 symm.stre., N-N-N stre.
465.49	NO_2 wagg.	1115.12	NO_2 symm.stre., N-N-N stre.
696.39	N-N-N bend.	1130.79	NO_2 symm.stre., N-N-N stre.
700.99	N-N-N bend.	1141.69	NO_2 symm.stre., N-N-N stre.
702.92	N-N-N bend.	1274.32	NO_2 symm.stre., N-N-N stre.
707.15	N-N-N bend.	1277.13	NO_2 symm.stre., N-N-N stre.
717.37	N-N-N See-saw	1279.69	NO_2 symm.stre., N-N-N stre.
717.53	N-N-N See-saw	1284.00	N-N-N symm.stre., N-N-N stre.
717.85	N-N-N See-saw	1365.03	NO_2 asymm.stre.
719.99	N-N-N See-saw	1376.03	NO_2 asymm.stre.
732.74	NO_2 sciss., N-N-N Rotat.	1384.29	NO_2 asymm.stre.
733.14	NO ₂ sciss., N-N-N Rotat.	1387.20	NO_2 asymm.stre.
734.32	NO_2 sciss., N-N-N Rotat.	1435.01	NO_2 asymm.stre.
735.11	NO_2 sciss., N-N-N Rotat.	1448.65	NO_2 asymm.stre.
793.79	NO_2 sciss.N-N-N bend.	1449.13	NO_2 asymm.stre.
795.29	NO_2 sciss., N-N-N bend.	1451.92	NO_2 asymm.stre.

^aRef. [55]

	A	M. 1	A: C - 2
Mode	Assignment of modes	Mode	Assignment of modes
42.27	N-O Trans.	214.09	NH ₃ - NH ₂ Rotat.
52.12	N-O Trans.	216.55	NH ₃ - NH ₂ Rotat.
60.99	NO_2 Trans.	223.21	NH ₃ - NH ₂ , NO ₂ Rotat.
64.61	NO_2 , NH_2 Trans.	235.06	NH ₃ Rotat
67.78	NO_2 , NH_2 Trans.	236.38	NH ₂ Rotat.
68.13	NO_2 , NH_2 Trans.	237.79	NH ₃ - NH ₂ , NO ₂ Rotat.
74.77	NH_2 Trans.	237.98	NH_3 - NH_2 , NO_2 Rotat.
77.94	NO_2 , NH_2 Trans.	250.02	NH_3 - NH_2 Rotat.
78.92	NO_2 Rotat.	251.31	NH_3 Rotat.
79.92	NO_2 , NH_2 Trans.	257.64	NH ₃ - NH ₂ , NO ₂ Rotat.
83.14	NO_2 , NH_2 Trans.	257.88	NH ₃ - NH ₂ , NO ₂ Rotat.
89.42	NO_2 , NH_2 Trans.	259.83	NH ₃ - NH ₂ , NO ₂ Rotat.
89.46	NO_2 , NH_2 Rotat.	260.69	$\mathrm{NH_{3}\text{-}\ NH_{2},\ NO_{2}\ Rotat}$
93.72	NO_2 Rotat.	286.60	$\mathrm{NH_{3}}\text{-}\ \mathrm{NH_{2}}\ \mathrm{Rotat}.$
98.82	NO_2 , NH_2 Trans.	288.12	$\mathrm{NH_{3}\text{-}\ NH_{2},\ NO_{2}\ Rotat.}$
102.49	NO_2 , NH_2 Rotat.	390.15	$\mathrm{NH_{3}\text{-}\ NH_{2},\ NO_{2}\ Rotat}.$
103.87	NO_2 Rotat.	391.71	$\mathrm{NH_{3^-}\ NH_{2}},\ \mathrm{NO_{2}\ Rotat}.$
104.91	NH_2 Rotat.	406.31	NO_2 Rock.
108.46	NO_2 , NH_2 Trans.	406.32	NO_2 Rock.
109.40	NO_2 Rotat.	410.29	NO_2 Rock.
115.08	NO_2 Rotat.	410.80	NO_2 Rotat.
117.05	NO_2 , NH_2 Rotat.	415.44	NH ₂ Rotat., NO ₂ Sciss.
117.45	NH ₂ Rotat.	418.90	NH ₂ Rotat., NO ₂ Sciss.
119.27	NO_2 , NH_2 Trans.	419.35	NO ₂ Sciss.
120.98	NH_2 Rotat.	421.49	NO ₂ Sciss.
125.14	NO_2 Rotat.	451.35	NO ₂ Sciss.
128.91	NO ₂ Rotat.	451.74	NO ₂ Sciss.
134.35	NO_2 , NH_3 Trans.	452.04	NO ₂ Sciss.
139.79	NO ₂ Rotat. , NH ₃ -NH ₂ Trans.	452.89	NH ₃ Rotat, NO ₂ Sciss.
140.65	NH ₃ -NH ₂ Trans.	473.43	NH ₂ Rock.
143.43	NH_3 - NH_2 Trans.	488.84	NH ₂ Rock.
144.44	NH ₃ -NH ₂ Rotat.	511.22	NH ₃ Rock.
145.20	NH ₃ -NH ₂ Rotat.	511.76	NH ₃ Rock.
145.90	NH ₃ -NH ₂ Rotat.,NO ₂ Trans.	519.66	NH ₃ , NO ₂ Rotat.
152.01	NH ₂ Rotat.	520.28	NH ₃ , NO ₂ Rotat.
153.14	NH ₂ Rotat.	521.81	NH ₃ , NO ₂ Rotat.
156.48	NO ₂ NH ₂ Rotat.	522.53	NO ₂ Rotat.
157.20	NO ₂ Rotat.	528.89	NH ₃ Rock.
160.61	NO ₂ , NH ₃ - NH ₂ Rotat.	530.01	NH ₃ Rock.
164.06	NO_2 Rotat.	648.68	NO ₂ wagg
167.78	NO ₂ Rotat.	648.77	NO_2 wagg.
169.36	NH ₂ Rotat.	650.74	NO_2 wagg. NO_2 wagg.
170.84	NH ₃ - NH ₂ Rotat.	650.80	NO_2 wagg. NO_2 wagg.
170.84	NH ₃ - NH ₂ Rotat.	698.48	NO_2 wagg. NO_2 wagg.
	NH ₃ - NH ₂ Rotat. NH ₃ - NH ₂ Rotat.		NO_2 wagg. NO_2 wagg.
173.59	NH ₃ - NH ₂ NO ₂ Rotat.	698.91	
179.57	NH_3 - NH_2 , NO_2 Rotat. NH_3 - NH_2 , NO_2 Rotat.	699.9	NO ₂ wagg.
187.03	-/ -	700.32	N-C-N wagg.
190.66	NO ₂ Rotat.	717.44	N-C-N wagg.
201.52	NO ₂ Rotat.	717.76	N-C-N wagg.
212.31	NH ₃ - NH ₂ Rotat.	719.20	N-C-N wagg.

Table 5.5 The Calculated frequencies in(cm⁻¹ of HNF 720 cm⁻¹ to 3378 cm⁻¹, representing Bending:bend., Wagging:Wagg., Rocking:Rock, Scissoring:Sciss., streatching: Stre., symmetric:symm.stre., asymmetric:asymm.stre., for HNF.

Mode	Assignment of modes	Mode	Assignment of modes
720.34	N-C-N wagg.	1340.95	NH ₂ Twist.
752.72	NH ₂ Sciss.	1344.66	NH_2 Twist.
753.22	NH_2 Sciss.	1351.32	NH_2 Twist.
753.53	NH_2 Sciss.	1388.20	NH_2 Twist.
754.15	$C(NO_2)_3$) in Sciss.	1388.26	NH_3 Wagg., NH_2 Twist.
763.38	$C(NO_2)_3)$ in Sciss.	1390.56	NH ₃ Wagg., NH ₂ Twist.
763.44	$C(NO_2)_3$) in Sciss.	1392.66	$\mathrm{NH_{3}\ Wagg.,\ NH_{2}\ Twist.}$
765.89	$C(NO_2)_3$) in Sciss.	1409.70	$\mathrm{NH_{3}}$ Wagg., N-O Stretch.
767.28	$C(NO_2)_3)$ in Sciss.	1414.35	NH ₃ Wagg., N-O Stretch.
842.05	NO_2 Sciss., C-N stretch.	1419.42	$\mathrm{NH_{3}}\text{-}\ \mathrm{NH_{2}}\ \mathrm{Wagg.},\ \mathrm{NO_{2}}\ \mathrm{Stretch.}$
842.54	NO ₂ Sciss., C-N stretch.	1420.62	NH ₃ - NH ₂ Wagg., NO ₂ Stretch.
843.47	NO ₂ Sciss., C-N stretch.	1448.65	NO ₂ Asymm. Stretch.
843.51	NO_2 Sciss., C-N stretch.	1456.37	NO ₂ Asymm. Stretch.
945.67	NH_{3} - NH_{2} Wagg.	1461.69	NO ₂ Asymm. Stretch.
948.84	NH ₃ - NH ₂ Wagg.	1465.92	NO ₂ Asymm. Stretch.
957.78	NH_{3} - NH_{2} Wagg.	1541.62	$_{ m NH_3}$ Bend.
958.04	NH_{3} - NH_{2} Wagg.	1542.63	NH_3 Bend.
1052.46	NH ₃ - NH ₂ Wagg. and Sciss.	1542.89	NH_3 Bend.
1055.57	NH ₃ - NH ₂ Wagg. and Sciss.	1542.93	$\mathrm{NH_{3}\ Bend}.$
1068.61	NH ₃ - NH ₂ Wagg. and Sciss.	1582.46	NH ₃ - NH ₂ Sciss.
1076.09	NH ₃ - NH ₂ Wagg. and Sciss.	1583.89	NH ₃ - NH ₂ Sciss.
1087.20	NH ₃ - NH ₂ Wagg. and Sciss.	1583.93	NH ₃ - NH ₂ Sciss.
1087.52	NH ₃ - NH ₂ Wagg. and Sciss.	1584.68	NH ₃ - NH ₂ Sciss.
1105.50	NH ₃ - NH ₂ Twist.	1610.71	NH ₃ - NH ₂ Sciss., Twist.
1106.59	NH ₃ - NH ₂ Wagg., NH ₂ Stretch.	1613.70	NH ₃ - NH ₂ Sciss., Twist.
1111.54	NH ₃ - NH ₂ Wagg., NH ₂ Stretch.	1623.28	NH ₃ - NH ₂ Sciss., Twist.
1112.77	NH ₃ - NH ₂ Wagg., NH ₂ Stretch.	1625.35	NH ₃ - NH ₂ Sciss., Twist.
1113.72	NH ₃ - NH ₂ Wagg., N-C Stretch.	1632.85	NH ₃ Sciss.
1115.10	N-C Stretch.	1633.20	NH_3 Sciss.
1116.95	N-C , N-O Stretch.	1651.99	$\mathrm{NH_{3}\ Sciss}.$
1118.10	NH ₃ - NH ₂ Twist.	1652.74	NH_3 Sciss.
1119.60	NH ₃ - NH ₂ Twist.	2566.51	N-H Stretch.
1134.91	NH ₃ - NH ₂ Wagg. and Sciss.	2566.69	N-H Stretch.
1226.06	NH ₃ - NH ₂ Wagg.	2663.64	N-H Stretch.
1226.09	NH_3 - NH_2 Wagg.	2691.88	N-H Stretch.
1238.59	NH ₃ - NH ₂ Wagg.	2981.60	N-H Stretch.
1238.98	NH ₃ - NH ₂ Wagg.	2982.45	N-H Stretch.
1251.15	NH ₃ - NH ₂ Wagg.	2987.07	N-H Stretch.
1253.19	NH ₂ Wagg., NO ₂ Stretch.	2997.26	N-H Stretch.
1254.66	NH ₃ - NH ₂ Wagg., C-N Stretch.	3255.89	N-H Stretch.
1254.00	C-N Stretch	3256.24	N-H Stretch., NH ₂ Symmt. Stretch.
1294.69	C-N Stretch.	3257.73	N-H Stretch.
1297.77	C-N Stretch.	3266.68	NH ₂ Symmt. Stretch.
1301.54	C-N Stretch	3267.36	NH ₂ Symmt. Stretch.
1304.62	N-C-N Asymm. Stretch.	3268.95	NH ₂ Symmt. Stretch.
1304.02	N-C-N Asymm. Stretch.	3270.01	NH ₂ Symmt. Stretch.
1326.46	N-C-N Asymm. Stretch.	3376.30	NH ₂ Asymmt. Stretch.
1327.53	C-N-C Sciss. N-O Stretch.	3376.90	NH ₂ Asymmt. Stretch.
1328.80	C-N-C Sciss. N-O Stretch.	3377.09	NH ₂ Asymmt. Stretch.
			= *
1340.34	NH ₃ - NH ₂ Twist., N-O Stretch.	3378.14	NH ₂ Asymmt. Stretch.

5.3.3 Phonon dispersion of ADN and KDN

The full phonon dispersion along various high symmetry direction in these compounds are calculated using van der Waals semi-empirical correction built-in VASP [48–50]. The computed phonon dispersion curves do not show any imaginary modes ensuring dynamical stability. The total phonon dispersion of ADN and KDN extends up to 420 meV and 230 meV respectively. However, for better visibility, we have shown the dispersion curve up to 25 meV in Figure-5.3. The acoustic branches along various high symmetric directions are extended up to 5 meV in both compounds. It can be seen that low-lying acoustic branches interact with the optical branches. Moreover, there exists a small gap near 16meV in phonon spectra of ADN, whereas the phonon spectra of KDN are gapless. Furthermore, the atomic vibrational contribution of various atoms in these compounds is shown in Figure-5.4. Optical vibrations in the low-energy region in KDN are due to the high atomic mass of the K atom, the vibrations corresponding to N and O atoms spread over a similar range of 230 meV in both ADN and KDN compounds. In ADN, optical vibrations spread over a wide range till 420 meV due to H atoms lowest atomic mass compared to other atoms, and the same can be observed in earlier reported vibrational properties of ADN [13]. The partial phonon density of states shows that optical branches seem to be relatively more dispersive in the low-energy region for KDN than ADN because of the K atom. This concludes that KDN will have low thermal conductivity and heat dissipation than ADN.

5.3.4 Born effective charges (BEC's)

Theoretically, born effective charges describe the atomic polarizability of tensors. The Born effective charge tensor of an ion is the partial derivative of the macroscopic polarization with respect to a periodic displacement of all the periodic images of that ion at zero macroscopic electric field. The Born effective charge tensor is calculated within the linear response formalism by applying a Gonze approximation. We have calculated effective charges for HNF, ADN, and KDN compounds by slightly displacing each ion, one at a time, along with three directions of cartesian coordinates and calculating the resulting difference in polarization, established by King-Smith and Vanderbilt in 1993 [57]. The born effective charges control the amplitude of long-range Coulomb interactions between nuclei and splitting between longitudinal optic (LO), transverse optic (TO) phonon mode. Advances in ab initio techniques now enable one to determine BEC's using perturbation theory [57] or finite difference in polarization [57]. It is a measure of the coupling between the polarization and the displacement of sublattice in the zero electric field. If α and β define the two directions (such as x and y) and i denotes an atom, then, the BEC tensor $Z_{i,\alpha\beta}^*$ of the ith atom is defined as

$$Z_{i,\alpha\beta}^* = \frac{\Omega_{cell}}{e} \frac{\partial P_{\alpha}}{\partial u_{i\beta}}$$

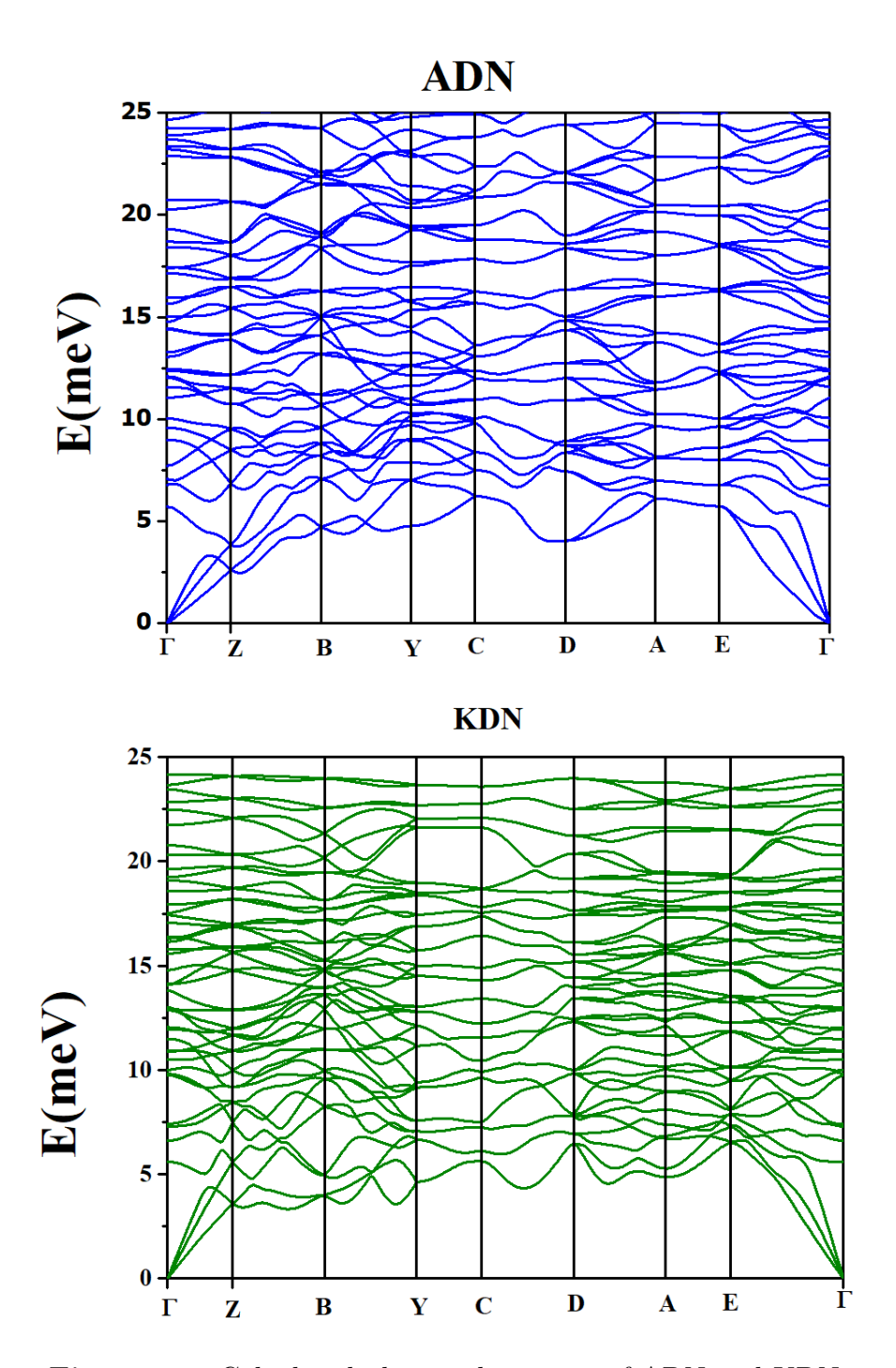


Figure. 5.3 Calculated phonon dispersion of ADN and KDN.

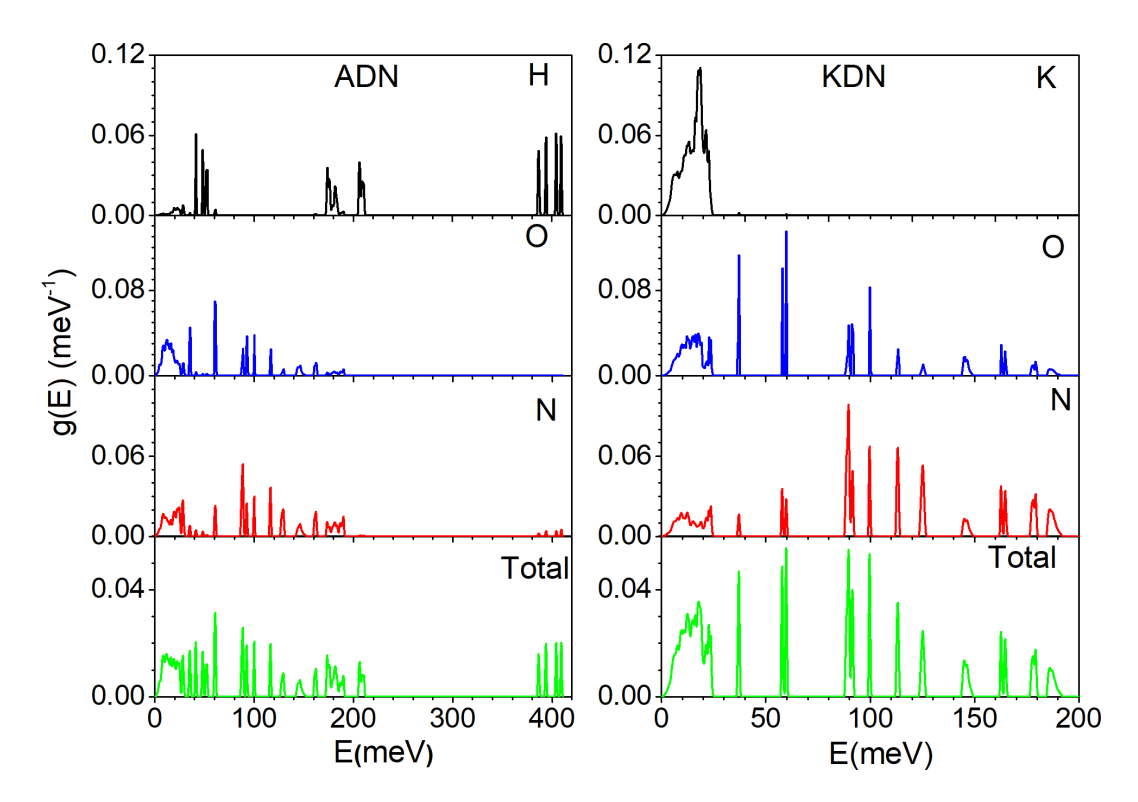


Figure. 5.4 Calculated phonon density of states for ADN and KDN crystal structures.

where P_{α} is the component of the polarization in the α direction, $u_{i\beta}$ is the periodic displacement of the ith atom in the β direction, and Ω_{cell} is the unit cell volume. Moreover, the acoustic sum rule is enforced in these calculations. The anisotropic diagonal components of BEC's $(Z^*_{xx} \neq Z^*_{yy} \neq Z^*_{zz})$ in HNF, ADN and KDN result from the monoclinic structure. Here, the formal valence of H, N, O, K and C are +1, -3, -2, +1, +4 respectively. The maximum effective charge has been reported in Table-5.6. The BEC's of all atoms are larger than their nominal ionic values owing to the displacement of ions. The rigid shift of charges and the ion displacement describe the ionic charge term, while the dynamic charge transfer is related to electrons' electronic response. However, results show that the absolute values of BEC have deviated from their nominal charges, indicating that there might be a covalent or ionic character. Effective charge of C, N1, N3, N5 in HNF and H, N4 atoms in ADN show larger deviation from its nominal charge, concludes covalent nature in N-C bond in HNF and NH₄ in ADN. In KDN, K atoms have slightly deviated from their ionic charge proving that there might be an ionic bond with the surrounding N and O atoms. However, nitrogen (N2, N3) ions in ADN and KDN show a maximum effective charge with respect to its static charge. In detail, more deviation can be seen in the Z₁₁ direction in N ion, and deviation in oxygen ions is seen in three directions, but the maximum can be observed in Z_{22} direction. In the case of HNF, the maximum deviation can be noticed in directions Z₃₃, Z₁₁, Z₃₃ in N1, N3, N5 ions, respectively. Whereas O1, O2, O4 atoms deviate mostly in Z_{11} and O3, O6 in Z_{33} direction. Overall, from the

Table 5.6 Theoretical Born effective charge tensors and percentage deviation from nominal charge of ADN, KDN and HNF)(H=+1,N=-3,O=-2,C=+4, K=+1) at the theoretical equilibrium volumes.

Ion	Z_{11}	Z_{22}	Z_{33}	Ion	Z_{11}	Z_{22}	Z_{33}	Ion	Z_{11}	Z_{22}	Z_{33}
	ADN				KDN				HNF		
H1	0.38	0.83	0.47	K	1.34	1.14	1.31	H1	0.21	0.61	0.83
H2	0.54	0.25	0.77	N1	-1.79	-0.52	-0.52	H2	0.50	0.51	0.31
Н3	0.44	0.30	0.64	N2	2.83	1.26	1.21	Н3	0.29	0.23	0.48
H4	0.70	0.57	0.31	N3	2.68	0.44	2.08	H4	0.27	0.37	0.39
N1	-1.78	-0.32	-0.86	O1	-2.08	-0.58	-0.42	Н5	0.31	0.68	1.21
N2	2.84	1.43	1.18	O2	-0.72	-0.82	-0.97	С	-0.31	-0.38	-1.40
N3	2.63	0.29	2.37	О3	-1.28	-0.57	-1.23	N1	1.54	1.50	2.10
N4	-0.67	-0.65	-0.71	O4	-0.97	-0.33	-1.46	N2	-0.05	-0.55	-0.89
O1	-1.25	-1.03	-0.50					N3	1.88	1.43	1.35
O2	-1.13	-1.01	-1.19					N4	-0.30	-0.35	-0.82
О3	-0.64	-0.24	-1.54					N5	1.51	1.33	2.32
04	-2.05	-0.40	-0.96					O1	-1.28	-0.62	-0.75
								O2	-1.06	-1.02	-0.56
								O4	-1.34	-0.79	-0.74
								О5	-0.64	-1.02	-0.88
								O6	-0.54	-1.18	-1

structural similarity in ADN and KDN, it can be observed that the trend of deviation for all the atoms is almost similar. Finally, between the two sterically active NO₂ groups, valence electrons between N atoms are shared, due to the same electronegativity, end up in sharing of electrons. While oxygen has slightly high electronegativity than nitrogen(N), oxygen(O) atoms share electrons with N leading to more deviations from their nominal charge. Hence, a strong covalent bond between NO₂ group is observed in ADN and KDN while N-C bond in HNF.

The static dielectric tensor ϵ_0 includes the contribution of the electronic and the ionic dielectric constant, it has been calculated from the BEC's of the mentioned atoms of the HNF, ADN, KDN respectively. The calculated $\epsilon(\infty)$ describes the optical dielectric tensor and $\epsilon(0)$ is the contribution to the dielectric constant of each phonon mode. The $\epsilon(\infty)$ and $\epsilon(0)$ of HNF, ADN and KDN are mentioned below:

$$\epsilon(\infty)^{HNF} \begin{bmatrix} 2.75 & 0 & -0.16 \\ 0 & 2.70 & 0 \\ -0.16 & 0 & 3.11 \end{bmatrix} \quad \epsilon(0)^{HNF} \begin{bmatrix} 4.62 & 0 & -0.87 \\ 0 & 6.42 & 0 \\ -0.87 & 0 & 6.74 \end{bmatrix}$$

$$\epsilon(\infty)^{ADN} \begin{bmatrix} 3.05 & 0.0 & -0.26 \\ 0.0 & 2.18 & 0.0 \\ -0.20 & 0.0 & 2.64 \end{bmatrix} \quad \epsilon(0)^{ADN} \begin{bmatrix} 6.46 & 0.0 & -0.02 \\ 0.0 & 4.31 & 0.0 \\ -0.02 & 0.0 & 5.92 \end{bmatrix}$$

$$\epsilon(\infty)^{KDN} \begin{bmatrix} 2.98 & 0.0 & 0.06 \\ 0.0 & 2.15 & 0.0 \\ 0.06 & 0.0 & 2.42 \end{bmatrix} \quad \epsilon(0)^{KDN} \begin{bmatrix} 5.64 & 0.0 & 0.12 \\ 0.0 & 3.82 & 0.0 \\ 0.12 & 0.0 & 4.43 \end{bmatrix}$$

The calculated diagonal elements of dielectric tensors show anisotropic nature in xx, yy, and zz directions. The electronic and ionic dielectric constants values are averaged 2.87(HNF), 5.92(HNF) and 2.62(ADN), 5.56(ADN) and 2.51(KDN), 4.63(KDN). It can be noticed that the dielectric constant is dominated by the ionic contribution in all the compounds. The value of $\epsilon(\infty)$ and $\epsilon(0)$ value is larger in zz direction for HNF and xx direction for ADN and KDN. This result shows that the ϵ_0 main contribution in HNF is from the zz direction and xx direction for ADN and KDN. The total static dielectric contribution of HNF, ADN, and KDN is obtained by summing up the electronic and ionic part. So, we conclude the sum of the electronic and ionic dielectric constant of HNF (8.79), ADN(8.18), and KDN(7.14).

5.3.5 Elastic constants

Elastic properties play a key role to determine various fundamental properties such as interatomic bonding, intermolecular interactions, mechanical stability in different axis, and thermal expansion. Hence, it is crucial in the case of high-energy materials to understand how materials respond along different axis due to shock and friction at ambient conditions. In particular, the stiffer the lattice, the lesser the sensitivity. The HNF obtained from nitroform and hydrazine and the dinitramide-based ADN and KDN crystallize in the monoclinic system with 13 independent elastic constants. In our previous work, Yedukondalu et al. [24] reported the elastic constants of ADN to understand the mechanical response under applied stress [13]. Elastic constants of ADN satisfy the Born stability criteria and it is found to be less sensitive in C_{11} direction and more sensitive along C_{22} direction. As per our knowledge, no experimental reports are addressing the mechanical stability of HNF, KDN to date. The calculated elastic constants satisfy the corresponding mechanical stability criteria and the same is reported in Table-5.7. We have reported the calculated elastic constants C_{ij} and bulk modulus B of HNF, ADN, and KDN, mentioned in the table. Bulk modulus of HNF (24.71 GPa), KDN (20.9 GPa) is higher than the reported value of ADN 16.4 GPa (experiment) [58], 18.48 (theory) [24]. Besides diagonal elements C_{11} , C_{22} , C_{33} show that C_{11} value is lowered in HNF and C_{22} , C_{33} are enhanced in HNF when compared to ADN and KDN. The diagonal elements show that coefficient C_{22} in HNF, C_{11} in ADN, C_{33} in KDN are found to be more rigid due to strong interactions. In

Table 5.7 Comparison of elastic constants of Ammonium dinitramide (ADN), Potassium dinitramide (KDN) and Hydrazinium nitroformate(HNF).

Elastic const.(GPa)	Earlier work ADN^a	KDN	HNF
C_{11}	49.4	41.5	33.7
C_{12}	10.6	17.8	14.3
C_{13}	17.6	11.7	12.5
C_{15}	-9.7	-3.9	-12.5
C_{22}	22.4	30.4	61.1
C_{23}	10.7	9.1	20.7
C_{25}	0.6	-0.5	7.7
C_{33}	28.2	47.9	54.2
C_{35}	1.0	-2.5	-16.2
C_{44}	9.1	6.6	17.4
C_{46}	0.6	-0.7	-0.3
C_{55}	14.4	10.3	48.2
C_{66}	6.2	17.8	23.1
aD C [10]	·		

^aRef. [13]

detail, the magnitude of the elastic constant of HNF is compared with ADN, we can see that C_{11} decreases by 31.78%, C_{22} increases by 177.54%, C_{33} increases by 92.34% and see notable values such as C_{12} and C_{13} decreases by 34.52%, 28.92% and C_{33} , C_{44} , C_{55} increases by 90.98%, 235.06%, 272.90%. In addition, the magnitude of the elastic constants of KDN is compared with ADN. The coefficient C_{11} of KDN decreases by 15.95% when compared to ADN, whereas the coefficient C_{22} and C_{33} of KDN are enhanced by 35.85% and 69.72%. The increment in C_{12} and C_{66} by 68.21%, and 187.58% and decrement in C_{13} , C_{44} , C_{55} 33.52%, 27.14%, 28.75% are noticed, respectively. This summarizes that HNF and KDN have a slightly larger magnitude than ADN for C_{12} , C_{22} , C_{33} , C_{35} , C_{66} . This study shows that the high coefficient values C_{11} and C_{33} crystallographic axis suggest that HNF and KDN will be less susceptible to shear deformations. Hence, one may conclude that HNF and KDN are mechanically stable at ambient conditions, less sensitive to denotation along C_{22} for HNF, C_{33} direction for KDN and more sensitive towards C_{11} for HNF and KDN in C_{22} direction.

5.3.6 Electronic structure and chemical bonding

In the following section, band structure calculations of HNF, ADN, and KDN are carried out using experimental structure along with high-symmetry directions Figure-5.5. Band structure and density of states of ADN are reported earlier using the PW/PP method implemented in CASTEP with GGA-PBE functional [12]. Nevertheless, another group reported using Vanderbilt-type ultra-soft pseudopotential using LDA functional [54]. Both

LDA (local density approximation) and GGA (generalized gradient approximation) are well known to underestimate the band gap of semiconductors, insulators by 50% due to self-interaction error and also lack the derivative discontinuities [59, 60]. Therefore, we have used TB-mBJ potential to predict accurate band gaps for semiconductors and insulators. The band structure Figure-5.5 obtained with TB-mBJ for ADN is in good agreement with previously reported results [12, 54], and the trend of the energy gap is remarkably similar when compared with KDN. The Fermi level located at 0.0 eV shows ADN having direct and KDN having an indirect bandgap. The energy gap was found to be 2.04 eV (GGA) and 3.01 eV (TB-mBJ) for HNF; 2.7 eV (GGA), 4.1 eV (TBmBJ) for ADN and KDN 3.0 eV (GGA), 4.3 eV (TB-mBJ). For further elucidation of the electronic structure nature, the density of states calculated with mBJ potential is shown in Figure-(5.6,5.7). We should emphasize that there are distinct features in the band structure of HNF, ADN, and KDN. In HNF there are two groups, one is hydrazine N_2H_4 and nitroform $CN(NO_2)_3$. According to PDOS, the highest valence band located at -1 eV to 0 eV is entirely dominated by O-2p states and minimal contribution of N-p states. This indicates that 2p states of oxygen(O) play an important role in the chemical reaction. Then, around -1.1 eV to -3.0 eV it is composed of the O-2p states and H-s states. The lower valence band located below -6 eV, originates from N-p states and C-p states. The contribution of O-2p states and N-p states to the conduction band is quite large, particularly in the energy range from 3 eV, and two N atoms without any contribution near 3 eV belong to hydrazinium group N₂H₅. In the dinitramide molecule, there are three nitrogen atoms (N1, N2, N3 atoms) N1 is bonded to N2 and N3, where N2 and N3 share a bond with oxygen atoms in dinitramide. In ADN, the extra N4 atom shows a different type of contribution than other nitrogen atoms (N1, N2, and N3) due to four hydrogen atoms bonded with it. The valence band region (-5 eV to 0 eV) in ADN and KDN can be partitioned into two regions. The first is from -2.0 to 0 eV, in this region, the main contribution is due to N1-s/p, O-2p states and a minimal of H-s states. The second region is between -3.6 to -2 eV, it is mainly due to O-2p states and N1/N2/N3/N4-p states, while conduction band is composed of O-2p and N2/N3/N4-p states. Similarly, in KDN the first region from -2 eV to 0 eV is due to N1-p, O-2p, and K-p/d states overlap within the atomic states results in hybridization. In the second region, around -3.6 to -2 eV, the main contribution is due to N1-s/p, N2/N3-p, and O-2p states same as ADN (except N4 atom). Moreover, K-d, N2/N3-p, and O-2p states in conduction band of KDN show a dominant nature, N1-p states are not observed in KDN as seen in ADN. Finally, PDOS (partial density of states) of ADN and KDN is almost similar except nitrogen (N4) atom bonded with hydrogen atoms which are not observed in KDN. A mixed ionic-covalent nature between metal atom K and N/O atoms in KDN and a covalent nature in between N atoms and NO_2 in dinitramide of both compounds is observed.

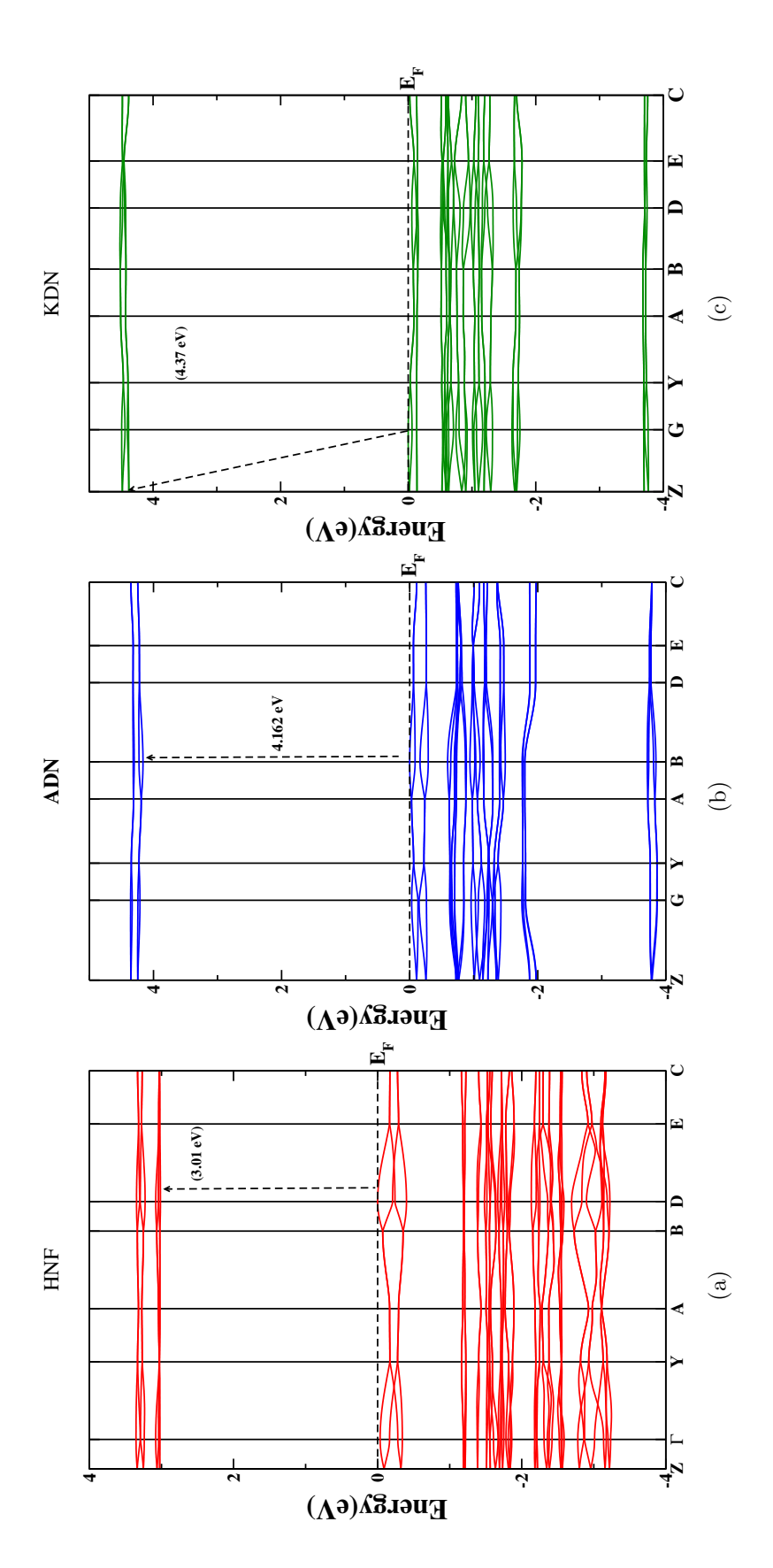


Figure. 5.5 Calculated band gap of (a) Hydrazinium nitroformate (b) Ammonium dinitramide (c) Potassium dinitramide.

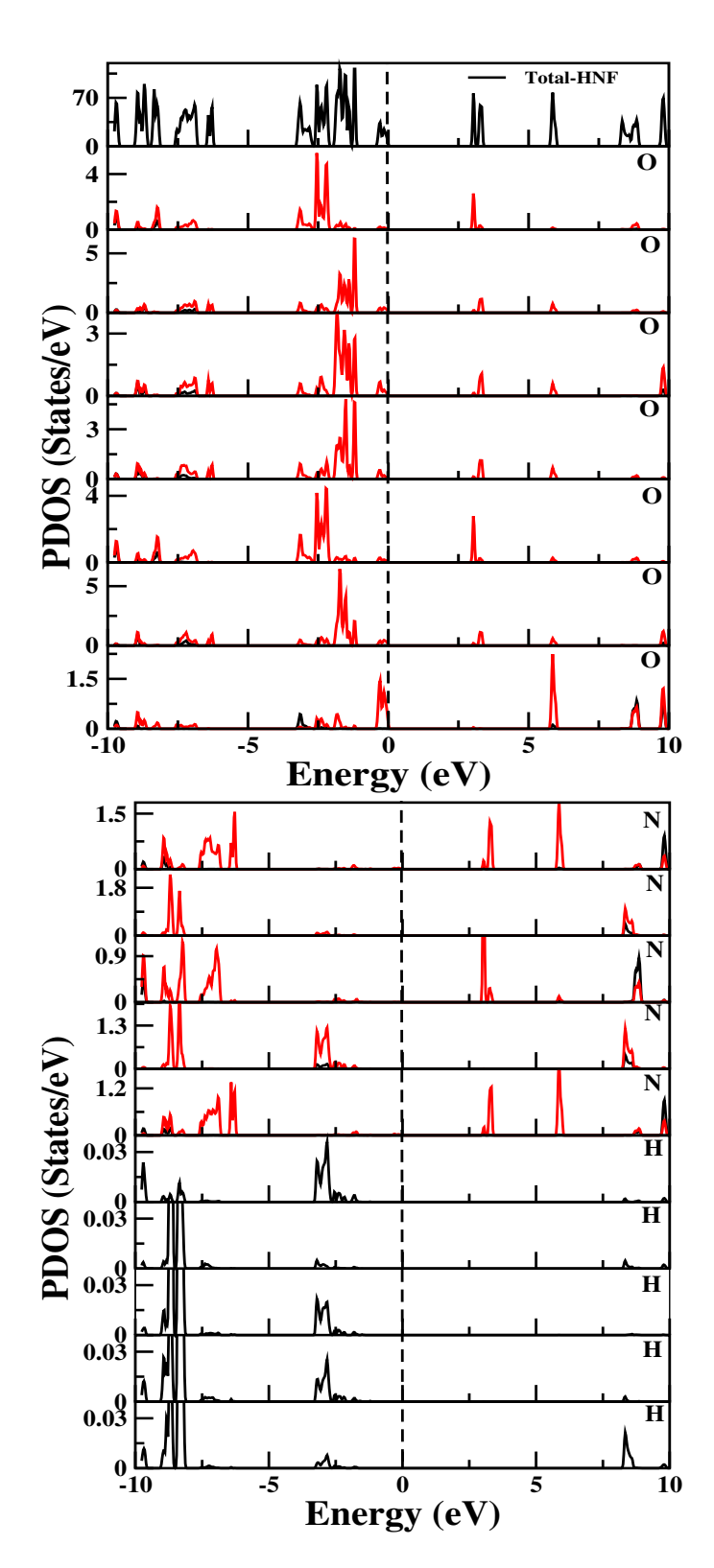


Figure. 5.6 Total and Partial DOS of Hydrazinium nitroformate (HNF).

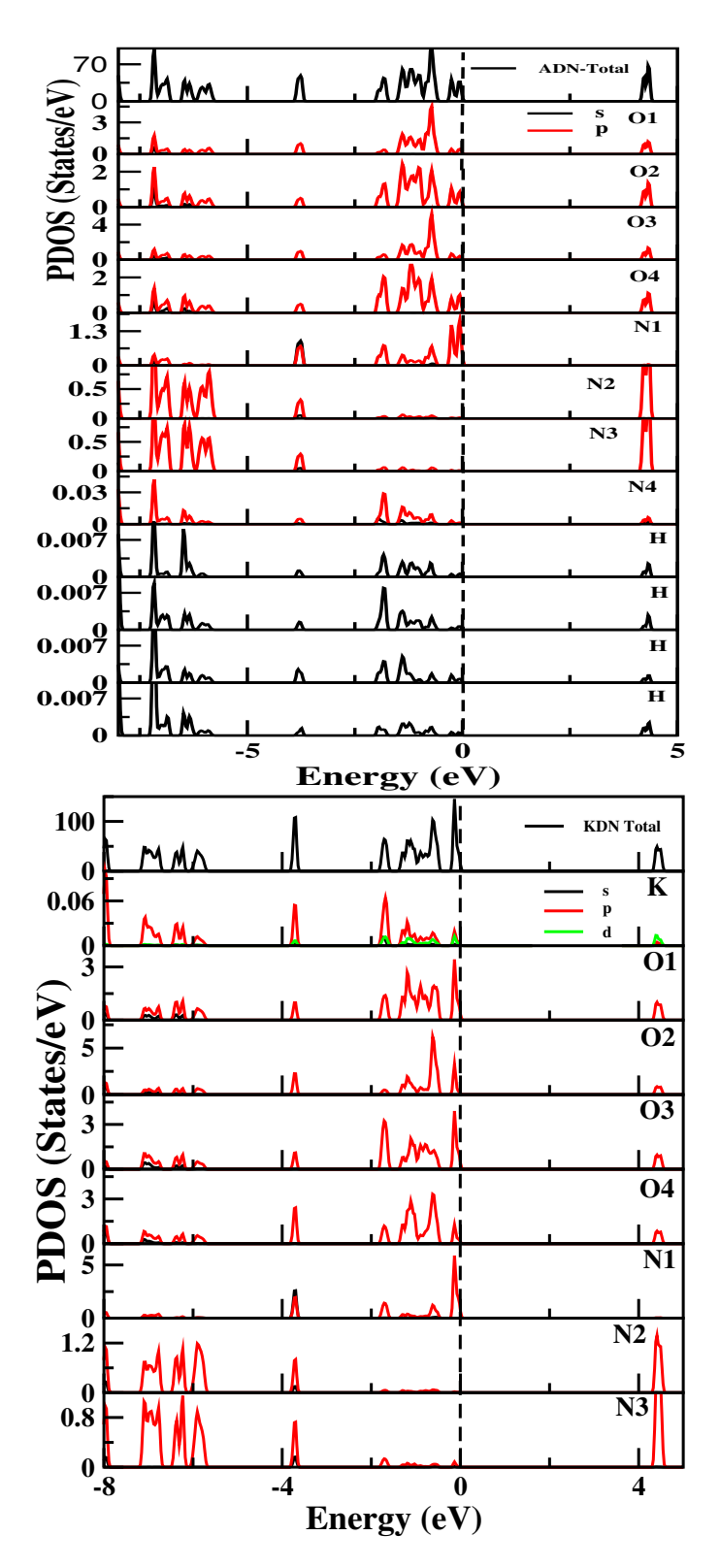


Figure. 5.7 Total and Partial DOS of Ammonium dinitramide (ADN) and Potassium dinitramide (KDN).

5.3.7 Optical properties

Investigation of optical properties for energetic materials is of significant interest in determining the photodecomposition mechanism. It represents the material's response to an external electromagnetic field expressed by the complex dielectric function $\epsilon(\omega)$. The complex dielectric $\epsilon(\omega) = \epsilon_1(\omega) + i\epsilon_2(\omega)$ imaginary part $\epsilon_2(\omega)$ is calculated from electronic structure through joint density of states and momentum matrix elements between occupied and unoccupied eigenstates within the selections rules [61]. In these calculations, excitonic effects are not taken into account. However, the real dielectric part is obtained using Kramer Kronig relation [62] and other optical constants are derived from a complex dielectric function. Figure-(5.8,5.9) shows results on the energy dependence of complex dielectric real and imaginary, absorption, refraction index, reflectivity, and loss function until 10 (eV), respectively. The real quantity describes the polarization of material due to the applied electric field. When photon energy is 0 eV, $\epsilon_1(\omega)$ at zero frequency can be labeled as $\epsilon_1(0)$. The calculated values of $\epsilon_1(0)$ in x,y,z-directions for HNF are 2.84(xx), 2.80(yy), 3.18(zz); ADN are 2.22 (xx), 1.33(yy), 1.99(zz) and for KDN it is 2.38 (xx), 1.40(yy), 1.91(zz) as given in Table-5.8. As photon energy increases, the values of $\epsilon_1(\omega)$ in the optical spectra rapidly rise after the $\epsilon_1(0)$, reaching a maximum 7.06 at 3.17 eV for HNF, 4.66 at about 4.1 eV in ADN and the case of KDN 9.3 at 4.4 eV. The $\epsilon_1(\omega)$ spectra initially decrease, followed by an increase and decrease variations. The imaginary part of the dielectric function curve is closely related to band structure and it can be seen that $\epsilon_2(\omega)$ curves have threshold energy, where transitions are close to band gap values of the compounds 3.1 eV (HNF), 4.1 eV (ADN) and 4.3 eV (KDN). Eventually, the first curve increases rapidly, the sharp peak is located at 3.4 eV, 4.5 eV, and 4 eV due to hybridization. Thus, the most probable transitions from the valence to conduction band in ADN and KDN are due to N-s to O-2p states and H-s to O-2p and N-p states and O-2pstates to N-p states. It is observed from the PDOS figure, that the dielectric peaks in HNF at 3.63 eV(xx), 3.14 eV(yy), 3.14 eV(zz) in the low energy region is because of the direct transition from VB to top of CB bottom. The absorption coefficient $\alpha(\omega)$ presents, where the material begins to absorb the electromagnetic radiations above the threshold limit to interact with electrons. The absorption occurs from 3 eV to 9 eV in HNF, ADN, and KDN, resulting in insulating nature and absorption in the ultraviolet region. Also, the value drops down to zero at about 9 eV in KDN, indicating that this material might become transparent; the same cannot be seen in HNF and ADN. We observe high absorption at two peaks in 001 direction [70.127 at 3.68], [73.182 at 5.42 eV] and three peaks in 100 directions [78.26 at 4.80 eV][57.50 at 6.190 eV][73.11 at 7.49 eV] for HNF, (71.50 at 6.7 eV) 001, (26.194 at 5.34 eV) 100 for ADN, (114.60 at 4.63 eV) 100, (93.23 at 5.59 eV) 001, corresponding to a minimum in the real part of the dielectric function. The calculated $R(\omega)$ and zero frequency R(0) of the compounds are presented. R(0) is found to increase as a result of absorption. Reflectivity starts at 3.5 eV - 4 eV and goes to 8

Table 5.8 Real part of dielectric function $\varepsilon_1(\omega)$ and refractive index $n(\omega)$ of HNF, ADN and KDN.

$\varepsilon_1(\omega)$	$\varepsilon_1^{[xx]}(\omega)$	$\varepsilon_1^{[yy]}(\omega)$	$\varepsilon_1^{[zz]}(\omega)$
HNF	2.84	2.80	3.18
ADN	2.22	1.33	1.99
KDN	2.38	1.40	1.91
$n(\omega)$	$n^{[xx]}(\omega)$	$n^{[yy]}(\omega)$	${\bf n}^{[zz]}(\omega)$
HNF	1.68	1.67	1.78
ADN	1.49	1.15	1.41
KDN	1.54	1.18	1.38

eV, showing that the compounds are highly transparent below 3.5 eV. From absorption and reflectivity, we conclude that ADN and KDN are photosensitive materials that are in accord with the earlier report by Pace [63] and Östmark et al. [27]. The figure shows $n(\omega)$ spectra for ADN and KDN. By comparing $n(\omega)$ spectra characteristics with $\epsilon_1(\omega)$, it is clear that ADN and KDN follow similar trend $\varepsilon_1^{[xx]}(\omega) > \varepsilon_1^{[zz]}(\omega) > \varepsilon_1^{[yy]}(\omega)$, $n^{[xx]}(\omega) > \varepsilon_1^{[xy]}(\omega)$ $n^{[zz]}(\omega) > n^{[yy]}(\omega)$, which means that $\epsilon_1(\omega)$ resembles to the static refraction index n(0). The refractive indices spectrum exhibits an anisotropic behavior in different directions xx, yy, and zz, mentioned in Table-5.8. The calculated static refractive index n(0) of the HNF, ADN, KDN is mentioned in table, as energy (eV) increases, peaks of $n(\omega)$ reach maximum for HNF at 3.25 eV, ADN at 2.22 (4.23 eV), KDN (3.23 (4.44 eV) respectively. Hence, the refractive index is high in between 3 eV - 4 eV and gradually decreases. It can be seen that HFN exhibits a slightly higher refractive index than ADN and KDN. The energy loss function represents, a key factor for the assessment of the usefulness of the fast-moving electron energy of the material. The energy-loss function shows intense maxima due to the excitation of plasmons. It is obvious that the major peaks located in HNF at 1.21 at 3.98 eV, 1.71 at 5.91 eV in xx, ADN at 2.5 at 7.7 eV in zz, 2.1 at 7.5 eV in xx direction, and KDN 4.64 at 7.63 eV xx, 4.54 at 8.38 eV zz in direction indicates strong absorption for UV light. From the above discussions, it is clear that at the maximum peak of the energy loss function, the real part of dielectric function and reflectivity decreases rapidly, which lies in the UV region. From this, we conclude that both ADN and KDN crystals are sensitive toward ultraviolet light.

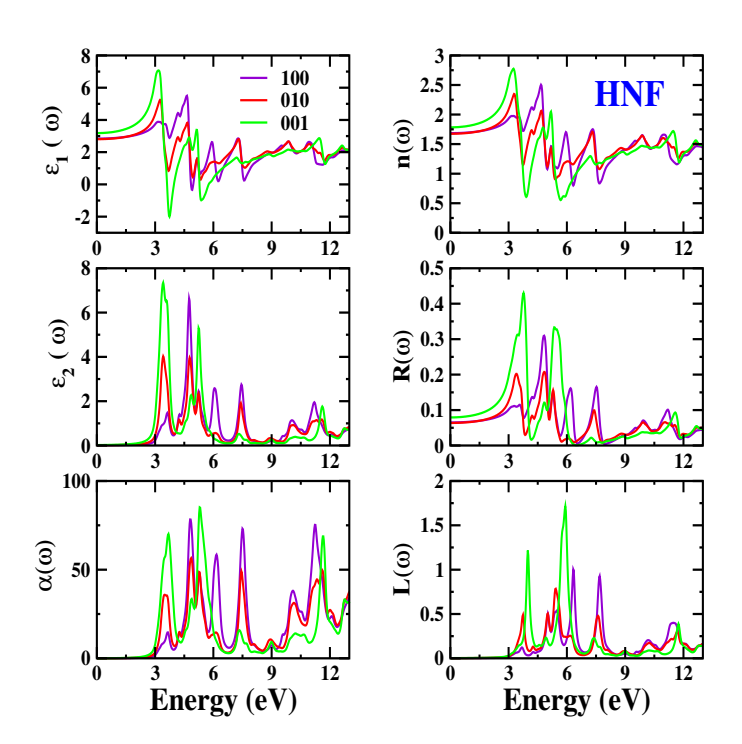


Figure. 5.8 The figure represents Dielectric constant $\epsilon_1(\omega)$, Dielectric loss $\epsilon_2(\omega)$, Absorption $\alpha(\omega)$, Reflectivity R(ω), Refractionn n(ω), Eloss function L(ω) of HNF using TB-mBJ functional at experimental crystal structures.

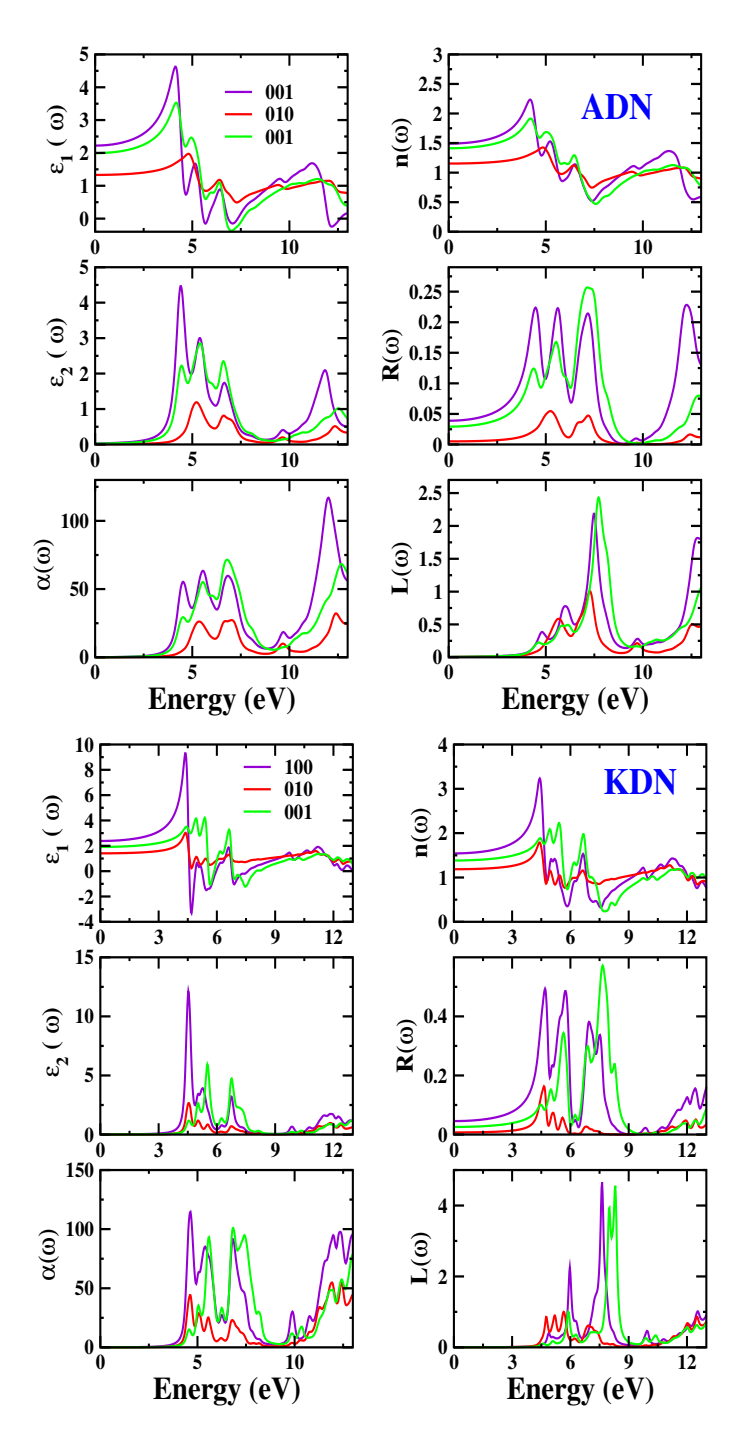


Figure. 5.9 The figure represents Dielectric constant $\epsilon_1(\omega)$, Dielectric loss $\epsilon_2(\omega)$, Absorption $\alpha(\omega)$, Reflectivity R(ω), Refractionn n(ω), Eloss function L(ω) of ADN and KDN using TB-mBJ functional at experimental crystal structures.

5.4 Conclusions

In summary, we have performed a comparative study of HNF, ADN, and KDN. We have investigated several quantities including structural, vibrational, born effective charges, electronic and optical for HNF, ADN, and KDN. In addition, phonon dispersion for ADN and KDN. The study of vibrational frequencies reveals that vibrations in HNF are N-H bond, NH₂ group and in KDN mainly due to NO₂. We have also calculated and presented BEC's and dielectric tensors. From the computed elastic constants we can clearly say that HNF and KDN are mechanically stable materials satisfying the stability criteria. The phonon spectra of ADN and KDN have been investigated for the first time where, both ADN and KDN are found to be dynamically stable. From the phonon density of states, it is clear that the lower atomic mass of H may be expressed as frequencies shift toward higher wave number, and due to K atom high atomic mass, frequencies shifts towards lower wavenumber. In addition, we can conclude that KDN might possess lower thermal conductivity than ADN. The electronic bandgap for HNF, ADN, and KDN has been calculated by TB-mBJ potential using the FP-LAPW method. It is found that HNF, ADN, and KDN are insulators, with O-2p and N-p states contribution mainly in the valency region. Further various optical constants are studied and analyzed.

References

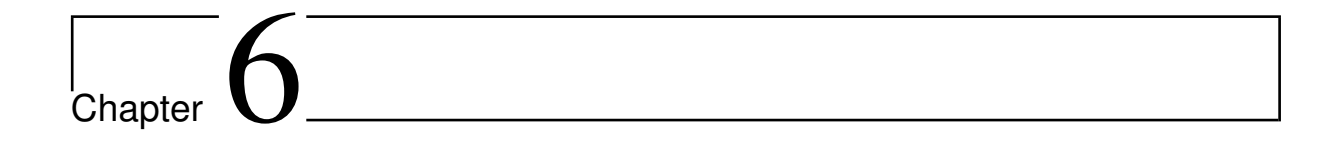
- [1] Pratim. K., An Overview on Properties, Thermal Decomposition, and Combustion Behavior of ADN and ADN based solid propellants, Defence Technology, 2018, 14, 6, 661-673.
- [2] Rahm. M., Brinck. T., On the Anomalous Decomposition and Reactivity of Ammonium and Potassium Dinitramide. J. Phys. Chem. A, 2010, 114, 8, 2845-2854.
- [3] Pratim. K., Advances in Phase Stabilization Techniques of AN using KDN and other Chemical Compounds for Preparing Green Oxidizers, Defence Technology, 2019, 15, 6, 949-957.
- [4] Richard. Gilardi, J. Flippen-Anderson, Clifford George, Ray J. Butcher, J. Am. Chem. Soc., 1997, 119, 40, 9411-9416.
- [5] Chen. B., Jin. B., Peng. R. et al. The Thermal Decomposition of Silver Dinitramide AgN(NO₂)₂,
 J. Therm. Anal. Calorim, 2016, 126, 1491-1498.
- [6] Klapötke. T. M., Krumm. B., Scherr. M., First Structural Characterization of Solvate Free Silver Dinitramide, Ag[N(NO₂)₂], Dalton Trans., 2008, 5876-5878.
- [7] How. Ghee. A., Fraenk. W., Karaghiosoff. K., Klapötke. T. M., Mayer. P., Nöth. H., Sprott. J., Warchhold. M., Zeitschrift für anorganische und allgemeine Chemie, 2002, 628, 2894-2900.
- [8] Kim. W., Kwon. Y., Adelodun. A. A., Jo. Y., Synthesis and Characterization of a New Energy Material: Pyridinium Dinitramide (Py-DN). J Ind Eng Chem, 2017, 43, 411e5.
- [9] Tanbug. R., Kirschbaum. K., Pinkerton. A. A. Energetic materials: The Preparation and Structural Characterization of melaminium Dinitramide and Melaminium Nitrate. Journal of Chemical Crystallography, 1999, 29, 45-55.
- [10] Russell. T. P., Piermarini. G. J., Block. S., Miller. P. J., Pressure, Temperature Reaction Phase Diagram for Ammonium Dinitramide. J. Phys. Chem., 1996, 100, 8, 3248-3251.
- [11] Indu. B. M., Russell. T. P., Thermal Stability of Ammonium Dinitramide, Thermochimica Acta, 2002, 384, 1-2, 47-56.
- [12] Dan. C. Sorescu, Donald. L. T., Classical and Quantum Mechanical Studies of Crystalline Ammonium Nitrate, J. Phys. Chem. A., 2001, 105, 4, 720-733.

- [13] Yedukondalu. N., Vikas D., Vaitheeswaran. G., High pressure structural, elastic and vibrational properties of green energetic oxidizer ammonium dinitramide, J. Chem. Phys., 2016, 145, 064706.
- [14] Jianhua. C., Jinyu, H., Jiange. W., Rui. H., Study on the Crystal Structure and Hygroscopicity of Ammonium Dinitramide, J. Chem. Eng. Data, 2010, 55, 9, 3229-3234.
- [15] Hardie. M., Martin. A., Pinkerton. A., Zhurova. Elizabeth, Anisotropic thermal expansion of potassium dinitramide: A variable-temperature crystallographic study. Acta crystallographica. Section B, Structural science., 2001, 57, 113-8.
- [16] Sorescu. Dan C., Thompson. Donald L., Classical and Quantum Mechanical Studies of Crystalline Ammonium Nitrate J. Phys. Chem. B., 1999, 103, 6774-6782.
- [17] Rahm. M., Tyrode. E., Brinck. T., Johnson. C., The Molecular Surface Structure of Ammonium and Potassium Dinitramide: A Vibrational Sum Frequency Spectroscopy and Quantum Chemical Study. J. Phys. Chem., 2011, 115, 10588-10596.
- [18] Rahm. M., Tore. B., The Anomalous Solid State Decomposition of Ammonium Dinitramide, A Matter of Surface Polarization, Chem. Common., 2009, 2896-2898.
- [19] Rahm. M., KTH, Physical Chemistry, Green Propellants, 43, 2010, 978-91-7415-758-1.
- [20] Yang. R., Thakre. P., Yang. V., Thermal Decomposition and Combustion of Ammonium Dinitramide (Review). Combust Explos Shock Waves 41, 2005, 657-679.
- [21] Kuan. W., Bing, X., Jian-Gang. C., Zhen-Hong. H., Yueping. Ji,c., Bozhou. W., Jian. Lu,c., Zhong-Wen. L., Zhao-Tie. L., New J. Chem., 2020, 44, 6833-6844.
- [22] Bondarchuk. S., Theoretical Evaluation of Hexazinane as a Basic Component of Nitrogen Rich Energetic Onium salts. Mol. Syst. Des. Eng., 2020, 5, 1003-1011.
- [23] Rahm. M., Tore. B., Kinetic Stability and Propellant Performance of Green Energetic Materials. Chem. Eur. J., 2010, 16, 6590-6600.
- [24] Yedukondalu. N., Vaitheewaran. G., Polymorphism, Phase Transition, and Lattice Dynamics of Energetic Oxidizer Ammonium Perchlorate under High Pressure, J. Phys. Chem. C., 2019, 123, 4, 2114-2126.
- [25] Valery. P. Sinditskii, Viacheslav. Y. E., Anton I. L., and Valery V. S., J. Propuls. Power, Combustion of Ammonium Dinitramide, Part 2: Combustion Mechanism., 2006, 22, 4, 769-776.
- [26] Valery. P. S., Anton. N. C., Daniil. S. S., Viacheslav. Yu. E., Sergey. A. F., Alexey. A. M., Yuriy. M. M., Combustion of potassium dinitramide and its binary mixtures with nitroester binder, Combustion and Flame, 2016, 172, 206-214.
- [27] H. Östmark, Bemm, U., Langlet, A., R. Sandén. N. Wingborg, The Properties of Ammonium Dinitramide (ADN): Part 1, Basic Properties and Spectroscopic data, J Energ. Mater., 2000, 18:2-3, 123-138

- [28] Pratim. K., Puran. C. J., Rajiv K., Thermal Decomposition and Combustion Studies of Catalyzed AN/KDN Based Solid Propellants, Combustion and Flame, 2016, 166, 316-332.
- [29] Chan. M. L., R. Reed Jr., Ciaramitaro, D.A., Advances in Solid Propellant Formulations, Chapter 1.7, Progress in Astronautics and Aeronautics Solid Propellant Chemistry, Combustion, and Motor Interior Ballistics, 2000, 185-206.
- [30] Pavlov. A. N., Grebennikov, V., Nazina, L., Nazin, G., Manelis, G., Thermal decomposition of ammonium dinitramide and mechanism of anomalous decay of dinitramide salts, Russ. Chem. Bull., 1999, 48, 50-54.
- [31] Lei. M., Liu. Z., Kong. Y., Liu. C., Wang. B., Wang. Y., Zhang. P., The Thermal Stability of Potassium Dinitramide. Part 2. Mechaanism of thermal decomposition, Thermochim. Acta., 1999, 335, 113-120.
- [32] Lei. M., Zhang. Z., Kong. Y., Liu. Z., Zhu. C., Shao. Y., Zhang. P., The Thermal Stability of Potassium Dinitramide. Part 1. Thermal Stability., Thermochim. Acta., 1999, 335, 105-112.
- [33] Yin. C., Liu, Z., Kong, Y., Zhao, F., Wang, Y., Lei, M., Luo, Y., Zhang, P., Shao, S. li S., Thermal Decomposition of Potassium Dinitramide at Elevated Pressure. Chapter 2.7. In: Progress in Astronautics and Aeronautics: solid propellant chemistry, combustion, and motor inte- rior ballistics, 2000, 425e37.
- [34] Segall. M. D., Lindon. P.J.D., Probert. M. J., Pickard .C. J., Hasnip. P. J., Clark. S. J., Payne. M. C. Phys. Condens Mat., 2002, 14, 2717-2744.
- [35] Troullier. N., Martins. J. L., Efficient pseudopotentials for plane-wave calculations, Phys. Rev. B., 1993, 43, 1993-2006.
- [36] Monkhorst. H. J., Pack. J. D., Special points for Brillouin-zone integrations Phys. Rev. B., 1976, 13, 5188-5192.
- [37] Fischer .T. H., Almlof. J., J. General methods for geometry and wave function optimization, Phys. Chem., 1992, 96, 9768-9774.
- [38] Ceperley. D. M., Alder. B. J., Ground State of the Electron Gas by a Stochastic Method, Phys. Rev. Lett., 1980, 45, 566-569.
- [39] Perdew.J. P., Zunger.A., Self-interaction correction to density-functional approximations for many-electron systems, Phys. Rev. B., 1981, 23, 5048-5079.
- [40] Perdew. J. P., S. Burke, Generalized Gradient Approximation Made Simple, M. Ernzerhof, Phys. Rev. Lett., 1996, 77, 3865-3868.
- [41] Perdew. J. P., Wang, Y., Accurate and simple analytic representation of the electron-gas correlation energy, Phys. Rev. B., 1992, 45, 13244-13249.
- [42] Tkatchenko. A., Scheffler.M., Accurate Molecular Van Der Waals Interactions from Ground-State Electron Density and Free-Atom Reference Data, Phys. Rev. Lett., 2009, 102, 073005.
- [43] Grimme. S., Semiempirical GGA-type density functional constructed with a long-range disper-

- sion correction, J. Comput. Chem., 2006, 27, 1787-1799.
- [44] Ortmann. F., Bechstedt. F., Schmidt. W. G., Semiempirical van der Waals correction to the density functional description of solids and molecular structures, Phys. Rev. B., 2006, 73, 205101.
- [45] Baroni. S., de Gironcoli, S., Dal. Corso, A., Giannozzi.P., Phonons and related crystal properties from density-functional perturbation theory, Rev. Mod. Phys., 2001, 73, 515-562.
- [46] Blaha. P., Schwarz, K., Madsen.G. K. H., Kvasnicka.D., Luitz,J., 2001 WIEN2K, an Augmented Plane Wave + LocalOrbitals Program for Calculating Crystal Properties (Austria: Techn. Universitat)
- [47] Singh..D. J., Electronic structure calculations with the Tran-Blaha modified Becke-Johnson density functional, Phys. Rev., B., 2010, 82, 205102.
- [48] Kresse. G., Furthmuller, Efficiency of ab-initio total energy calculations for metals and semi-conductors using a plane-wave basis set, J., Comput. Mater. Sci., 1996, 6, 15.
- [49] Kresse. G., Furthmuller, Efficient iterative schemes for ab initio total-energy calculations using a plane-wave basis set, J., Phys. Rev. B., 1996, 54, 11169-11186.
- [50] Kresse. G., Joubert.D., From ultrasoft pseudopotentials to the projector augmented-wave method, Phys. Rev. B., 1999, 59, 1758-1775.
- [51] Togo. A., Tanaka.I., First Principles Phonon Calculations in Materials Science., Scr. Mater., 2015, 108, 1-5.
- [52] Politzer. Seminario, P., Concha. J. M., Redgern. P. C., J.Mol. Struct., THEOCHEM, 1993, 287, 235-36.
 (b) Michels, H. H., Montgomery, J. A. Jr., J. Phys. Chem., 1993, 97, 6602.
 (c) Mebel, A. M., Lin, M. C., Morokuma, K., Melius, C. F., J. Phys. Chem., 1995, 99, 6842.
- [53] Goofit. T., Maksimowski. P., Biernacki, A., Optimization of Potassium Dinitramide Preparation., Propellants Explos. Pyrotech., 2013 38, 261-265.
- [54] Zhu. W., Wei, T., Zhu. W., Xiao. H., Comparative DFT Study of Crystalline Ammonium Perchlorate and Ammonium Dinitramide. Am. J. Phys. Chem., 2008, 112, 4688-4693.
- [55] Karl. O. C., William. W. W., Mark. A. P., Harvey. H. M., Jeffrey, C. B., Richard G., Inorg. Chem., 1996, 35, 17, 5068-5071.
- [56] Badgujar. D. M., Bulakh. N.R., Wagh, R.M., Btalawar. M., Synthesis, characterization and purity determination of ammonium dinitramide (ADN) and its precursors., Sci. Tech. Energetic. Materials., 2016, 77, 59-64.
- [57] King-Smith. R. D., David. V., Phys. Rev. B.,1993, 47, 1651. (a) Gonze, X., Allan, D. C., Teter, M.
 P., Phys. Rev. Lett., 1992, 68, 3603 (b) Resta, R., Europhys. Lett., 1993, 22, 133.
- [58] Pulham. C. R., Davidson.A. J., Oswald.I. D. H., Millar. D. I. A., Fabbiani. F. P. A., Francis,.. J., Marshall.W. G., Cumming.A. S., Allan.D. R., Lenniee. A. R., Prior, T. J., in 24th European Crystallographic Meeting, ECM24, Marrakech, Acta Cryst., Sect. A, 2007, 63, s44.
- [59] Perdew. J. P., Parr, R. G., Levy. M., J. L. Balduz, Density-Functional Theory for Fractional

- Particle Number: Derivative Discontinuities of the Energy, Phys. Rev.Lett., 1982, 49, 1691-1694.
- [60] Schlüter. M., Sham, L. J., Density-Functional Theory of the Band Gap, Editor(s): Per-Olov Löwdin, Advances in Quantum Chemistry, Academic Press, 1990, 21, 97-112, 0065-3276.
- [61] Ambrosch. C. D., Sofo, J.O., Linear Optical Properties of Solids within the Full Potential Linearized Augmented Planewave Method, Comput. Phys.Commun., 2006, 175, 1, 114.
- [62] Toll.J. S., Causality and the Dispersion Relation Logical Foundations, Phys. Rev., 1956, 104, 1760-1770.
- [63] M. D. Pace, Spin Trapping of Nitrogen Dioxide from Photolysis of Sodium Nitrite, Ammonium Nitrate, Ammonium Dinitramide, and Cyclic Nitramines, J. Phys. Chem., 1994, 98, 25, 6251-6257



Potential Replacement of Lead Azide: DBX-1 $(C_2Cu_2N_{10}O_4)$

Abstract

In the present work plane-wave, pseudopotential method (PW/PP) is used to calculate structural, vibrational, elastic, born effective charges and full-potential linearized augmented plane-wave (FP-LAPW) method for calculating electronic structure and optical properties of DBX-1. The optimized structural parameters, volume are in good agreement with the reported experimental data. The high-frequency optical modes are due to symmetric and asymmetric stretching of the NO₂ group. Mechanically stability at ambient conditions is addressed through elastic properties. In addition, we have calculated electronic band structure and optical constants employing TB-mBJ potential. The fundamental energy bandgap appears to be indirect around 1.08 eV. To explicate the contribution of anion and cation states, the partial and total density of states for DBX-1 has been discussed. The valence band and conduction band in DBX-1 is dominated by Cu-p/d states, O-2p and N-p state. Using electronic structure results, we discuss directional independent optical properties such as the real and imaginary parts of the dielectric function, refractive index, reflection, absorption coefficient, and energy loss spectra.

Prathap kumar Jharapla, G. Vaitheeswaran, To be communicated

6.1 Introduction

Primary explosives (PE) are substances that exhibit an extreme swift transition from combustion to an explosion (fast deflagration to detonation transition, DDT). They are also considerably more sensitive towards the flame, friction, electrostatic, or electrostatic friction than secondary explosives. The less sensitive secondary explosive is ignited by the detonation transfer from the shock wave produced by the primary explosive. Primary explosives are mainly used as blasting caps, secondary booster charges, primers, propellants initiators in detonators. Research towards finding a proper replacement of primary explosive lead azide (LA) has grabbed attention recently. The inorganic lead azide (LA) is undoubtedly one of the most well-known effective primary explosives in the last 90 years. LA has been commonly accepted as a primary explosive, and it was substituted by mercury fulminate (MF) in the early 20th century because of its high toxicity [1]. Furthermore, the reaction of azide anions in LA with moisture in the presence of carbon dioxide generates hydrazoic acid, making LA toxic and harmful to the environment. While a large variety of modern materials have been synthesized and considered as replacements of lead azide which includes silver azide, [2-4], copper chlorotetrazolate [5] calcium nitriminotetrazolate [6], copper(II) coordination complexes of the 5-nitrotetrazolate anion [7] and diazodinitrophenol (DDNP) [8–10], all of them have constraints preventing their extensive use. In this context, a detailed search was initiated to find a possible potential replacement meeting the minimum requirement. DBX-1 (copper(I) 5-nitrotetrazolate) exhibits exceptional explosive output when compared to LA, due to which it is known as a volumetric drop-in green replacement candidate for LA [11-14]. Although DBX-1 $(C_2Cu_2N_{10}O_4)$ is not studied extensively due to its sensitivity and complexity, but a series of experimental papers have been published in the last few years on various properties such as characterization, kinetic measurements, critical temperature, thermal analysis, compatibility test, and sensitivity [14–16]. DBX-1 is synthesized using sodium 5-nitrotetrazolate (NaNT), which is not available commercially. It must be synthesized from 5-aminotetrazole (5-At) [17] while tetrazolate is a novel energetic material with high nitrogen content but with low carbon contents. DBX-1 decomposes in the presence of copper components, unlike LA, which decomposes in non-hermetic systems (anything made with polymeric materials including). DBX-1 has tended to decompose with periodate salts, hence inhibiting its explosive activity [18]. Moreover, when compared to LA, DBX-1 is more compatible with secondary explosives and other ordnance materials [14]. Therefore, DBX-1 has desirable properties making it a promising candidate for industrial and military applications. This paper reports the ground state properties of DBX-1 calculated using first-principle calculations. Initially, we have carried out geometry optimization, executing iterative operations in which the atomic coordinates and structural parameters are altered so that the total enthalpy of the structure is reduced. Then, using the optimized structure, we have calculated structural properties, zone center vibrational properties, born effective charges (BEC's), and mechanical properties. Additionally, we addressed the electronic structure and dielectric function, absorption coefficient, refractive index, reflectivity, and frequency-dependent loss function. These results give a detailed explanation of the physical and chemical properties of DBX-1. The motivation of this work is to provide some additional information regarding DBX-1 using ab initio DFT calculations. Organization of paper goes as introduction regarding the material following with the theoretical parameters calculations used to obtain structural, vibrational, elastic, electronic and optical properties results and finally conclusions.

6.2 Computational details

In this work, we have employed (PW-PP) the plane-wave pseudopotential (PW-PP) method implemented in the Cambridge Series of the Total Energy Package (CASTEP) [19–21] to calculate, zone center vibrational, elastic properties and born effective charges and dielectric tensor. We use the generalized gradient approximation (GGA) [22] proposed by Perdew-Burke-Ernzerhof (PBE) for the treatment electron exchange and correlation interactions, the interactions within ionic core and valence electrons were defined by the ultrasoft pseudopotential (US) and Norm-conserving pseudopotential (NC). The total energy of the system is obtained using the conjugate gradient technique pertaining to the plane wave's coefficient. Using periodic boundary conditions and Bloch's theorem, structural, elastic properties are calculated using US pseudopotential with plane wave cut-off energy of 500 eV and vibrational properties, born effective charges were computed using NC pseudopotential with cutoff 950 eV. A Monkhorst pack grid of $(3\times3\times4)$ was used. Geometry optimization is done to relax the electronic wave functions using the Broyden-Fletcher-Goldfarb-Shanno method (BFGS) [23]. The maximum tolerances forces for energy, stress, the maximum displacement and maximum force between atoms were set as $5.0 \times e^{-6}$ (eV per atom), 0.02 GPa, 5.0×10^{-4} Å, 0.01 eV/A, respectively. Initially, crystal parameters are optimized using different exchange-correlation potential LDA [24, 25], GGA-PBE [22] and GGA-PW91 (Perdew-Wang 91) [26]. Then, to correct the DFT missing dispersive interaction, van der Waals dispersion correction methods (TS) Tkatchenko-Scheffler [27] and (G06) Grimme [28] to PBE, (OBS) Ortmann-Bechstedt-Schmidt [29] to GGA-PW91 has been included. The zone center vibrational property and BEC's calculations are performed within the (DFPT) density functional perturbation theory [30] with the inclusion of van der Waals correction. Electronic and optical properties are calculated using the full-potential linearized augmented plane wave method (FP-LAPW) implemented in the WIEN2k [31]. Initially, standard generalized gradient approximation(GGA) [22] is adopted for the treatment of exchange-correlation effects. Knowing that GGA-PBE underestimates the bandgap, we employed TB-mBJ [32] potential in combination with PBE to calculate the accurate bandgap. To separate core

states from valence states, an energy threshold of -6 Ryd is used. The cut-off energy for plane wave expansion of wave functions in the interstitial region is restricted to be $k_{max} = 7/R_{MT} \ (a.u)^{-1}$ for DBX-1, where RMT is the smallest atomic sphere radii of the muffin tin. The muffin-tin radii used in the calculations for DBX-1 N-1.11 a.u, C-1.21 a.u, O-1.71 a.u, Cu-1.99 a.u. The largest k vector plane in the plane-wave expansion is limited to be Gmax = 14 in DBX-1. To compute the electronic band structure we have used 500 kpoints, and for partial density of states and optical properties, much denser k-mesh with 5000 kpoints has been used.

6.3 Results and discussion

6.3.1 Crystal structure

DBX-1 possess the monoclinic crystal structure with space group $P2_1/c$, Z=4 formula units [14] Figure-6.1. Initially, input parameters of un-relaxed atomic positions, lattice constants, volume are considered for geometry optimization. To ensure the parameters used in the calculations are accurate, optimized lattice parameters and the corresponding volume with an error percentage of the unit cell, along with available experimental data are reported in Table-6.1. In this process, different exchange-correlation potentials are used such as LDA, PBE, PW91. These standard potentials resulted in a large deviation from experimental lattice parameters and volume which lead to investigating the effect of van der Waals interaction using semi-empirical dispersion DFT-D correction i.e. LDA + OBS, GGA + G06, GGA + TS, and PW91 + OBS. There is a noticeable difference in the error percentage of exchange-correlation potential and the DFT-D method mentioned in Table-6.1. So, the studied lattice parameters lead to much better structures with semi-empirical dispersion correction. The structural parameters obtained using PW91+OBS, GGA+TS in DBX-1 show good agreement with experimental values. Hence all the calculations performed for DBX-1 are by GGA+PW91. The experimental data were measured at room temperature, whereas the calculated results are simulated at 0 K due to which lattice parameters are slightly different from the experimental values. These small deviations from the experimental values confirm the reliability of DFT-based calculations.

6.3.2 Vibrational properties

With the optimized structure, we investigate the vibrational properties of monoclinic crystal DBX-1 within the framework of DFPT [30]. Phonon modes at the gamma point have been analyzed using group theory, according to irreducible representations DBX-1 has 216 phonon branches obtained from 72 atoms in the conventional cell. The group theory analysis gives the following zone center modes $\Gamma_{acoustic} = A_u \oplus 2B_u$, $\Gamma_{optic} = 54A_g \oplus 53A_u \oplus 54B_g \oplus 52B_u$, which contain Raman modes $(54A_g \oplus 54B_g)$ active modes and IR active modes $(53A_u \oplus 52B_u)$. The phonon frequencies obtained are due to intramolecular interactions and the lattice modes due to intermolecular interactions. To describe intermolecular interaction, we have considered GGA + PW91 approximation for

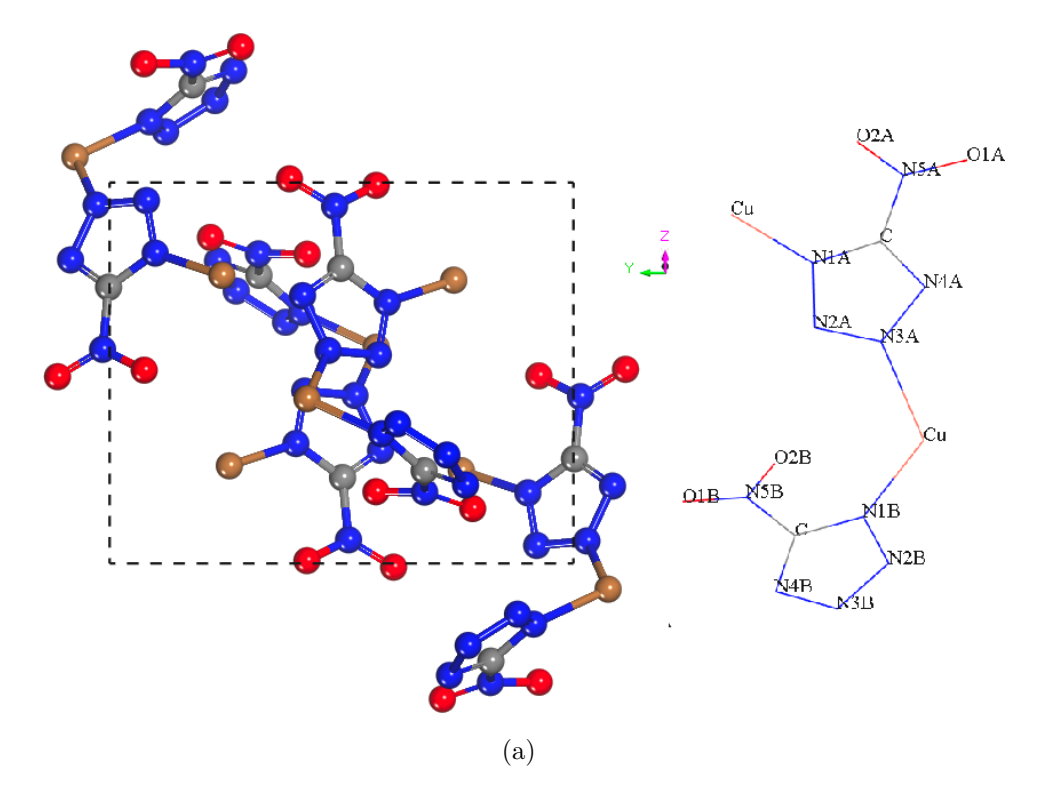


Figure. 6.1 Crystal structure of DBX-1 (Copper(I) 5-nitrotetrazolate).

 $\begin{tabular}{ll} \textbf{Table 6.1} & Calculated lattice parameters (a, b, c in Å) and Volume (V in ų) of DBX-1 \\ using standard LDA (CA-PZ), GGA (PBE) and semiempirical schemes LDA+OBS, \\ PBE+G06, PW91+OBS with the experiment data. \\ \end{tabular}$

Funtionals	a (Å)	b (Å)	c (Å)	$V (Å^3)$
LDA	10.19	9.92	9.10	833.49(-8.7%)
LDA+OBS	10.04	10.05	8.80	803.75 (-11.96%)
PBE	10.69	10.07	9.96	960.20(5.14%)
PBE+G06	10.49	10.12	9.43	902.15(-1.2%)
PBE+TS	10.48	10.19	9.49	910.33(-0.29%)
PW91	10.65	10.06	9.94	956.58(4.54%)
PW91+OBS	10.54	10.11	9.65	921.48(0.9%)
Experiment b	10.51	10.28	7.918	913.0

DBX-1. As per our knowledge, we are not aware of any theoretical and experimental reports in the literature to compare. The IR spectra of DBX-1 are presented in Figure-6.2. The calculated IR frequencies (cm⁻¹) and the vibrational assignments are listed in Table-(6.2,6.3,6.4). We report vibrational frequencies that starts from 42.23 cm⁻¹ to 1500 cm⁻¹ for DBX-1. The same is divided into three sections, that is low frequency (<400 cm⁻¹), mid-frequency (400 cm⁻¹ to 850 cm⁻¹) and high frequency region (950 cm⁻¹ to 1500 cm⁻¹). There are 18 peaks visible in the low-frequency region, related to the translation of the Cu atom with translation, rotation, and liberation in 5-Nt. The liberation is mainly caused by N-C, N-C-N bonds in tetrazole. Furthermore, the mid-frequency region shows mainly ten peaks, due to the NO₂ scissoring, rocking, liberation, and stretching in 5-Nt. Finally, the high energy region consists of 13 peaks which represent symmetric and asymmetric stretch of NO₂ group and N-C and N-N stretching. This result concludes that the NO₂ group performs a notable role in the decomposition of DBX-1. Overall, the NO₂ group in DBX-1 plays a vital part in the stability and decomposition of DBX-1.

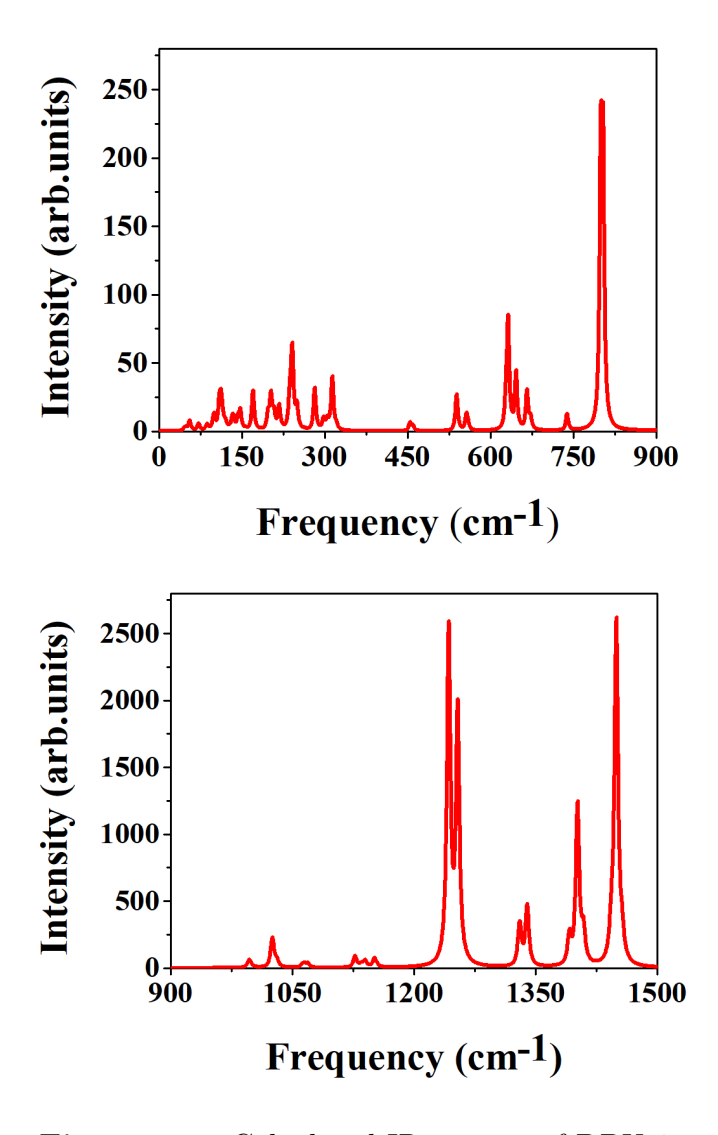


Figure. 6.2 Calculated IR spectra of DBX-1.

Mode	Symmetry	IR	Raman active	Assignment of modes	Mode	Symmetry	${ m IR}$	Raman active	Assignment of modes
42.23	Bg	Z	Y	NO_2 Trans.	116.13	Ag	Z	Y	NO ₂ Rotat.
43.26	Ag	Z	Y	NO_2 Trans.	116.21	Bu	\prec	Z	NO_2 Rotat.
47.01	Au	Χ	Z	NO_2 Trans.	117.75	Ag	Z	Y	NO_2 Rotat.
49.67	Au	Χ	Z	5- Nt Trans.	120.52	Au	\prec	Z	NO_2 Rotat.
52.24	Ag	Z	Y	NO_2 Rotat.	128.05	Au	\prec	Z	NO_2 Rotat.
55.22	Au	\prec	Z	NO_2 Rotat.	131.06	Bg	Z	⋆	5-Nt Trans., Cu Trans.
55.97	Bg	Z	Y	NO_2 Rotat.	133.48	Bu	\prec	Z	5-Nt Trans., Cu Trans.
59.03	Bu	Τ	Z	NO_2 Trans.	135.16	Au	Χ	Z	NO_2 Rotat.
64.56	Bu	\prec	Z	NO_2 Trans.	142.37	Ag	Z	Y	5-Nt Rotat., Cu Trans.
69.71	Au	\times	Z	5- Nt Trans.	143.15	Bu	\prec	Z	5-Nt Rotat., Cu Trans.
70.30	Ag	Z	Y	NO_2 Rotat.	144.84	Bg	Z	X	5-Nt Rotat., Cu Trans.
72.48	Au	\times	Z	NO_2 Trans.	147.24	Bu	\prec	Z	, Cu Trans.
73.30	Bu	Χ	Z	NO_2 Trans.	148.64	Bg	Z	Y	5-Nt Rotat., Cu Trans.
73.47	Bg	Z	Y	NO_2 Trans.	152.13	Ag	Z	Y	5-Nt Rotat., Cu Trans.
76.49	$^{\mathrm{Ag}}$	Z	Y	NO_2 Rotat.	153.98	Au	\prec	Z	5-Nt Trans., Cu Trans.
78.19	$_{\mathrm{Bg}}$	Z	Y	NO_2 Rotat.	157.90	Bg	Z	Y	5-Nt Rotat., Cu Trans.
83.03	Bu	\prec	Z	NO_2 Rotat.	158.64	Bu	\prec	Z	5-Nt Trans.
86.11	$_{\mathrm{Bg}}$	Z	Y	NO_2 Rotat.	162.90	$_{ m Bg}$	Z	Y	Cu Trans.
86.39	Ag	Z	Y	NO ₂ Rotat., Cu Trans.	169.81	Au	\prec	Z	5-Nt Trans., Cu Trans.
87.05	Au	\prec	Z	NO ₂ Rotat., Cu Trans.	170.99	Bu	\prec	Z	Tetrazole Librat.
88.28	Bu	\prec	Z	NO_2 Trans.	171.83	$_{ m Bg}$	Z	Y	Tetrazole Librat.
89.65	Ag	Z	Y	NO_2 Trans	171.94	Ag	Z	Y	Cu, Tetrazole Trans.
91.12	Ag	Z	Y	NO ₂ Trans., Cu Trans.	171.94	$^{\mathrm{Ag}}$	Z	Y	Cu, Tetrazole Trans.
96.33	Au	Χ	Z	5-Nt Trans., Cu Trans.	183.36	Bg	Z	Y	Tetrazole Librat.
97.14	$_{\mathrm{Bg}}$	Z	Y	5-Nt Rotat., Cu Trans.	195.04	Au	\prec	Z	Tetrazole Rotat., Cu-N Stretch.
98.07	Ag	Z	Y	5-Nt Rotat., Cu Trans.	196.69	Bg	Z	Y	Tetrazole Librat.
100.24	$_{\mathrm{Bg}}$	Z	Y	NO_2 Trans.	196.97	$^{\mathrm{Ag}}$	Z	Y	Tetrazole Librat., Cu-N Stretch
100.29	Au	Χ	Z	NO_2 Trans.	197.90	Bu	\prec	Z	Tetrazole Librat.
105.23	Bg	Z	Y	NO ₂ Trans., Cu Trans.	203.10	Bu	\prec	N	Tetrazole Librat., Cu-N Stretch.
106.22	Ag	Z	Y	NO ₂ Rotat., Cu Trans.	208.23	Au	\prec	Z	Tetrazole Librat.
109.91	Bu	\prec	Z	NO ₂ Rotat., Cu Trans.	212.04	$^{ m Ag}$	Z	Y	Tetrazole Librat.
112.04	Ag	Z	Y	NO ₂ Rotat., Cu Trans.	213.15	$_{ m Bg}$	Z	Y	5-Nt Rotat., Cu Trans.
112.09	Bu	\prec	Z	5-Nt Trans., Cu Trans.	217.32	Bu	\prec	Z	5-Nt Rotat., Cu-N Stretch.
113.21	Au	\prec	Z	NO_2 Rotat.	219.66	Au	\prec	Z	Tetrazole Librat.
11.400	1	;							

Table 6.3 Calculated vibrational frequencies (in cm $^{-1}$) for DBX-1 (233 cm $^{-1}$ to 1253 cm $^{-1}$).

Mode	Symmetry	H	Raman active	Assignment of modes	Mode	Symmetry	IK	Raman active	Assignment of modes
233.15	$_{ m Bg}$	Z	Y	Tetrazole Librat.	1000.92	Bg	Z	Y	N-N-N Sciss., N-N Stretch.
236.70	Au	Υ	Z	Tetrazole Librat.	1004.17	Bu	Χ	Z	N-N-N Sciss., N-N Stretch.
238.61	Bg	Z	Y	Tetrazole Librat.	1025.56	Bu	X	Z	N-N Stretch.
238.77	Ag	Z	Y	Tetrazole Librat.	1027.20	Bg	Z	Y	N-N Stretch.
239.16	Bu	Υ	Z	Tetrazole Librat.	1028.74	Ag	Z	Y	N-N Stretch.
241.71	Bu	Υ	Z	Tetrazole Librat.	1030.13	Au	Χ	Z	N-N Stretch.
244.88	Au	X	Z	Tetrazole Librat.	1031.22	Bu	X	Z	N-N Stretch.
246.32	Ag	Z	Y	Tetrazole Librat.	1031.98	Bg	Z	Y	N-N-N Sciss., N-N Stretch.
249.94	Bu	Υ	Z	Tetrazole Librat.	1033.99	Au	Υ	Z	N-N-N Sciss., N-N Stretch.
256.72	Bg	Z	Y	5-Nt Rotat.	1039.50	Ag	Z	Y	N-N-N Sciss., N-N Stretch.
262.81	Au	Υ	Z	5-Nt Rotat., Cu Trans.	1059.32	Bg	Z	Y	N-N-N Sciss., N-N Stretch.
272.11	Ag	Z	Y	5-Nt Rotat., Cu Trans.	1061.85	Bu	X	Z	N-N-N Sciss., N-N Stretch.
282.12	Bu	Υ	Z	5-Nt Trans, Cu Trans.	1063.45	Ag	Z	Y	N-N-N Sciss., N-N Stretch.
282.19	Bg	Z	Y	5-Nt Trans, Cu Trans.	1064.79	Bu	Υ	Z	N-N-N Sciss.
297.75	Bg	Z	Y	5-Nt Trans	1066.17	Bg	Z	Y	N-N-N Sciss.
297.79	Bu	Υ	Z	5-Nt Trans	1066.91	Au	Υ	Z	N-N-N Sciss., N-N Stretch.
303.38	Ag	Z	Y	5-Nt Rotat.	1069.04	Au	Χ	Z	N-N-N Sciss., N-N Stretch.
304.11	Au	X	Z	5-Nt Rotat., Cu Trans.	1070.03	Ag	Z	Y	N-N Stretch.
308.42	Ag	Z	Y	Tetrazole Trans., NO ₂ Rotat.	1127.31	Bu	X	Z	N-N Stretch.
308.59	Au	Y	Z	Tetrazole Trans., NO_2 Rotat	1127.54	Au	Υ	Z	N-N Stretch.
311.58	Bg	Z	Y	5-Nt Rotat.	1128.03	Bg	Z	Y	N-N Stretch.
314.10	Bu	Y	Z	5-Nt Rotat.	1128.5	Ag	Z	Y	N-N Stretch.
314.35	Ag	Z	Y	5-Nt Rotat.	1134.23	Ag	Z	Y	N-N Stretch.
321.22	Au	Υ	Z	5-Nt Rotat.	1134.42	Au	\times	Z	N-N, N-C Stretch.
453.78	Bu	Υ	Z	NO ₂ Rock., Tetrazole Trans.	1134.70	Bu	Χ	Z	N-N, N-C Stretch.
454.40	Au	X	Z	NO ₂ Rock., Tetrazole Trans.	1134.85	Bg	Z	Y	N-N, N-C Stretch.
454.60	Ag	Z	Y	NO ₂ Rock., Tetrazole Trans.	1139.40	Bu	X	Z	N-N-N Stretch.
458.09	Bg	Z	Y	NO ₂ Rock., Tetrazole Trans.	1139.73	Ag	Z	Y	N-N-N Stretch.
458.12	Ag	Z	Y	NO ₂ Rock., Tetrazole Trans.	1139.85	Au	Χ	Z	N-N Stretch.
458.73	Bg	Z	Y	NO ₂ Rock., Tetrazole Trans.	1140.45	Bg	Z	Y	N-N Stretch.
458.76	Au	Υ	Z	NO ₂ Rock., Tetrazole Trans.	1150.86	Ag	Z	Y	N-N Stretch.
459.83	Bu	Υ	Z	NO ₂ Rock., Tetrazole Trans.	1151.36	Bu	\times	Z	N-N Stretch.
535.35	Au	Υ	Z	NO ₂ Rock., N-C-N Rotat.	1153.91	Bg	Z	Y	N-N Stretch.
537.15	Ag	Z	Y	NO ₂ Rock., N-C-N Rotat.	1154.59	Au	Χ	Z	N-N Stretch.
538.6	Bg	Z	Y	NO ₂ Rock., N-C-N Rotat.	1243.12	Bu	X	Z	$\mbox{N-C}$ Stretch., \mbox{NO}_2 Symmet. Stretch
539.03	Bu	Y	Z	NO ₂ Rock., N-C-N Rotat.	1244.54	Au	Υ	Z	$\mbox{N-C}$ Stretch., \mbox{NO}_2 Symmet. Stretch
556.38	Bu	Y	Z	NO ₂ Rock., N-C-N Rotat.	1246.18	Ag	Z	Y	$\mbox{N-C}$ Stretch., \mbox{NO}_2 Symmet. Stretch
556.70	Bg	Z	Y	NO ₂ Rock., N-C-N Rotat.	1250.00	Bg	Z	Y	N-C Stretch., NO ₂ Symmet. Stretch.
559.28	Au	Χ	Z	NO ₂ Rock., N-C-N Rotat.	1252.02	Au	Υ	Z	N-C Stretch NO, Symmet. Stretch.

Table 6.4 Calculated vibrational frequencies (in cm⁻¹) for DBX-1 (628 cm⁻¹ to 1457 cm⁻¹).

Mode	Symmetry	\mathbb{R}	Raman active	Assignment of modes	Mode	Symmetry	\mathbb{H}	Raman active	Assignment of modes
628.52	Au	Y	N	N-C-N Librat.	1254.27	$_{\mathrm{Bu}}$	Y	N	$\mbox{N-C}$ Stretch., \mbox{NO}_2 Symmet. Stretch.
629.63	Ag	Z	Y	N-C-N Librat.	1255.18	$^{\mathrm{Ag}}$	Z	Y	N-C Stretch., NO ₂ Symmet. Stretch.
632.17	Bu	X	Z	N-C-N Librat.	1329.04	Bg	Z	Y	N-C Stretch.
633.15	Bg	Z	Y	N-C-N Librat.	1329.22	Au	Χ	Z	N-C Stretch.
645.14	Ag	Z	Y	N-C-N Librat.	1330.60	Bu	Χ	Z	N-C Stretch.
646.51	Bu	X	Z	N-C-N Librat.	1331.64	Ag	Z	Y	N-C-N Stretch.
646.61	Au	X	Z	N-C-N Librat.	1339.71	Bu	\prec	Z	N-C-N Stretch.
647.22	Bg	Z	Y	N-C-N Librat.	1340.32	Bg	Z	Y	N-C-N Stretch.
666.28	Bu	X	Z	N-C-N Librat.	1340.66	Au	\prec	Z	N-C-N Stretch.
667.20	Ag	Z	Y	N-C-N Librat.	1342.28	Ag	Z	Y	N-C-N Stretch.
668.39	Bg	Z	Y	N-C-N Librat.	1389.56	Ag	Z	Y	N-C-N Stretch.
670.25	Au	Υ	Z	N-C-N Librat.	1391.76	Au	Y	Z	N-C-N Stretch.
672.60	Bu	X	Z	N-C-N Librat.	1392.71	Bu	\prec	Z	N-C-N Stretch.
673.60	Bg	Z	Y	N-C-N Librat.	1395.72	Bg	Z	Y	N-C-N Stretch.
674.49	Au	X	Z	N-C-N Librat.	1402.09	Au	\prec	Z	NO ₂ Asymmet. Stretch.
675.99	Ag	Z	Y	N-C-N Librat.	1402.62	$^{\mathrm{Ag}}$	Z	Y	NO ₂ Asymmet. Stretch.
737.47	Au	Χ	Z	C-N Librat.	1405.36	Bg	Z	Y	NO ₂ Asymmet. Stretch.
738.55	Bu	Χ	Z	C-N Librat.	1409.39	Bu	\prec	Z	NO ₂ Asymmet. Stretch.
738.81	Ag	Z	Y	C-N Librat.	1443.61	Bu	Χ	Z	NO ₂ Asymmet. Stretch.
739.90	$_{\mathrm{Bg}}$	Z	Y	C-N Librat.	1443.61	Ag	Z	Y	NO ₂ Asymmet. Stretch.
740.59	Au	Χ	Z	C-N Librat.	1445.38	$_{ m Bg}$	Z	Y	NO ₂ Asymmet. Stretch.
740.90	A_{g}	Z	¥	C-N Librat.	1447.13	Au	\prec	Z	NO ₂ Asymmet. Stretch.
742.17	$_{ m gg}$	Z	¥	C-N Librat.	1449.99	Au	\prec	Z	NO ₂ Asymmet. Stretch.
742.38	Bu	Χ	Z	C-N Librat.	1454.93	$_{ m Bg}$	Z	Y	NO ₂ Asymmet. Stretch.
798.59	Ag	Z	Y	NO_2 Sciss., C-N Stretch.	1456.28	Ag	Z	Y	NO ₂ Asymmet. Stretch.
799.57	$_{ m Bg}$	Z	Y	NO_2 Sciss., C-N Stretch.	1457.00	Bu	\prec	Z	NO ₂ Asymmet. Stretch.
799.95	Au	Τ	Z	NO ₂ Sciss., C-N Stretch.					
800.00	Bu	Χ	Z	NO_2 Sciss.					
803.37	Ag	Z	X	NO_2 Sciss.					
804.19	Bu	Χ	Z	NO_2 Sciss.					
805.15	Au	Χ	Z	NO_2 Sciss.					
805.66	Bg	Z	Y	NO_2 Sciss.					
995.95	Ag	Z	Y	N-N-N Sciss., N-N Stretch.					
90.966	Au	Χ	Z	N-N-N Sciss., N-N Stretch.					
996.94	$_{ m gg}$	Z	Y	N-N-N Sciss., N-N Stretch.					
997.16	Ag	Z	Y	N-N-N Sciss., N-N Stretch.					
997.33	Au	Χ		N-N-N Sciss., N-N Stretch.					
69 800	В,	>	2	N-N-N Sciss N-N Stretch					

6.3.3 Born effective charges (BEC's)

BEC's of DBX-1 are calculated using a linear response method with respect to the external electric field. The polarization for DBX-1 has been obtained from the Bloch functions to describe the ground state by using the Berry phase method [33, 34]. Table-6.5 shows the difference between the eigenvalues along principal axis for all atoms which can be attributed to strong anisotropy in $Z_{11} \neq Z_{22} \neq Z_{33}$. However, the sign of the nominal ionic value of Z* for the metal atom Cu and C are positive, and other atoms N, O are negative. The difference in sign of Z* in DBX-1 can be due to a change in polarization around the atom, which arises due to the difference between electronic structure, orbital hybridization, and even depends on the electronic configuration of atoms. The calculated diagonal elements Z₁₁, Z₂₂, Z₃₃ for C, N, O of DBX-1 are not close to nominal ionic values except Cu, indicating ionic interaction of Cu with surrounding N atoms. The electronegativity of C, N, and O atoms plays an important role in bonding and hybridization. The effective charge deviates from their nominal ionic values significantly for N, C, O, which indicate mixed ionic-covalent bond, as mentioned in the partial density of states. Moreover, the effective charge of N5, N10, C1, C2 are exceptionally large, where N atom is bonded with C atom and the same N atom is even bonded to O atoms, which can be noticed in Figure-6.1. The other N1, N2, N3, N4 atoms have an identical deviation because they are bonded together in the ring. This results in a stronger covalent interaction and hybridization between N-C, N-O bonds. The static dielectric tensor ϵ_0 consists of electronic and ionic contributions, it has been determined from the BEC's of the specified atoms. The calculated $\epsilon(\infty)$ defines the optical dielectric tensor and $\epsilon(0)$ describes the dielectric constant of each phonon mode. The $\epsilon(\infty)$ and $\epsilon(0)$ of DBX-1 are mentioned below:

The electronic and ionic dielectric constants values are averaged to 3.7 and 4.1. It can be noticed that the difference between electronic and ionic part contribution is not very large here which can be due to the lower bandgap within the semiconductor region. This result shows that the ϵ_0 main contribution is from [010] direction for DBX-1. The total static dielectric contribution of DBX-1 is obtained by summing up electronic and ionic parts, so the electronic dielectric constant of DBX-1 is 7.8.

$$\epsilon(\infty)^{DBX-1} \begin{bmatrix} 3.73 & 0 & -0.02 \\ 0 & 4.10 & 0 \\ -0.02 & 0 & 3.27 \end{bmatrix} \quad \epsilon(0)^{DBX-1} \begin{bmatrix} 4.07 & 0 & -0.03 \\ 0 & 4.66 & 0 \\ -0.03 & 0 & 3.66 \end{bmatrix}$$

6.3.4 Elastic properties

The mechanical stability of DBX-1 is understood using the elastic constants Cij(GPa), it is obtained using the stress-strain method implemented in CASTEP. This information plays a critical role in providing valuable information about the stability of the material

Table 6.5 Calculated BEC's of DBX-1 (C, N, O, Cu) at the theoretical equilibrium volumes.

Ion	Nominal ionic charge	Z_{11}	Z_{22}	Z_{33}
C1	+4	-0.227	0.242	-0.234
C2	+4	-0.234	0.124	-0.190
N1	-3	-0.005	0.145	-0.079
N2	-3	-0.453	-0.379	-0.218
N3	-3	-0.373	-0.053	-0.182
N4	-3	-0.255	-0.134	-0.039
N5	-3	1.740	1.798	1.635
N6	-3	-0.119	0.065	-0.368
N7	-3	-0.417	-0.200	0.170
N8	-3	0.303	-0.144	-0.106
N9	-3	-0.198	0.067	-0.152
N10	-3	1.610	2.161	1.408
O1	-2	-0.512	-1.389	-0.932
O2	-2	-1.142	-0.794	-0.567
O3	-2	-0.555	-1.220	-0.837
O4	-2	-0.956	-1.229	-0.519
Cu1	+1	0.534	0.407	0.657
Cu2	+1	0.517	0.532	0.558

and anisotropic binding characteristics between adjacent atomic planes. Moreover, it provides a link between the mechanical and dynamical behavior of crystal, at the same time crucial information related to the nature of the forces operating in solids is also revealed. DBX-1 being sensitive material, no experimental data has been reported to date. So, we tried to address the sensitivity and complexity through elastic constants Table-6.6. As mentioned in structural properties DBX-1 crystallize in monoclinic system, possessing 13 independent elastic constants, namely; C_{11} , C_{12} , C_{13} , C_{22} , C_{23} , C_{25} , C_{33} , C_{35} , C_{46} , C_{44} , C_{55} , C_{66} . The relative ordering of the three diagonal elastic stiffness constants for DBX-1 is as follows ($C_{22} > C_{11} > C_{33}$). Also, the calculated elastic stiffness constants satisfy mechanical stability criteria showing these compounds are mechanically stable. To have a better understanding of the stability, we have compared DBX-1 with well-known compound lead azide [35]. The diagonal elements C_{11} , C_{22} , C_{33} are very large for LA than DBX-1. This result shows LA is stiffest across a,b,c-axis than DBX-1. Also, it is observed that C_{22} in DBX-1 is the stiffest elastic constant which makes DBX-1 least sensitive along the b-axis, which is due to strong intermolecular interaction. The value of C_{33} is lesser

Table 6.6 Calculated elastic constants of DBX-1 compared with previously reported lead azide.

Elastic const.(GPa)	DBX-1(This work)	Lead azide [35]
C_{11}	66.69	103.5
C_{12}	62.133	46.19
C_{13}	19.81	37.30
C_{15}	-4.063	-
C_{22}	87.68	126.0
C_{23}	32.48	37.16
C_{25}	-3.688	-
C_{33}	36.56	47.98
C_{35}	-6.52	-
C_{46}	1.496	-
C_{44}	15.70	17.53
C_{55}	26.811	28.59
C_{66}	27.572	25.14
В	37.37	45.81

than the value of C_{11} , C_{22} , showing that the DBX-1 material is sensitive towards the c-axis. While the other values show that, C_{12} is less in LA than DBX-1, whereas C_{13} values tend to be high in LA. The other constant like C_4 and C_{55} show that $C_{44} < C_{55}$ in both DBX-1 and LA. The calculated bulk modulus for DBX-1 is around 37.37 GPa and the reported bulk modulus of LA is 45.81 GPa [35]. These bulk modulus values suggest that LA is harder than DBX-1.

6.3.5 Electronic band structure and density of states

The electronic structure and optical properties are obtained by considering the experimental crystal structure. To calculate the optical properties, as a first step it is necessary to obtain a good description of electronic structure. The band structure calculated across the high symmetry directions of the Brillouin zone of DBX-1 at 0 GPa is studied using GGA and improved modified Becke and Johnson potential (TB-mBJ) Figure-6.3. The Fermi level is chosen at zero value of energy. The highest valence band (VB) and lowest conduction band (CB) occur at A-B implying an indirect bandgap. It is well known that in the case of direct bandgap materials when an electron from the conduction band annihilates a hole in the valence band, surplus energy is released as a photon. Therefore emission of a photon is faster in the direct bandgap materials than in the indirect bandgap materials. The calculated band gap of 1.01 eV with GGA and 1.09 eV by TB-mBJ is in the range of semiconductors. There is no notable difference observed in the bandgap of DBX-1. This might be due to the fact that TB-mBJ potential, which underestimates the bandgap

of some solids (e.g. semiconductor, noble-gas solids, and transitions metal-oxides) [36]. Furthermore, the sensitivity of a material can be understood from its bandgap, Weihua Zhu and Heming Xiao et. al reported that the lesser the bandgap, the simpler the electron transfer from VB to CB, faster the solid decomposes and rapid it explodes. Also, impact sensitivity decreases as the bandgap decrease. For further understanding about the sensitivity of the DBX-1 we have compared the bandgap of some well-known materials i.e bandgap of lead styphnate (1.64 eV), [37] is quite close whereas lead azide (7.7 eV) [38] and mercury fulminate (4.92 eV) [39] have a wide bandgap. It may be thus inferred that DBX-1 is more sensitive to impact. Furthermore, as shown in Figure-6.3, there are three regions in the band structure: valence band (VB), the forbidden gap, and conduction band (CB). The energy distribution of VB and CB electronic states can be visualized using the partial DOS and total density of states (TDOS) Figure-6.4. For DOS calculation inputs are the energy eigenfunctions and eigenvalues are obtained from band structure calculation. The partial contribution of s, p and d orbital of N, C, O, and Cu are shown. To describe the electronic structure TDOS and PDOS, the first band in the PDOS is centered below 0 eV which arises mainly from Cu-d states and with a minimum contribution from O-2p and C/N-p states. The next band appears around between -2.5 eV to -4 eV, it is an attribute of O-2p, C/N-p states and occupies the largest number of states playing an important role in the bonding. While the valence band around 2.5 eV to 6 eV consists of hybridized C_p , N_p and O_{2p} state, stating strong covalent bond. Above the Fermi level (CB) near 1 eV, the PDOS originate mainly from O-2p states, N/C-pstates. To conclude, the bandgap lies in the visible region and has a stronger covalent character between N-C, N-O bonds.

6.3.6 Optical properties

The crystal structure of a material can be discussed efficiently by considering its optical properties. It helps us understand the occupied and unoccupied parts of the electronic band structure, and it also determines important information about the character of the bands. Figure-6.5 shows optical parameters reported to the energy range of 10 eV. The complex dielectric function is directly related to the propagation of electromagnetic (EM) waves in a medium and the interaction within EM waves and electrons. The response to electromagnetic radiation is measured by various optical constants such as real and imaginary parts of the dielectric function, absorption spectra, refractive index, reflection spectra, and energy-dependent loss function. The real part describes the dispersion and reveals to what extent the material can be polarized, whereas the imaginary parts represent the attenuation of light. The Figure shows the real and imaginary part of the complex dielectric function versus the photon energy (eV). The static dielectric constant $\epsilon_1(0)$ value in x,y,z-directions are 4.53[100], 5.38[010], 4.20[001] which averages to 4.70. From these results, we notice that the highest peak value of the real part corresponds to the high degree of polarization. The real part of the dielectric function $\epsilon_1(\omega)$ obtained

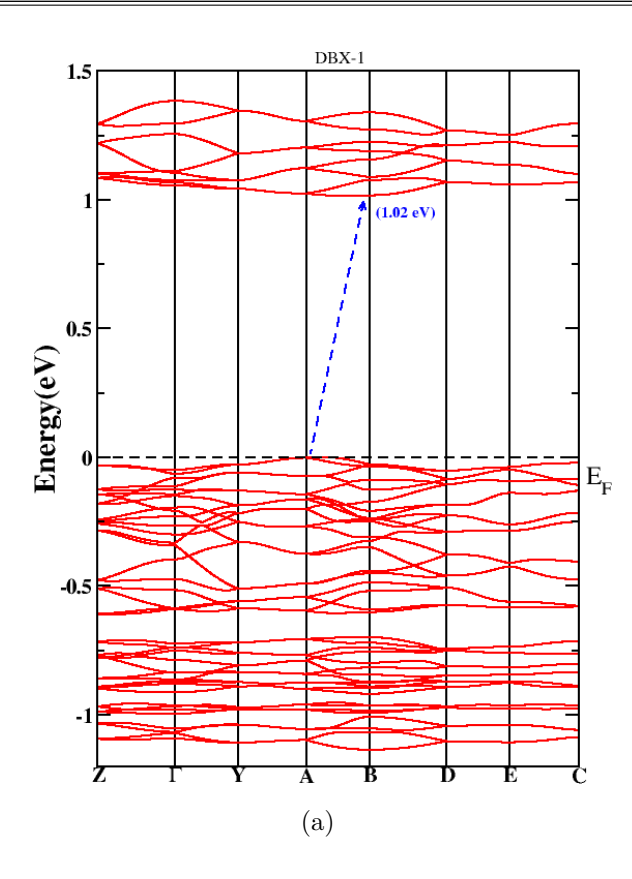


Figure. 6.3 Electronic band structure of DBX-1 along the high symmetry directions in the Brillouin zone.

at zero frequency is in visible region, then as photon energy increases peaks rise swiftly around [001: 5.62 at 1.12 eV], [010: 7.38 at 1.04 eV], [001:5.26 at 1.02 eV]. This result indicates the optical anisotropy in the low energy region, and the same continues in the high energy region. We are owing to the close relationship between the interband transitions and the imaginary part $\epsilon_2(\omega)$ of the dielectric function. We notice that high energy region $\epsilon_2(\omega)$ decreases gradually, showing that as energy increases the optical absorption of inter-band electron transitions decreases. It is observed from PDOS figure, dielectric peaks around 1.29 eV [100], 1.26 eV [010], 1.37 eV [001] occurs due to indirect transitions by N/C-p states to Cu-d states. The incident photon having energy greater than the threshold limit can interact with electrons in the VB and get absorbed. The absorption coefficient of DBX-1 starts at about 1 eV, which is the visible range. We notice that the absorption coefficient increases almost linearly with an increase in photons energy till 4 eV, then as the energy increases beyond 5 eV absorption tends to be maximum in the UV region. The magnitude of the highest peaks denote high absorption is at 77.84 at 4.74 eV and 67.95 at 6.25 in [010] direction. Moreover, the threshold value of absorption spectra is at 0.96 eV, which is usually smaller than the electronic gap, and the variation is because of the Coulomb energy. This result shows less absorption in the visible region when compared to the high-energy region (UV). From the refractive index $n(\omega)$ deter-

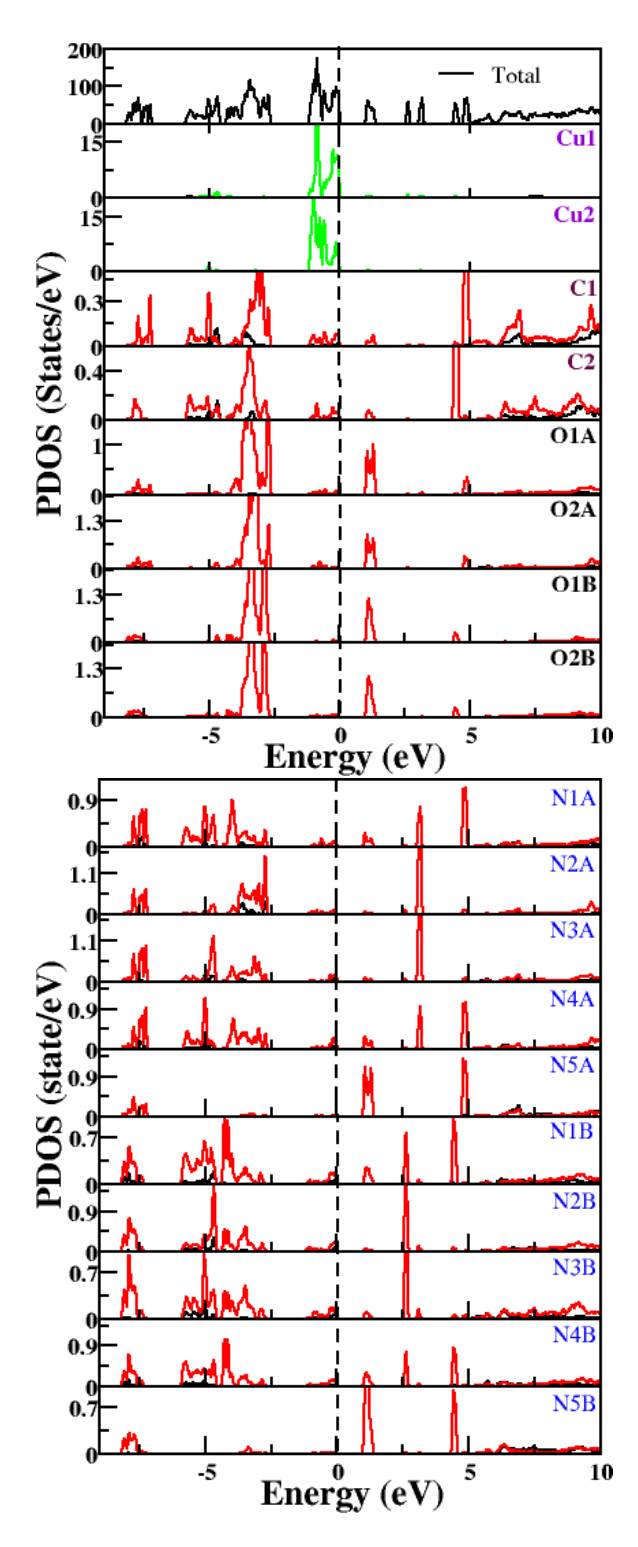


Figure. 6.4 Calculated partial and total density of states of DBX-1.

mines how much light travels while entering the material. The static refractive index $n(\omega)(0)$ of DBX-1 [001-2.31, 010-2.32, 001-2.05], these values are derived from the real part of dielectric function. As photon energy increases, the maximum refractive index is at 4.3 eV, then as energy increases the magnitude of the peak gradually decreases in the UV region. We show that DBX-1 shows anisotropic nature over the entire spectra. Reflectivity $R(\omega)$ at 0 eV is 0.13 and then swiftly rises with an increase in energy, around 1.07 eV there is a strong peak in [010] direction, y-direction due to the strong absorption. Also, the peak near 4.8 eV shows a sharp drop in reflectivity, implying a reduction of $\epsilon_1(\omega)$ close to zero. The results show that minimum reflectivity can be noticed in the visible region, and maximum reflectivity can be seen in the UV region. The electron energy loss spectra $L(\omega)$ describe how fast electron transfers through the medium. The energy-dependent loss function. The maximum energy loss can be noticed at 0.38, which can be seen at 4.99 eV in [100] and 0.47 at 6.68 eV [010] direction. These prominent peaks, which occur at maximum energy loss indicate a rapid reduction in the reflection. Finally, DBX-1 shows optical anisotropic nature, and maximum absorption tends to be in a higher energy region.

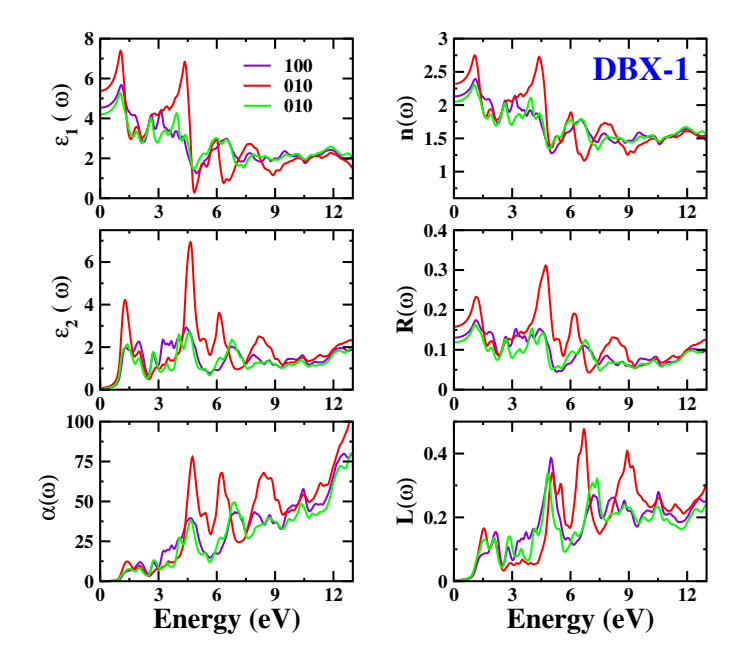


Figure. 6.5 The figure represents Dielectric constant, Dielectric loss, Absorption, Refraction, Reflectivity, Eloss function of DBX-1 using TB-mBJ functional at the experimental crystal structure.

6.4 Conclusions

In summary, ground-state properties such as structural, vibrational, born effective charges, elastic constants, electronic and optical properties of DBX-1 are investigated employing Density functional theory. The optimized lattice parameters are in good agreement with the experimentally reported values. Our results demonstrate that peak near 800cm^{-1} is due to N-C-N stretching, and high-intensity peaks from 1200 cm^{-1} to 1500 ^{-1} are because of symmetric and asymmetric stretching of NO₂ group. The born effective charges reveal the ionic nature between copper (Cu) and nearby nitrogen (N) atoms and the covalent nature in N-O bonds. Also, the difference between electronic and ionic contributions is not very large. At ambient conditions, the calculated elastic constants determine that DBX-1 is a mechanically stable material. Also, DBX-1 tends to be more sensitive towards C_{33} 'c' axis. The electronic bandgap lies in the visible region, stating DBX-1 would decompose fast and be more sensitive towards external stimuli. Based on the dielectric functions obtained, the static dielectric constant is 4.70, and 2.1 is the refractive index. In addition, DBX-1 is optically anisotropic in visible and UV regions.

References

- [1] Klapötke. T. M., Davin. P., Neha. M., O. Karl, S. Jesse., Reaction of DBX-1 with Sodium m-Periodate., Z. Naturforsch., 2014, 69b, 125-127.
- [2] Costain. T., F. B. Wells in Energetic Materials, Vol. 2, Technology of the Inorganic Azides (Eds.: H. D. Fair, R. F. Walker), 1977, Plenum Press, New York, NY. 11.
- [3] Fischer. D., Klapötke. T. M., Piercey. D. G., Stierstorfer J., Copper Salts of Halo Tetrazoles Laser-Ignitable Primary Explosives, J. Energ. Mater., 2012, 30, 1, 40-54.
- [4] Costain, A New Method for Making Silver Azide, Technical Report 4595, Picatinny Arsenal, Dover, N.J., February 1974, U.S. Pat., 1976, 3, 943, 235.
- [5] Fischer. D., Klapötke. T. M., Piercey D. G., Stierstorfer. J., Copper Salts of Halo Tetrazoles Laser-Ignitable Primary Explosives, Journal of Energetic Materials, 2012, 30, 1, 40-54.
- [6] Fischer. N., Klapötke. T. M., Stierstorfer. J., Calcium 5-Nitriminotetrazolate, A Green Replacement for Lead Azide in Priming Charges, J. Energ. Mater., 2011, 29, 1, 61-74.
- [7] Huynh. M. H. V., Hiskey. M. A., Meyer. T. J., Wetzler M., Green primaries Environmentally friendly energetic complexes, Proc. Natl. Acad. Sci. USA, 2006, 103, 14, 5409-5412.
- [8] Clark. L. V., Diazodinitrophenol, a Detonating Explosive, Ind. Eng. Chem., 1933, 25, 6, 663-669.
- [9] Davis. T. L., The Chemistry of Powder and Explosives, GSG Associates, San Pedro, CA, 1943, 191-458.
- [10] Holl G, Klapötke. T. M, Polborn K, Rienacker C, Structure and Bonding in 2-diazo-4,6-dinitrophenol (DDNP), Propellants Explosives Pyrotechnics, 2003, 28, 3, 153-156.
- [11] Dorman. D. C., National Research Council Report Potential Health Risks to DoD Firing-Range Personnel from Recurrent Lead Exposure, The National Academies Press, Washington, D. C., 2012.
- [12] Barsan. M. E., Miller A., Lead Health Hazard Evaluation, HETA, National Institute for Occupational Safety and Health, Cincinnati, OH, USA 1996.
- [13] Giles. J., Collateral damage. Nature, 2004, 427, 580-581.

- [14] Fronabarger. J. W., Williams. M. D., Sanborn W. B., Bragg J. G., Parrish D. A., Bichay M., DBX-1 A lead free replacement for lead azide., Propellants Explos. Pyrotech., 2011, 36, 541-550.
- [15] Sanborn W., Fronabarger J., Williams M., Critical Temperature Determinations for the Lead-Free Primary Explosives DBX-1 and KDNP. 2010, 46th AIAA/ASME/SAE/ASEE Joint Propulsion Conference, Exhibit 25 to 28 July 2010.
- [16] Jan. A. P., Neha M., Karl. D. Oyler, Gartung. C., Akash. S., KinYee, Magdy. B., Improved Safety and Loadability of Coated DBX-1., J. Energ. Mater., 2016, 35, 2.
- [17] Thomas. K., Davin. P., Neha. M., Karl O., Matthew. J., Salan. L. S., Fronabarger. J. W, Williams. M. D., Preparation of High Purity Sodium 5-Nitrotetrazolate (NaNT) An Essential Precursor to the Environmentally Acceptable Primary Explosive, DBX-1., Z. Anorg. Allg. Chem., 2013, 639, 681-688.
- [18] Dennis. F., Thomas, M. Klapötke, Jörg. Stierstorfer, Potassium 1,1'-Dinitramino-5,5'-bistetrazolate: A Primary Explosive with Fast Detonation and High Initiation Power, 2014, 53, 31, 8172-8175.
- [19] Segall. M. D., Lindan. P. J. D., Probert. M. J., Pickard. C. J., Hasnip. P. J., Clark S. J., Payne M. C., First-principles simulation ideas, illustrations and the CASTEP code, J. Phys. Condens., 2002, 14, 2717-2743.
- [20] Milman. V., Refson K., Clark. S. J., Pickard. C. J., Yates. J. R., Gao S-P, Hasnip P. J., Probert M. I. J., Perlov A., Segall M. D., Electron and vibrational spectroscopies using DFT, plane waves and pseudopotentials CASTEP implementation, J. Mol. Struct., 2010, 954, 1-3, 22-35.
- [21] Ceperley. D., Alder. B. J., Ground-State of the Electron-Gas by A Stochastic Method, Phys. Rev. Lett., 1980, 45, 566.
- [22] Perdew. J., Burke. K., Ernzerhof M., Generalized Gradient Approximation Made Simple, Phys. Rev. Lett., 1996, 77, 3865-3868.
- [23] Fischer. T., Almlof. J., General Methods for Geometry and Wave Function Optimization, J. Phys. Chem., 1992, 96.
- [24] Ceperley. D., Alder. B. J., Ground-State of the Electron-Gas by A Stochastic Method, Phys. Rev. Lett., 1980, 45, 566.
- [25] Perdew. J., Zunger. A., Self-Interaction Correction to Density-Functional Approximations for Many-Body Systems. Phys. Rev. B., 1981, 23, 5048-5079.
- [26] Perdew. J. P., Chevary. J. A., Vosko. S. H., Jackson. K. A., Pederson. M. R., Singh, D. J., Fiolhais, C., Atoms, molecules, solids, and surfaces: Applications of the generalized gradient approximation for exchange and correlation, Phys. Rev. B,1992, 46, 6671-6687
- [27] Tkatchenko. A., Scheffler. M., Accurate Molecular Van Der Waals Interactions from Ground-State Electron Density and Free-Atom Reference Data, Phy. Rev. Lett., 2009, 102, 073005.
- [28] Grimme. S., Semiempirical GGA-type density functional constructed with a long-range disper-

- sion correction, J. Compu. Chem., 2006, 27, 1787.
- [29] Ortmann. F., Bechstedt. F., Schmidt. W. G., Semiempirical van der Waals correction to the density functional description of solids and molecular structures, Phys. Rev. B., 2006, 73, 205101.
- [30] Baroni. S., de Gironcoli, S., Dal. Corso, A., Giannozzi. P., Phonons and related crystal properties from density-functional perturbation theory, Rev. Mod. Phys., 2001, 73, 515-562.
- [31] Blaha. P., Schwarz, K., Madsen, G. K. H., Kvasnicka, D., Luitz, J., 2001 WIEN2K, an Augmented Plane Wave + LocalOrbitals Program for Calculating Crystal Properties (Austria: Techn. Universitat).
- [32] David. K., Fabien T., Peter B., Improving the modified Becke-Johnson exchange potential. Phys. Rev. B., 2012, 85, 155109.
- [33] King Smith. R. D., Vanderbilt. D., Theory of polarization of crystalline solids, , Phys. Rev. B., 1993, 47, 1651.
- [34] Resta. R., Macroscopic Electric Polarization as a Geometric Quantum Phase, Europhys. Lett., 1993, 22, 133.
- [35] Perger. W., First-Principles Calculation of Second-Order Elastic Constants and Equations of State for Lithium Azide, LiN3, and Lead Azide, International Journal of Quantum Chemistry - Int. J Quantum. Chem., 2009, 110.
- [36] Koller. David., Fabien. Tran., P. Blaha., Improving the modified Becke-Johnson exchange potential., Phys. Rev. B., 85, 2012, 155109.
- [37] Weihua. Z., Heming X., First-Principles Study of Electronic, Absorption, and Thermodynamic Properties of Crystalline Styphnic Acid and Its Metal Salts, J. Phys. Chem. B, 2009, 113, 30, 10315-10321.
- [38] Aduev. B. P., Aluker, E. D., Belokurov, G. M., Drobchik A. N., Krechetov, A. N., Mitrofanov, A. Yu., Kuklya, M. M., Younk, E. H., Kunz, A. B., Lead azide pre-explosive luminescence., Russ. Phys. J., 2000, 43, 181-184.
- [39] Yedukondalu. N., Vaitheeswaran. G., Structural, electronic and optical properties of well-known primary explosive Mercury fulminate. J. Chem. Phys., 2015, 143, 204704.



Summary & Future scope

7.1 Summary

The results reported in this thesis are based on first-principles calculations within density functional theory (DFT). The focus has been directed to calculate the ground-state properties of solid energetic materials. The first chapter gives a brief introduction about materials chosen and background literature regarding it, while the second chapter introduces the techniques and computational parameters used. The calculations were carried out using a quantum mechanics-based plane-wave pseudopotential method implemented in CASTEP. Norm conserving and ultrasoft pseudopotential approach with fully converged parameters have been considered to calculate structural, vibrational, Born effective charges, and elastic constants. In addition, electronic and optical properties computed in the entire thesis were performed using the FP-LAPW method implemented in WIEN2k. The goal of this thesis is to explore the physical and chemical properties of alkali metal series with two different functional groups, namely perchlorates and 5-aminotetrazole. We have also studied the effect of hydrostatic pressure (till 3 GPa) on hydrogen bonds in nitrogen-rich alkali metal 5-aminotetrazole materials. In the last two chapters, we have focused on possible replacement materials for rooted ammonium perchlorate and lead azide. Furthermore, we also have studied the role of van der Waals interactions in alkali metals perchlorate, alkali metal 5-aminotetrazole, HNF, ADN, KDN, and DBX-1. We even address the effect of hydrogen bonds influencing the macroscopic properties and energetic performance of hydrogen-based HNF and ADN. The structural properties calculated using PBE+G06 and PW91+OBS show a good agreement with the experimental data, respectively. Summary of the main results are presented at the end of each subsection in Chapters 3, 4, 5, and 6 will be briefly highlighted here:

We have investigated structural, vibrational, born effective charge (BEC), electronic and

optical properties of the alkali metal perchlorates and alkali metal 5-aminotetrazole. Due to the poisonous and harmful nature of perchlorate to humans in several forms. In chapter four, we have again chosen alkali metal series with a 5-aminotetrazole group, where 5-aminotetrazole is known for its high nitrogen content. The structural parameters obtained in perchlorates and 5-aminotetrazole show that PBE+G06 and PW91+OBS functional agree with experimental values compared with GGA-PBE, PW91, and LDA functional. This study shows van der Waals's interaction in crystal binding and the structure-related properties with the ionic solids. Whereas in the case of HNF ADN, KDN and DBX-1 vdW are predominant, assuring the importance of dispersion corrected DFT to describe the oxidizers and primary explosive.

The ground state structural and vibrational properties of perchlorates and 5-aminotetraozle are mentioned. Our results show that symmetric and asymmetric stretching modes are more pronounced in ClO₄, and the effective charge of Cl highly deviates from nominal charge indicating high polarization in perchlorates. Also, as the wavelength decreases with an increase in the frequency from $Li \rightarrow Na \rightarrow K \rightarrow Rb \rightarrow Cs$. In the case of 5-At, We have shown that computed vibrational frequencies at ambient pressure show that vibrational modes in high energy regions are due to the N-H bond of NH₂ group. Pressure variation IR spectra of these materials show clear frequency shifts where Li 5-At shows an overall redshift below 900 cm⁻¹ contrary to the blue shift seen in other materials in this range. The born effective charge of Cl highly deviates from nominal charge indicating high polarization in perchlorate's, whereas, in 5-At presence of strong covalency between N, H, and C atoms and an increased ionic nature as the atomic number increases has been noticed in both the groups. This concluded that ClO_4 in perchlorates and NH_2 group in 5-At play a crucial role in decomposition. The main point to be noted is that in both the systems, ground-state properties of NaClO₄ and Na 5-At properties are slightly different when compared to other materials and the same is observed in high-pressure studies in Na 5-At.

The electronic band structure of alkali metal perchlorates and 5-aminotetrazole are calculated using TB-mBJ potential and found that all the studied compounds are wide-bandgap insulators. The calculated band gap by TB-mBJ potential is improved to a greater extent when compared with conventional PBE. Several theoretical works have been carried for MClO₄, whereas for M 5-At, there are no experimental results to compare. The present study shows, all the compounds in MClO₄(M = Li. Na, K, Rb, Cs) show indirect bandgap while in the M 5-At (M = Na, K, Rb, Cs) compounds depict an indirect bandgap and Li 5-At shows a direct bandgap. Furthermore, the partial and total density of states MClO₄(M = Li. Na, K, Rb, Cs) reveal that valance bands are flat and narrow. The bands near the valence states are highly dominated with O-2p states and Cl-d states, and increasing s/p states in metal atoms have been observed as atomic mass increases. Around 3 eV,

we observe there is overlap between O-2p and Cl-d states resulting in hybridization. This concludes that alkali metal perchlorates have a mixed nature of bonding and may find application as inorganic scintillators. In the case of M 5-At, PDOS for monoclinic, triclinic, and orthorhombic structures shown reveals that the ultraviolet response of alkali metal 5-aminotetrazole is mainly contributed by the transitions of N/C-p states in the valence band (VB) to metal atom K, Rb, Cs-d states in the conduction band (CB). The above observation reveals that bonding in the alkali metals perchlorates and 5-aminotetrazole is ionic in metal atoms and covalent nature ClO₄ group and NH₂ group. Optical properties calculated from electronic band structure are of significant interest in determining the photodecomposition mechanism. While the optical constant such as real and imaginary dielectric constant, absorption, refraction, reflection, loss spectrum as functions of photon energy is discussed. In alkali metal perchlorates, all the studied compounds are optically isotropic with an anisotropic structure, whereas M 5-At, all the studied compounds are optically anisotropic. We concluded that Na metal shows distinct behavior according to the molecule group.

Further in the 5 chapters, we have chosen HNF, ADN, and KDN, where HNF is a replacement for ADN and ADN is a possible replacement for rooted ammonium perchlorate. As discussed in the previous chapter, the perchlorates molecule causes environmental problems such as ozone depletion in the stratosphere and acid rain. So we have done a comparative study of three oxidizers, HNF, ADN, and KDN. Structural, vibrational, born effective charges, phonon spectra, electronic and optical properties are calculated and discussed. The three compounds belong to the same space group number 14, where HNF and ADN crystallize in different settings $P2_1/c$ and KDN in $P2_1/n$. The vibrational properties, Born effective charges, and dielectric tensors were calculated using the DFPT analysis of vibrational frequencies reveal that vibrations in HNF are N-H bond, NH₂ group and in ADN and KDN, its is mainly due to NO₂. We have also calculated and presented BEC's and dielectric tensors. In the phonon dispersion curves of ADN and KDN, both compounds are found to be dynamically stable. From the phonon density of states, it is clear that the lower atomic mass of H may be expressed as frequencies shift toward higher wave number, and due to K atom high atomic mass, frequencies shifts towards lower wavenumber. We can clearly say that KDN is a mechanically stable material satisfying the stability criteria from the computed elastic constants. In addition, we can conclude that KDN might possess lower thermal conductivity than ADN. Furthermore, the electronic bandgap for HNF, ADN, and KDN has been calculated by TB-mBJ potential using the FP-LAPW method. It is found that HNF, ADN, and KDN are insulators, with O-2p and N-p states contributing mainly in the valency region. From the optical constant, we show that all three compounds are sensitive to ultraviolet light.

In the last chapter, this work presents the primary explosive known for its sensitivity and

rapid transition from combustion to detonation. Lead azide has been regularly utilized as a primary explosive for decades. Due to toxic nature, many materials have been synthesized where DBX-1 is one of possible replacement of lead azide. Therefore, we have studied structural, vibrational, elastic, born effective charges, electronic and optical properties of DBX-1. The structural parameters, volume are in good agreement with the experimental data. The vibrational modes from the optimized lattice constants are analyzed at Γ point from the crystal symmetry. Our results demonstrate that in peak about $800 \mathrm{cm}^{-1}$ is due to N-C-N stretching, and high intensity peaks from 1200 cm⁻¹ to 1500 ⁻¹ are due to symmetric and asymmetric stretching of NO₂ group. Furthermore, the calculated elastic properties show that DBX-1 is mechanically stable in ambient situations. The Born effective charge and the static dielectric tensor of these materials have also been calculated. The sign and the absolute value of the BEC's are different, leading to a significant difference in their interlayer interaction and interaction strength, which is directly related to anisotropy in k lattice. The born effective charges reveal the ionic nature between copper (Cu) and nearby nitrogen (N) atoms and the covalent nature in N-O bonds. At ambient conditions, the calculated elastic constants determine that DBX-1 is a mechanically stable material. Also, DBX-1 tends to be more sensitive towards C₃₃ 'c' direction. In addition, we have calculated electronic structure and optical properties using TB-mBJ potential. The fundamental energy bandgap appears to be indirect around 1.08 eV. The electronic bandgap lies in the visible region, stating DBX-1 would decompose fast and be more sensitive towards external stimuli. The partial and total density of states has been explained to explicate the contribution of anion and cation states from the electronic band structure. The valence band and conduction band in DBX-1 is dominated by Cu-p/d states, O-2pand N-p state. Using electronic structure results, we discuss directional optical properties and predict the optically anisotropic nature of these materials, the real and imaginary parts of the dielectric function, refractive index, absorption coefficient, and energy loss spectra. The obtained dielectric functions show that the static dielectric constant is 4.70, and 2.1 is the refractive index. In addition, DBX-1 is optically anisotropic in visible and UV regions.

7.2 Future scope

This thesis presents the basic physical and chemical properties of various materials mentioned, but work can be improved in various aspects. In continuation to this work, the next work would be on 2,4-Dinitroanisole (DNAN) and 5-Aminotetrazolium (5-ATZN or 5-ATN). In high energy materials, sensitivity, hygroscopic nature, stability play an important role in structure-property-performance. By using DFT techniques, we can add various groups and specific elements by replacing known elements in the system with various energetic materials, by which we can predict new materials. This can give a new path way to synthesize new green energetic materials.

List of Publications

Journal Papers:

- 1. **Prathap Kumar Jharapla**, E. Narsimha Rao, and G. Vaitheeswaran, *Unusual optical isotropy in anisotropic alkali metal perchlorates MClO*₄ (M = Li, Na, K, Rb, Cs), J. Phys.: Condens. Matter, 28, 30, 47, 475402, **2018**.
- Prathap Kumar Jharapla, Subrata Mondal, G. Vaitheeswaran, Comparative DFT study of vibrational, electronic and optical properties of energetic metal salts based on nitrogen rich 5-aminotetrazole, J. Comput. Chem., 42, 180-191, 2021.
- 3. Prathap kumar Jharapla, G. Vaitheeswaran, M.K. Gupta, R. Mittal, Comparative study of electronic structure, optical properties, lattice dynamics and thermal expansion behavior of energetic ammonium and potassium dinitramide salts, Materials Chemistry and Physics, 267, 124645, 2021.

Publications not included in the thesis:

- 1. B. Moses Abraham, **Prathap Kumar Jharapla** and G. Vaitheeswaran, *High pressure studies of hydrogen bonded energetic material* 3,6-dihydrazino-s-tetrazine using DFT, ACS Omega, 3, 8, 9388, (2018).
- 2. S.Mondal, **Prathap kumar Jharapla** and G. Vaitheeswaran, Structure-property correlations of bis(nitrofurazano) furazan (BNFF-1): A density functional theory study, DAE Solid State Physics Symposium, AIP Conf. Proc., 2115, 030391-1-030391-4, (2018).
- 3. Bagvanth Reddy Sangala, **Prathap Kumar Jharapla**, Rajkumar Golconda, Kurumurthy Guda and G. Vaitheeswaran, *Terahertz Optical Constants of Solid CO*₂, Journal of Infrared, Millimeter, and Terahertz Waves, 41, 871–879, (2020).

Manuscripts under preparation:

• Prathap Kumar Jharapla, First principle study of potential replacement of lead azide and Ammonium dinitramide: DBX-1 and HNF, (2021).

Schools/Workshops:

- 10th International High Energy Materials Conference and Exhibit (HEMCE), 11-13th February (2016).
- Workshop on "Modeling and Simulations of Nanomaterials using VASP" organized by Centre for Clean Energy and Nanoconvergence, Hindustan University, Chennai during 20 - 21st February, (2017)
- National conference on physics at small scales and advance materials, School of physics, University of Hyderabad, 8-9th September, (2017)
- Sorbonne-JNCASR School on Advanced Computational Material Science jointly organized by Sorbonne University, Paris and JNCASR, Bangalore, 29 th Jan - 02nd Feb, (2018)
- Workshop on Functional Magnetic Materials organized by UGC Networking Resource Centre, School of Physics, University of Hyderabad during 26th February - 3rd March, (2018)
- Workshop on Characterization and Modelling of Magnetic materials Department of physics, Birla Institute of technology and science, Hyderabad, 13th-14th July, (2018)

Conference Proceedings:

• S.Mondal, **Prathap kumar Jharapla**, G. Vaitheeswaran, Structure-property correlations of bis(nitrofurazano) furazan (BNFF-1): A density functional theory study, DAE Solid State Physics Symposium, AIP Conf. Proc., (2018).(POSTER)

Conference Presentations (National/International):

- B. Moses Abraham, **Prathap Kumar Jharapla** and G. Vaitheeswaran, *High pressure studies of hydrogen bonded energetic material 3,6-dihydrazino-s-tetrazine using DFT*, International Conference on Electronics, Physics and Chemistry, Jyothi Nivas College, Bangalore, February, **(2017)** (ORAL)
- S.Mondal, **Prathap kumar Jharapla** and G. Vaitheeswaran, Structure property correlations of bis(nitrofurazano) furazan (BNFF-1)- A density functional theory study, DAE Solid State Physics Symposium, AIP Conf. Proc., (2018).(POSTER)
- Prathap Kumar Jharapla, Subrata Mondal, G. Vaitheeswaran, Comparative DFT study of vibrational, electronic and optical properties of energetic metal salts

based on nitrogen rich 5-aminotetrazole, International conference on condensed matter physics, Institute of Engineering and Management, Kolkata, collaboration with AIP, $14-16^{th}$ November., **(2019)** (**ORAL**)

Ab initio study of solid energetic materials

by Prathap Kumar Jharapla

G. Vaithees wor an

Dr. G.S. Vaitheeswaran
Associate Professor
School of Physics
University of Hyderabad
Hyderabad-500 046. (TS) INDIA

Submission date: 01-Nov-2021 11:21AM (UTC+0530)

Submission ID: 1689740087

File name: Thesisplagarism.pdf (5.03M)

Word count: 50506

Character count: 248137

ORIGINALITY REPORT

44%
SIMILARITY INDEX

10%
INTERNET SOURCES

38%

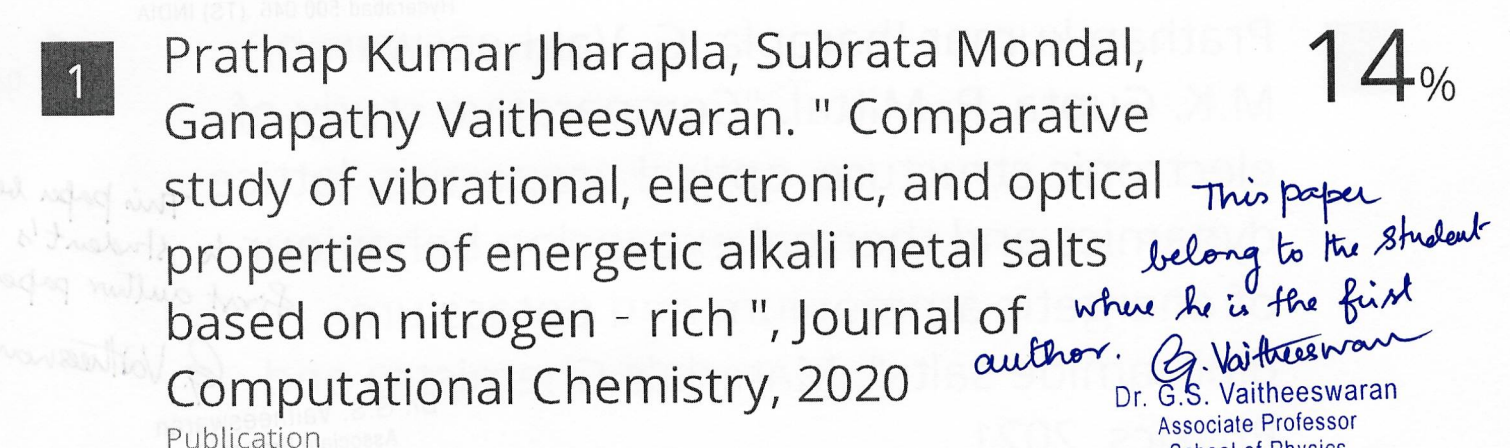
4%

STUDENT PAPERS

School of Physics University of Hyderabad

Hyderabad-500 046. (TS) INDIA

PRIMARY SOURCES



2

Prathap kumar Jharapla, G. Vaitheeswaran, 10% M.K. Gupta, R. Mittal. "Comparative Study of Electronic structure, Optical properties, Lattice this paper dynamics and Thermal expansion behaviour to the of energetic Ammonium and Potassium the first author dinitramide salts", Materials Chemistry and G. Witherson Or. G.S. Vaitheeswaran Associate Professor School of Physics University of Hyderabad

2

Prathap kumar Jharapla, NARSIMHA RAO

Elaprolu, Ganapathy Vaitheeswaran. "Unusual optical isotropy in anisotropic alkali metal to the shellow perchlorates MClO₄ (M = Li, Na, K, Rb, Cs)", first aultur belan Journal of Physics: Condensed Matter, 2018 G. William Publication

Dr. G.S. Vaitheeswaran
Associate Professor
School of Physics
University of Hyderabad
Hyderabad-500 046. (TS) INDIA

4	Prathap Kumar Jharapla, Elaprolu Narsimha Rao, G Vaitheeswaran. "Unusual optical This paid isotropy in anisotropic alkali metal to Shudent's firm perchlorates M (M = Li, Na, K, Rb, Cs) ", Journal of Physics: Condensed Matter, 2018pr. G.S. Vaitheeswara Associate Professor School of Physics	of author G. Voitherswar
5	Prathap kumar Jharapla, G. Vaitheeswaran, M.K. Gupta, R. Mittal. "Comparative study of electronic structure, optical properties, lattice dynamics and thermal expansion behaviour & of energetic ammonium and potassium	1% This paper below student's wither paper
SWaran essor sics lerabad (TS) WDIA	dinitramide salts", Materials Chemistry and Pr. 6.S. Vaitheesward Associate Professor School of Physics University of Hyderabad Hyderabad-500 046. (TS) INI	
6	www.researchgate.net Internet Source	1%
7	Submitted to University of Hyderabad, Hyderabad Student Paper	1%
8	edoc.ub.uni-muenchen.de Internet Source	1%
9	physik.uni-graz.at Internet Source	<1%
10	research.chalmers.se Internet Source	<1%
	othes.univie.ac.at	

othes.univie.ac.at
Internet Source

()	moo.iqpm	<1%
12	raiith.iith.ac.in Internet Source	<1%
13	Submitted to Higher Education Commission Pakistan Student Paper	<1%
14	mafiadoc.com Internet Source	<1%
15	Submitted to University of Sheffield Student Paper	<1%
16	kth.diva-portal.org Internet Source	<1%
17	silo.pub Internet Source	<1%
18	Submitted to University of Witwatersrand Student Paper	<1%
19	www-users.york.ac.uk Internet Source	<1%
20	B. Moses Abraham, J. Prathap Kumar, G. Vaitheeswaran. "High-Pressure Studies of Hydrogen-Bonded Energetic Material 3,6-Dihydrazinotetrazine Using DFT", ACS Omega, 2018 Publication	<1%

21	mdpi.com Internet Source	<1%
22	www.mdpi.com Internet Source	<1%
23	Submitted to Otto-von-Guericke-Universität Magdeburg Student Paper	<1%
24	hdl.handle.net Internet Source	<1%
25	Submitted to University of Leicester Student Paper	<1%
26	worldwidescience.org Internet Source	<1%
27	comporgchem.com Internet Source	<1%
28	www.science.gov Internet Source	<1%
29	Submitted to Indian Institute of Technology Student Paper	<1%
30	www.currentscience.ac.in Internet Source	<1%
31	etheses.dur.ac.uk Internet Source	<1%
32	publica.fraunhofer.de	

Submitted to University of Glamorgan

. 42	Student Paper	<1%
43	ntnuopen.ntnu.no Internet Source	<1%
44	Submitted to Central University of Gujarat Student Paper	<1%
45	home.iitk.ac.in Internet Source	<1%
46	thesesups.ups-tlse.fr Internet Source	<1%
47	www.ncbi.nlm.nih.gov Internet Source	<1%
48	arxiv.org Internet Source	<1%
49	www.dbs.informatik.uni-muenchen.de Internet Source	<1%
50	www.scielo.br Internet Source	<1%
51	Submitted to Universiti Sains Malaysia Student Paper	<1%
52	Submitted to University of Westminster Student Paper	<1%
53	scholarbank.nus.edu.sg	<1%

54	dspace5.zcu.cz Internet Source	<1%
55	epdf.pub Internet Source	<1%
56	pt.scribd.com Internet Source	<1%
57	ijceronline.com Internet Source	<1%
58	wiredspace.wits.ac.za Internet Source	<1%
59	www.gidb.itu.edu.tr Internet Source	<1%
60	Submitted to Middle East Technical University Student Paper	<1%
61	moam.info Internet Source	<1%
62	skinny.dk Internet Source	<1%
63	G. Shwetha, V. Kanchana, K. Ramesh Babu, G. Vaitheeswaran, M. C. Valsakumar. "High-Pressure Structural Stability and Optical Properties of Scheelite-type ZrGeO and HfGeO X-ray Phosphor Hosts", The Journal of Physical Chemistry C, 2014	<1%

64	Submitted to Pacific University Student Paper	<1%
65	repositorio.ucv.edu.pe Internet Source	<1%
66	tsukuba.repo.nii.ac.jp Internet Source	<1%
67	www.yumpu.com Internet Source	<1%
68	E. Narsimha Rao, G. Vaitheeswaran, A. H. Reshak, S. Auluck. "Effect of lead and caesium on the mechanical, vibrational and thermodynamic properties of hexagonal fluorocarbonates: a comparative first principles study", RSC Advances, 2016 Publication	<1%
69	Submitted to Indian Institute of Technology, Madras Student Paper	<1%
70	Submitted to Southern New Hampshire University - Continuing Education Student Paper	<1%
71	Submitted to University College London Student Paper	<1 %
72	Submitted to University of Lancaster Student Paper	<1%

73	cmt.ua.ac.be Internet Source	<1%
74	iopscience.iop.org Internet Source	<1%
75	repository.lib.ncsu.edu Internet Source	<1%
76	websiteyonetimi.ahievran.edu.tr	<1%
77	www.doria.fi Internet Source	<1%
78	www.tandfonline.com Internet Source	<1%
79	Submitted to University of Rajshahi Student Paper	<1%
80	Yedukondalu, N., and G. Vaitheeswaran. "Abinitio study of structural, vibrational and optical properties of solid oxidizers", Materials Chemistry and Physics, 2016. Publication	<1 %
81	amsdottorato.unibo.it Internet Source	<1 %